

TO MY PARENTS

DYNAMIC CHARACTERISTICS OF TURBINE JOURNAL BEARINGS

by

METİN AKKÖK

A thesis submitted for the degree of

Doctor of Philosophy

of the

University of London

and also for the

Diploma of Imperial College

March 1980

Applied Mechanics Group
Department of Mechanical Engineering
Imperial College of Science & Technology
London SW7 2BX

ABSTRACT

The dynamic characteristics of circular and non-circular bearings are investigated theoretically and experimentally for various geometric parameters.

The analysis is based on the precept that the dynamic properties of a bearing can be represented by a set of stiffness and damping coefficients. These coefficients were used directly in unbalance response calculations and in the determination of self-excited whirl instability.

A test rig and suitable methods of bearing assessment were developed. The static and dynamic characteristics of four basic bearing types were experimentally determined. The bearings investigated were: circumferential groove 360° circular bearing with $L/D = \frac{1}{2}$, circular 30° and 90° axial groove bearings with $L/D = \frac{1}{2}$, 30° axial groove elliptical bearing with preloading of 0.4, 0.5, 0.6 and 0.75 with $L/D = \frac{3}{4}$, and 60° axial groove offset halves bearing with preloading of 0.4, 0.5 and 0.6 with $L/D = \frac{3}{4}$.

The steady-state and dynamic characteristics of the bearings tested were calculated for a range of eccentricity ratios and presented as non-dimensional variables in graphical form. These were compared with the measured performance of the bearings. It was found that the experimental results were in good agreement with the theoretical analysis.

In moderately and heavily loaded conditions, the elliptical bearing has the best stability and dynamic response characteristics, while in lightly loaded conditions, the offset halves bearing is superior.

* the ratio of the geometric preset of the arc centre to the arc clearance

ACKNOWLEDGEMENTS

I would like to express my gratitude to my supervisor, Dr C.M.M. Ettles, for his invaluable suggestions, guidance and encouragement during the course of this investigation.

Thanks are also due to Mr R. Church for his helpful suggestions in the construction and operation of the test rig, and to Mr R. Dobson and Mr T. Wymark for their technical advice. My thanks also to Mrs E.A. Hall for the typing of this manuscript.

My appreciation is also due to the Science Research Council for their financial support and for providing me with a two-year research assistantship.

Finally, thanks are due to the Middle East Technical University, Department of Mechanical Engineering, for allowing me four years to complete this research work at Imperial College.

CONTENTS

	<u>Page</u>
Abstract	2
Acknowledgements	3
Contents	4
List of Figures	6
Nomenclature	12
<u>CHAPTER 1: INTRODUCTION</u>	14
1.1 Statement of Problem	14
1.2 Linearised Model of Journal Bearing System	15
1.3 Methods of Determination of Bearing Coefficients	16
1.4 Non-Circular Bearings	17
<u>CHAPTER 2: DYNAMICALLY LOADED JOURNAL BEARINGS</u>	20
2.1 Reynolds Equation	20
2.2 The Steady-State Characteristics of an Oil Film	23
2.3 The Dynamic Characteristics of an Oil Film	25
<u>CHAPTER 3: THE DYNAMIC ANALYSIS OF A RIGID ROTOR-BEARING SYSTEM</u>	30
3.1 Governing Equations of Motion	30
3.2 Response to External Excitation	33
3.3 General Stability Analysis	35
3.4 A Method for the Determination of the Coefficients from the Dynamic Response	37
<u>CHAPTER 4: EXPERIMENTAL APPARATUS</u>	47
4.1 Design Requirements	47

	<u>Page</u>
4.2 Description of Experimental Apparatus	48
4.3 Instrumentation	59
4.4 Experimental Procedure	62
4.4.1 Clearance setting and alignment check	62
4.4.2 Determination of clearance shape and steady-state operating positions	63
4.4.3 Determination of the stiffness coefficients	64
4.4.4 Determination of the dynamic response	64
<u>CHAPTER 5: DISCUSSION AND CONCLUSIONS</u>	66
5.1 Discussion of Experimental Results	66
5.1.1 The circular circumferentially grooved bearing	67
5.1.2 The circular two axial groove bearing	73
5.1.3 The elliptical two axial groove bearing	74
5.1.4 The offset halves two axial groove bearing	86
5.1.5 General comments	111
5.1.6 Comparison of bearing bore types	124
5.1.7 The dynamic test results	126
5.2 Conclusions	153
References	155
APPENDIX A: Geometry of the Non-Circular Test Bearings	160
APPENDIX B: Analytical Description of the Elliptical Orbit	166
APPENDIX C: The Incremental Loading Method	170
APPENDIX D: The Stability Threshold Condition	172

LIST OF FIGURES

	<u>Page</u>
Figure 2.1 : Dynamically loaded journal bearing	21
Figure 2.2 : Oil film forces at the displaced journal position	28
Figure 3.1 : Simulated model of a dynamically loaded bearing	32
(a) Rigid shaft bearing system	32
(b) Simple model of a rigid shaft bearing system	32
Figure 3.2 : Variation of the errors in the coefficients of a circular bearing	43
(a) Stiffness coefficients	43
(b) Damping coefficients	44
Figure 3.3 : Variation of the errors in the coefficients of an elliptical bearing	45
(a) Stiffness coefficients	45
(b) Damping coefficients	46
Figure 4.1 : A sectional view of the experimental rig	51
Figure 4.2 : A view from the test apparatus	52
Figure 4.3 : Circular circumferentially grooved bearing	54
Figure 4.4 : Circular two axial groove bearing	55
Figure 4.5 : Elliptical bore bearing	56
Figure 4.6 : Offset halves bearing	57
Figure 4.7 : A view of the test bearings	58
Figure 4.8 : Viscosity-temperature relationship of the test oil	60
Figure 5.1 : (a) Load capacity of the circumferentially grooved bearing	69

	<u>Page</u>
(b) Locus of the shaft centre in the circumferentially grooved bearing	70
Figure 5.2 : The effect of feed pressure ratio on the stability threshold, showing also the extent of whirl hysteresis	71
Figure 5.3 : Temperature profiles around the circumferentially grooved bearing on the top land centre-line	72
Figure 5.4 : (a) Load capacity of the 30° two axial groove bearing	75
(b) Locus of shaft centre in the 30° two axial groove bearing	76
Figure 5.5 : Experimental whirl orbits, $\omega = 1990$ RPM, $\alpha = 30^\circ$, $\epsilon_0 = 0.67$	77
Figure 5.6 : The stability threshold parameter for the 30° two axial groove bearing	78
Figure 5.7 : Temperature profiles around the two axial groove bearing centre-line	79
Figure 5.8 : (a) Load capacity of the 90° two axial groove bearing	80
(b) Locus of the shaft centre in the 90° two axial groove bearing	81
Figure 5.9 : The stability threshold parameter for the 90° two axial groove bearing	82
Figure 5.10: Temperature profiles around the two axial groove circular bearing centre-line	83
Figure 5.11: The elliptical bore bearing with $\delta = 0.4$	87
(a) The variation of load capacity with journal eccentricity	87

	<u>Page</u>
(b) Locus of shaft centre due to static loading	88
(c) Stability threshold	89
Figure 5.12: The elliptical bore bearing with $\delta = 0.5$	90
(a) The variation of load capacity with journal eccentricity	90
(b) Locus of shaft centre due to static loading	91
(c) Stability threshold	92
Figure 5.13: The elliptical bore bearing with $\delta = 0.6$	93
(a) The variation of load capacity with journal eccentricity	93
(b) Locus of shaft centre due to static loading	94
(c) Stability threshold	95
Figure 5.14: The elliptical bore bearing with $\delta = 0.75$	96
(a) The variation of load capacity with journal eccentricity	96
(b) Locus of shaft centre due to static loading	97
(c) Stability threshold	98
Figure 5.15: Temperature profiles around the elliptical bearing centre-line	99/100
Figure 5.16: Whirl orbits of the elliptical bearing motion	101-103
Figure 5.17: The variation of the stiffness coefficients for the elliptical bearing, $\delta = 0.5$	104
(a) Stiffness coefficients K_{XX} and K_{YY}	104
(b) Stiffness coefficients K_{XY} and K_{YX}	105
Figure 5.18: The variation of the stiffness coefficients for the elliptical bearing, $\delta = 0.6$	106
(a) Stiffness coefficients K_{XX} and K_{YY}	106

	<u>Page</u>
(b) Stiffness coefficient K_{XY}	107
(c) Stiffness coefficient K_{YX}	108
Figure 5.19: The stability threshold of the elliptical bearing based on the minimum clearance	109
Figure 5.20: The offset halves bearing with $\delta = 0.4$	113
(a) The variation of load capacity and stability threshold with journal eccentricity	113
(b) Locus of shaft centre in the clearance shape due to static loading	114
Figure 5.21: The offset halves bearing with $\delta = 0.5$	115
(a) The variation of load capacity and stability threshold with journal eccentricity	115
(b) Locus of shaft centre in the clearance shape due to static loading	116
Figure 5.22: The offset halves bearing with $\delta = 0.6$	117
(a) The variation of load capacity and stability threshold with journal eccentricity	117
(b) Locus of shaft centre in the clearance shape due to static loading	118
Figure 5.23: Temperature profiles around the offset halves bearing centre-line	119
Figure 5.24: Some oscilloscope photographs of the offset halves bearing whirling motion	120/121
Figure 5.25: The variation of the stiffness coefficients for the offset halves bearing with $\delta = 0.5$	122
(a) Stiffness coefficients K_{XX} and K_{YX}	122
(b) Stiffness coefficients K_{YY} and K_{XY}	123

	<u>Page</u>
Figure 5.26: (a) Comparison of the load capacities of the bearing types	127
(b) Comparison of the stability thresholds of the bearing types	128
Figure 5.27: Typical dynamic response of the circumferentially grooved circular bearing to external excitation	131/132
Figure 5.28: Typical dynamic response of the elliptical bearing to external excitation	133/134
Figure 5.29: Typical dynamic response of the offset halves bearing to external excitation	135/136
Figure 5.30: Experimental and theoretical response of the circumferentially grooved bearing to synchronous excitation	137
(a) The amplitude of the major semi-axis	137
(b) The amplitude of the minor semi-axis	138
(c) The theoretical phase angle and angle of inclination	139
Figure 5.31: The theoretical response of the circumferentially grooved bearing to half-synchronous excitation	140
Figure 5.32: The response of the 30° two axial groove bearing to synchronous external excitation	141
(a) The amplitudes of the major and minor semi-axes	141
(b) The phase angle and angle of inclination	142
Figure 5.33: The response of the 90° two axial groove angle bearing to synchronous external excitation	143
(a) The amplitudes of the major and minor semi-axes	143
(b) The phase angle and angle of inclination	144

	<u>Page</u>
Figure 5.34: The response of the elliptical bearing with	
$\delta = 0.4$	145
(a) The amplitudes of the major and minor semi-axes	145
(b) The phase angle and angle of inclination	146
Figure 5.35: The response of the elliptical bearing with	
$\delta = 0.6$	147
(a) The amplitudes of the major and minor semi-axes	147
(b) The phase angle and angle of inclination	148
Figure 5.36: The response of the offset halves bearing with	
$\delta = 0.4$	149
(a) The amplitudes of the major and minor semi-axes	149
(b) The phase angle and angle of inclination	150
Figure 5.37: The response of the offset halves bearing with	
$\delta = 0.6$	151
(a) The amplitudes of the major and minor semi-axes	151
(b) The phase angle and angle of inclination	152
Figure A.1 : Elliptical bearing geometry	162
(a) Elliptical bearing	162
(b) Clearance shape and lobe centre geometry	162
Figure A.2 : Offset halves bearing geometry	165
(a) Offset halves bearing	165
(b) Clearance shape and lobe centre geometry	165
Figure B.1 : Dynamic load orbit	169
Figure C.1 : Method of determining the stiffness coefficients	170

NOMENCLATURE

a	:	major semi-axis of elliptical orbit
b	:	minor semi-axis of elliptical orbit
c	:	radial arc clearance
c_{ij}	:	oil film damping coefficients
C_{ij}	:	non-dimensional oil film damping coefficients, $c_{ij} \omega c/W$
d	:	radial preload of bearing arc
e	:	eccentricity of the journal with respect to the bearing centre
F_o	:	constant rotating load
f_x, f_y	:	oil film force components
F_X, F_Y	:	non-dimensional oil film force components
h	:	film thickness
H	:	non-dimensional film thickness, h/c
i	:	$\sqrt{-1}$
k_{ij}	:	oil film stiffness coefficients
K_{ij}	:	non-dimensional oil film stiffness coefficients, $k_{ij} c/W$
L	:	bearing length
M	:	bearing housing mass
n	:	non-dimensional excitation frequency, Ω/ω
N	:	rotational speed of the shaft, RPS
p	:	pressure
P	:	non-dimensional pressure, $p (c/R)^2 / (\delta \omega \eta)$
r_o	:	shaft run-out radius
R	:	shaft radius
So	:	Sommerfeld Number, $p_b (c/R)^2 / (\eta N)$
S_p	:	stability parameter, $W/M c \omega^2$
t	:	time

- T : non-dimensional time, ωt
 W : static bearing load
 x, y, z
 X, Y, Z : fixed coordinates
 $[Z]_n$: oil film impedance matrix

Greek Symbols

- α : bearing axial groove angle
 β : inclination of elliptical orbit from horizontal axis
 γ : oil feed pressure ratio, p_f/p_b
 δ : non-dimensional preload, d/c
 ε : eccentricity ratio, e/c
 η : absolute viscosity of lubricating oil
 θ : angular coordinate
 λ_k : an eigenvalue of the characteristic equation
 ν : non-dimensional whirl frequency
 σ_k : real part of λ_k
 ϕ : attitude angle of line of centres
 ψ : phase angle between the exciting force and displacement
 ω : angular speed of the shaft (rad/s)
 Ω : excitation frequency

Subscripts

- b : bearing
 in : inlet
 min : minimum
 max : maximum
 n : refers to non-dimensional excitation frequency
 ε : along the line of centres
 ϕ : normal to the line of centres in the direction of rotation

CHAPTER 1

INTRODUCTION

1.1 STATEMENT OF THE PROBLEM

It is well known that a rigid rotating shaft supported in oil lubricated journal bearings may vibrate due to one or more reasons. Vibrations at the rotational frequency of the shaft (synchronous) result from run-out or forces due to out-of-balance of the shaft. Under certain operating conditions, other types of motion may occur. In these, the oil film causes a transfer of energy from the rotational motion about the axis of the shaft to the translatory motion of that axis. This leads to what are called self-excited oscillations in which the vibration amplitudes may reach inadmissibly high levels. This particular form of instability induced by the fluid film forces manifests itself by the frequency of rotor precession which is found to be half or less of the rotor speed for circular bearings. The origin of the non-synchronous precession is due principally to the anisotropic non-linear properties of the oil film forces, which include the effect of film rupture and reformation conditions. The operating conditions and resonant vibration amplitude and frequency are largely influenced by the design of the journal bearing.

The objective of this investigation was to determine experimentally the stability characteristics and coefficients of 41 mm nominal diameter bearings of different bore shapes. Due to the difficulty of machining the multi-lobe bearing, the two basic types of bearings, elliptical and offset halves, with different preloads and groove angles, were tested and assessed using linearised theory. Because of the inevitable difficulties in the experimental determination of the coefficients, more attention has been devoted to the stability threshold. The results are compared with the prediction of linearised analysis.

1.2 LINEARISED MODEL OF JOURNAL BEARING SYSTEM

In order to understand the dynamical characteristics of a journal bearing system, it is necessary to have an accurate knowledge of the bearing fluid film forces under dynamic conditions. Numerous investigators have discussed, both experimentally and analytically, the properties of the oil film forces for some fifty years. Many authors have assumed that variations in the oil film force acting on the journal can be linearly related to the variations in the journal displacement and velocity relative to its steady running position [1,2,3]. The stiffness coefficients arise from the change in the oil film shape and the damping coefficients arise from the squeeze film considerations.

The linearised model has proved extremely useful in rotor bearing system analysis. The influence of the bearings on the critical speeds, stability and response of rotors has been shown to depend upon the eight linearised stiffness and damping coefficients. The theoretical derivations of these coefficients are now well known, many being based on the finite difference solutions of the Reynolds equation with constant viscosity. Although linearisation is valid only for small amplitudes, Lund & Thomsen [4] state that, in practice, it had been found to hold for amplitudes of up to one half of the clearance. However, considering the highly non-linear oil film forces with respect to the eccentricity ratio, it is much more appropriate to mention the limitation in terms of the minimum film thickness as proposed by Lund & Orcutt [5]. They state that the linearisation represents the actual oil film force also for large amplitudes with surprisingly good accuracy as long as the minimum film thickness during the vibration does not become less than approximately 25% of the radial clearance.

Using various analytical approximations for the relationships between

the oil film force and the position and velocity of the journal for circular bearings, many authors have predicted shaft behaviour under dynamic conditions [6,7,8]. Although these approximate analytical solutions may be helpful in explaining the behaviour of systems with circular bearings, they are not applicable to bearings of non-circular profile. In engineering practice, it has been found that system stability is greater with bearings of non-circular profile [9].

1.3 METHODS OF DETERMINATION OF BEARING COEFFICIENTS

Although the analysis of rotor bearing systems is considerably simplified by the eight linearised bearing coefficients, unless the coefficients can be measured experimentally such an analysis is of limited value.

There are two basic methods available for the determination of the coefficients experimentally. These are classified according to the use of:

- (a) the static characteristics;
- (b) the dynamic response characteristics of the bearing.

The stiffness coefficients can be derived from the static testing of the journal locus curve. The definite relationship between the load and the eccentricity and the attitude angle is given by Morrison [3]. The other method given by Mitchell et al [10] is termed the incremental loading method, which is based on the measurements of the quasi-static equilibrium positions under the small changes of the imposed component of the load.

The eight coefficients can also be determined from the dynamic response of bearings. The technique of exciting the bearing sinusoidally in two mutually perpendicular directions, and in each case measuring the

amplitude and phase angle of the resulting motions was adapted by Glienicke [11] for a series of tests on 120 mm diameter bearings. Full-scale bearing tests with this method were presented by Morton [12].

With the known values of the stiffness coefficients, the damping coefficients were calculated by Woodcock et al [13] from the measurements of the vibration amplitudes and phase angles relative to the unbalance force.

Morton [14] has developed a transient technique which involves a step change in the force applied to a rotating shaft. Full-scale test results were presented.

In all these methods, it is generally accepted that the coefficients derived from static testing data are extremely sensitive to measurement errors. The sensitivity of dynamically derived coefficients is more difficult to assess due to the ill-conditioning of the matrix formed in the evaluation of the coefficients. In particular, the cross-coupling stiffness coefficients, one of which always changes sign over the loading range, affect the accuracy of the calculations. Iwatsubo [15] analytically found that the damped natural frequency is not greatly affected by the effects of bearing coefficients, but the damping characteristics of the system which are very important for instability and unbalance response are sensitively affected.

1.4 NON-CIRCULAR BEARINGS

In recent years, considerable attention has been paid to non-circular bore bearings due to their substantially better dynamic behaviour compared to conventional circular bearings. These bearings have found extensive use in high speed machinery and the support of turbo-generator rotors.

Various types of special-purpose journal bearings are used in

engineering. There are many geometric parameters available in the design of fixed arc, multi-lobe bearings. These include the number of arcs, arc clearance, preload, offset of arcs and groove angles and positions between the arcs. Complex bearing geometries can be designed by the proper choice of these variables in order to greatly improve the stability of a rotor. However, generally speaking, these bearings are more costly to manufacture, install and maintain than circular bearings.

The standard design is to modify the two axial-groove circular bearings but displacing the arc centres from the geometric centre. This type of bearing is widely used in turbomachinery due to the simplicity of design. Examples are the elliptical and offset halves bearings.

Although extensive literature is available on circular bearings, the literature concerning the effects of different non-circular bearing designs on the dynamic characteristics of rotors is comparatively very little.

The steady-state load capacity and power loss of the elliptical and the symmetric three-lobe bearing have been theoretically and experimentally investigated by Pinkus [16,17,18,19,20]. Pinkus & Sternlicht [21] have extended these results to a greater range of geometric variables. The static and stiffness properties of the elliptical and offset halves bearings have been analysed by Wilcock [22].

Using linearisation theory, the coefficients and the stability of some multi-lobe bearings have been investigated experimentally by Glienicke [11]. Falkenhagen et al [23] examined the stability and transient characteristics of a three-lobe bearing. The stability characteristics of six different bearing bore shapes are investigated for various geometric parameters in [24]. Recently, stability and transient and unbalance characteristics of four specific multi-lobe bearings have been reported in [25,26].

In all these analyses, it has been found that in applications where

the load carrying capacity is of secondary importance, the multi-lobe bearings can show better performance, depending on the operating condition.

CHAPTER 2

DYNAMICALLY LOADED JOURNAL BEARINGS

2.1 REYNOLDS EQUATION

The full form of the Reynolds equation for a dynamically loaded bearing, shown in Figure 2.1, is derived by Pinkus & Sternlicht [21], and is given for an isoviscous lubricant as:

$$\frac{\partial}{\partial x} \left(h^3 \frac{\partial p}{\partial x} \right) + \frac{\partial}{\partial z} \left(h^3 \frac{\partial p}{\partial z} \right) = 6\eta \left[\left(\omega - 2 \frac{d\phi}{dt} \right) R \frac{dh}{dx} + 2 \frac{de}{dt} \cos \theta \right] \quad (2.1)$$

It is convenient to use the non-dimensional form of the equation in order to maintain the generality of the solution. Introducing the following non-dimensional variables:

$$\left. \begin{aligned} \theta &= \frac{x'}{R} \quad , \quad Z = \frac{z}{L/2} \quad , \quad P = \frac{p}{6\omega\eta(R/c)^2} \quad , \quad H = \frac{h}{c} \\ \epsilon &= \frac{e}{c} \quad , \quad \dot{\epsilon} = \frac{1}{\omega} \frac{d\epsilon}{dt} \quad , \quad \dot{\phi} = \frac{1}{\omega} \frac{d\phi}{dt} \end{aligned} \right\} \quad (2.2)$$

into equation (2.1) gives the following non-dimensional form of the Reynolds equation:

$$\frac{\partial}{\partial \theta} \left(H^3 \frac{\partial P}{\partial \theta} \right) + \left(\frac{D}{L} \right)^2 H^3 \frac{\partial^2 P}{\partial Z^2} = (1 - 2\dot{\phi}) \frac{dH}{d\theta} + 2\dot{\epsilon} \cos \theta \quad (2.3)$$

The boundary conditions used in the integration of this equation are, for a circumferentially grooved bearing:

$$\left. \begin{aligned} P(\theta, 0) &= P_f \\ P(\theta, 1) &= 0 \\ P(0, Z) &= P(2\pi, Z) \end{aligned} \right\} \quad (2.4)$$

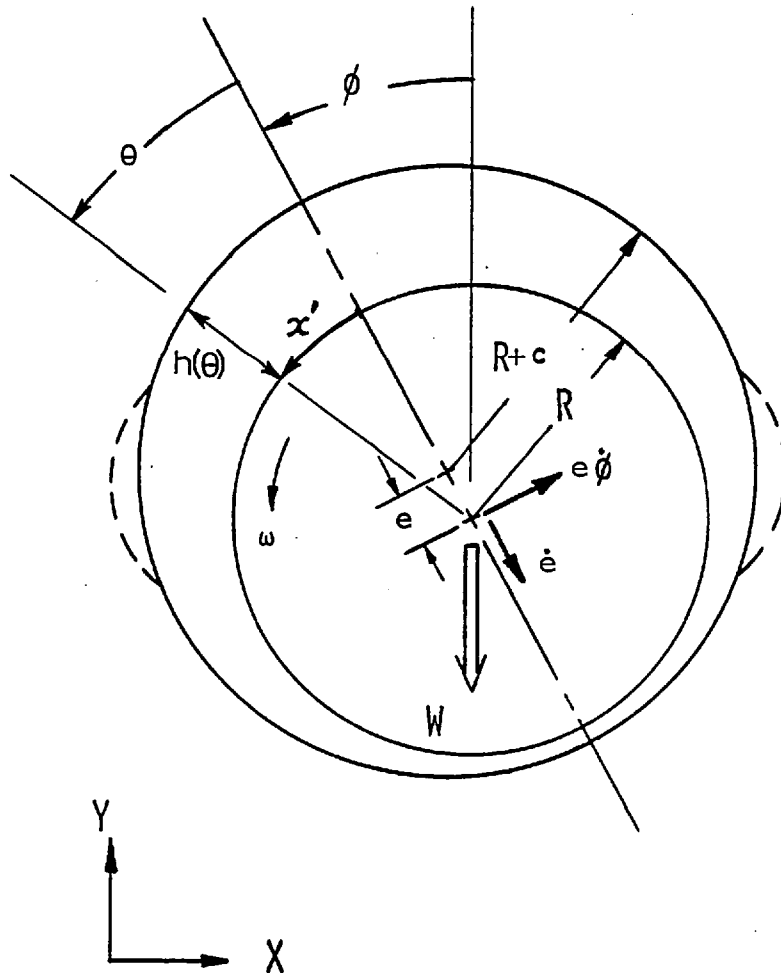


Figure 2.1: Dynamically loaded journal bearing

and for axial groove bearings:

$$\left. \begin{aligned} P(\theta_{in}, Z) &= P(\theta_{out}, Z) = 0 \\ P(\theta, 1) &= P(\theta, -1) = 0 \end{aligned} \right\} (2.5)$$

The cavitation condition was also imposed by introducing:

$$\frac{\partial P}{\partial s} = 0 \quad \text{when} \quad P = 0 \quad (2.6)$$

where s is the coordinate normal to the cavitation boundary in the θ - Z plane.

It is to be noted that the Reynolds equation is a strong function of film thickness due to the cubic terms. For the preloaded non-circular bearing types, the film thickness may be defined in terms of eccentricity and attitude angle relative to the bearing centre. However, to actually calculate the film thickness, it is the eccentricity and associated attitude angle of each lobe relative to the centre of the bearing arc which is of interest. These relationships are well defined and given in Appendix A for the tested elliptical and offset halves bearings.

The Reynolds equation was integrated by using a conventional finite difference procedure. The mesh size used in the calculations was 72 divisions circumferentially and 10 divisions axially for half of the bearing. The Gauss-Seidel iteration method was applied to the finite difference equation and the following convergence limit was imposed which had to be satisfied before the termination of the iterative procedure:

$$\frac{\sum \sum (P_{ij}^k - P_{ij}^{k-1})}{\sum \sum P_{ij}^k} \leq 10^{-6}$$

The cavitation condition was allowed for by setting all negative pressures to zero as they were generated. When the pressure distribution, which is a function of the bearing bore geometry, aspect ratio and eccentricity, is obtained, the steady-state and dynamic characteristics of the oil film can be computed.

2.2 THE STEADY-STATE CHARACTERISTICS OF AN OIL FILM

The principal steady-state characteristics are the bearing load capacity and attitude angle for a given eccentricity. With a chosen bearing geometry with axial grooves, the eccentricity and attitude angle are preset, giving a set of lobe eccentricities and attitude angles for which the solution of the Reynolds equation for steady conditions (i.e. $\dot{\phi} = \dot{e} = 0$) gives the pressure distribution generated in the wedges. The oil film forces along and perpendicular to the line of centres of the journal and bearing, f_e and f_ϕ , respectively, are obtained by integration as follows:

$$f_e = \int_{-L/2}^{L/2} \int_0^{2\pi} p \cos \theta (R d\theta) dz$$

$$f_\phi = \int_{-L/2}^{L/2} \int_0^{2\pi} p \sin \theta (R d\theta) dz$$

By using the non-dimensional variables defined in equations (2.2), the non-dimensional oil film forces can be written as:

$$F_e = \frac{f_e/L R}{3 \omega \eta (R/c)^2} = \int_{-1}^1 \int_0^{2\pi} P \cos \theta d\theta dz$$

$$F_\phi = \frac{f_\phi/L R}{3 \omega \eta (R/c)^2} = \int_{-1}^1 \int_0^{2\pi} P \sin \theta d\theta dz$$

} (2.7)

and the attitude angle in centrally loaded bearings (as shown in Figure

2.1) is:

$$\phi = \tan^{-1} \left(- \frac{F_{\phi}}{F_{\epsilon}} \right)$$

Having obtained an accurate attitude angle, ϕ^k , it is possible to compute a new ϕ^{k+1} from a similar procedure. This iterative process may converge slowly. Hence, a relaxation factor between 1.0 and 1.4 can be employed to increase the convergence rate. A sufficient condition for convergence was set as $|\phi^{k+1} - \phi^k| \leq 1^\circ$. This procedure locates the shaft at the correct equilibrium position where all the forces in the horizontal direction are zero. Then, for this position, the load capacity can be expressed in terms of Sommerfeld number as:

$$S_o = \frac{P_b}{\eta N} \left(\frac{c}{R} \right)^2 = 3\pi [F_{\epsilon}^2 + F_{\phi}^2]^{\frac{1}{2}} \quad (2.8)$$

and the non-dimensional mean bearing pressure is:

$$P_b = \frac{P_b}{6 \omega \eta (R/c)^2} = \frac{f/L D}{6 \omega \eta (R/c)^2} = \frac{[F_{\epsilon}^2 + F_{\phi}^2]^{\frac{1}{2}}}{4} = \frac{S_o}{12\pi}$$

In this analysis, the following points should be clearly borne in mind:

- the oil viscosity is an effective uniform viscosity at the operating condition;
- for the circumferentially grooved circular bearing, the attitude angle is directly calculated from the oil film forces; therefore, there is no need for iteration of the journal position;
- there are two clearances in preloaded two-wedge bearings, namely, maximum and minimum clearances. For mathematical simplicity and

uniformity, the bearing arc clearance, c , was used in all the non-dimensionalisations.

The forces in the polar coordinate system are related to the forces in the cartesian coordinate system as follows:

$$\begin{bmatrix} F_X \\ F_Y \end{bmatrix} = \begin{bmatrix} \sin \phi & \cos \phi \\ -\cos \phi & \sin \phi \end{bmatrix} \begin{bmatrix} F_\epsilon \\ F_\phi \end{bmatrix} \quad (2.9)$$

2.3 THE DYNAMIC CHARACTERISTICS OF AN OIL FILM

The hydrodynamic oil film force obtained from the Reynolds equation is a non-linear function of the eccentricity, the attitude angle, and the corresponding velocity components. If the journal is in motion at the coordinates (x,y) around the equilibrium position, then the dynamic part of the oil film force can be linearised for small amplitude motion. This can be done by the first order Taylor expansion of the film force about the equilibrium position. The dynamic part of the film force can be expressed as:

$$\left. \begin{aligned} \Delta f_x &= -k_{xxx} x - k_{xy} y - c_{xx} \dot{x} - c_{xy} \dot{y} \\ \Delta f_y &= -k_{yx} x - k_{yy} y - c_{yx} \dot{x} - c_{yy} \dot{y} \end{aligned} \right\} \quad (2.10)$$

where the oil film stiffness coefficients are:

$$k_{xxx} = -\frac{\partial f_x}{\partial x}, \quad k_{xy} = -\frac{\partial f_x}{\partial y}, \quad k_{yx} = -\frac{\partial f_y}{\partial x}, \quad k_{yy} = -\frac{\partial f_y}{\partial y} \quad (2.11a)$$

and the damping coefficients are:

$$c_{xx} = -\frac{\partial f_x}{\partial \dot{x}}, \quad c_{xy} = -\frac{\partial f_x}{\partial \dot{y}}, \quad c_{yx} = -\frac{\partial f_y}{\partial \dot{x}}, \quad c_{yy} = -\frac{\partial f_y}{\partial \dot{y}} \quad (2.11b)$$

where f_x and f_y are the components of the fluid film force. The first index of the coefficients gives the direction of the fluid film force and the second index gives the direction of the perturbation. In general, due to the anisotropy of the oil film, the direction of the perturbation is not colinear with that of the disturbing force. Therefore, the cross-coupling terms are introduced.

In rotor bearing analysis, it is common practice to non-dimensionalise the oil film force with the steady load. By introducing the following dimensionless variables:

$$X = \frac{x}{c}, \quad Y = \frac{y}{c}, \quad \dot{X} = \frac{\dot{x}}{c\omega}, \quad \dot{Y} = \frac{\dot{y}}{c\omega}$$

$$\Delta F'_i = \frac{\Delta f_i}{W}, \quad F'_i = \frac{f_i}{W}, \quad i = X, Y$$

Equations (2.10) can be written as:

$$\begin{bmatrix} \Delta F'_X \\ \Delta F'_Y \end{bmatrix} = - \begin{bmatrix} K_{XX} & K_{XY} \\ K_{YX} & K_{YY} \end{bmatrix} \begin{bmatrix} X \\ Y \end{bmatrix} - \begin{bmatrix} C_{XX} & C_{XY} \\ C_{YX} & C_{YY} \end{bmatrix} \begin{bmatrix} \dot{X} \\ \dot{Y} \end{bmatrix}$$

where the non-dimensional film coefficients are:

$$K_{ij} = \frac{k_{ij} c}{W} = -\frac{\partial F'_i}{\partial X_j}$$

$$C_{ij} = \frac{c_{ij} \omega c}{W} = -\frac{\partial F'_i}{\partial \dot{X}_j}, \quad \begin{matrix} i = X, Y \\ j = X, Y \end{matrix}$$

The non-dimensional oil film forces, F'_i , are related with the forces given in equations (2.9) through equation (2.8) as follows:

$$F'_i = F_i \frac{3\pi}{50}$$

The linearised dynamic coefficients of the oil film are obtained from the perturbation solution of the Reynolds equation. Small perturbations in displacement and velocity about the equilibrium journal position give the incremental fluid film forces which are used to calculate the coefficients defined in equation (2.11).

For the calculation of the stiffness coefficients, the journal centre is displaced from its equilibrium locus to the disturbed position, J_1 , in the X-direction, as shown in Figure 2.2, where the journal is in equilibrium, i.e. $\dot{X} = \dot{Y} = 0$. Then, the fluid film force at the disturbed position for the eccentricity ratio of ϵ is the same as that for the journal at J_2 on the equilibrium locus, where $\overline{O_b J_2}$ represents an eccentricity ratio equal to ϵ . And the direction of the force is inclined from the vertical load with an angle α . Then, the additional oil film force components are:

$$\Delta F'_X = F' \sin \alpha$$

$$\Delta F'_Y = F' \cos \alpha - 1$$

The corresponding stiffness coefficients are:

$$K_{XX} = -\frac{\partial F'_X}{\partial X} = -\left(\frac{\Delta F'_X}{X}\right)_{Y=\dot{X}=\dot{Y}=0}$$

$$K_{YX} = -\frac{\partial F'_Y}{\partial X} = -\left(\frac{\Delta F'_Y}{X}\right)_{Y=\dot{X}=\dot{Y}=0}$$

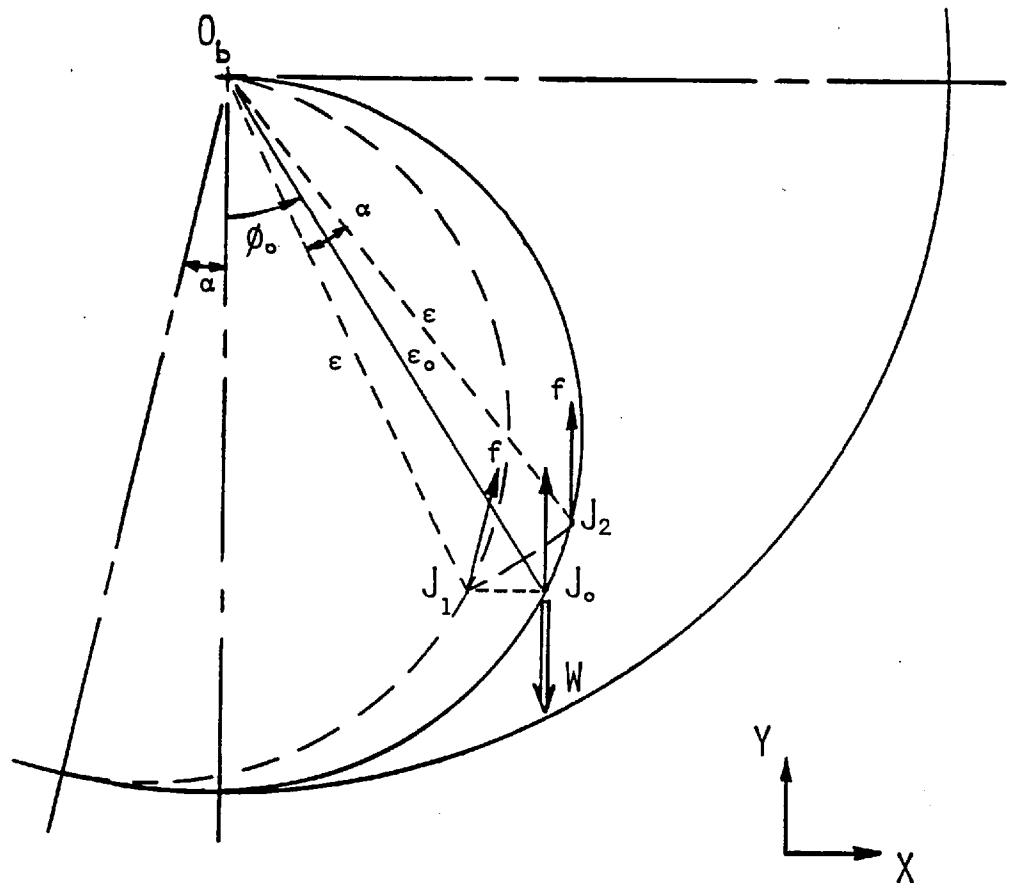


Figure 2.2: Oil film forces at the displaced journal position
(for full circular bearings only)

Similarly, by a small displacement in the Y-direction and calculation of the additional film force components give the other two stiffness coefficients K_{YX} and K_{YY} .

For the calculation of the damping coefficients, the journal is given small velocities either in the X-direction or the Y-direction at the equilibrium position, i.e. $X = Y = 0$. The velocity components along the line of centres and normal to it are calculated from the following transformation:

$$\begin{bmatrix} \dot{\epsilon} \\ \dot{\phi} \end{bmatrix} = \begin{bmatrix} \sin \phi & -\cos \phi \\ \frac{\cos \phi}{\epsilon} & \frac{\sin \phi}{\epsilon} \end{bmatrix} \begin{bmatrix} \dot{X} \\ \dot{Y} \end{bmatrix}$$

The Reynolds equation (2.3) is solved with these velocity components and the resulting additional film force components are used to calculate the damping coefficients given in equation (2.11b).

In the calculations of the linearised dynamic coefficients by direct perturbations of the journal position and velocity, the magnitude of perturbations were found to be immaterial provided these were small. In this work, the non-dimensional displacement and velocity perturbations were set at 0.001.

CHAPTER 3

THE DYNAMIC ANALYSIS OF A RIGID ROTOR BEARING SYSTEM

The dynamics of a rotor supported in bearings is strongly influenced by the properties of the bearings. In the case of a stiff rotor, the response to excitation and the stability characteristics are almost entirely determined by the stiffness and damping of the bearing. It is the purpose of this chapter to describe how the bearing properties can be used in calculations.

3.1 GOVERNING EQUATIONS OF MOTION

A fixed cartesian coordinate system has been employed. This has eliminated either the transformation of the bearing forces from rotating to non-rotating coordinates or the formulation of the journal equations of motion in the rotating, non-inertial coordinate system, which are highly non-linear in the acceleration terms.

The equations of motion are derived considering the translational motion of a rigid shaft in a rigid bearing which is free to move in the clearance space, as shown in Figure 3.1(a). The bearing is supported eccentrically by the oil film at a stable equilibrium position, B , under the application of a static load, W_b . If the geometric centre of the journal, C , is not concentric with the rotation centre, J , due to the run-out, r_o , the oil film will be excited at the synchronous speed. If the bearing housing with a mass M is excited by a constant rotating force, F_o , at a speed of Ω , then the equations of motion of the bearing housing about the equilibrium position can be written as follows:

$$\left. \begin{aligned} M \ddot{x} &= \Delta f_x + F_o \cos \Omega t \\ M \ddot{y} &= \Delta f_y + F_o \sin \Omega t \end{aligned} \right\} (3.1)$$

where Δf_x and Δf_y are the additional fluid film forces acting on the bearing when it is at a position (x,y) . If there is a phase difference, β , between the run-out and the excitation force at the time $t = 0$, then from Figure 3.1(b) it can be seen that the oil film forces can be expressed in terms of relative quantities by using equation (2.10) as follows:

$$\left. \begin{aligned} \Delta f_x &= -k_{xx}(x-x_0) - k_{xy}(y-y_0) - c_{xx}(\dot{x}-\dot{x}_0) - c_{xy}(\dot{y}-\dot{y}_0) \\ \Delta f_y &= -k_{yx}(x-x_0) - k_{yy}(y-y_0) - c_{yx}(\dot{x}-\dot{x}_0) - c_{yy}(\dot{y}-\dot{y}_0) \end{aligned} \right\} \quad (3.2)$$

where:

$$x_0 = r_0 \cos(\omega t - \beta)$$

$$y_0 = r_0 \sin(\omega t - \beta)$$

By substituting equation (3.2) into equation (3.1) and introducing the following non-dimensional variables:

$$X = \frac{x}{c}, \quad Y = \frac{y}{c}, \quad K_{ij} = \frac{k_{ij} c}{W}, \quad C_{ij} = \frac{c_{ij} \omega c}{W}$$

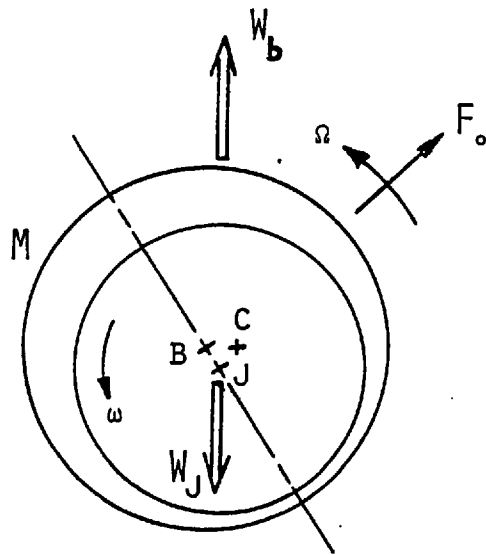
$$T = \omega t, \quad R_0 = \frac{r_0}{c}, \quad n = \frac{\Omega}{\omega}, \quad S_P = \frac{W}{M c \omega^2}$$

one can obtain:

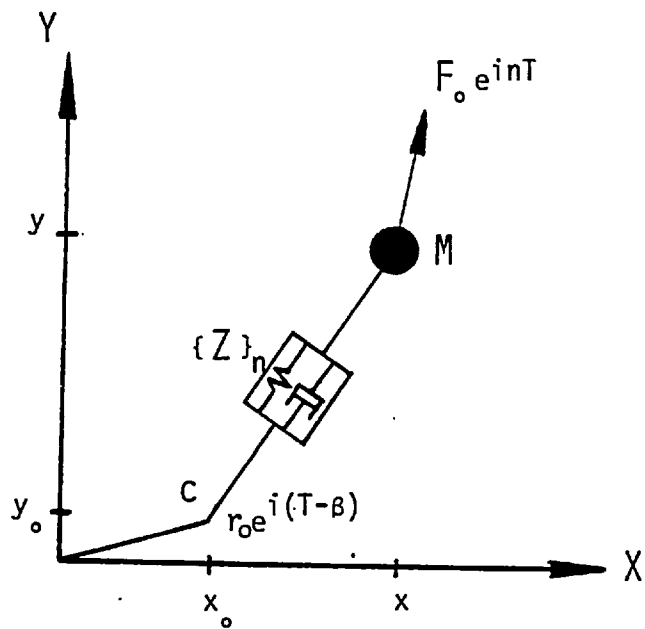
$$\frac{1}{S_P} \begin{bmatrix} \ddot{X} \\ \ddot{Y} \end{bmatrix} + \begin{bmatrix} C_{XX} & C_{XY} \\ C_{YX} & C_{YY} \end{bmatrix} \begin{bmatrix} \dot{X} - \dot{X}_0 \\ \dot{Y} - \dot{Y}_0 \end{bmatrix} + \begin{bmatrix} K_{XX} & K_{XY} \\ K_{YX} & K_{YY} \end{bmatrix} \begin{bmatrix} X - X_0 \\ Y - Y_0 \end{bmatrix} = \frac{F_0}{W} \begin{bmatrix} \cos n T \\ \sin n T \end{bmatrix} \quad (3.3)$$

where:

$$\begin{bmatrix} X_0 \\ Y_0 \end{bmatrix} = R_0 \begin{bmatrix} \cos(T - \beta) \\ \sin(T - \beta) \end{bmatrix}$$



(a) Rigid shaft bearing system



(b) Simple model of a rigid shaft bearing system

Figure 3.1: Simulated model of a dynamically loaded bearing

3.2 RESPONSE TO EXTERNAL EXCITATION

In practice, excitation at synchronous speed, ω , is almost always present due to run-out or unbalance. Excitation at some other frequency, $n\omega$, is often present, for example due to shaft ovality in flexible systems, where $n = 2$. In the apparatus constructed for this work, the test bearing can be excited at any independent speed up to 60 Hz. Since it proved most difficult to eliminate synchronous excitation, it is necessary to develop the equations for the response to excitation at two frequencies. Due to the cross-coupling damping terms present in equations (3.3), it is much easier to express all the state variables as complex quantities. Since there are two excitations at frequencies ω and $n\omega$, the solutions can be assumed as harmonic functions of these frequencies:

$$\left. \begin{aligned} X &= X_R + X_F = X_1 e^{i(T-\phi_{X1})} + X_n e^{i(nT-\phi_{Xn})} \\ Y &= Y_R + Y_F = Y_1 e^{i(T-\phi_{Y1})} + Y_n e^{i(nT-\phi_{Yn})} \end{aligned} \right\} (3.4)$$

Note that only the real part of equations (3.4) are the solutions and X_1 , Y_1 , X_n and Y_n are real quantities. The derivatives are:

$$\dot{X} = i X_R + i n X_F$$

$$\dot{Y} = i Y_R + i n Y_F$$

$$\ddot{X} = -X_R - n^2 X_F$$

$$\ddot{Y} = -Y_R - n^2 Y_F$$

Substituting into equation (3.3) and expressing the external and run-out excitations as parts of complex numbers, the equations can be separated

into the two frequencies as:

$$[[Z]_1 - \frac{1}{S_p} [I]] \begin{bmatrix} X_R \\ Y_R \end{bmatrix} = R_o e^{i(T-\beta)} [Z]_1 \begin{bmatrix} 1 \\ -i \end{bmatrix} \quad (3.5)$$

and:

$$[[Z]_n - \frac{n^2}{S_p} [I]] \begin{bmatrix} X_F \\ Y_F \end{bmatrix} = \frac{F_o}{W} e^{i n T} \begin{bmatrix} 1 \\ -i \end{bmatrix} \quad (3.6)$$

where $[Z]_n$ is the complex dynamic stiffness matrix or the impedance of the oil film and elements are:

$$\left. \begin{aligned} Z_{XX_n} &= K_{XX} + i n C_{XX} \\ Z_{XY_n} &= K_{XY} + i n C_{XY} \\ Z_{YX_n} &= K_{YX} + i n C_{YX} \\ Z_{YY_n} &= K_{YY} + i n C_{YY} \end{aligned} \right\} \quad (3.7)$$

It is to be noted that the oil film impedance is frequency dependent and subscript 1 refers to the synchronous impedance.

The amplitude of the response and the phase angles can be solved by inverting equations (3.5) and (3.6):

$$\begin{bmatrix} X_1 \\ Y_1 \end{bmatrix} \begin{bmatrix} e^{-i\phi_{X1}} \\ e^{-i\phi_{Y1}} \end{bmatrix} = R_o e^{-i\beta} [Z]_{11}^{-1} \left\{ [Z]_1 \begin{bmatrix} 1 \\ -i \end{bmatrix} \right\} \quad (3.8)$$

where:

$$[Z]_{11} = [Z]_1 - \frac{1}{S_p} [I]$$

and:

$$\begin{bmatrix} X_n & e^{-i\phi_{Xn}} \\ Y_n & e^{-i\phi_{Yn}} \end{bmatrix} = \frac{F_0}{W} [Z]_{nm}^{-1} \begin{bmatrix} 1 \\ -i \end{bmatrix} \quad (3.9)$$

where:

$$[Z]_{nm} = [Z]_n - \frac{n^2}{S_p} [I]$$

As it may be seen, the response variables are expressed as complex variables at the two excitation frequencies, in equation (3.4), and the amplitudes and the phase angles are given in equations (3.8) and (3.9). Since the responses are harmonic functions, a stationary double-loop orbit can be observed if the external excitation frequency is half of the shaft speed. This orbit converges to a single-loop elliptical orbit:

- (a) if there is no run-out (or its response is negligibly small compared to the external excitation response); or
- (b) if there is no external excitation.

In general, the major and minor semi-axes, their direction of inclination and the phase angle between the excitation force and the major semi-axis are of interest for comparison with experiment and are derived in Appendix B.

3.3 GENERAL STABILITY ANALYSIS

The stability of a linearised system can be tested by giving an arbitrary small motion with an assigned frequency around the equilibrium position. If the imposed motion persists with time, then the parameters defined by the equations of motion determine the threshold stability condition and the assigned frequency determines the threshold frequency.

This can be analysed mathematically by examining the system characteristic equation which can be obtained from the homogeneous part of the equations of motion.

For the journal bearing model described in section 3.1, the homogeneous part of the equations of motion given in equation (3.3) are:

$$\frac{1}{S_p} \begin{bmatrix} \dot{X} \\ \dot{Y} \end{bmatrix} + \begin{bmatrix} C_{XX} & C_{XY} \\ C_{YX} & C_{YY} \end{bmatrix} \begin{bmatrix} X \\ Y \end{bmatrix} + \begin{bmatrix} K_{XX} & K_{XY} \\ K_{YX} & K_{YY} \end{bmatrix} \begin{bmatrix} X \\ Y \end{bmatrix} = 0 \quad (3.10)$$

Thus, for a bearing operating at a certain equilibrium eccentricity, its stability is dependent on only the stability parameter, S_p . Assuming the solutions of the form:

$$\left. \begin{aligned} X &= X_0 e^{\lambda T} \\ Y &= Y_0 e^{\lambda T} \end{aligned} \right\} \quad (3.11)$$

where λ is a complex eigenvalue, and substituting into equation (3.10) gives an explicit solution of the stability parameter at which the real part of the eigenvalue vanishes. The derivation of the instability threshold condition is presented and discussed in Appendix D.

Thus, the boundary of the stable region, being simply the curve of zero damping in the S_p - ϵ space, can be determined at the particular equilibrium eccentricity for which the bearing coefficients have been calculated.

It is to be noted that the destabilising property of the bearing coefficients stems from the lack of symmetry in the stiffness matrix and it does not vanish by the introduction of the principal axis transformation. Therefore, the oil film forces due to displacements are not elastic in the sense that $K_{XY} \neq K_{YX}$, hence the self-excited vibrations arise from these

terms are quite apart from those introduced by the damping in the vibration analysis. If the stiffness matrix is resolved into symmetric and cosymmetric parts:

$$\begin{bmatrix} K_{XX} & K_{XY} \\ K_{YX} & K_{YY} \end{bmatrix} = \begin{bmatrix} K_{XX} & \frac{K_{XY} + K_{YX}}{2} \\ \frac{K_{XY} + K_{YX}}{2} & K_{YY} \end{bmatrix} + \begin{bmatrix} 0 & \frac{K_{XY} - K_{YX}}{2} \\ -\frac{K_{XY} - K_{YX}}{2} & 0 \end{bmatrix}$$

The symmetric part characterises the usual elastic component of the force and the cosymmetric part characterises the circulatory (non-conservative) force component. If the journal is displaced from its equilibrium position to a distance $u = \sqrt{X^2 + Y^2}$, then the circulatory force $F = \frac{1}{2}(K_{XY} - K_{YX})u$ is perpendicular to the displacement u and therefore it maintains straight precession of the journal. Under certain operating conditions, this circulatory force, which always exists even at stable conditions, cannot be damped out and causes the transfer of the rotational energy of the shaft to the precession motion and makes it unstable.

The damping coefficients are not small and give rise to forces of the same order as those due to the stiffness terms; thus, they play an important rôle in the determination of the damped natural frequencies.

3.4 A METHOD FOR THE DETERMINATION OF THE COEFFICIENTS FROM THE DYNAMIC RESPONSE

In rotor dynamics calculations, knowledge of the oil film coefficients is necessary for the solution of the response and stability equations, as explained in previous sections. However, it is to be recalled that the oil film coefficients required are used in the dynamic situation.

Therefore, it is possibly of importance to calculate these coefficients from the dynamic response of the bearing and not from the quasi-static conditions.

An attempt has been made to calculate the coefficients by exciting at two frequencies, with a small difference between them, in order not to affect the equilibrium position of the shaft. However, in this case, the responses are very similar to each other, causing ill-conditioning in the calculations and giving no reasonable solutions.

In this section, feasible methods of experimental determination of the coefficients from the dynamic response are discussed.

The first attempt to determine the eight linearised coefficients directly from the response was adopted by Glienicke [11]. His technique involved the synchronous excitation of the bearing sinusoidally in two mutually perpendicular directions. In each case, the measurements of the vibration amplitudes and phase angles of the resulting motion in the two directions gave the necessary eight equations for the solution of the coefficients. However, he stated that "due to the accumulation of error in the calculations, an accuracy of measurement of about 1% in amplitude and of 1° phase angle resulted in about 5% error in the experimental coefficients, even if the measuring methods are optimised". However, the mean error of his results was about 20% to 30%, and in some coefficients it was about 50%. Morton [12] measured the coefficients with the same method but excited the bearing at a frequency non-synchronous with the running frequency. The error in his calculations was much higher than Glienicke's results.

By means of the equations of motion, experimental methods can be devised for the determination of the coefficients. From a practical point of view, unbalance excitation is the simplest way of applying

synchronous sinusoidal excitation. If the equations of motion given in equation (3.6) are considered with the unbalance excitation, then from measurements of the amplitudes and phase angles of the resulting motion in the two directions give four equations. In order to obtain the missing four equations, experiments must be carried out under varied conditions. The value of unbalance force, F_0 , cannot be changed because it will not produce linear independent equations, and the experiments cannot be carried out with different values of ω , c or W , because they all determine the operating condition of the bearing at which the coefficients are sought. The only parameter that can be changed is the vibrating mass, M . The experiments can be carried out at substantially different values of the mass in order to obtain reliable results. However, as it is seen in Figures 5.29(a) and 5.29(b) for different bearing geometries, there is a range^{of} eccentricity and stability parameter for which the amplitudes of response converge to the same value. Therefore, substantially different values of response for different values of M (i.e. for different values of S_p), for practical reasons, are limited to high eccentricities and low stability parameters (which, of course, should be well above the threshold value).

The method presented in this section makes use of the dependence of the oil film impedances on the excitation frequency. At a certain operating condition, response to excitation at a non-synchronous frequency gives a set of four equations. For the determination of the second set of equations, the oil film is to be excited at a different frequency in order to obtain a substantially different response. For practical purposes, it is advantageous to have stationary response orbits. This can be achieved at half of the shaft speed. Response to external excitation at half of the shaft speed is given in Figure 5.31 for comparison

with the synchronous response in Figures 5.29(a) and 5.29(b). They show different characteristics. In practice, these two excitations are applied simultaneously. Synchronous excitation occurs due to run-out and half-synchronous excitation from an external exciter. In this case, it is necessary to separate out the response to non-synchronous forcing from the synchronous vibration. In order to reduce the effect of measurement error, it is desirable to have deliberate run-out to obtain a large response orbit and in half-synchronous excitation the force amplitude should be kept small enough due to low damping of the fluid film bearing at this frequency ratio. Further, the overall response amplitude should be small enough in order not to violate the assumption of the linearisation of the oil film forces. If there is no run-out, then by exciting at synchronous and half-synchronous frequencies the necessary eight equations can be obtained.

If the amplitudes and phase angles of the resulting motions in the two directions are measured, then the vibrations can be expressed as:

For synchronous response:

$$\left. \begin{aligned} X_R &= X_1 e^{i(T-\phi_{X1})} = X_{R1} e^{iT} \\ Y_R &= Y_1 e^{i(T-\phi_{Y1})} = Y_{R1} e^{iT} \end{aligned} \right\} (3.12)$$

For half-synchronous response:

$$\left. \begin{aligned} X_F &= X_n e^{i(nT-\phi_{Xn})} = X_{Fn} e^{inT} \\ Y_F &= Y_n e^{i(nT-\phi_{Yn})} = Y_{Fn} e^{inT} \end{aligned} \right\} (3.13)$$

where $n = \frac{1}{2}$.

If these equations are substituted into equations (3.5) and (3.6), respectively, and keeping the terms including the impedances on the left hand side gives:

$$[Z]_1 \begin{bmatrix} X_{R1} & -R_o e^{-i\beta} \\ Y_{R1} & +i R_o e^{-i\beta} \end{bmatrix} = \frac{1}{S_p} \begin{bmatrix} X_{R1} \\ Y_{R1} \end{bmatrix}$$

$$[Z]_n \begin{bmatrix} X_{Fn} \\ Y_{Fn} \end{bmatrix} = \frac{F_o}{W} \begin{bmatrix} 1 \\ -i \end{bmatrix} + \frac{n^2}{S_p} \begin{bmatrix} X_{Fn} \\ Y_{Fn} \end{bmatrix}$$

If these equations are written with the impedances as unknowns:

$$\begin{bmatrix} X_{R1} - R_o e^{-i\beta} & Y_{R1} + i R_o e^{-i\beta} & 0 & 0 \\ 0 & 0 & X_{R1} - R_o e^{-i\beta} & Y_{R1} + i R_o e^{-i\beta} \end{bmatrix} \begin{bmatrix} Z_{XX_1} \\ Z_{XY_1} \\ Z_{YX_1} \\ Z_{YY_1} \end{bmatrix} = \frac{1}{S_p} \begin{bmatrix} X_{R1} \\ Y_{R1} \end{bmatrix}$$

$$\begin{bmatrix} X_{Fn} & Y_{Fn} & 0 & 0 \\ 0 & 0 & X_{Fn} & Y_{Fn} \end{bmatrix} \begin{bmatrix} Z_{XX_n} \\ Z_{XY_n} \\ Z_{YX_n} \\ Z_{YY_n} \end{bmatrix} = \begin{bmatrix} \frac{F_o}{W} + \frac{n^2}{S_p} * X_{Fn} \\ -i \frac{F_o}{W} + \frac{n^2}{S_p} * Y_{Fn} \end{bmatrix}$$

These equations are to be written as real variables for the solutions of the eight coefficients; then the two sets of four equations are:

$$[AZ] \begin{bmatrix} K_{XX} \\ C_{XX} \\ K_{XY} \\ C_{XY} \end{bmatrix} = \begin{bmatrix} 0 \\ 0 \\ F_o/W \\ 0 \end{bmatrix} + \frac{1}{S_p} \begin{bmatrix} Re(X_{R1}) \\ Im(X_{R1}) \\ n^2 Re(X_{Fn}) \\ n^2 Im(X_{Fn}) \end{bmatrix} \quad (3.14)$$

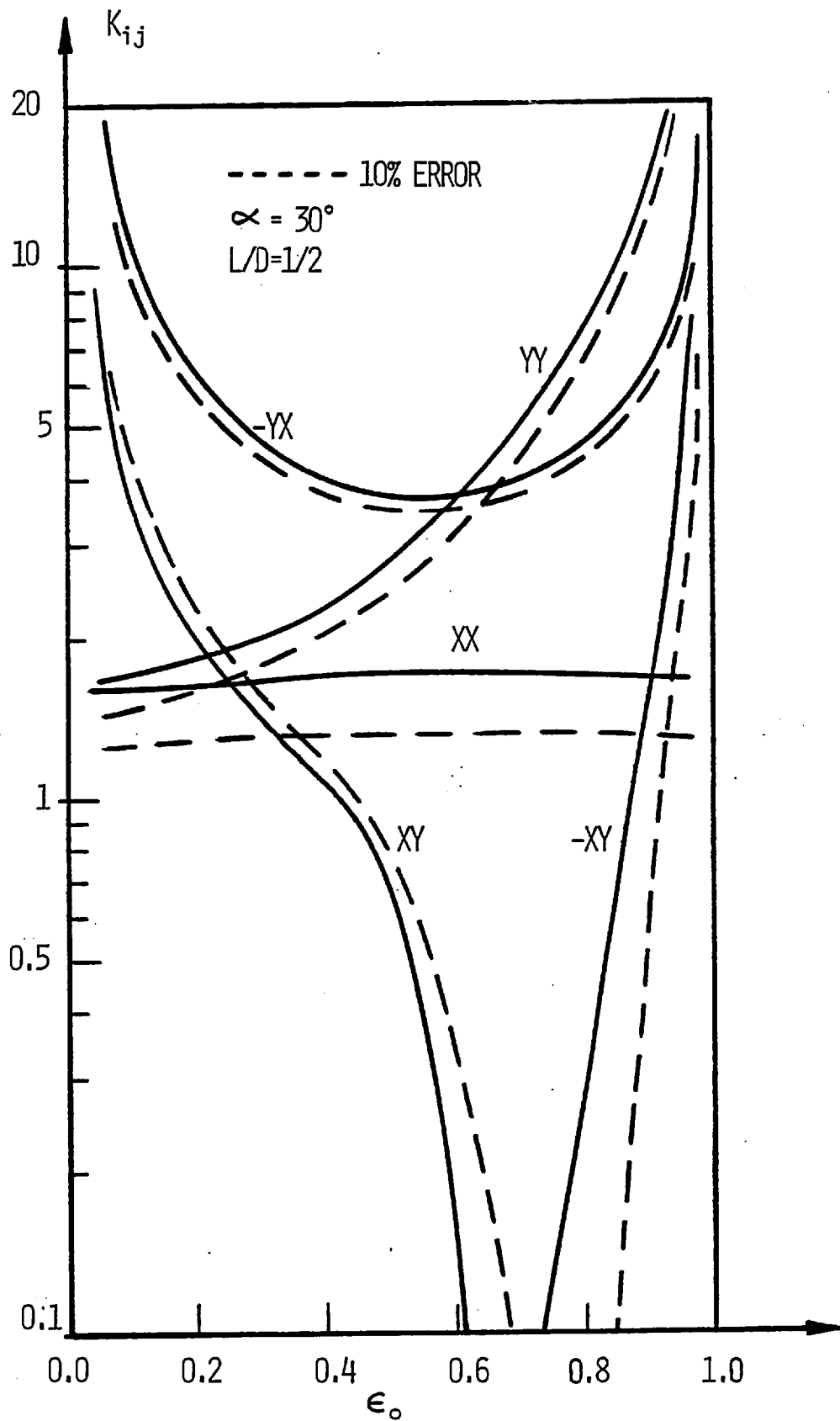
$$[AZ] \begin{bmatrix} K_{YX} \\ C_{YX} \\ K_{YY} \\ C_{YY} \end{bmatrix} = \begin{bmatrix} 0 \\ 0 \\ 0 \\ -F_o/W \end{bmatrix} + \frac{1}{S_p} \begin{bmatrix} Re(Y_{R1}') \\ Im(Y_{R1}') \\ n^2 Re(Y_{Fn}') \\ n^2 Im(Y_{Fn}') \end{bmatrix} \quad (3.15)$$

where $n = \frac{1}{2}$, and:

$$[AZ] = \begin{bmatrix} Re(X_{R1}^{-R_o} e^{-i\beta}) & -Im(X_{R1}^{-R_o} e^{-i\beta}) & Re(Y_{R1}^{+iR_o} e^{-i\beta}) & -Im(Y_{R1}^{+iR_o} e^{-i\beta}) \\ Im(X_{R1}^{-R_o} e^{-i\beta}) & Re(X_{R1}^{-R_o} e^{-i\beta}) & Im(Y_{R1}^{+iR_o} e^{-i\beta}) & Re(Y_{R1}^{+iR_o} e^{-i\beta}) \\ Re(X_{Fn}') & -n*Im(X_{Fn}') & Re(Y_{Fn}') & -n*Im(Y_{Fn}') \\ Im(X_{Fn}') & n*Re(X_{Fn}') & Im(Y_{Fn}') & n*Re(Y_{Fn}') \end{bmatrix} \quad (3.16)$$

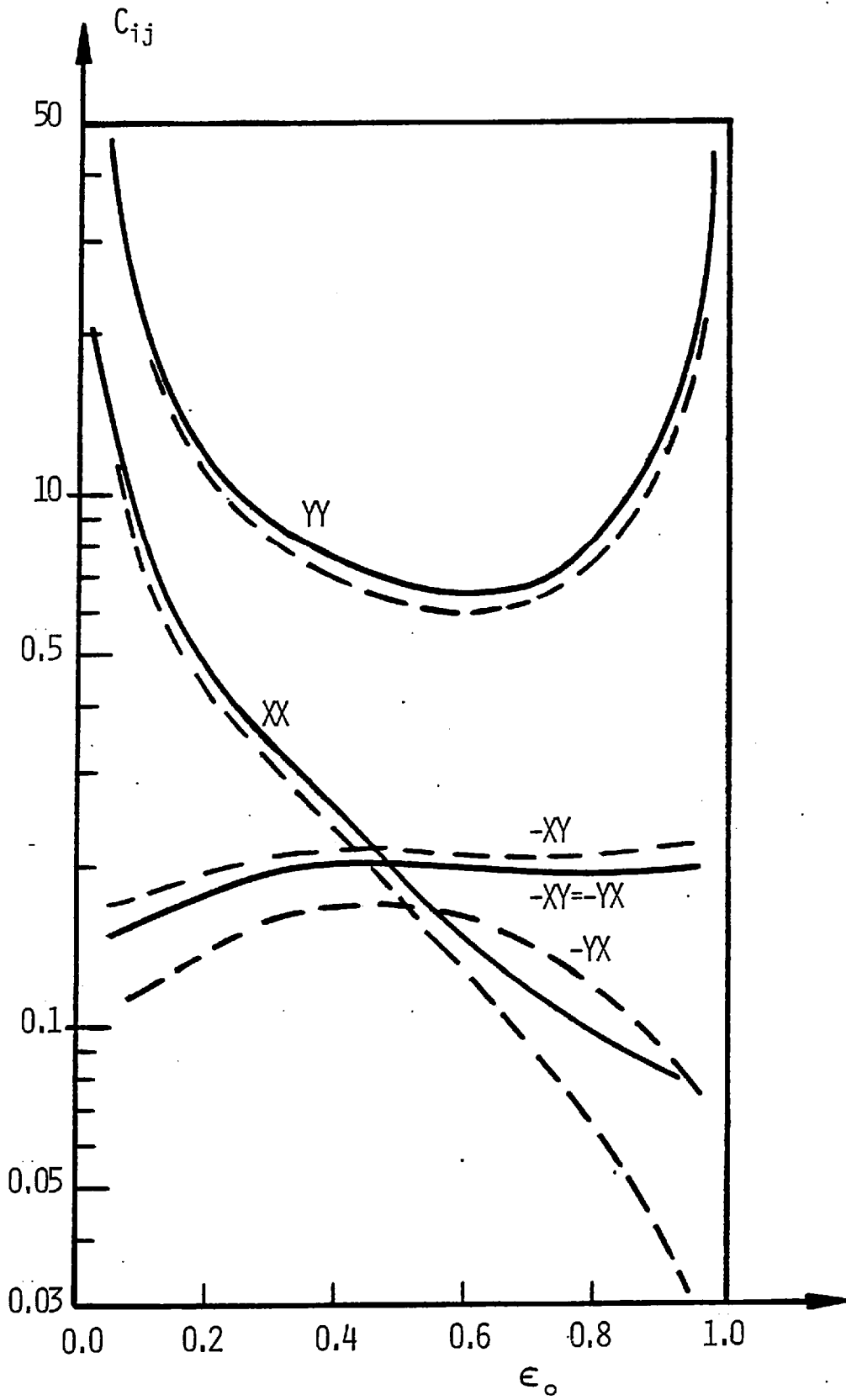
The coefficients can be solved by inverting equations (3.14) and (3.15) for given values of operating parameters F_o/W and S_p .

The effect of measurement errors on the calculations of the coefficients with this method is also investigated. For circular and elliptical bearings, the errors in the coefficients are calculated for +10% errors in amplitude of all measurements (i.e. in the elements of [AZ] and on the right hand sides of equations (3.14) and (3.15)) and the results are shown in Figures 3.2 and 3.3 as dashed lines. In equations (3.14) and (3.15), the parameters are taken as $F_o/W = 0.2$, $S_p = 1.0$, $R_o = 0.4$, $\alpha = 30^\circ$ and $\beta = 60^\circ$. Although the errors are small at high values of the coefficients, for low values of the coefficients (less than about 2.0) the errors can reach higher percentages.



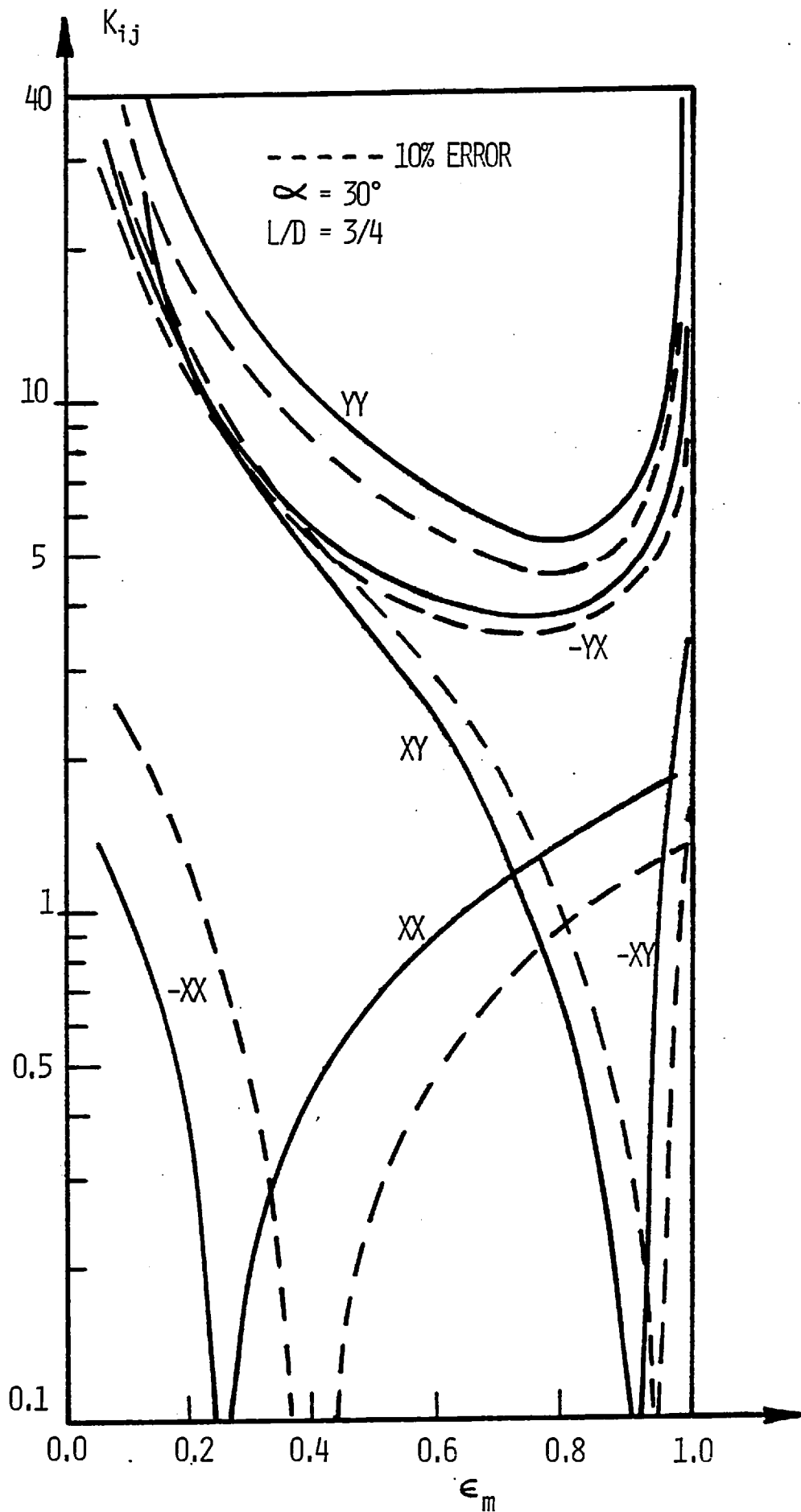
(a) Stiffness coefficients

Figure 3.2: Variation of the errors in the coefficients of a circular bearing



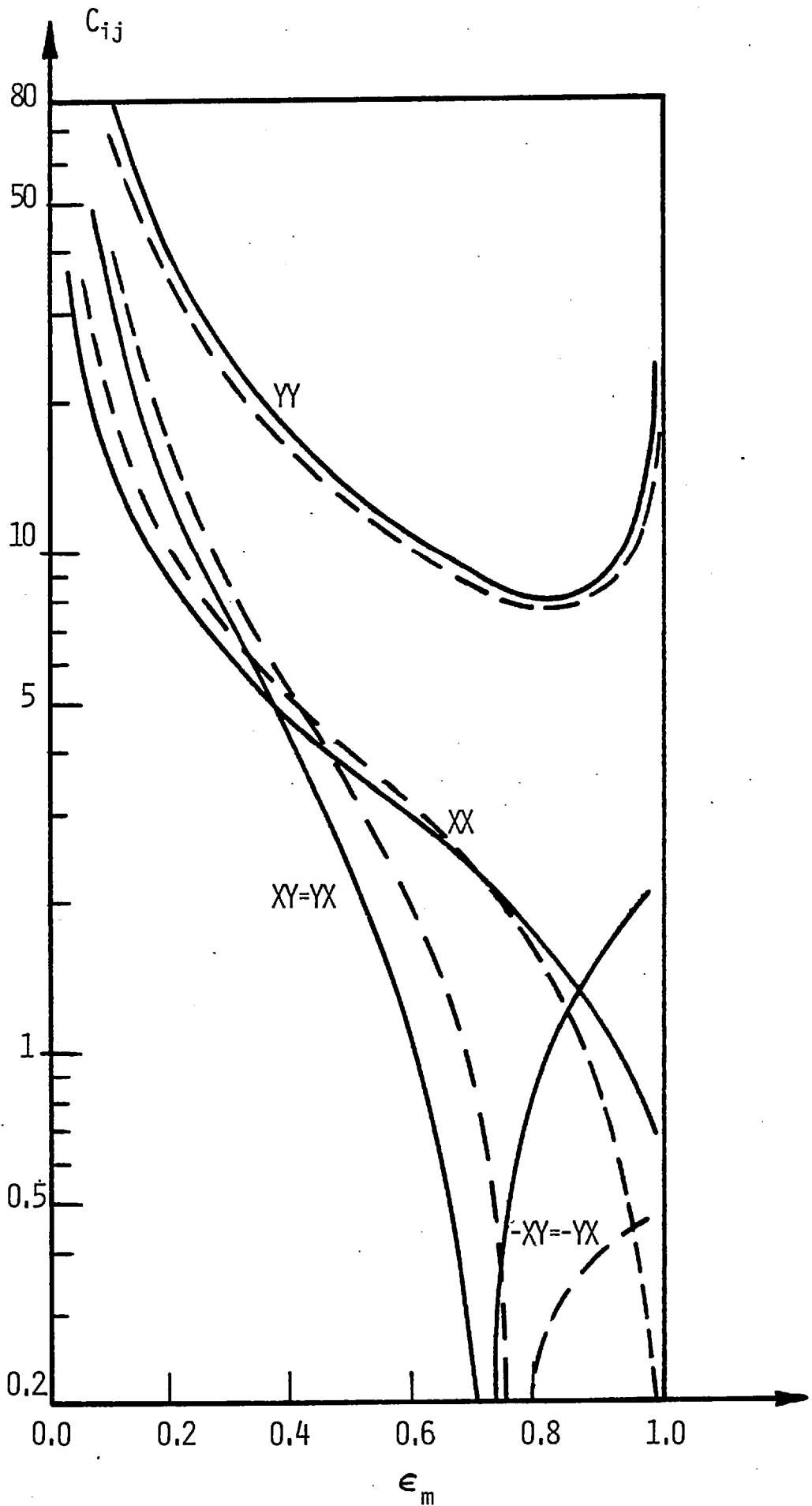
(b) Damping coefficients

Figure 3.2: Variation of the errors in the coefficients of a circular bearing



(a) Stiffness coefficients

Figure 3.3: Variation of the errors in the coefficients of an elliptical bearing



(b) Damping coefficients

Figure 3.3: Variation of the errors in the coefficients of an elliptical bearing

CHAPTER 4

EXPERIMENTAL APPARATUS

4.1 DESIGN REQUIREMENTS

In practice, shafts which carry large rotors have two sorts of motion, namely, rotation and vibration, while the bearings are mounted on structures that can usually be taken as rigid. However, for research purposes, dynamic bearing loads can be more readily adjusted and measured by allowing one element only to rotate and one only to vibrate. Therefore, it was advantageous to have a stationary shaft axis and a vibrating bearing. With this arrangement, the danger of a rotating heavy mass is diminished.

It was considered as an important design principle that various test parameters could be varied simply and with minimum effort. Therefore, several features were included in the design.

To avoid the effect of gravity on bearing loading, the shaft was mounted vertically so that the bearing and its housing vibrated in the horizontal plane. The bearing was supported and located in the horizontal plane by a hydrostatic air bearing which gave negligible resistance to vibration. By designing the centre of gravity of the "floating" mass to be at the test bearing centre, and the planes of application of static and dynamic loading to be at the mid-horizontal plane, it was possible to eliminate tilting effects.

To focus attention on the characteristics of the bearing and not to allow too many other factors to influence the system, it was necessary to simulate a rigid shaft and a rigid bearing housing system. An important requirement was that the test bearing be easily removed axially without disturbing the driven end of the shaft. It is well known that the performance of the test bearing could be greatly influenced by the

flexibility of its housing and shaft. Therefore, the choice of the arrangement was not arbitrary. The effect of shaft elasticity can be reduced considerably by placing the test bearing at the root of the overhanging part of the shaft.

Since the bearing housing was allowed to vibrate on the horizontal plane, the shaft had to be fixed firmly in its position in order to prevent any sort of motion. This was achieved by mounting the shaft housing in a relatively large concrete mass.

With this sort of arrangement, having a rigid shaft and a rigid bearing, it was possible to investigate easily the characteristics of only the bearings. Although the chosen experimental arrangement differs from that which normally occurs in rotating machinery, namely, bearing fixed-shaft free layout, it is important to consider that dynamic properties established in this test apparatus are valid for the conventional machinery arrangement. Details of loading arrangements were arranged so that all forces acting on the bearing would be known at any direction. Some extra care was taken to ensure that no extra unaccounted forces were present.

4.2 DESCRIPTION OF THE EXPERIMENTAL APPARATUS

An experimental rig and instrumentation were designed to cope with the requirements described in the previous section. A sectional view of the test machine design is shown in Figure 4.1. The essential features of the machine are as follows.

The test rig consists of two main assemblies. One of them is the shaft, its housing and auxiliary assemblies, and the other is the test bearing and its housing assembly.

Great care was taken in the design of the shaft support bearings in order to have a smooth running spindle. Since the running accuracy was

important, it was necessary to remove all internal clearances from the bearings and to maintain the balls in their correct running positions. Therefore, it was decided to design a spring-loaded angular contact ball bearing arrangement.

The shaft (1)* which was vertically placed in the housing (2) was mounted at the two places on angular contact ball bearings. Originally, the bearings were placed in back-to-back arrangement (the open side of the outer rings face in the opposite way) on the ends of the shaft. In order to increase the rigidity of the shaft on the test bearing end, a tandem unit was used on this side and a single row angular contact bearing was used on the drive end of the shaft. In this arrangement, the line of contact between the balls and their raceway diverges as they approach the shaft which gives a more rigid mounting. However, this arrangement caused misalignment and shaft axis movement when the shaft was loaded. Therefore, it was necessary to modify this arrangement by removing the inner one of the tandem unit. Again, this arrangement caused the movement of the shaft axis under the loaded condition. Therefore, at the test bearing end of the shaft, it was decided to have a paired face-to-face bearing (3) which was spaced by a small distance piece placed between the inner rings and clamped firmly on the outer rings. This unit has been preloaded against the ball bearing (4) at the drive end. This preload was necessary to ensure a minimum amount of run-out and to prevent the transmission of disturbances coming from the drive system. Although this arrangement gave a smooth running of the shaft with minimum run-out (measurement showed that there was 0.0003 in peak to peak run-out), due to high preloading on the bearings, it was not possible to run the shaft by a 2 HP DC variable speed

* () shows the part numbers in Figure 4.1.

controlled motor above 2000 RPM. Therefore, it was driven by a 10 HP AC motor at 2000 and 3000 RPM by using a toothed-belt and pulley drive.

Due to practical reasons, it was necessary to put the test section of the shaft at the overhung part of the shaft. The first critical speed (25,000 RPM) of the shaft was well above the maximum operating speed. The test section of the shaft was tapered with an included angle of two degrees to allow the clearance to be infinitely varied. The nominal diameter was 41 mm. At the drive end of the shaft, a pulley (5) and a timing gear (6) were placed.

The shaft housing was secured from the top plate (7) by eight anchor bolts and from the bottom by four screws to a 2.5 ton concrete block. This was necessary to eliminate the effect of journal vibration on the bearing and it was mounted on the ground at the four corner points.

On top of the rotor housing, an annular air thrust bearing (8) was placed. The test bearing housing (9) had a mass of 152 kg and could move freely on the air bearing. The part holding the test bearing (10) could be adjusted vertically up and down so that the clearance could be varied infinitely between the tapered shaft and bearing (11). The clearance was set by the three adjusting screws (12) and then this part was clamped to the housing by the clamping screws and wedge rings (13).

The air bearing and the test bearing mid-plane and the centre of gravity of the floating bearing housing were designed to be at the bearing centre. The static and dynamic loads were applied directly to the freely floating bearing housing in the same plane so that inertia forces and fluid film forces and all external forces acted on the mid-bearing plane.

(a) Test bearings: The detailed drawings of test bearings are shown in Figures 4.3, 4.4, 4.5 and 4.6. A photograph of the bearings is shown

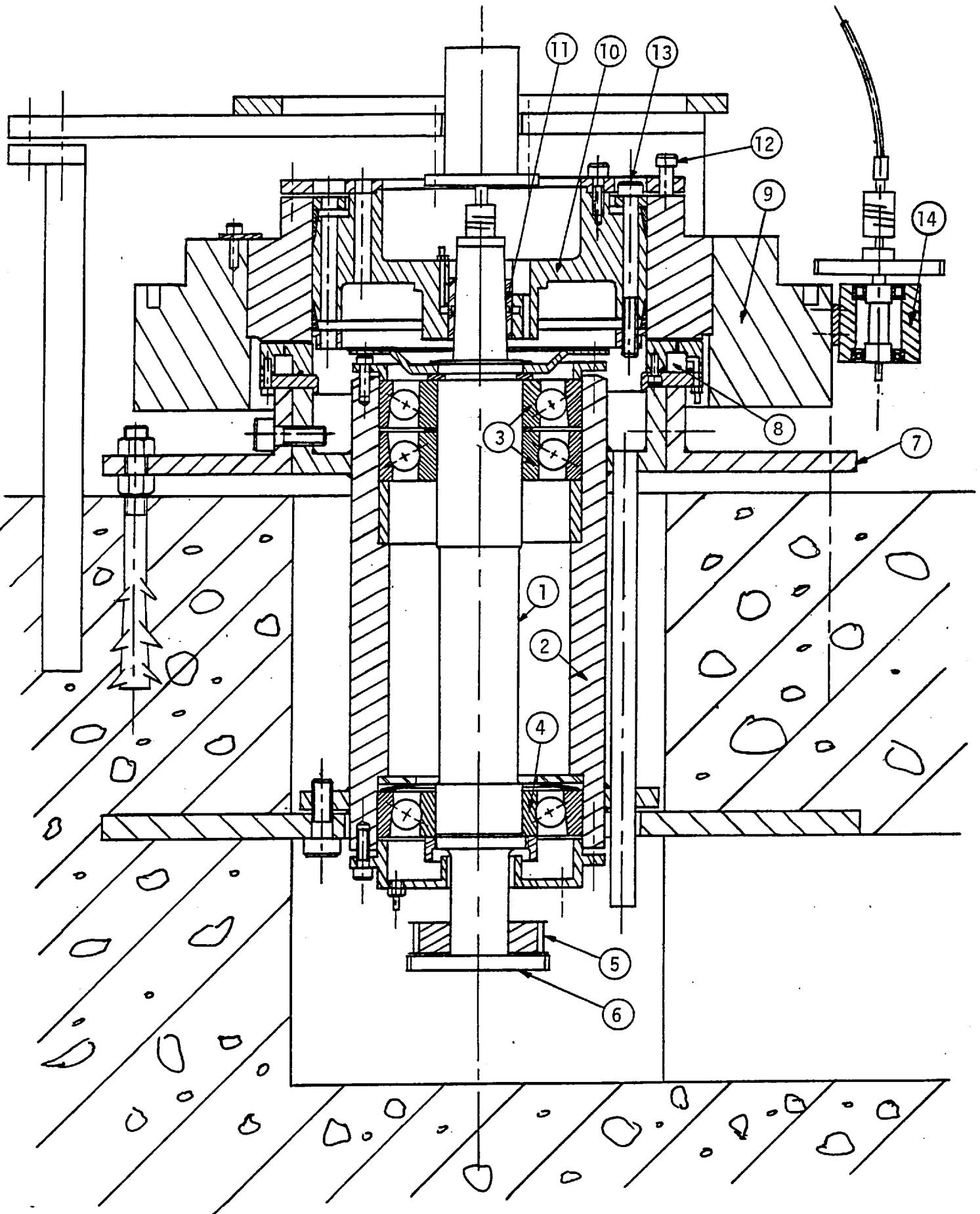


Figure 4.1: A sectional view of the experimental rig



Figure 4.2: A view from the test apparatus

in Figure 4.7. The test bearings were made of hard bronze with 41 mm nominal diameter. To ensure identical taper on shaft and bearing, the bearings were bored to fit a dummy shaft which was of the same taper as that of the test shaft. The oil was fed through the circumferential oil way which was behind the test bearing.

The circumferential groove bearing had a 3 mm wide \times 3 mm deep groove and the oil was fed through the eight equally spaced holes at the root of the groove.

The elliptical and offset halves bearings were split and, by inserting a shim of known thickness between the halves and machining the outer diameter of the bearing to the correct housing size, it was possible to change the preload. This procedure was repeated progressively from the maximum preload to zero preload value, i.e. the circular bearing.

Bearing temperatures were measured by thermocouples arranged around the mid-plane of bearings, about 1 mm below the bearing surface. The oil inlet temperature was measured by thermocouples placed into the grooves.

(b) Loading system: The "pull" type of static load was applied to the floating bearing housing at the mid-place of the test bearing by way of an air cylinder-piston arrangement. The load was measured directly by a spring balance placed between the air piston and the test bearing housing.

The dynamic load was superimposed on the static load by the two unbalance units (14). These units were assemblies of a small rotating shaft and a disc. They were attached at diametrically opposite positions on the bearing housing and driven by a 1.0 HP variable speed motor. By using a toothed-belt and pulley system, these units were driven in the same direction by two flexible drive cables. Unbalance force was produced by attaching an equal amount of out-of-balance masses on the discs and by

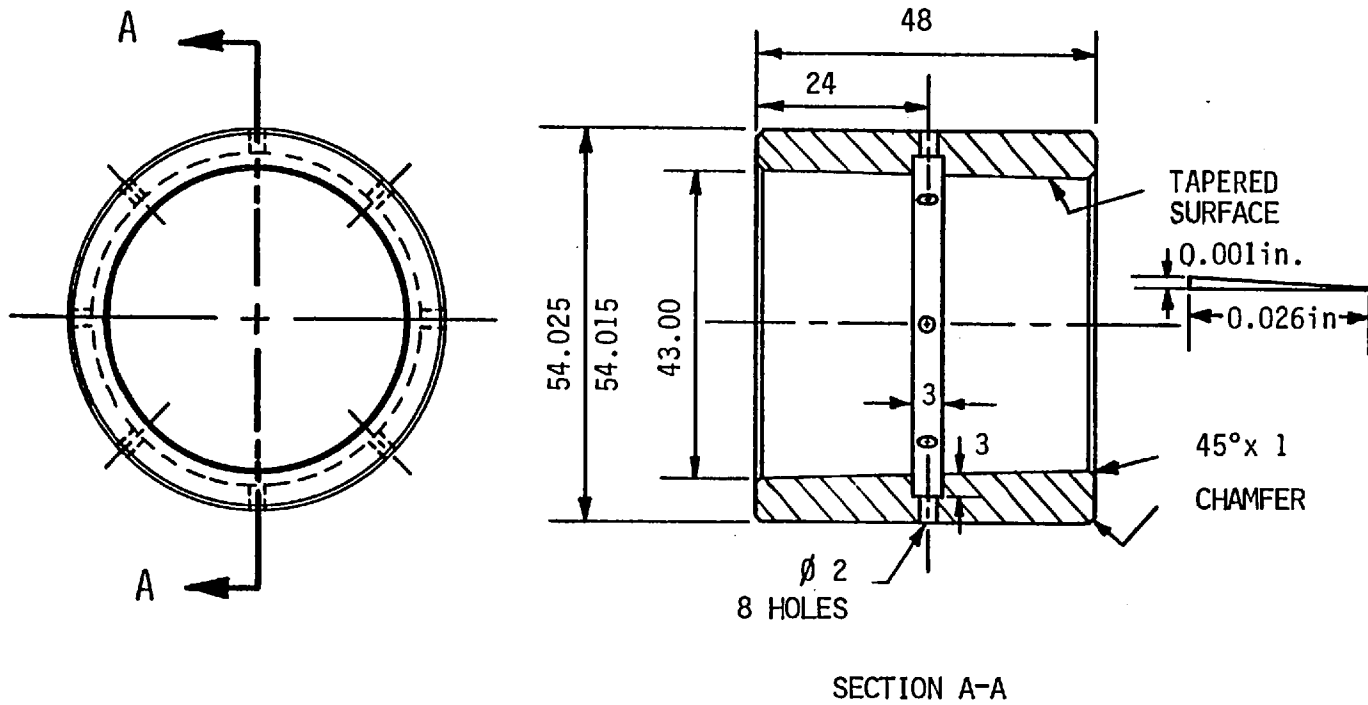


FIGURE 4.3 CIRCULAR CIRCUMFERENTIALLY GROOVED BEARING

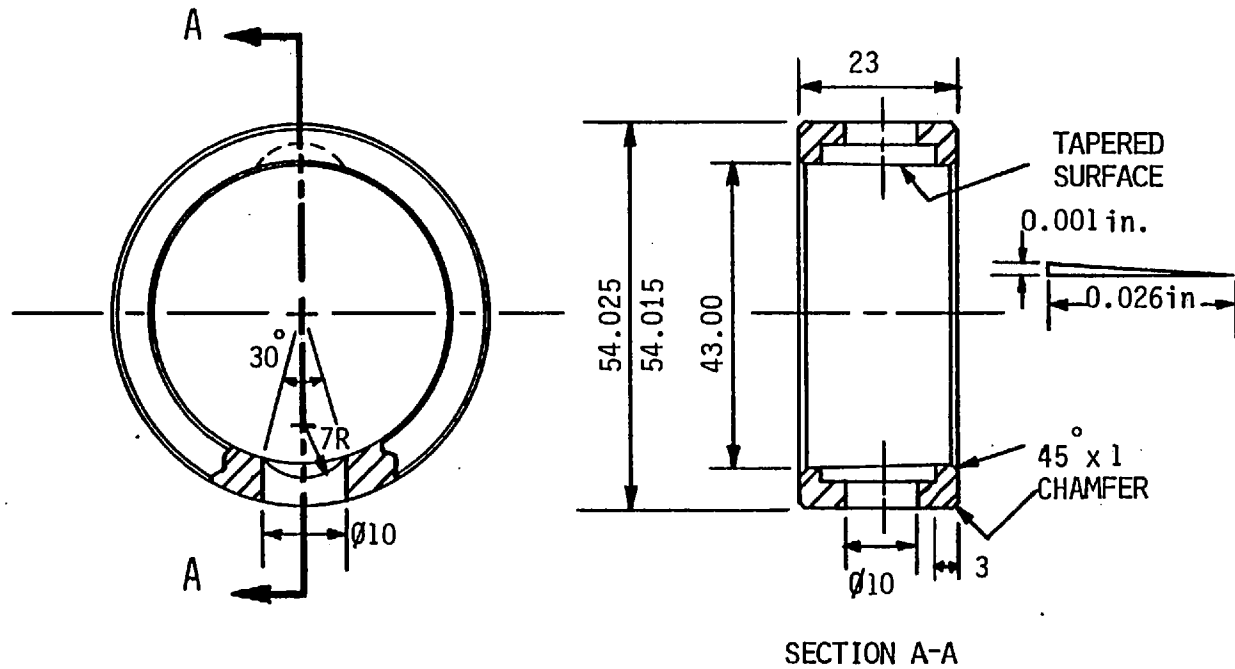


FIGURE 4.4 CIRCULAR TWO AXIAL-GROOVE BEARING

SCALE:1/1

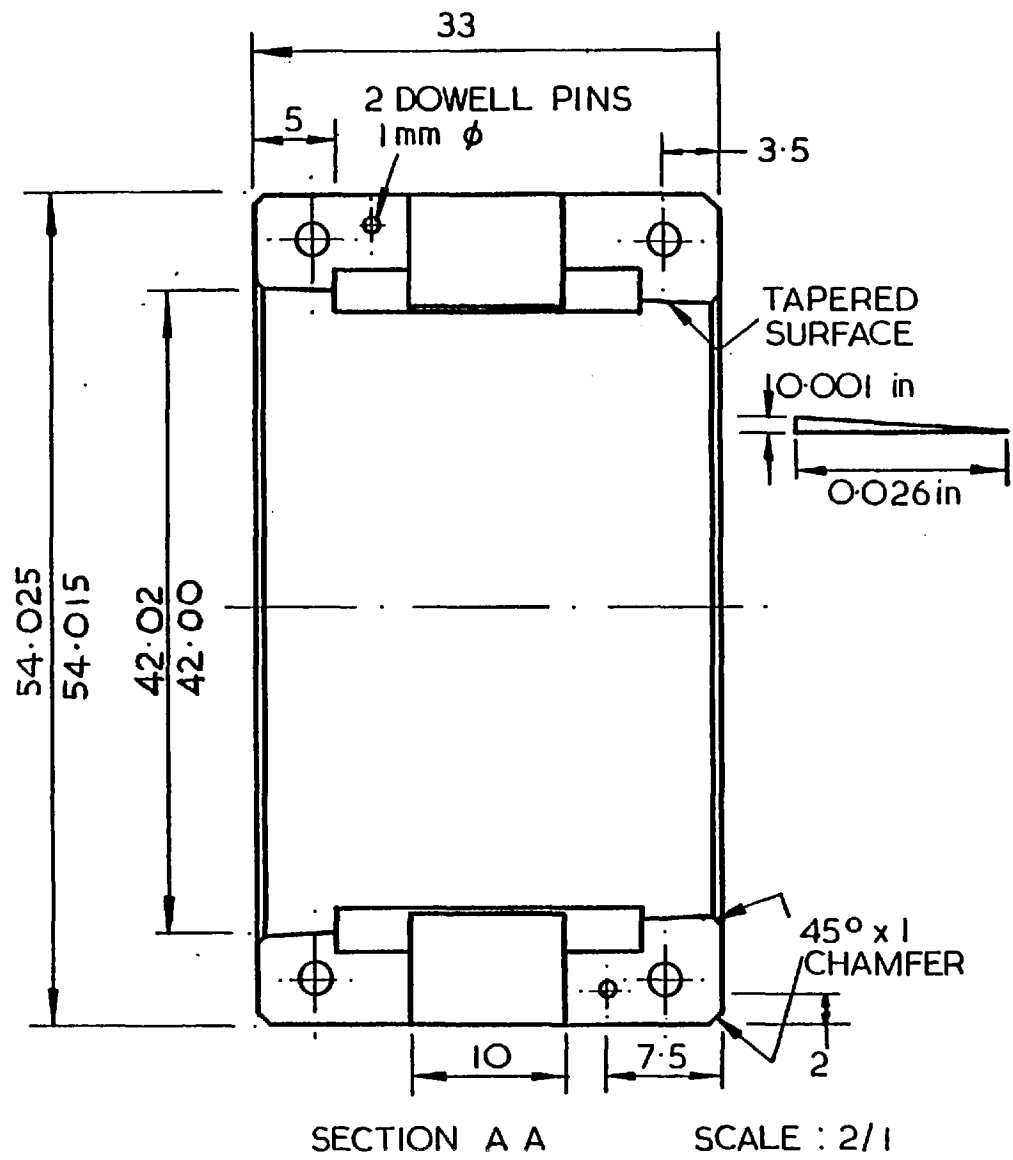
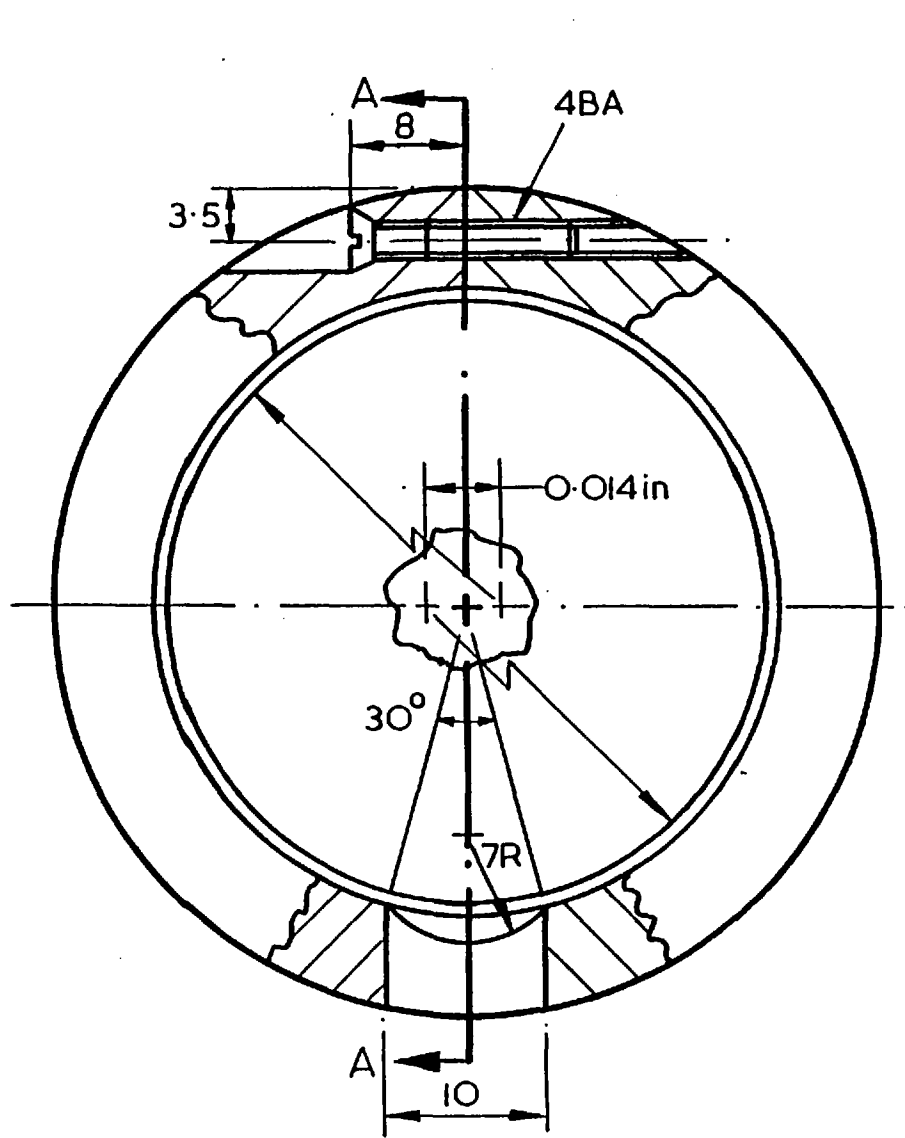


FIGURE 4.5 ELLIPTICAL BORE BEARING

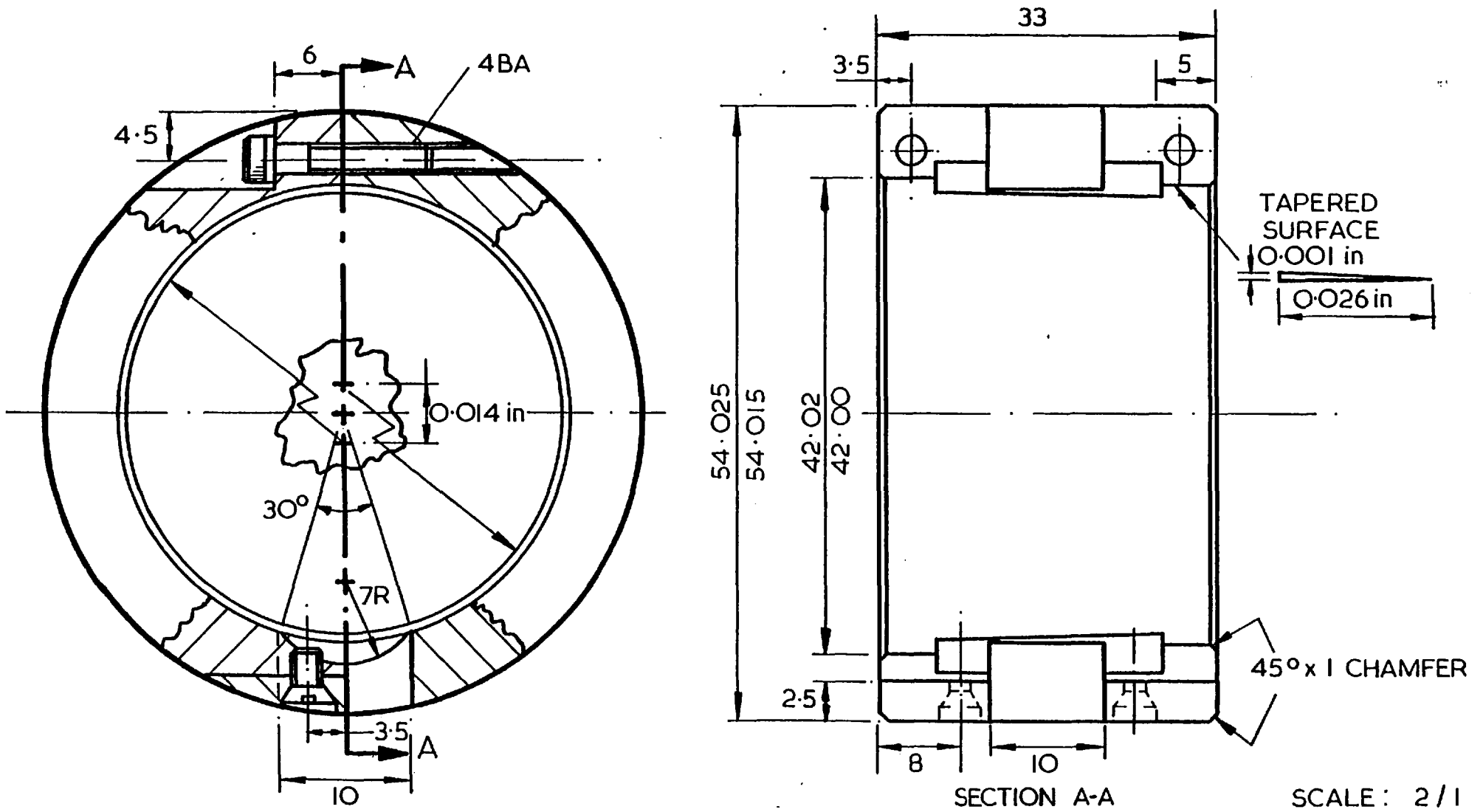


FIGURE 4.6 OFFSET HALVES BEARING

SCALE: 2/1



Figure 4.7: A view of the test bearings

adjusting at the couplings in order to rotate the masses in phase. The effect of any source of vibration coming from the drive system was prevented by the use of flexible couplings. These units were driven without out-of-balance masses and there has been no observable effect on bearing vibration.

(c) Oil supply system: A separate framework was built for the oil supply unit. Oil was supplied from a tank by means of a gear pump. A filter protected the oil supplied to both the test bearing and ball bearings. A cooler was incorporated on the by-pass circuit in order to control the oil temperature in the tank. The oil supply pressure to the test bearing could be set to any value by suitable adjustment of the by-pass valve and the throttle valve in the line supplying the test bearing. Flexible pipe was used immediately prior to the test bearing housing so that the supply pipe did not affect the housing motion and to prevent the transmission of vibration coming from the oil pump. Oil was delivered to the ball bearings through a small jet. Drained oil from the test bearing and ball bearings was collected under gravity by flexible pipes and returned to the tank.

The lubricant used was SAE50 oil, the calibrated values of the viscosity against temperature being shown in Figure 4.8. Oil inlet pressure in the oil way was measured on a calibrated Bourdon tube type gauge.

4.3 INSTRUMENTATION

In the investigation of journal bearing performance to find correlation with theoretical predictions, it is necessary to measure the applied load and the journal centre position and motion in the clearance space. Since

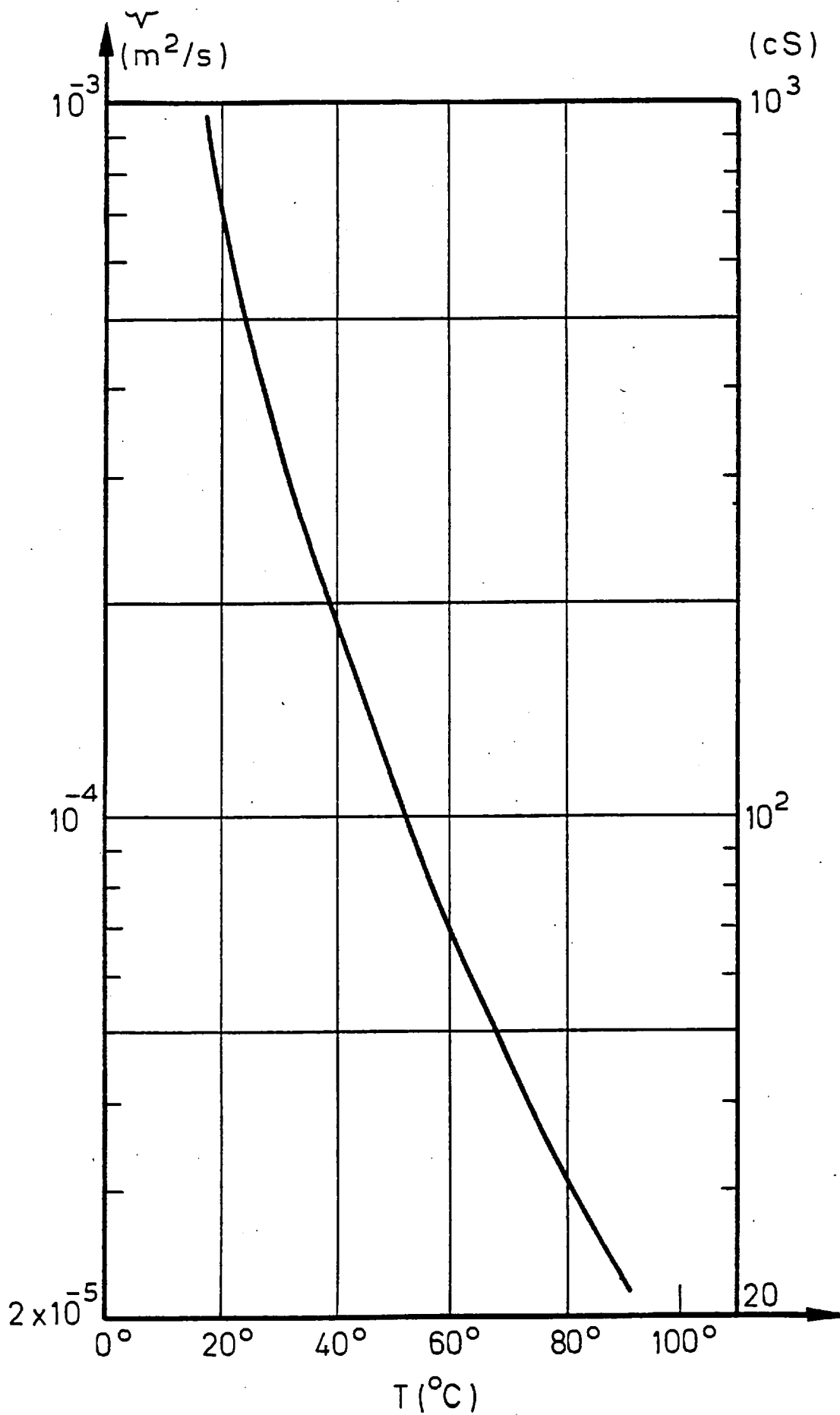


Figure 4.8: Viscosity-temperature relationship of the test oil
($\rho = 880 \text{ kg/m}^3$)

the film thickness is an important aspect in bearing design, the accuracy required for displacement measurements is high.

The horizontal and vertical displacements of the bearing relative to the journal were monitored by means of capacitive proximity transducers. In order to measure accurately the response of the bearing to imposed unbalance load, it was necessary to eliminate the effect of shaft ovality, eccentricity and axis motion due to the support bearings. The measurements showed that the shaft surface was round and concentric with the rotating axis to within less than 0.00015 in in radius. Therefore, the two orthogonally placed transducers were mounted horizontally on the bearing housing against the shaft surface. A two channel Wayne-Kerr frequency-modulated amplifier was used to give a voltage analogue of the transducer signals which were recorded on a two-channel oscilloscope. Each probe was calibrated before installation as a unit, together with its co-axial cables and amplifier. The sensitivity of the probes were nominally 1 V per 0.254 mm (0.010 in).

In this way, the bearing motion could be observed visually on the X-Y trace and any non-synchronous motion easily detected.

The shaft speed and the unbalance force excitation speeds were measured by inductive probes placed close to the toothed-discs. The speeds as number of revolutions were displayed on digital frequency meters with an accuracy of ± 5 RPM.

The temperatures of the bearing surface and the inlet and outlet oil temperatures were measured by chromel-alumel type thermocouples. These were calibrated after installation.

4.4 EXPERIMENTAL PROCEDURE

4.4.1 Clearance Setting and Alignment Check

Considerable care was taken in the design and manufacture of the apparatus to assure close alignment between the test bearing and the shaft axis.

With the bearing housing floating on the air thrust bearing, the test bearing housing was lowered on to the tapered shaft so that the bearing was concentric with the journal at zero clearance. Then the air pressure was turned off and the bearing housing was moved vertically upwards with the help of three adjusting screws equally placed around the housing. The incremental upward movement was obtained by rotating the $\frac{3}{8}$ BSF screws 45° each time in turn and was measured by three dial gauges (with 0.0005 in smallest division) equally spaced around the housing. The bearing housing movement was monitored as change in clearance observed on the oscilloscope connected to the capacitive transducers which were placed against the tapered shaft surface. By setting the same amount of gain for both channels of the oscilloscope (0.0005 in per major division), the beam on the X-Y trace moved at a 45° angle as the bearing was moved along the shaft axis. This procedure maintained the concentricity of the bearing throughout the clearance setting procedure. The bearing upward movement was measured to within ± 0.0005 in. From the geometry of the arrangement, the maximum misalignment would be of the order of $0.0005/12 \approx 0.04 \times 10^{-3}$ in per inch of bearing length, which was neglected. During the clamping procedure of the bearing housing to the floating mass, the subsequent clearance movement was kept within 0.0001 in (the smallest division) on the oscilloscope.

Alignment was also checked by comparing the bearing clearance shape dimensions, as measured by the capacitive transducers, against the

clearance dimensions calculated from the maximum movement of the journal inside the bearing for a given specific bearing geometry, as described in Appendix A. Any disagreement on the clearance shape due to the distorted form was attributed to the misalignment of the bearing housing, and therefore all the procedure described above was repeated again starting from zero clearance setting position until good agreement was reached.

It is to be noted that with this sort of clearance setting, it was possible to set the minimum clearance to a certain value and to check the maximum journal movement in the clearance shape with the known specific geometry of the bearing.

4.4.2 Determination of the Clearance Shape and Steady-State Operating Positions

At the beginning of each test, a clearance shape was established by applying a small load in different directions around the bearing housing, sufficient to cause contact between the journal and the bearing with no shaft rotation for a certain minimum clearance setting. At each of the corresponding bearing positions, a photo-record of the transducers in X-Y trace of the oscilloscope enabled one point on the clearance shape to be determined.

While the shaft was running at a certain speed, the static load applied to the bearing housing was reduced by small increments until the first indication of instability was observed in the form of non-synchronous vibration of the bearing housing. The load at which the instability began to build up was taken as the instability load and the load was then gradually decreased to zero. During this process, stable journal positions on the journal locus and unstable whirl orbits were recorded on the same photograph with the corresponding clearance shape.

Note that in the photographs journal rotation is in the clockwise direction unless otherwise stated.

Once the clearance shape was determined, for the other experiments the operating point in the clearance shape and the lowest position of the shape was marked when the shaft was at rest and the bearing housing was loaded lightly to the journal. This was checked by disturbing the bearing several times. By using this position as a reference, the bearing centre was located from the known geometric positions. This enabled the determination of the operating eccentricity, e , and the attitude angle, ϕ_0 , of the journal at any stable operating condition and at the instability onset condition.

4.4.3 Determination of the Stiffness Coefficients

The incremental loading method as outlined in Appendix C was employed in the determination of the stiffness coefficients. When the bearing was loaded against the rotating shaft at a certain equilibrium position, a small increment of load was applied in the x and y -directions successively and the resulting incremental displacements from the equilibrium position were measured. Great care was taken to avoid displacements greater than 0.3 of the bearing clearance and not less than 0.0003 in for accurate measurements.

4.4.4 Determination of the Dynamic Response

Dynamic tests were performed on the test bearing to observe the response to unbalance excitation at a variety of operating conditions.

In order to reduce the effect of run-out and measurement errors, it is desirable to impose a large unbalance force to obtain large response orbits. However, if the orbits are too large, the assumption of

linearisation of the dynamic oil film forces may be violated. Therefore, a compromise was established between these considerations by carefully chosen unbalance masses. For most operating conditions, the amplitude of the vibrations at synchronous excitation was not more than one third of the bearing clearance.

Throughout the excitation speed range, the amplitudes in the x and y -directions were taken, and at the synchronous speed, the major and minor axes of the elliptical orbits were measured.

CHAPTER 5

DISCUSSION AND CONCLUSIONS

5.1 DISCUSSION OF EXPERIMENTAL RESULTS

The static properties of different types of bearing are presented as the variation of the load capacity and the attitude angle against the eccentricity ratio. The experimental points were determined at a constant speed by varying the static loading for different values of clearance ratios. At every operating point, the journal was run for a few minutes to allow the oil film and the bearing temperatures to reach the equilibrium values. The experimentally measured load capacities for all bearing types were found to be somewhat lower than the theoretical values. The oil film temperature measurements around the top edge of the bearings were found to be the same as the bearing centre-line temperatures. However, due to the necessary preloading of the ball bearings on the shaft, the heat generated at those support bearings was conducted along the test section of the shaft. Therefore, the shaft surface temperature could be higher than the maximum bearing temperature. In order to take into account this complicated heat flow effect, the viscosity of the oil at the maximum bearing temperature was introduced into the Sommerfeld number as an effective viscosity.

During the experiments on static load capacity, the range of operating conditions was restricted because of the occurrence of large-amplitude whirl instability. At low values of eccentricity (corresponding to low values of load), meaningful data could not be obtained and the number of experimental points are comparatively scarce.

In the two axial groove bearings, the load is applied centrally to the bottom half of the bearing. With the non-circular bore bearings, the journal is unable to move within the whole bearing clearance space between

the bearing and the journal; therefore, with these bearings the static locus of the journal was shown relative to the envelope of maximum movement of the journal.

The bearing load at the stability threshold was obtained by reducing the static load in small increments at a constant shaft rotational speed. The first indication of instability was observed in the form of non-synchronous vibration of the bearing housing. The stability threshold parameter was calculated at that load and plotted against the measured eccentricity at the onset of instability. With this method of experimentation, the results were found to be repeatable.

In order to see the whirl orbit at the no load condition, the load was reduced further beyond the stability threshold value. In general, at high eccentricities, the whirl amplitudes gradually become larger as load was reduced, but at low eccentricities the whirl amplitude expanded suddenly at the onset condition.

In all these figures, theoretical predictions are shown by full lines and the experimental results are shown by the symbols given on the first figure of each bearing type. It is to be noted that the indices of the stiffness coefficients are consistent with Figure 2.1 and the stability parameters for non-circular bearings are calculated by using the bearing arc clearance.

5.1.1 The Circular Circumferentially Grooved Bearing

The effect of feed pressure on the whirl stability was investigated with this bearing. It is well known that the existence of unstable bearing operation is directly related to the extent of the fluid film cavitation in the bearing. Since the pressure distribution is determined by the wedge shape of the oil film, the effective way of

controlling the cavitation region in the diverging part of the film shape could be by a pressurised supply from the edge of the bearing.

The effect of ambient pressure on the extent of the cavitation region was investigated by Barrett et al [27]. By using the short bearing approximation and assuming that the oil film cavitates when the absolute pressure was zero, they showed that journal stability can effectively be controlled by the ambient pressure and for the ambient pressure to mean bearing pressure ratio greater than two, the journal always becomes unstable for eccentricity values less than 0.6.

In this series of tests, experiments were carried out by varying the oil feed pressure in the groove, i.e. at the inner edge of the land, while at the outer edge the pressure was the atmospheric pressure. Experimental data points and the corresponding theoretical predictions of the load capacity and the attitude angle variation are given in Figures 5.1(a) and 5.1(b). The full lines are the theoretical values for different feed pressure ratios, γ , defined as $\gamma = p_f/p_b = p_f/(W/LD)$. The feed pressure has a moderate effect on the load capacity, although this becomes negligibly small at high eccentricities. The experimental points are given for a feed pressure ratio of $\gamma = \frac{1}{2}$. The measured load capacities are below the theoretical values and show experimental scatter.

A comparison of the experimental bearing stability with the theoretical values for various oil feed pressure ratios are given in Figure 5.2. In each case, a hysteresis effect was observed, i.e. for the same clearance ratio, in that once the whirl was started, the load required to cease the whirl was found to be higher than the load at the onset. Therefore, for each data point, the instability onset and cessation values are connected by a line. This hysteresis effect can be explained by the fact that the cavitation region cannot easily re-locate to its original

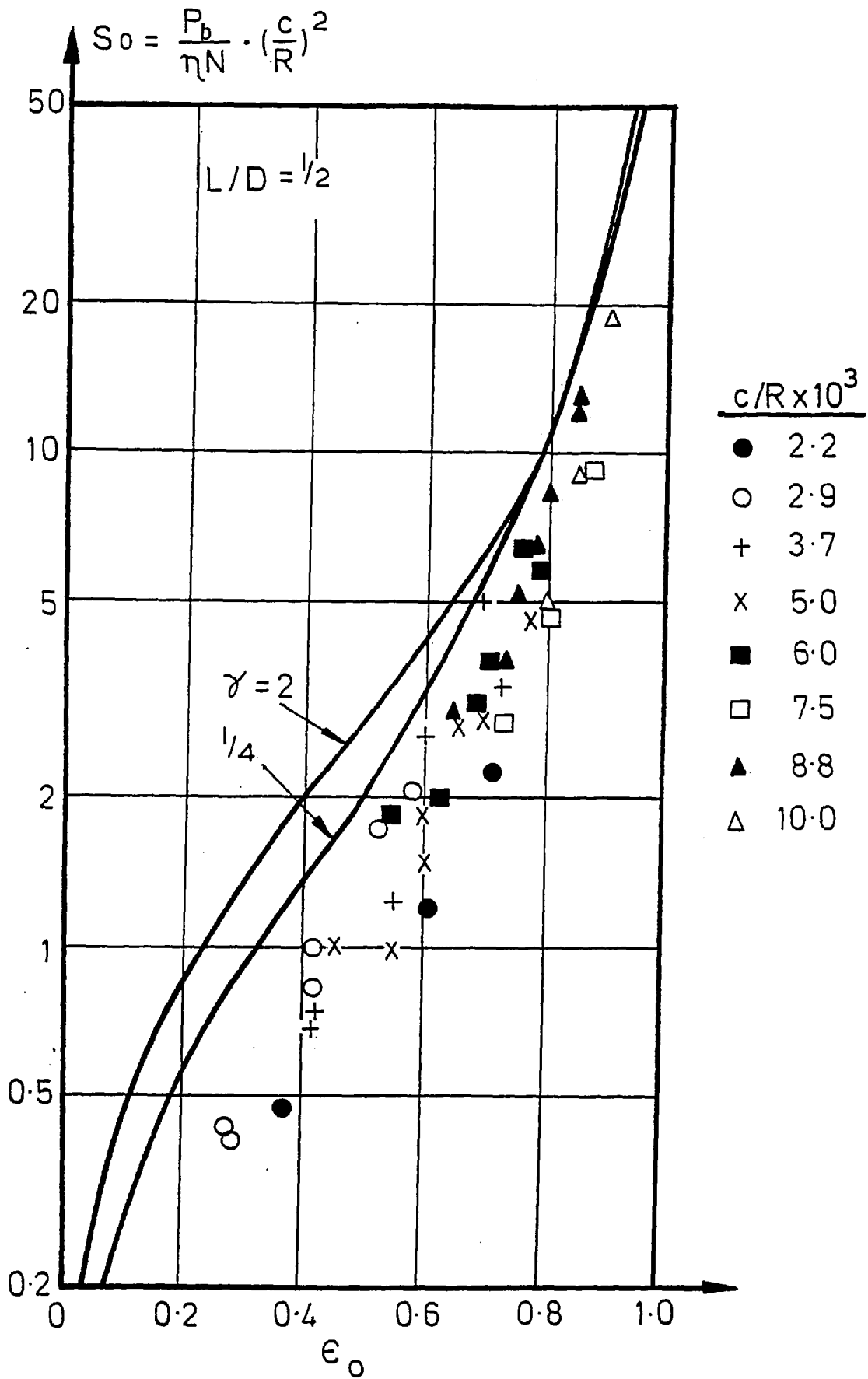


Figure 5.1: (a) Load capacity of the circumferentially grooved bearing

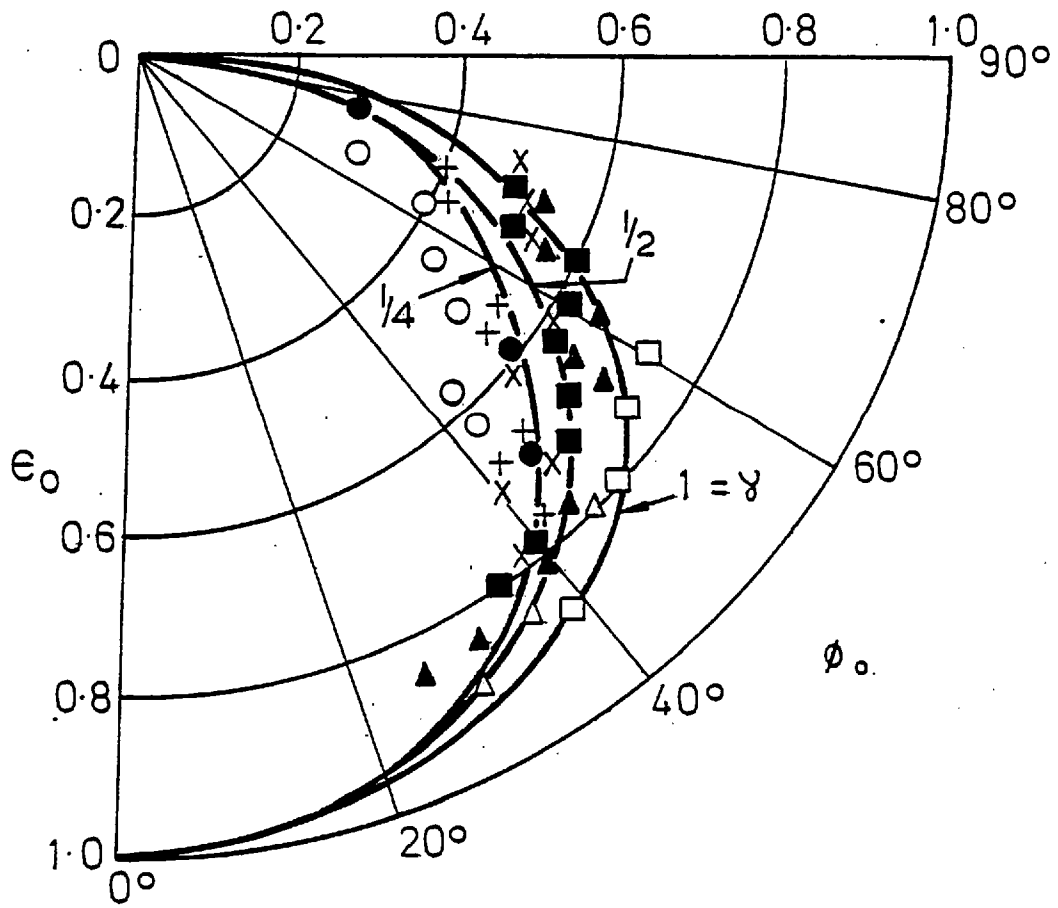


Figure 5.1: (b) Locus of the shaft centre in the circumferentially grooved bearing

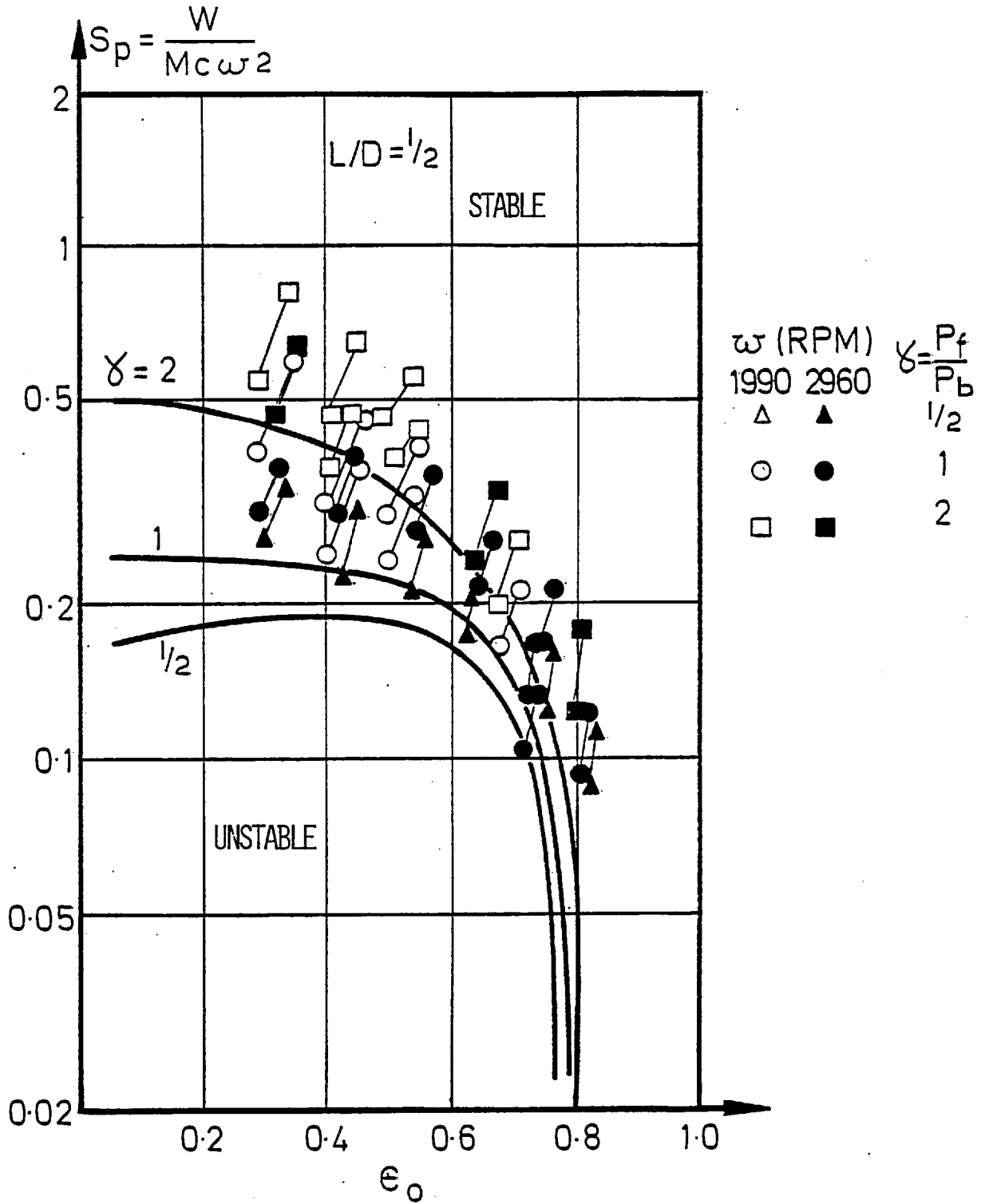


Figure 5.2: The effect of feed pressure ratio on the stability threshold, showing also the extent of whirl hysteresis

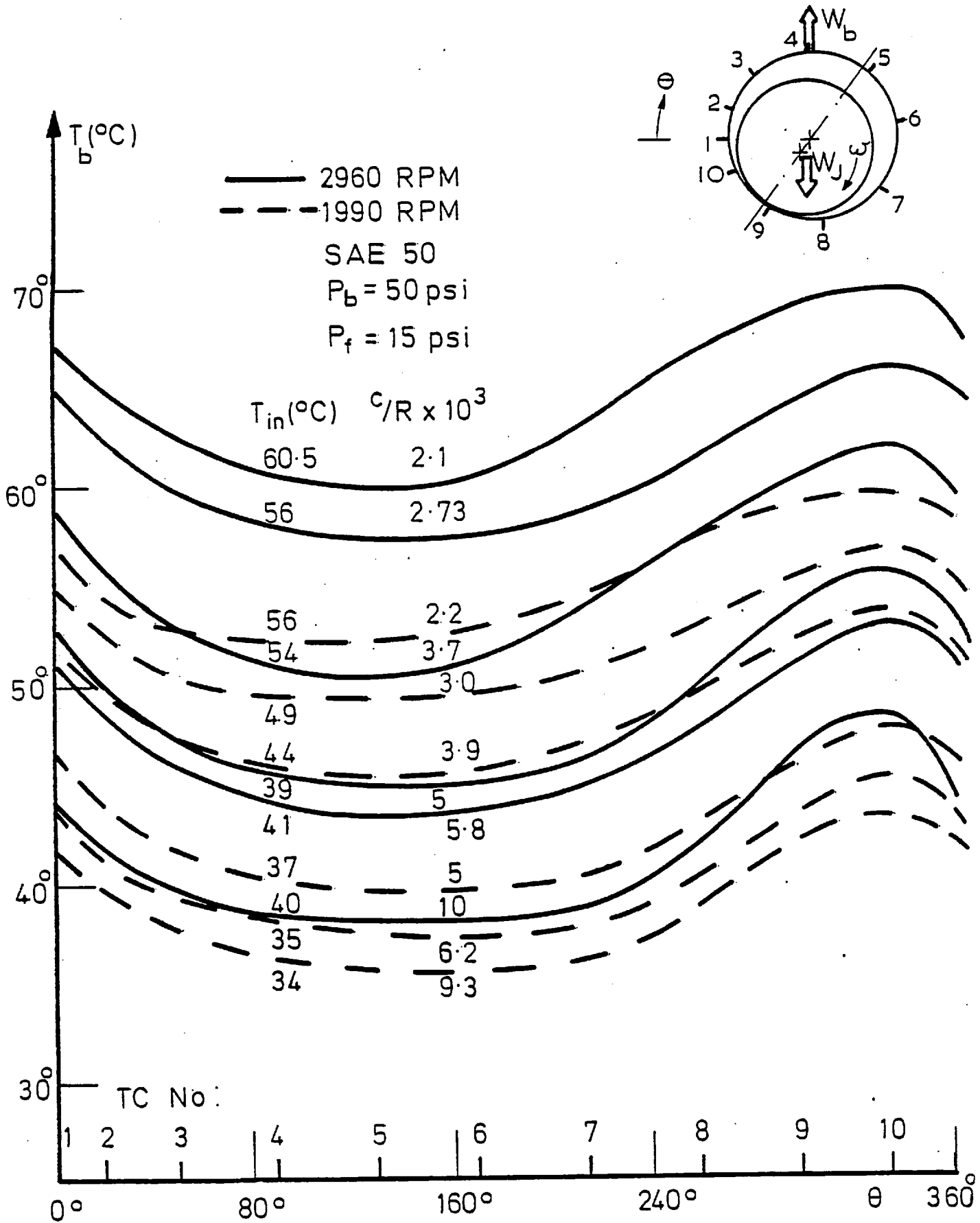


Figure 5.3: Temperature profiles around the circumferentially grooved bearing on the top land centre-line

position by increasing the loading once it starts whirling. This has been shown also experimentally in dynamically loaded bearings by Olsson [28]. He states that the position of the cavitation region boundaries are dependent not only on the present situation but also on the pre-history of the oil film. Therefore, it may require some extra force to recover the oil film forces during the transition from the stable to the unstable region.

The temperature profiles are shown in Figure 5.3. The bearing temperature at the maximum film thickness region is about at the oil inlet temperature and it reaches the maximum value around the minimum film thickness. The temperature increase is steeper at high clearance ratios due to the associated higher eccentricity ratios.

5.1.2 The Circular Two Axial Groove Bearing

The effect of groove angle on the whirl stability of a centrally loaded bearing was investigated for 30° and 90° groove angles. The steady-state load capacity and the attitude angle variation data against the equilibrium eccentricity are given in Figures 5.4 and 5.8 for 30° and 90° groove angles, respectively. The load capacity of the 90° groove angle bearing is slightly lower than the 30° angle bearing.

The experimentally determined stability threshold data are given, together with the theoretical stability borderline in Figures 5.6 and 5.9. From these figures, it is seen that increasing groove angle has a strong destabilising effect. For medium and low eccentricities, increasing the groove angle from 30° to 90° causes the instability borderline to rise by a factor of about 2.

Typical load dependent whirl orbits are shown in Figure 5.5 for a 30° groove angle bearing. The bearing begins to whirl almost in a

small elliptical orbit around the equilibrium eccentricity ratio of 0.67 at the bearing load of 48 lb. As the load is decreased successively from 40 lb to the no load condition in equal decrements below the stability threshold, the steady whirl orbits are observed. At the no load condition, it becomes full clearance whirling. The increasing importance of non-linearity effects as the whirl amplitudes increase can be clearly seen. The fluid film forces acting on the bearing will be largest when the journal is approaching the bearing wall and smallest when the journal is approaching the bearing centre. Therefore, as the load is decreased, the whirl orbit expands in a distorted elliptical shape and the centre of the orbits move closer to the bearing centre.

The typical temperature profile development along the 30° and 90° groove angle bearing centre-line are given in Figures 5.7 and 5.10, respectively. As the oil inlet pressure and temperature are kept constant, the bearing temperatures increase steadily as the clearance ratio decreases. The temperature increase for the 30° groove angle bearing is steeper than the 90° groove angle. In the top half of the bearing, the temperature increase is negligible for clearance ratios larger than 8×10^{-3} and 3×10^{-3} for the 30° and 90° angle bearings, respectively.

5.1.3 The Elliptical Two Axial Groove Bearing

The effect of preload on the stability characteristics of the elliptical bearing was investigated for a 30° groove angle. Experimental data points and the corresponding theoretical results of the steady-state load capacity, the attitude angle variation and the stability threshold maps are given in Figures 5.11, 5.12, 5.13 and 5.14 for different preload values.

At low eccentricities, the top half of the bearing is as

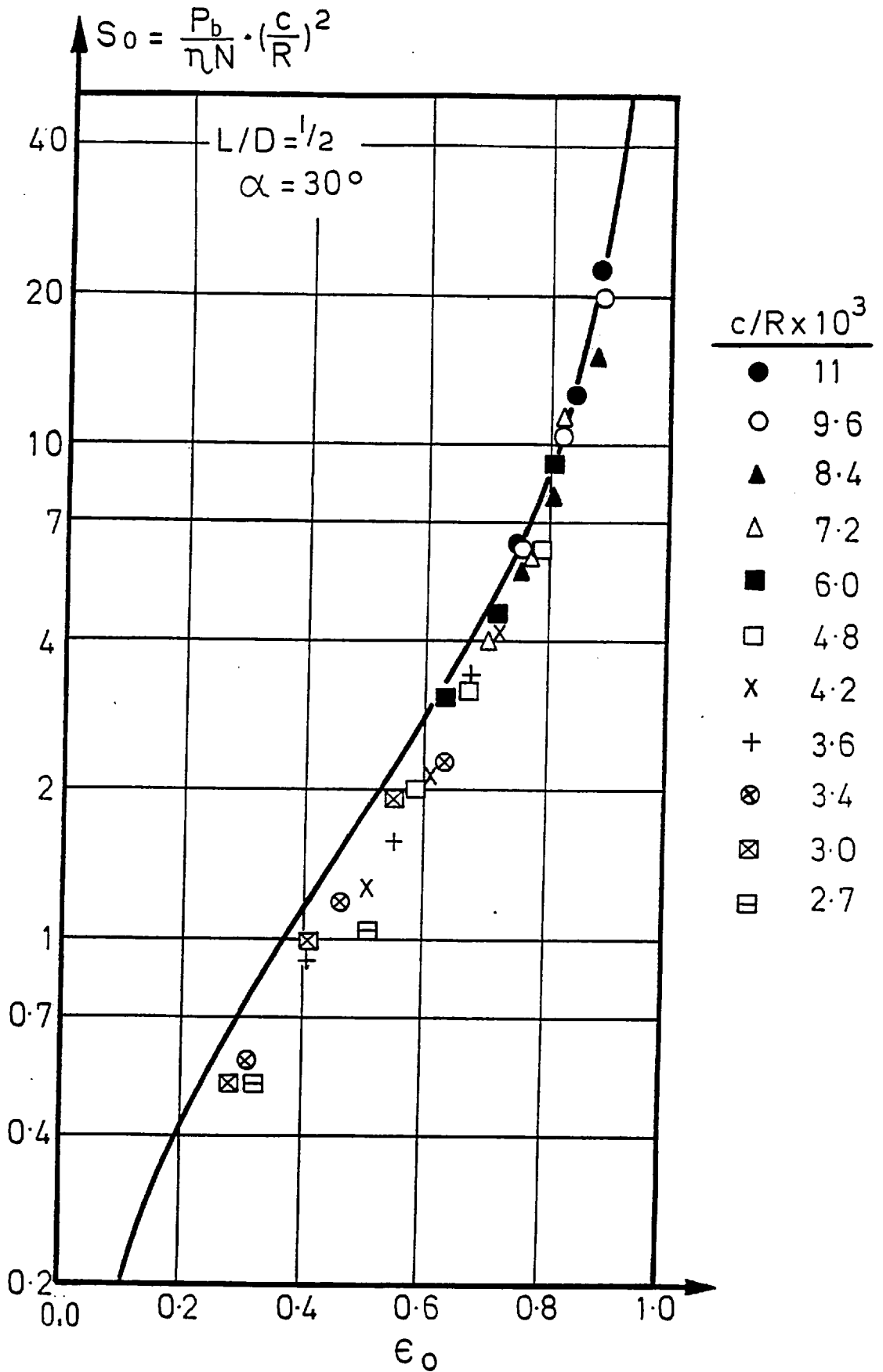


Figure 5.4: (a) Load capacity of the 30° two axial groove bearing

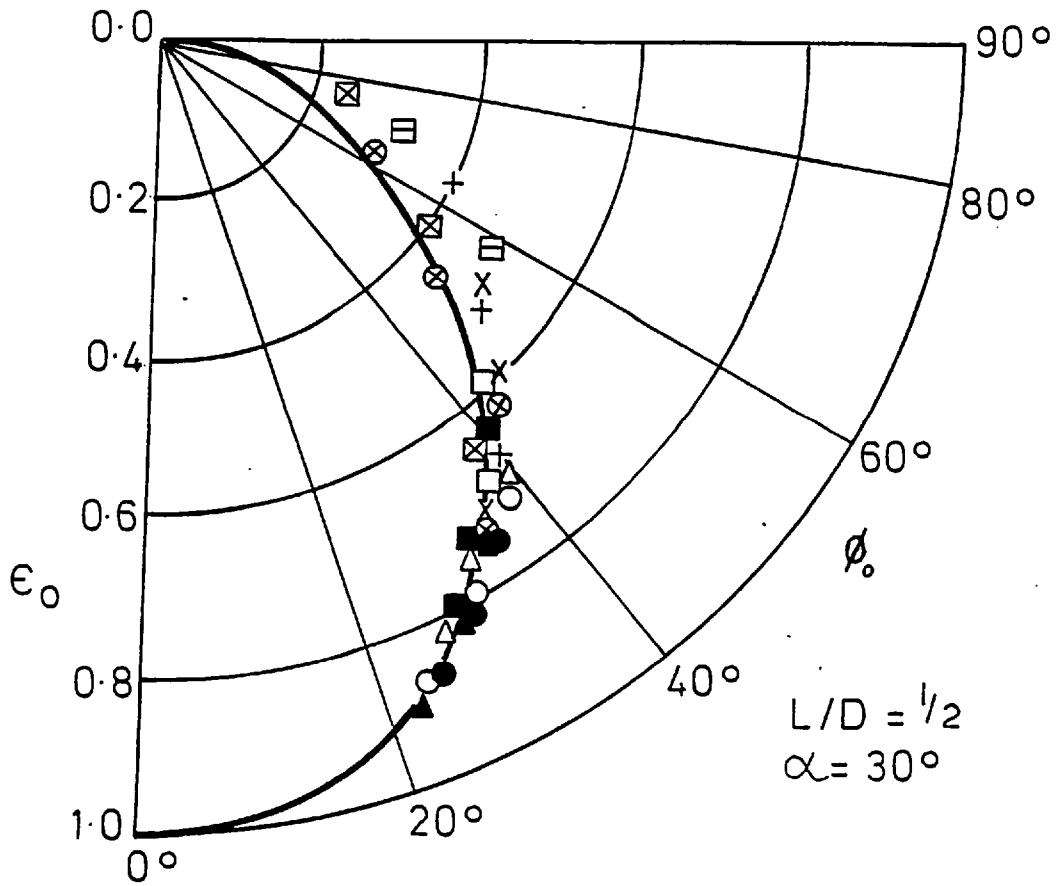


Figure 5.4: (b) Locus of shaft centre in the 30° two axial groove bearing

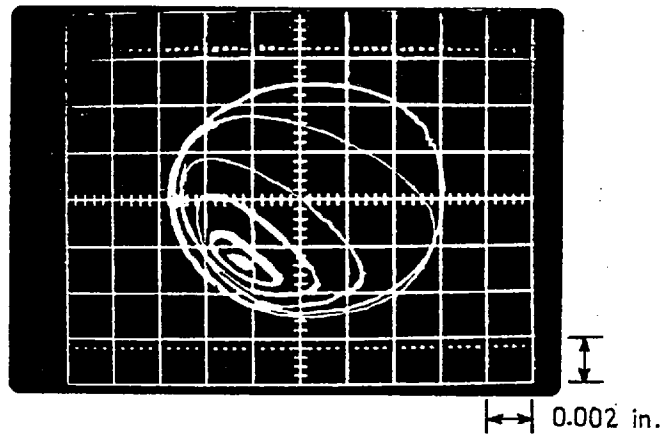


Figure 5.5: Experimental whirl orbits, $\omega = 1990$ RPM, $\alpha = 30^\circ$, $\epsilon_0 = 0.67$

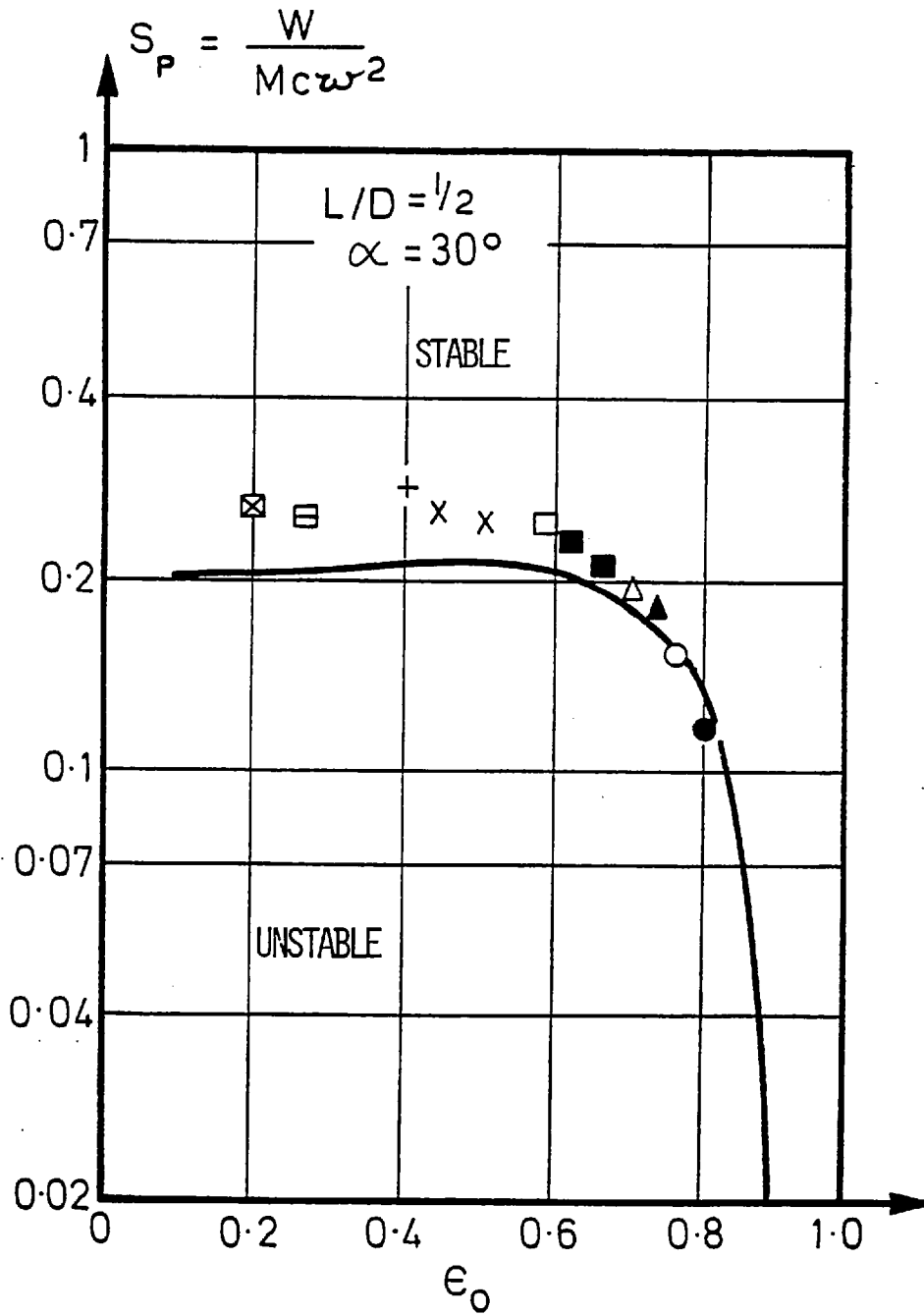


Figure 5.6: The stability threshold parameter for the 30° two axial groove bearing

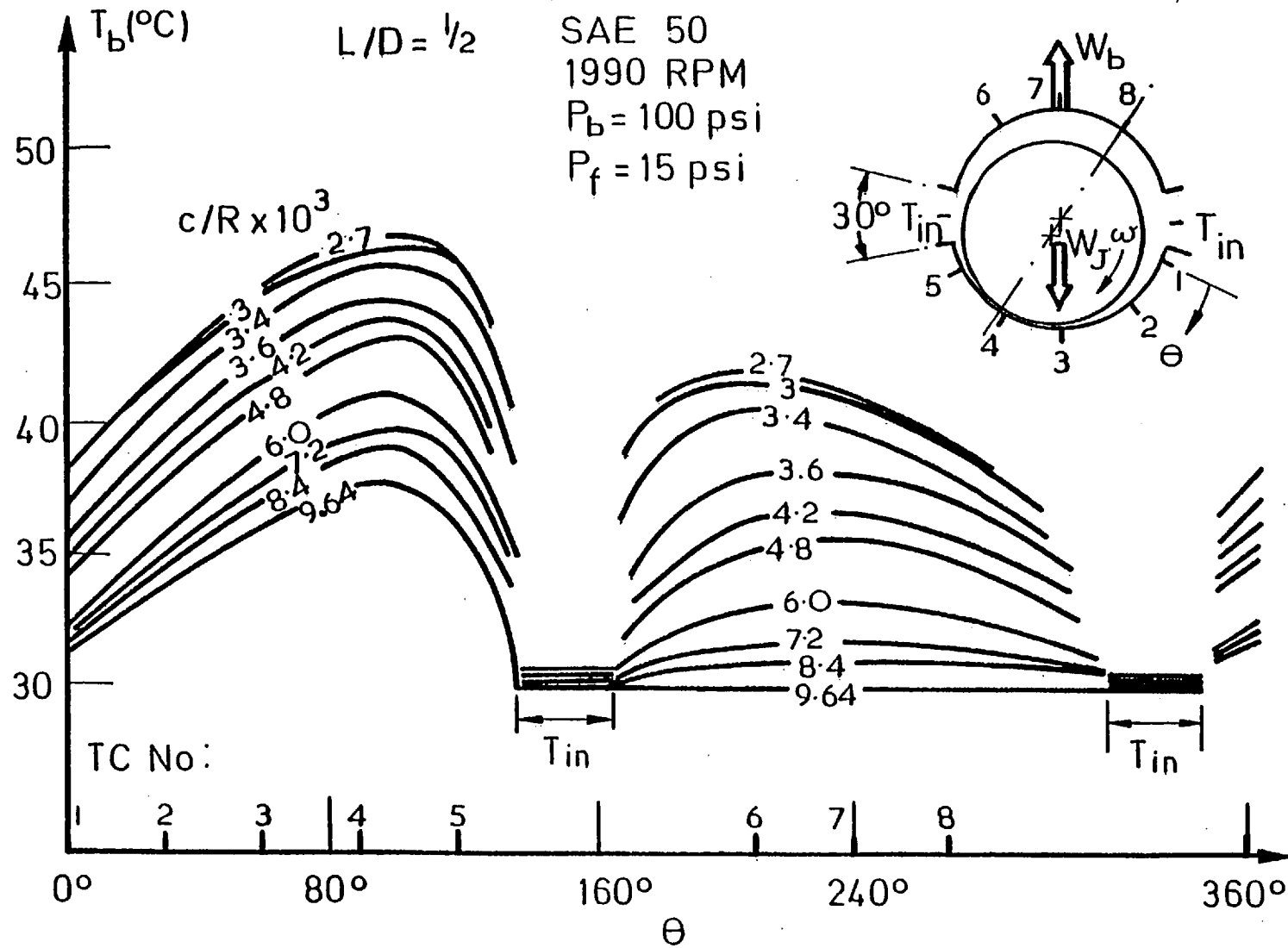


Figure 5.7: Temperature profiles around the two axial groove bearing centre-line

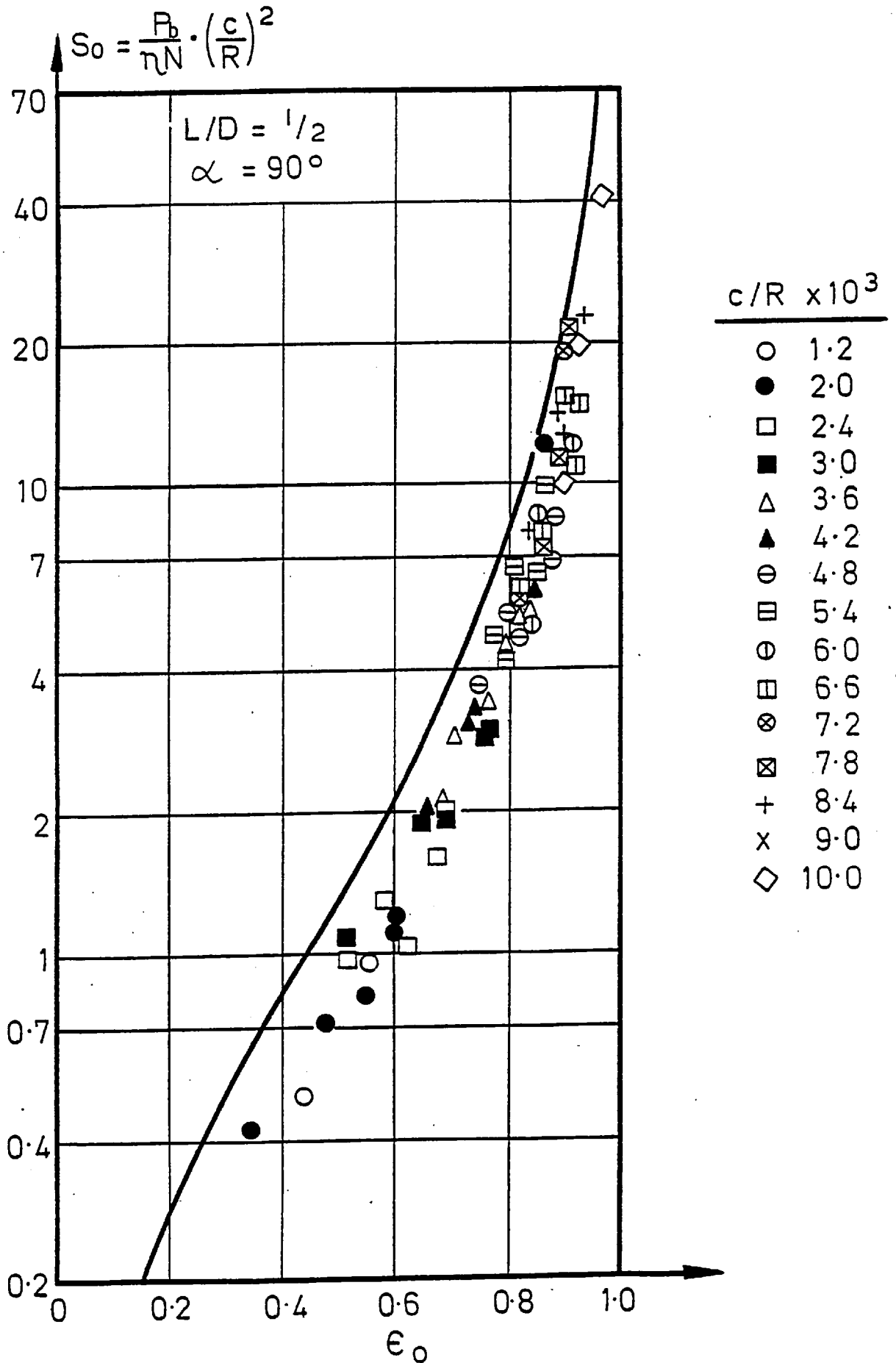


Figure 5.8: (a) Load capacity of the 90° two axial groove bearing

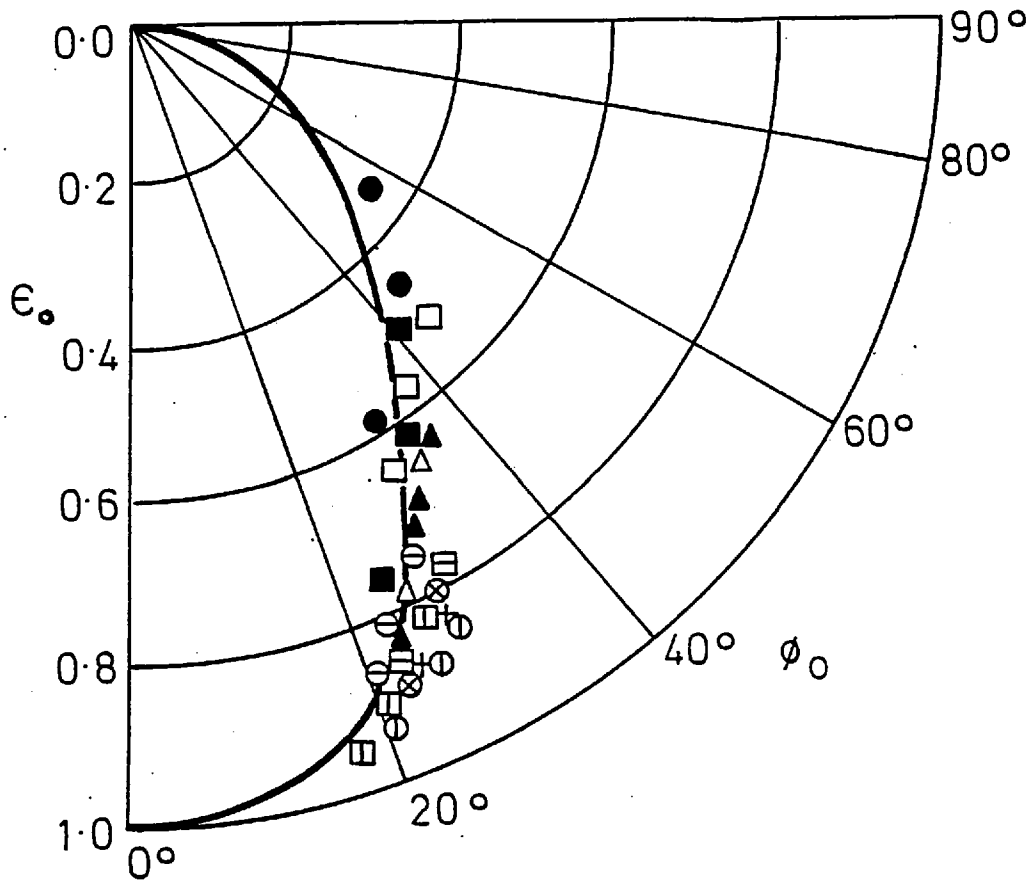


Figure 5.8: (b) Locus of shaft centre in the 90° two axial groove bearing

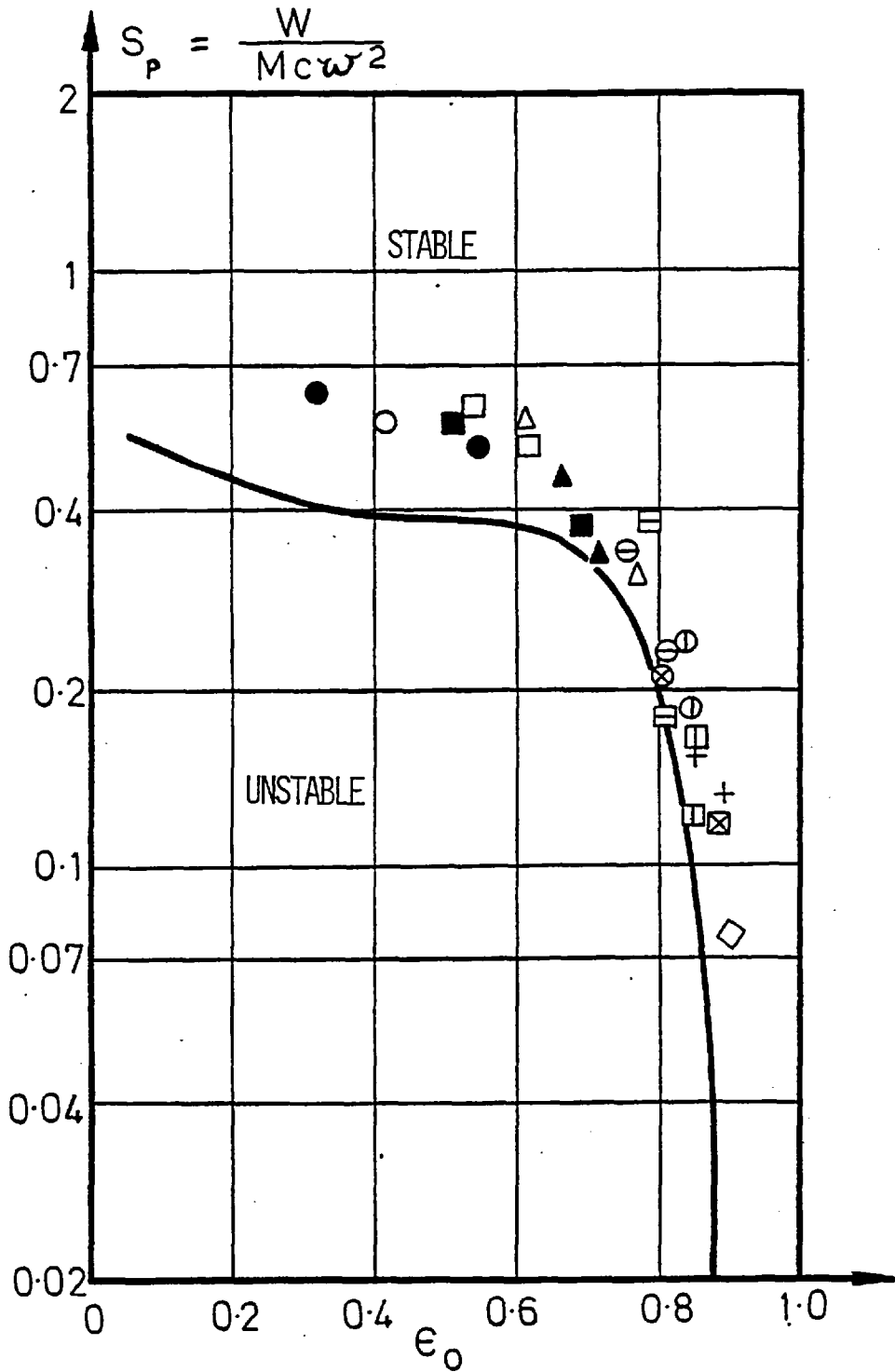


Figure 5.9: The stability threshold parameter for the 90° two axial groove bearing

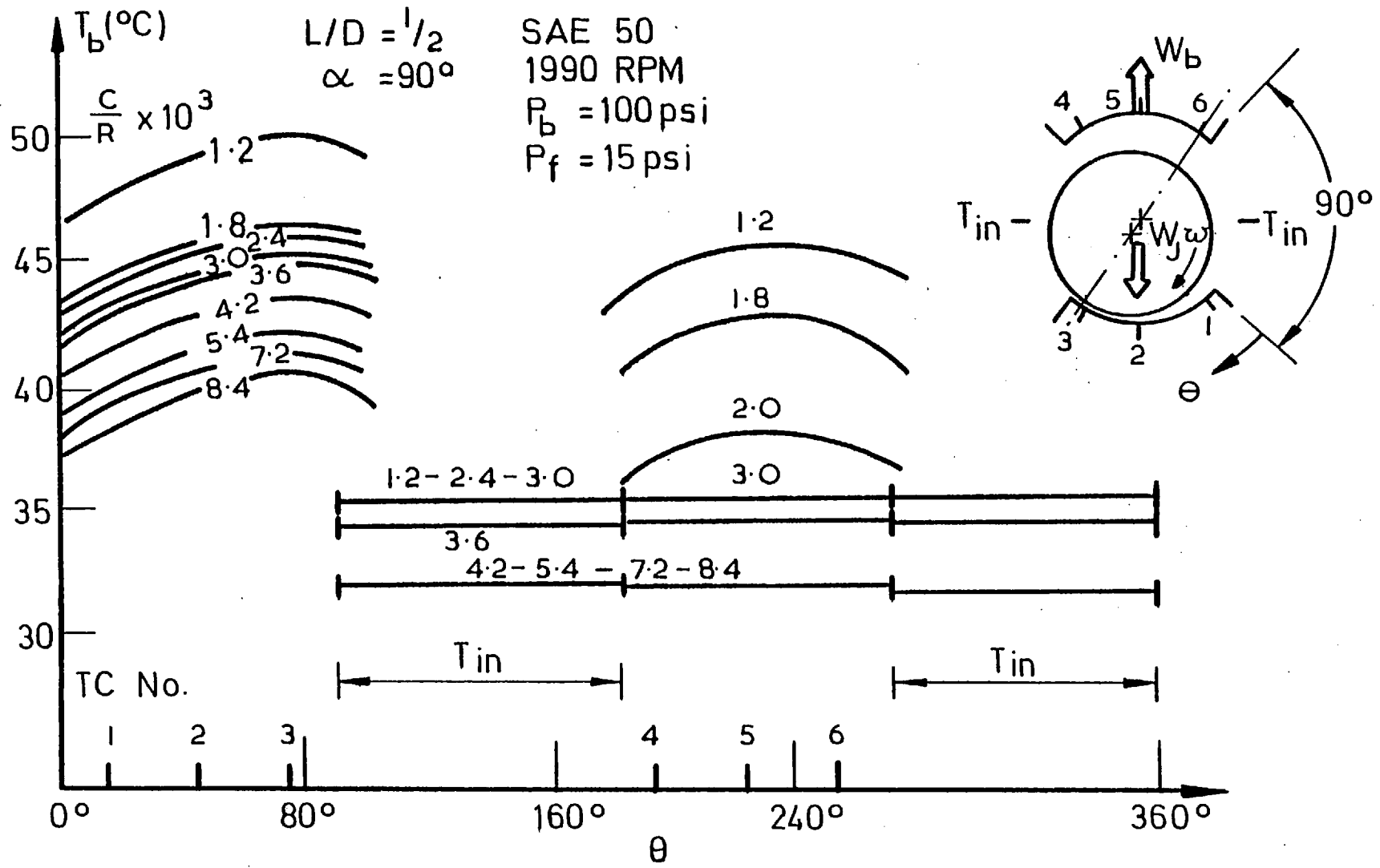


Figure 5.10: Temperature profiles around the two axial groove circular bearing centre-line

effective as the bottom half in the generation of pressure. The journal locus moves almost horizontally in the bearing at low loading conditions. As the loading increases, the effect of the top half decreases and the journal locus curves down to the bottom half. As the preload increases, the load carrying capacity of the bearing for the same minimum film thickness decreases.

The stability of the elliptical bearing increases as the preload increases. The preload has a considerable stabilising effect, especially at high preload and high and medium eccentricity ranges.

Some of the typical temperature profiles are shown in Figure 5.15 for the same bearing load and oil feed pressure. From Figures 5.15(a) and 5.15(b), it can be seen that, for the same preload, small clearances give rise to a larger circumferential temperature increase around the bearing. The temperature rise increases with the preload of the bearing. The temperature of the top half of the bearing is slightly less than the bottom half temperature. Even at high clearances, a circumferential temperature increase was observed on the top half due to the high lobe eccentricity.

Some typical whirl orbits for the elliptical bearing are shown in Figure 5.16 for various operating conditions. In these photographs, the small points around the bearing show the maximum available bearing movement. Some points of stable operation are shown in sequence with decreasing mean bearing pressures of 100 psi, 50 psi, 30 psi and, finally, at the bearing "point" locus just before whirling begins. The whirl orbits were found to be load dependent. As the load was further decreased, the whirl orbits expanded and at the no load condition the largest of the orbits was obtained. It is to be noted that the whirl orbits do not expand to the full clearance space, even at the no load condition.

From the following sequence of photographs (Figure 5.16), it can be seen that the preload has a strong influence on stability and whirl amplitudes for the same bearing arc clearance. In Figures 5.16(a) and 5.16(b), the bearing arc clearances are 0.0092 in and 0.00088 in, respectively. But the whirl amplitudes for $\delta = 0.75$ are much smaller than for $\delta = 0.6$. This effect can be seen also in Figures 5.16(d) and 5.16(g). In these figures, the bearing arc clearances are 0.0042 in and 0.0044 in, respectively.

At a constant preload, the effect of arc clearance and the preload distance can be seen in Figures 5.16(b), 5.16(c) and 5.16(d). As the preload distance and the arc clearance decrease, the whirl amplitudes decrease sharply and the bearing does not whirl for $d = 0.0025$ in at the same speed. Therefore, the photograph is given at 2960 RPM and it shows a relatively small whirl amplitude at the no load condition.

The effect of shaft speed can be seen in Figures 5.16(f) and 5.16(g) for the same bearing geometry. The whirl amplitudes increase with speed.

The stiffness coefficients obtained by the incremental loading method are shown in Figures 5.17 and 5.18 for different values of the preload. Although the experimental values show close agreement with the theoretical values, scattering in the actual stiffness measurements are quite large. This may be attributed to the difficulty in measuring the very small displacements and to the effect of non-linearity of the oil film forces.

It is to be noted that the arc clearance (prior to the application of preload) is used in the stability parameter when comparing the experimental data with the theoretical predictions for different values of the preload. However, for a given arc clearance, the higher values of

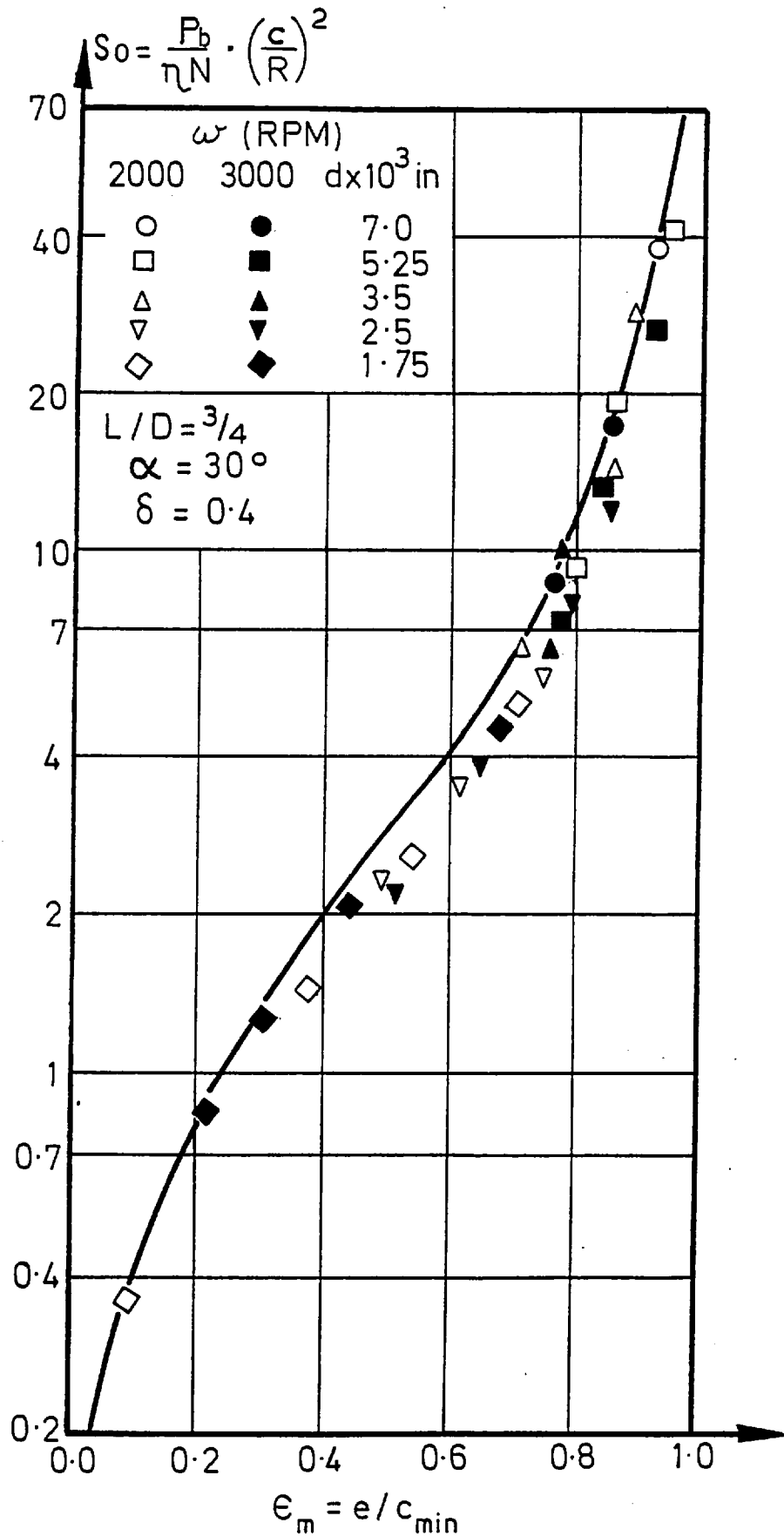
preload correspond to lower minimum assembled clearance. In practical applications, the minimum clearance is quite an important factor to maintain the bearing operating temperature within a reasonable upper limit. Therefore, depending on the application, the minimum clearance is limited. For a given minimum film thickness, the preload can be increased by increasing the arc clearance. Figure 5.19 shows a plot of the instability threshold parameter in which the minimum clearance is kept as an independent variable. As it is seen that as the preload is increased, the stability of the elliptical bearing increases, although the arc clearance increases.

5.1.4 The Offset Halves Two Axial Groove Bearing

The stability characteristics of the offset halves bearing were investigated for 30° and 60° groove angles. Within the operating parameters of the test machine, it was found that the 30° groove angle bearing had good stability characteristics. At high preloads, it was always stable. In order to have experimental data points for comparison with the theoretical predictions, it was decided to increase the groove angle to 60° in order to destabilise the bearing. Therefore, the effect of preload on the stability and the static load capacity of the bearing are given in Figures 5.20 to 5.22 for a 60° groove angle.

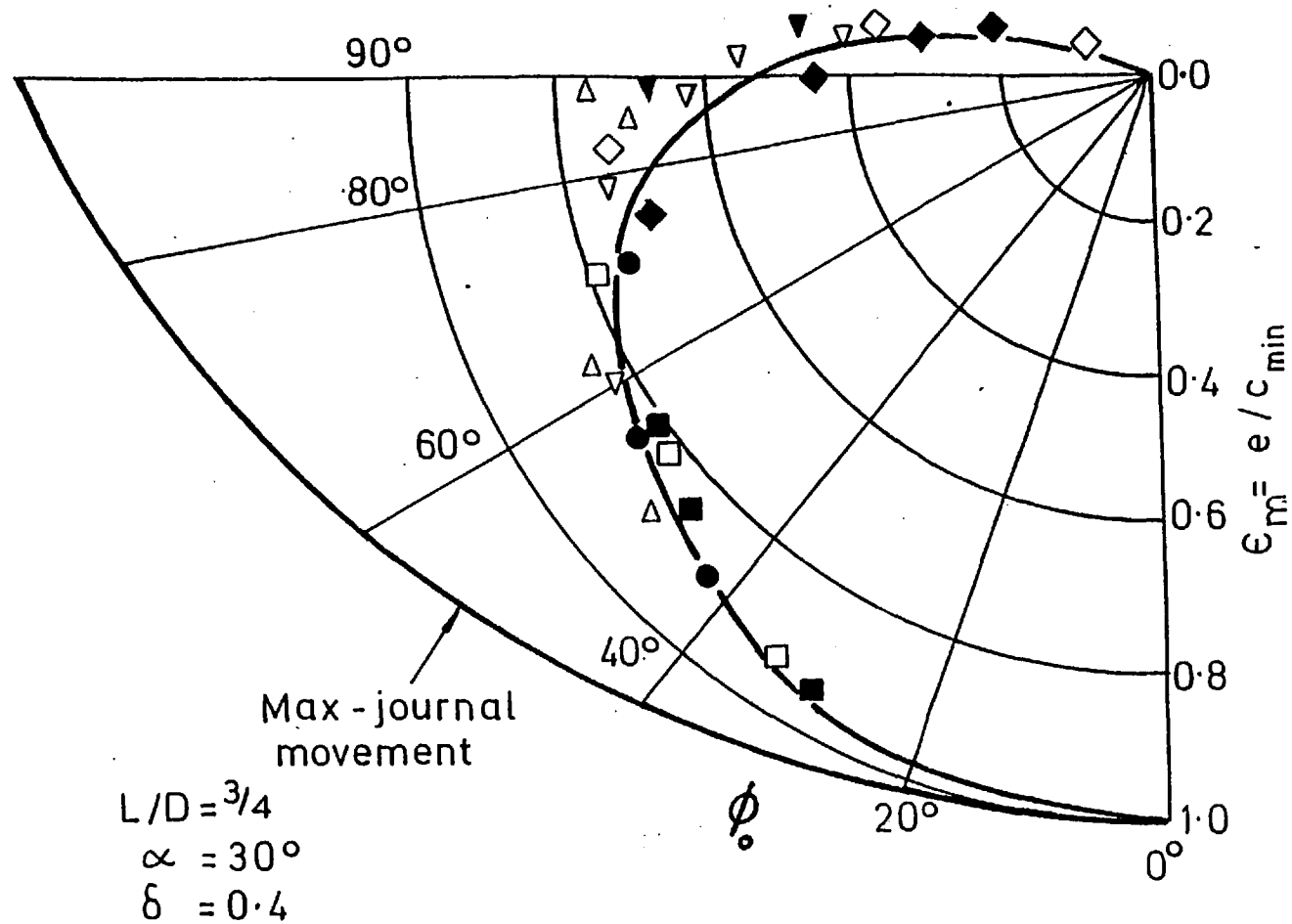
The load capacity of the offset halves bearing decreases with increase in the preload. This is due to the higher top half eccentricity ratio for the same minimum film thickness. For all the preload values and low and medium eccentricity ranges, the locus of the shaft centre follows nearly a vertical line.

The stability of the offset halves bearing increases with preload and the unstable region becomes smaller. As the preload increases,



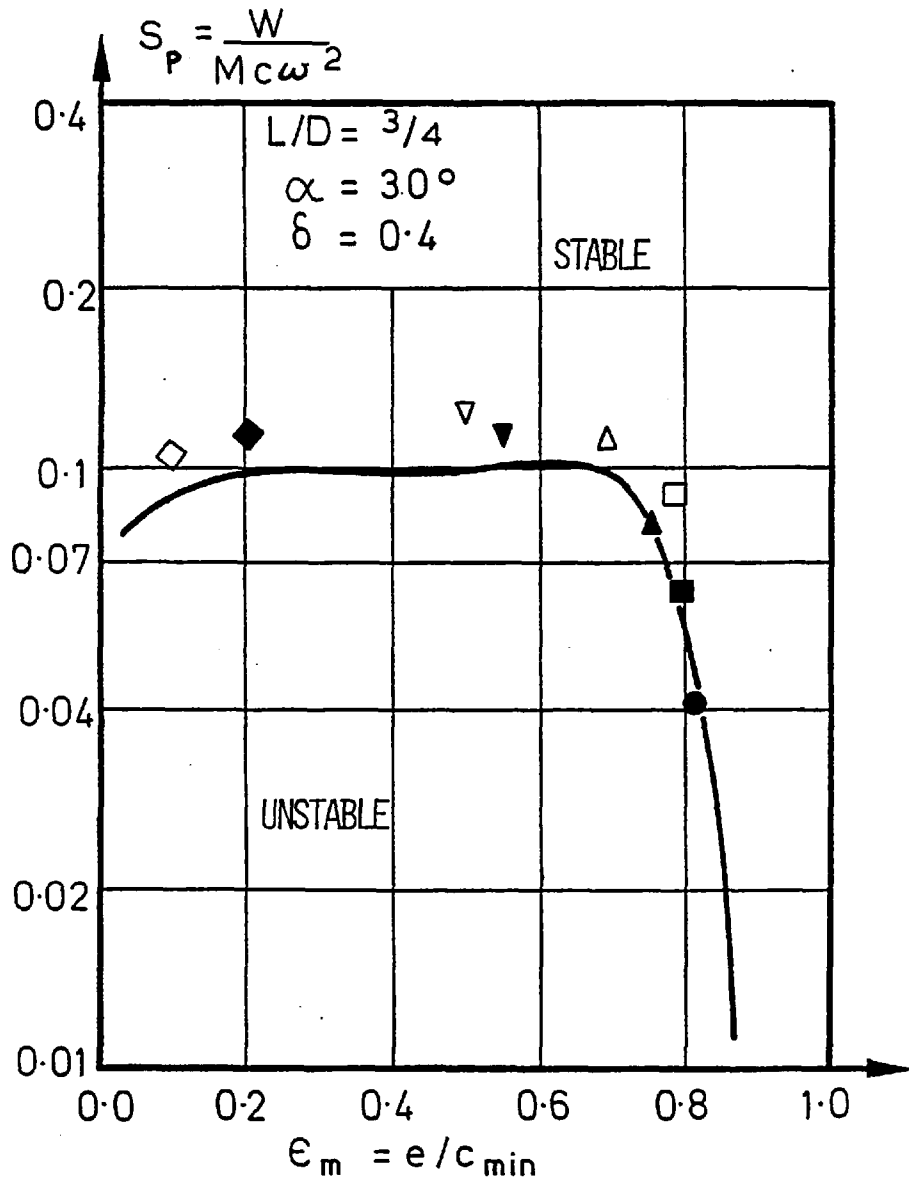
(a) The variation of load capacity with journal eccentricity

Figure 5.11: The elliptical bore bearing with $\delta = 0.4$



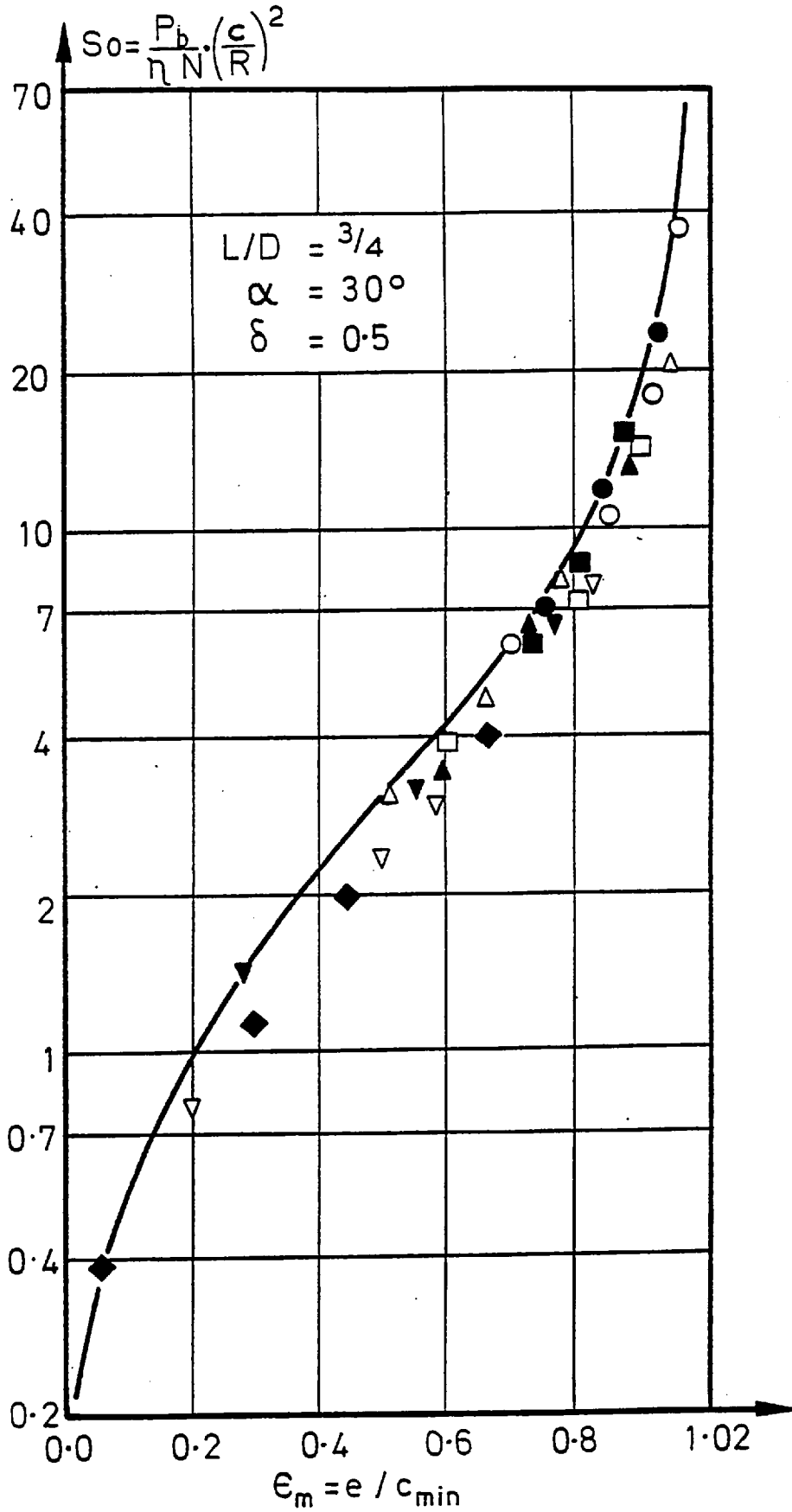
(b) Locus of shaft centre due to static loading

Figure 5.11: The elliptical bore bearing with $\delta = 0.4$



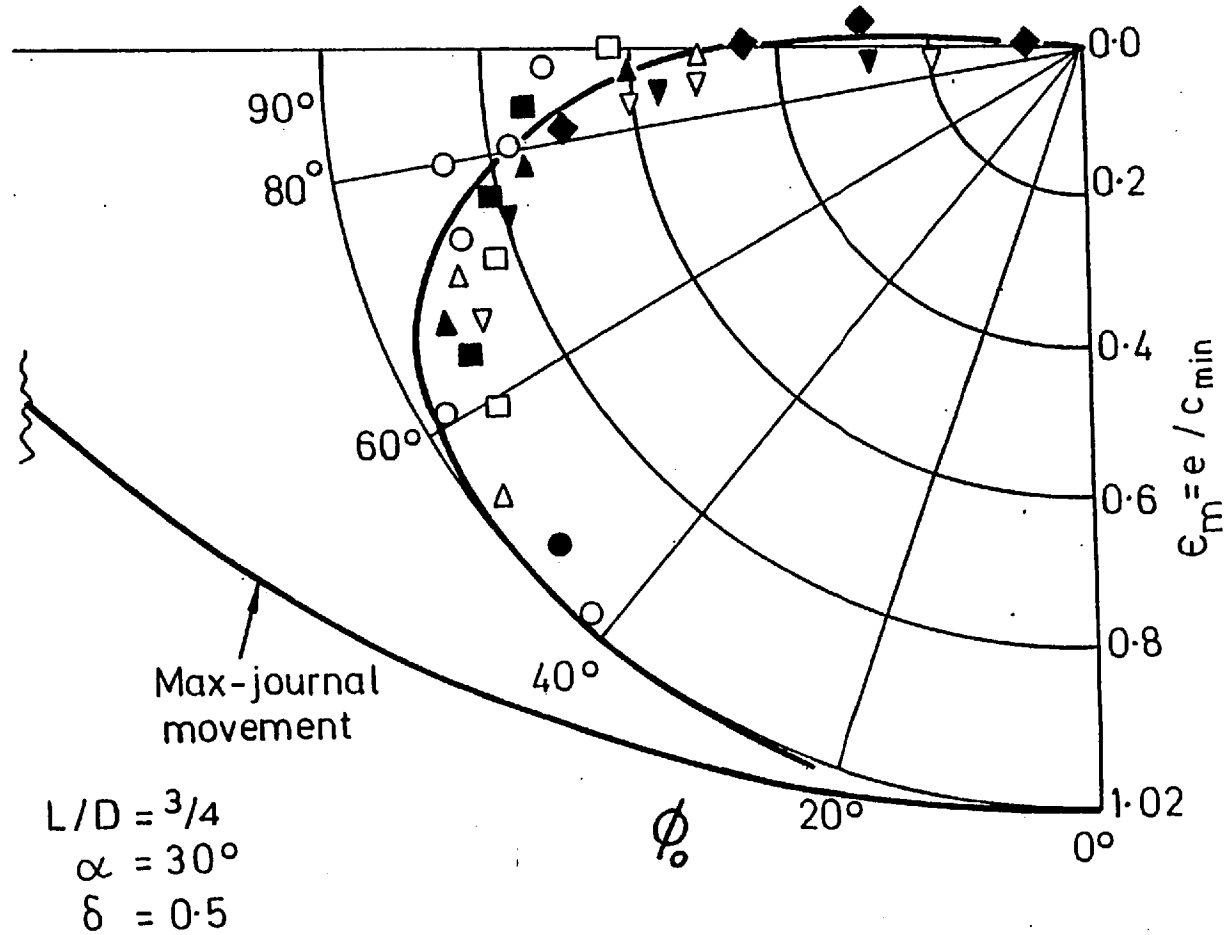
(c) Stability threshold

Figure 5.11: The elliptical bore bearing with $\delta = 0.4$



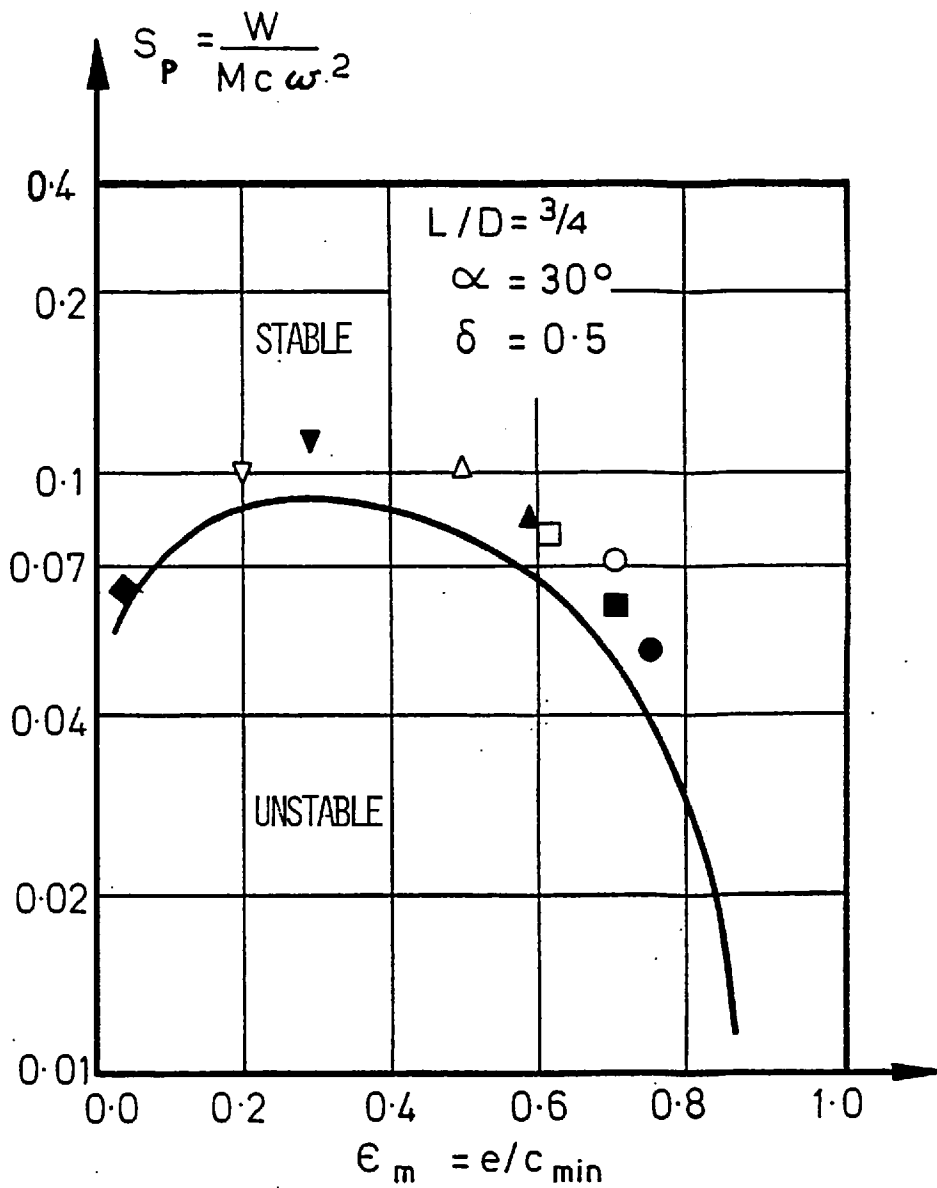
(a) The variation of load capacity with journal eccentricity

Figure 5.12: The elliptical bore bearing with $\delta = 0.5$



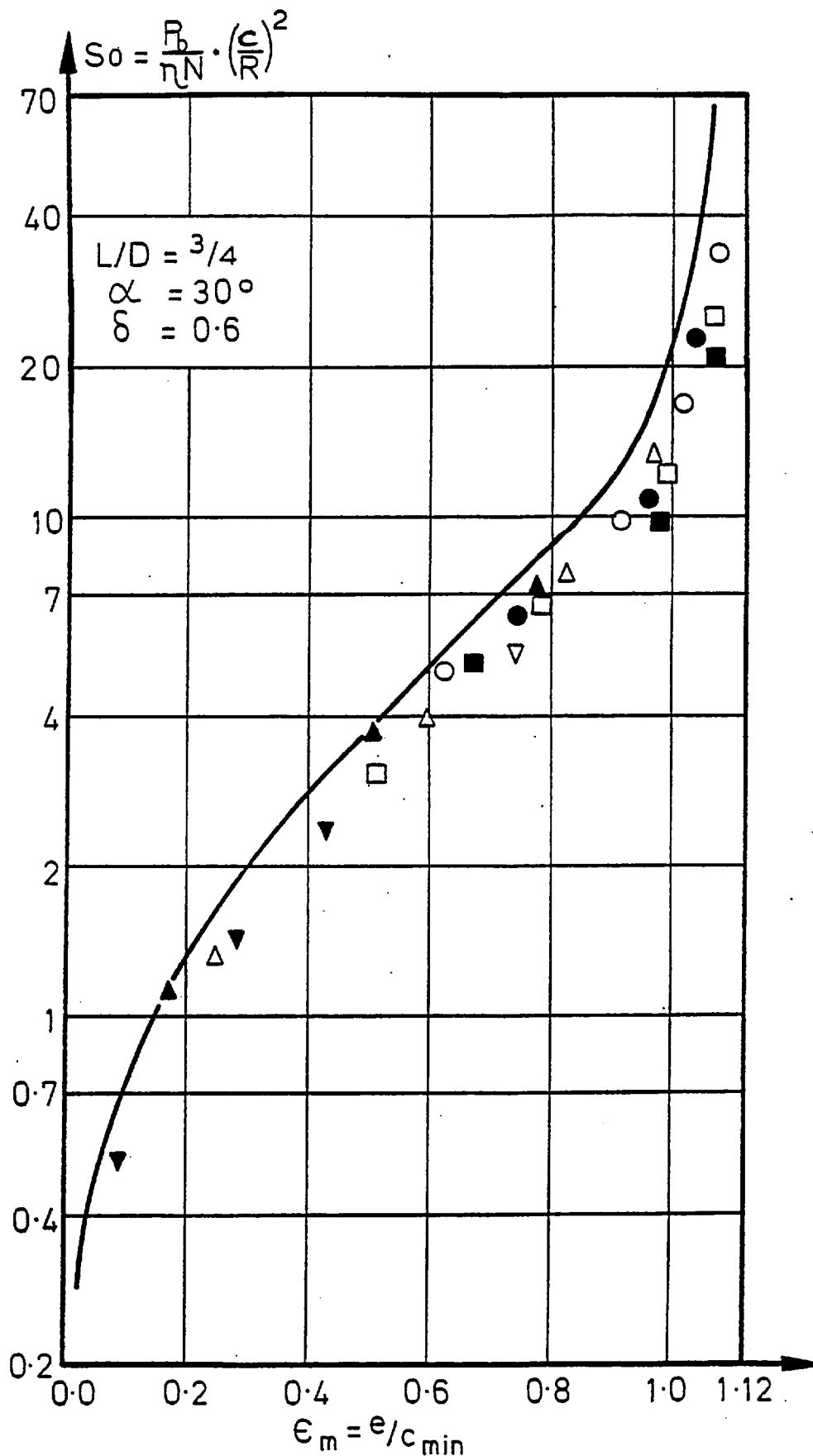
(b) Locus of shaft centre due to static loading

Figure 5.12: The elliptical bore bearing with $\delta = 0.5$



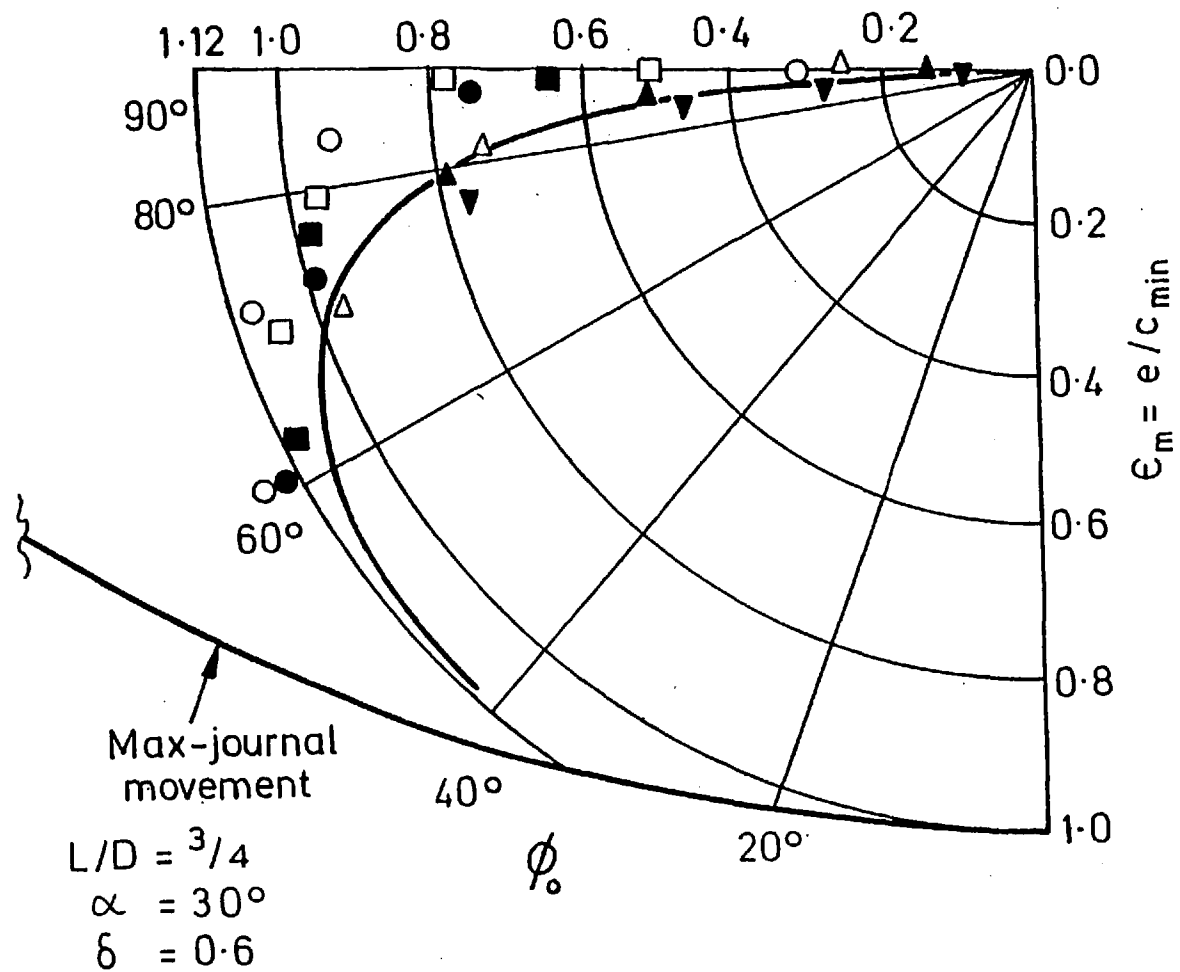
(c) Stability threshold

Figure 5.12: The elliptical bore bearing with $\delta = 0.5$



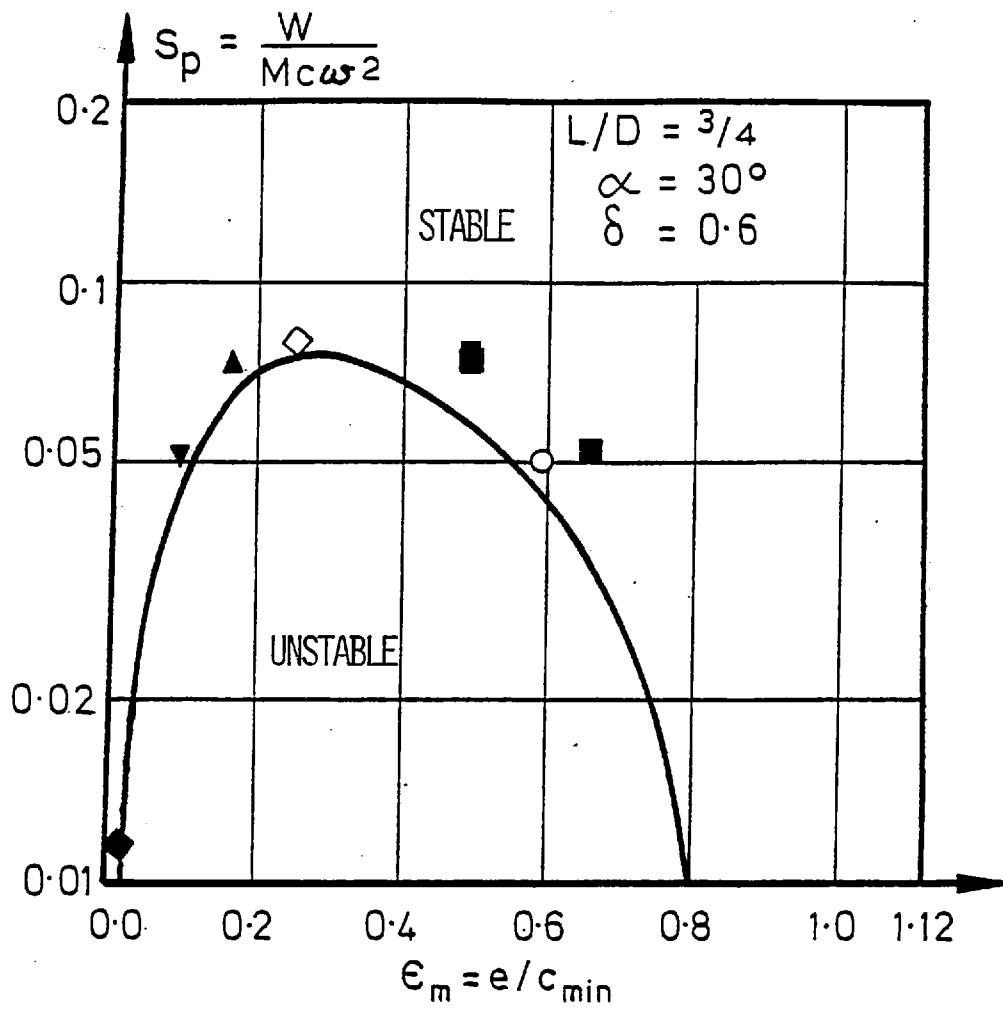
(a) The variation of load capacity with journal eccentricity

Figure 5.13: The elliptical bore bearing with $\delta = 0.6$



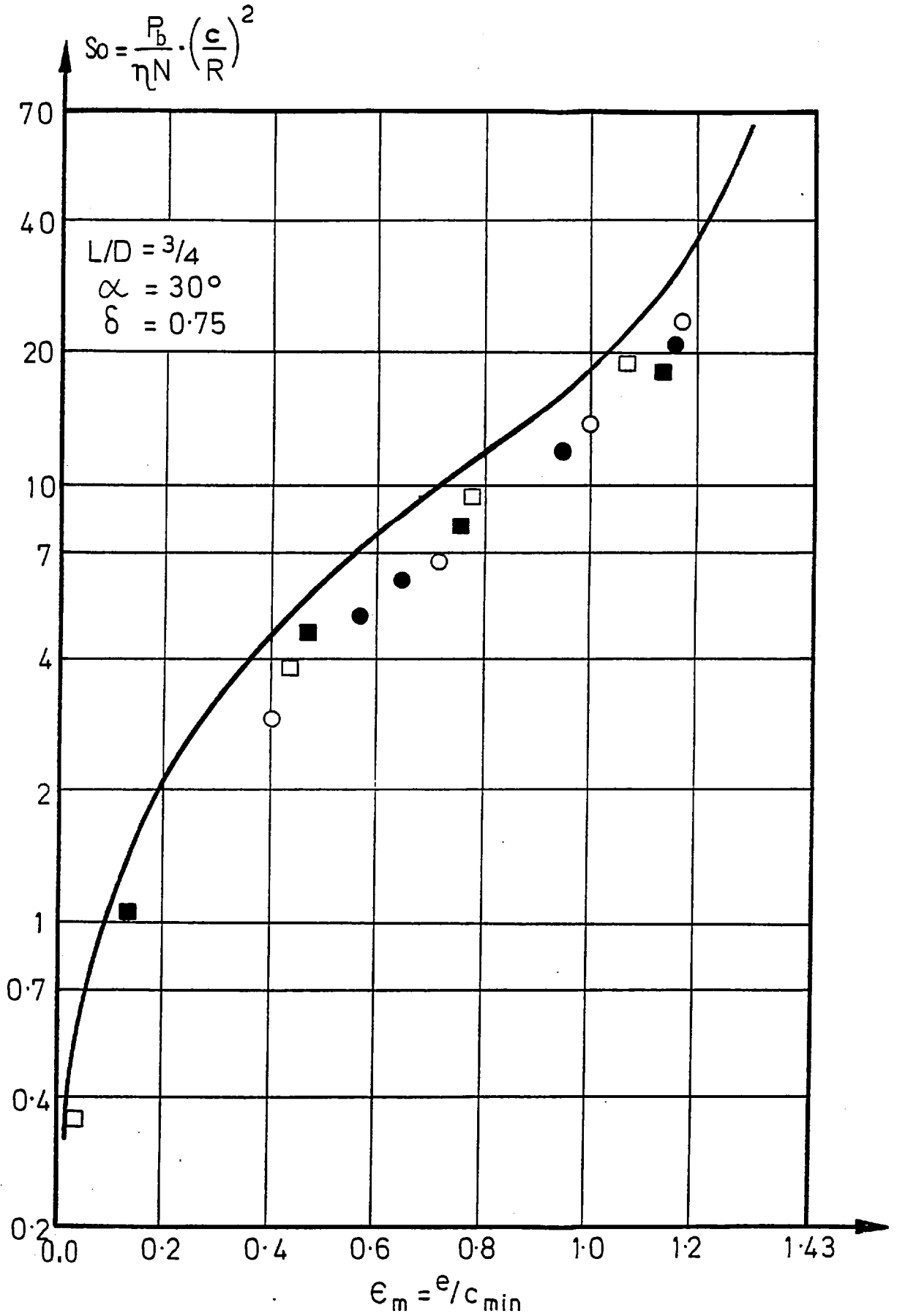
(b) Locus of shaft centre due to static loading

Figure 5.13: The elliptical bore bearing with $\delta = 0.6$



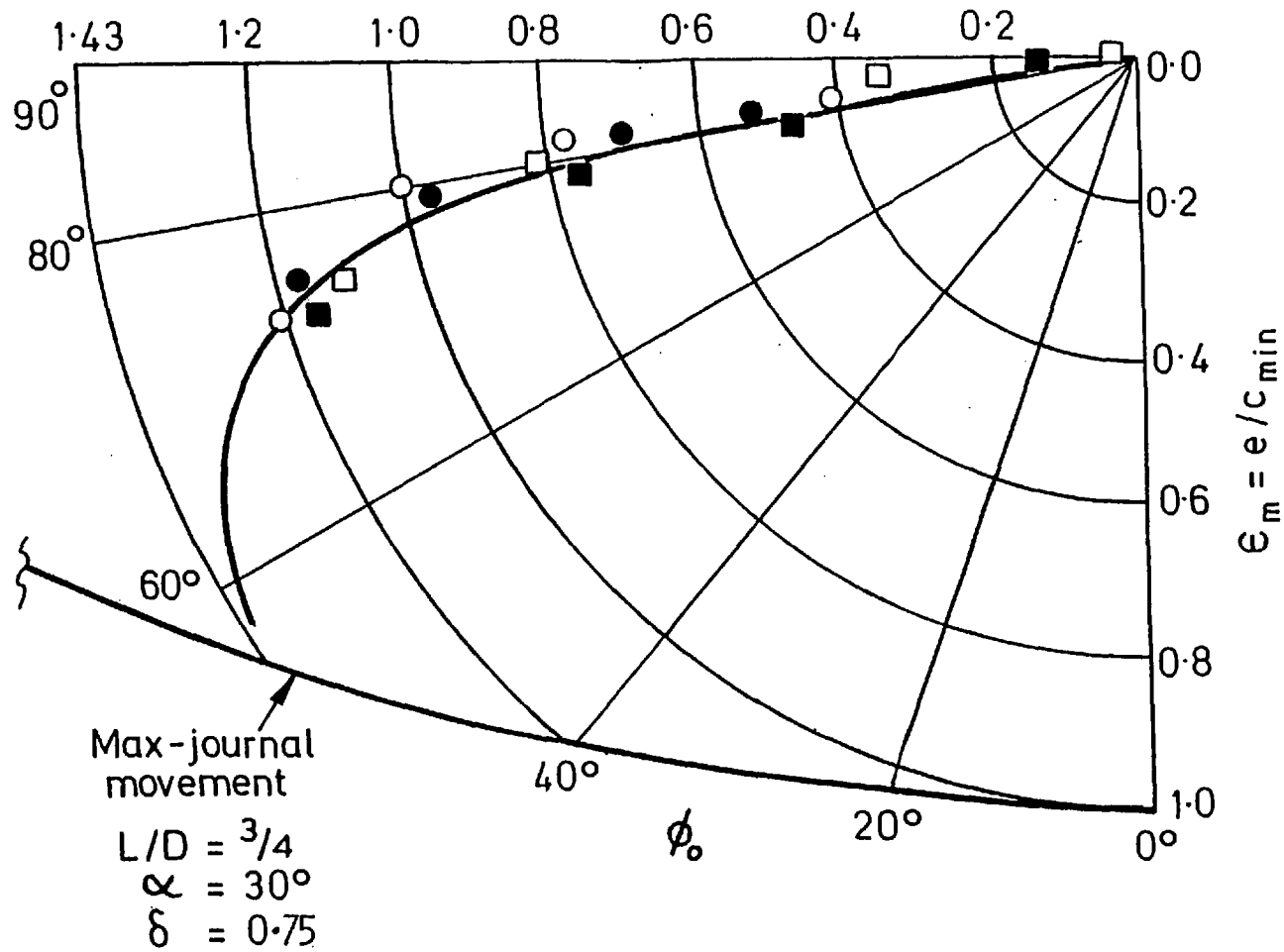
(c) Stability threshold

Figure 5.13: The elliptical bore bearing with $\delta = 0.6$



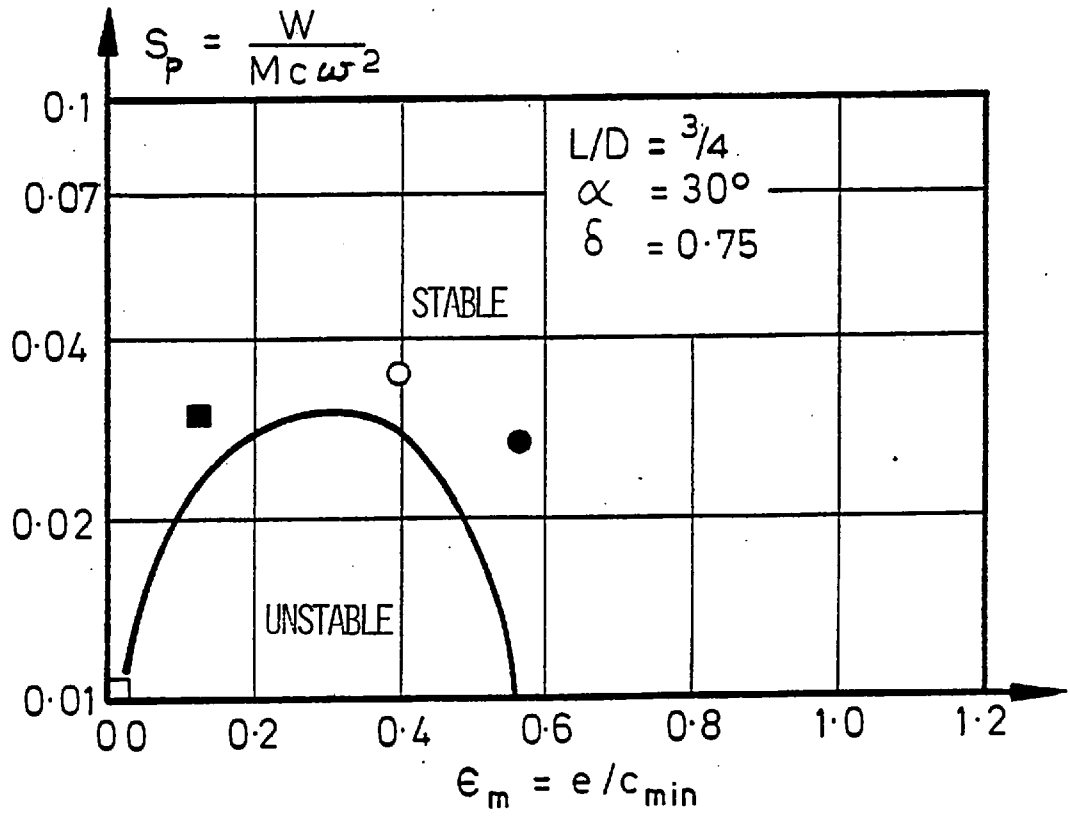
(a) The variation of load capacity with journal eccentricity

Figure 5.14: The elliptical bore bearing with $\delta = 0.75$



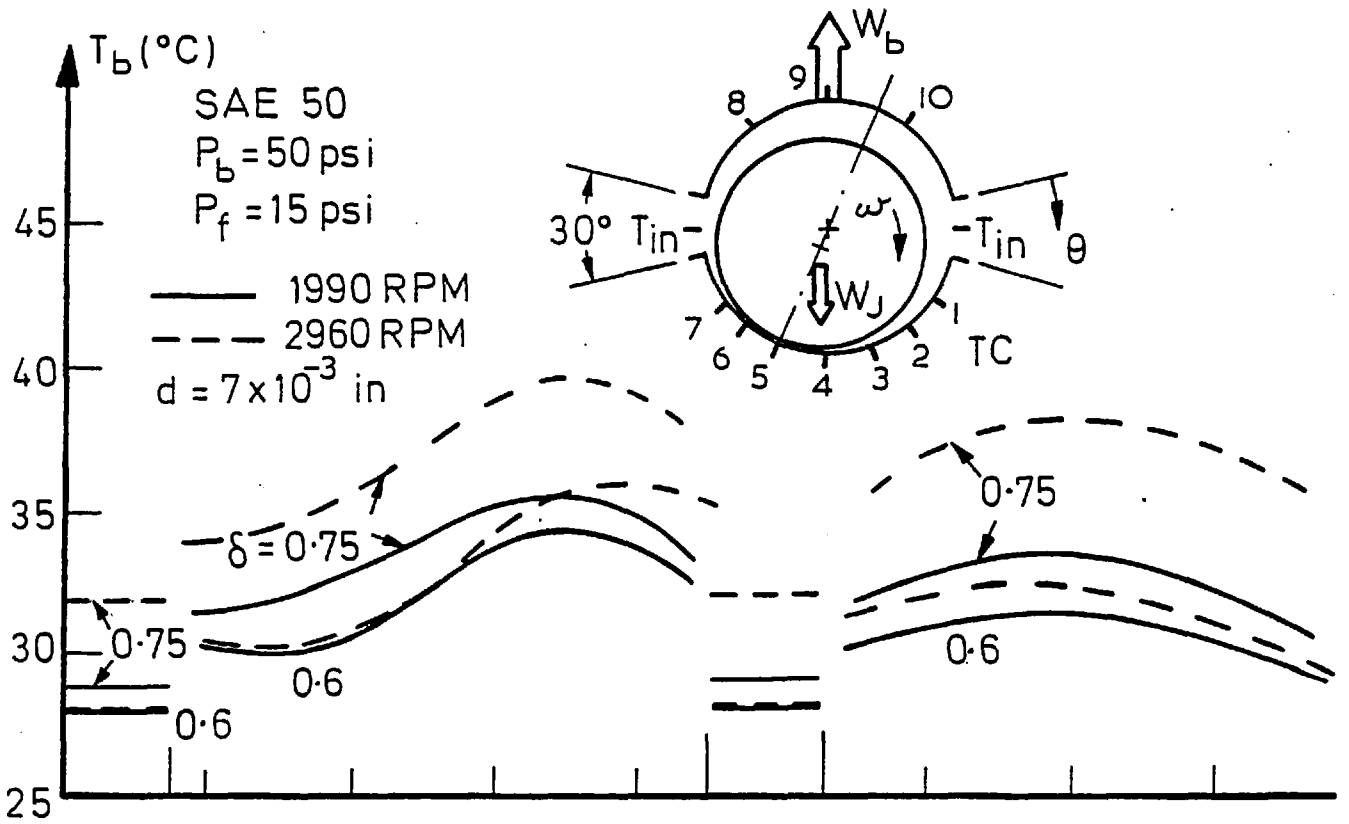
(b) Locus of shaft centre due to static loading

Figure 5.14: The elliptical bore bearing with $\delta = 0.75$

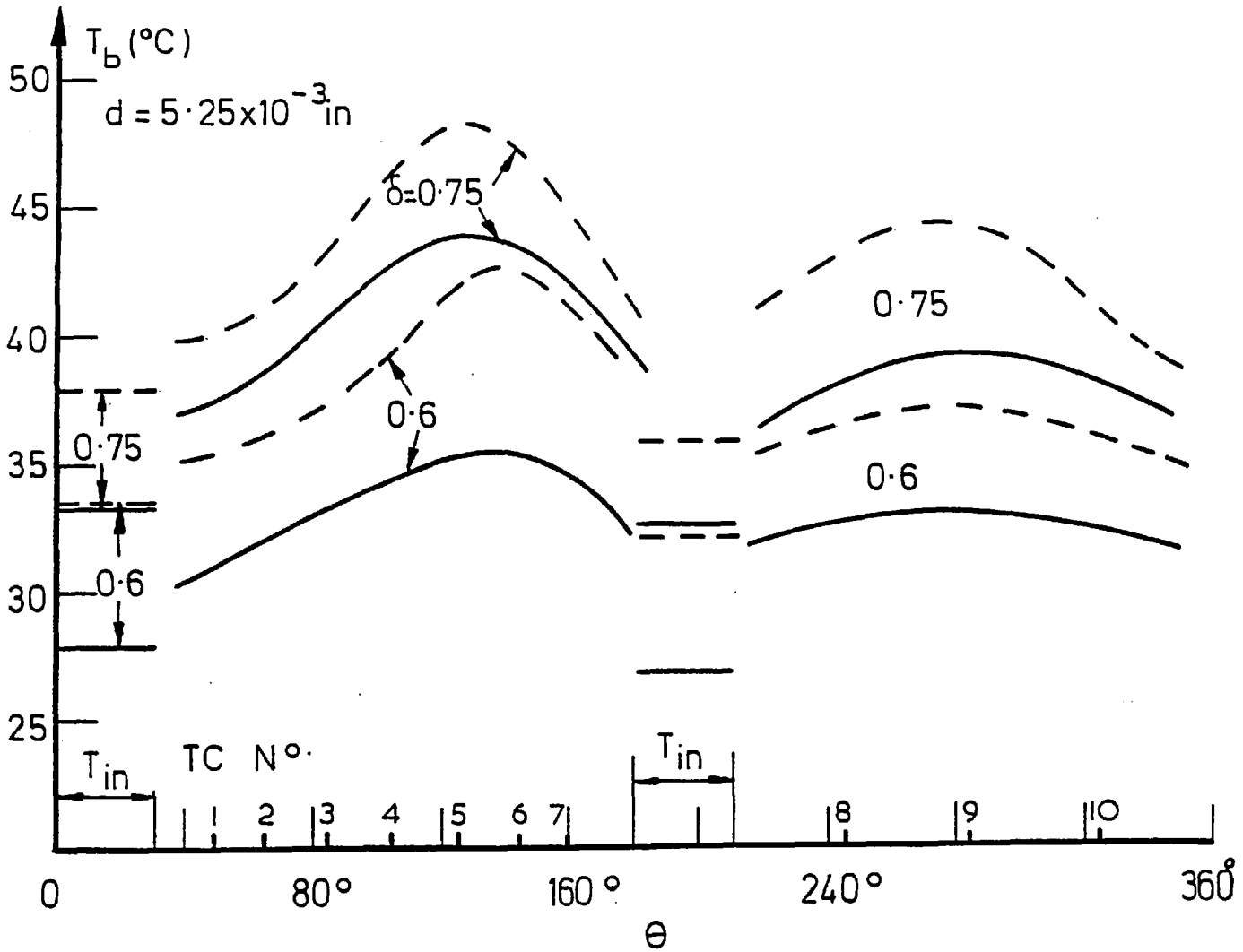


(c) Stability threshold.

Figure 5.14: The elliptical bore bearing with $\delta = 0.75$

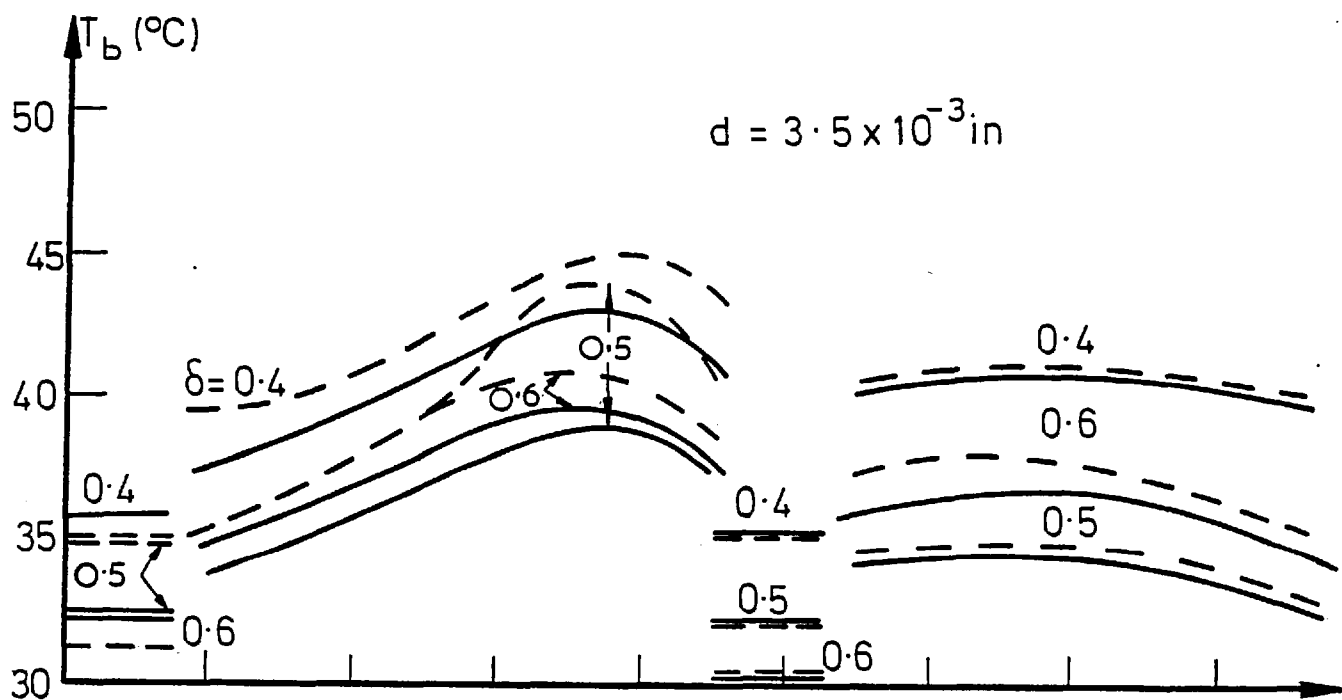


(a)

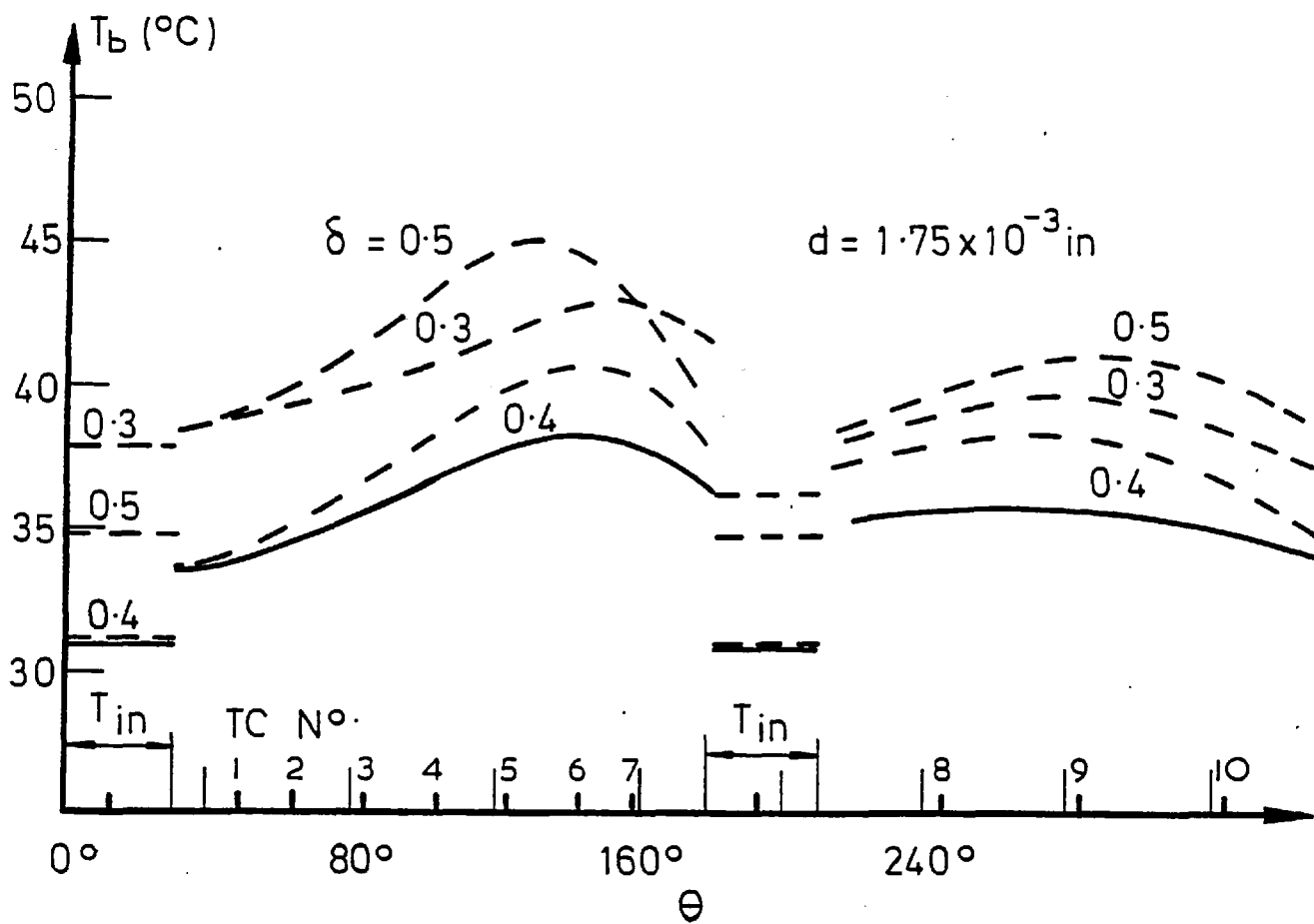


(b)

Figure 5.15: Temperature profiles around the elliptical bearing centre-line

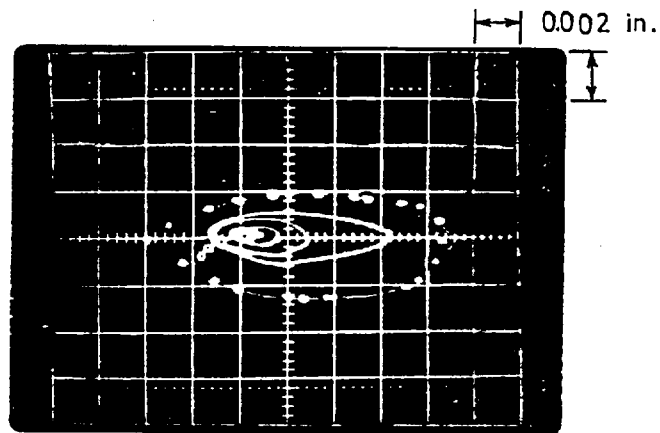


(c)



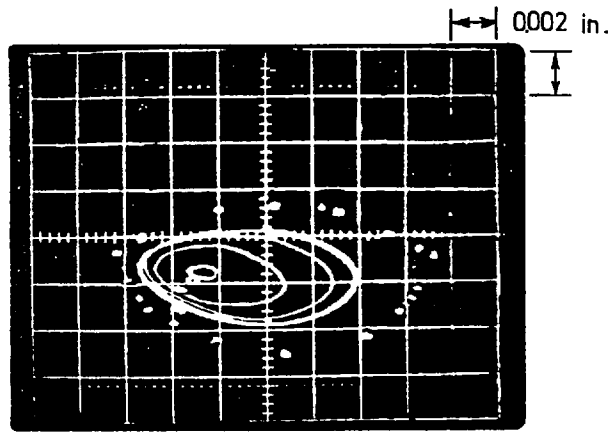
(d)

Figure 5.15: Temperature profiles around the elliptical bearing centre-line

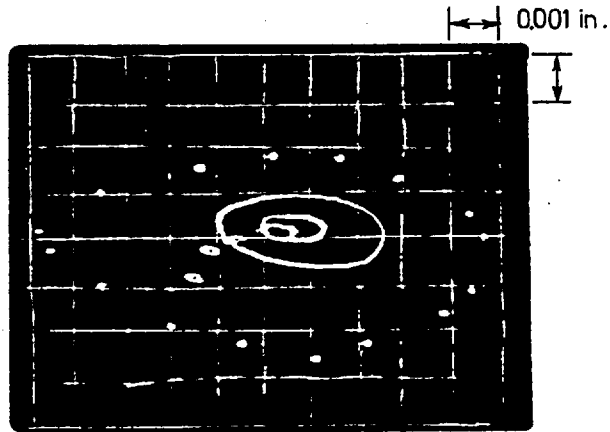


(a) 1990 RPM, $\delta = 0.75$, $d = 0.007$ in

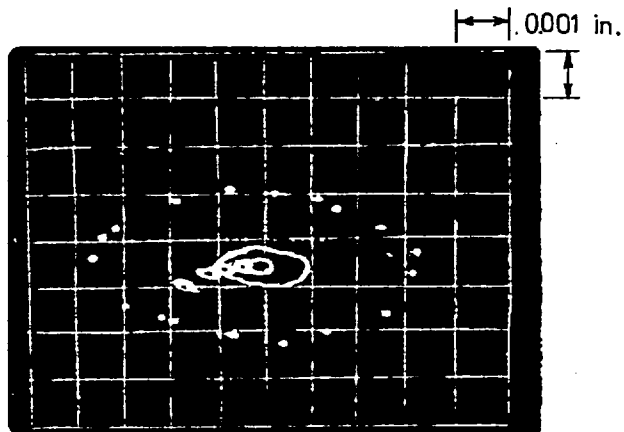
Figure 5.16: Whirl orbits of the elliptical bearing motion



(b) 1990 RPM, $\delta = 0.6$, $d = 0.00525$ in

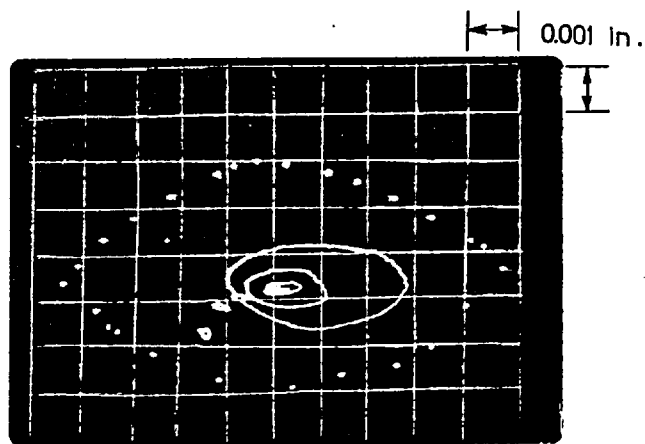


(c) 1990 RPM, $\delta = 0.6$, $d = 0.0035$ in

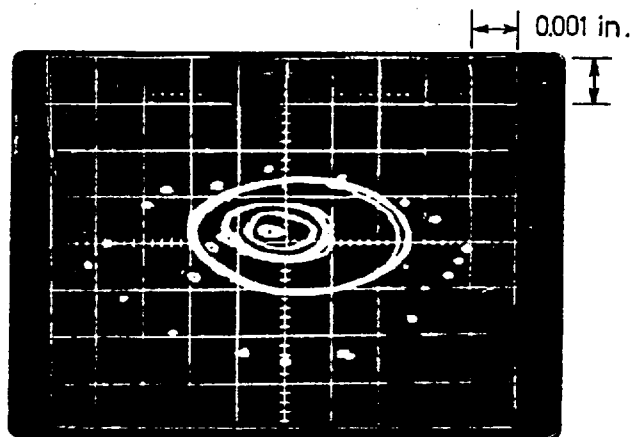


(d) 2960 RPM, $\delta = 0.6$, $d = 0.0025$ in

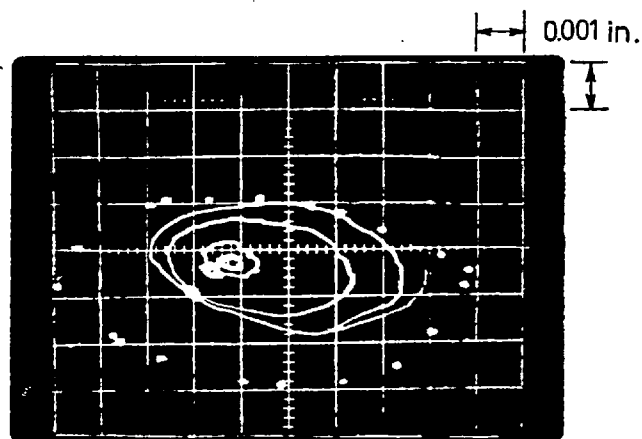
Figure 5.16: Whirl orbits of the elliptical bearing motion



(e) 1990 RPM, $\delta = 0.5$, $d = 0.0025$ in

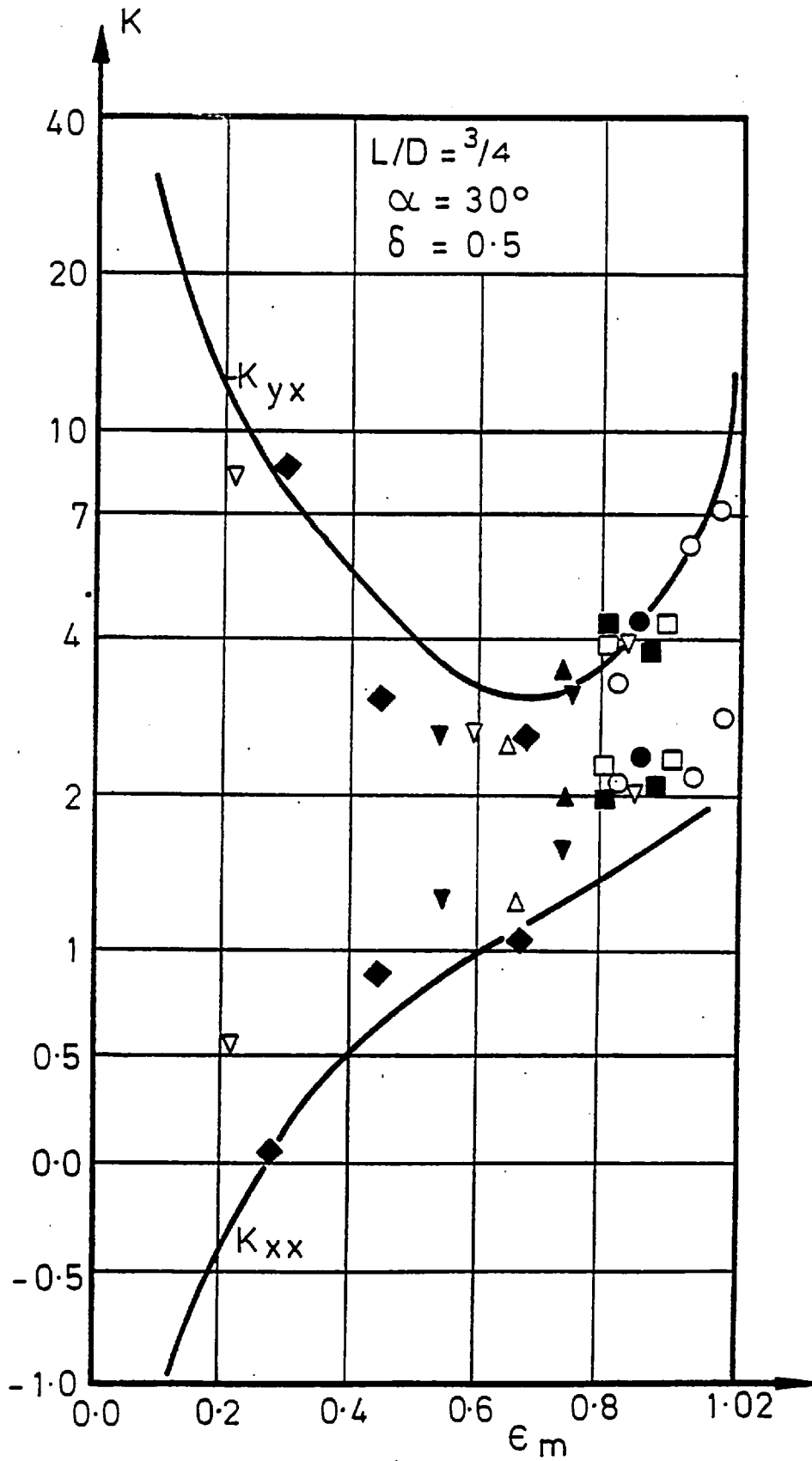


(f) 1990 RPM, $\delta = 0.4$, $d = 0.00175$ in



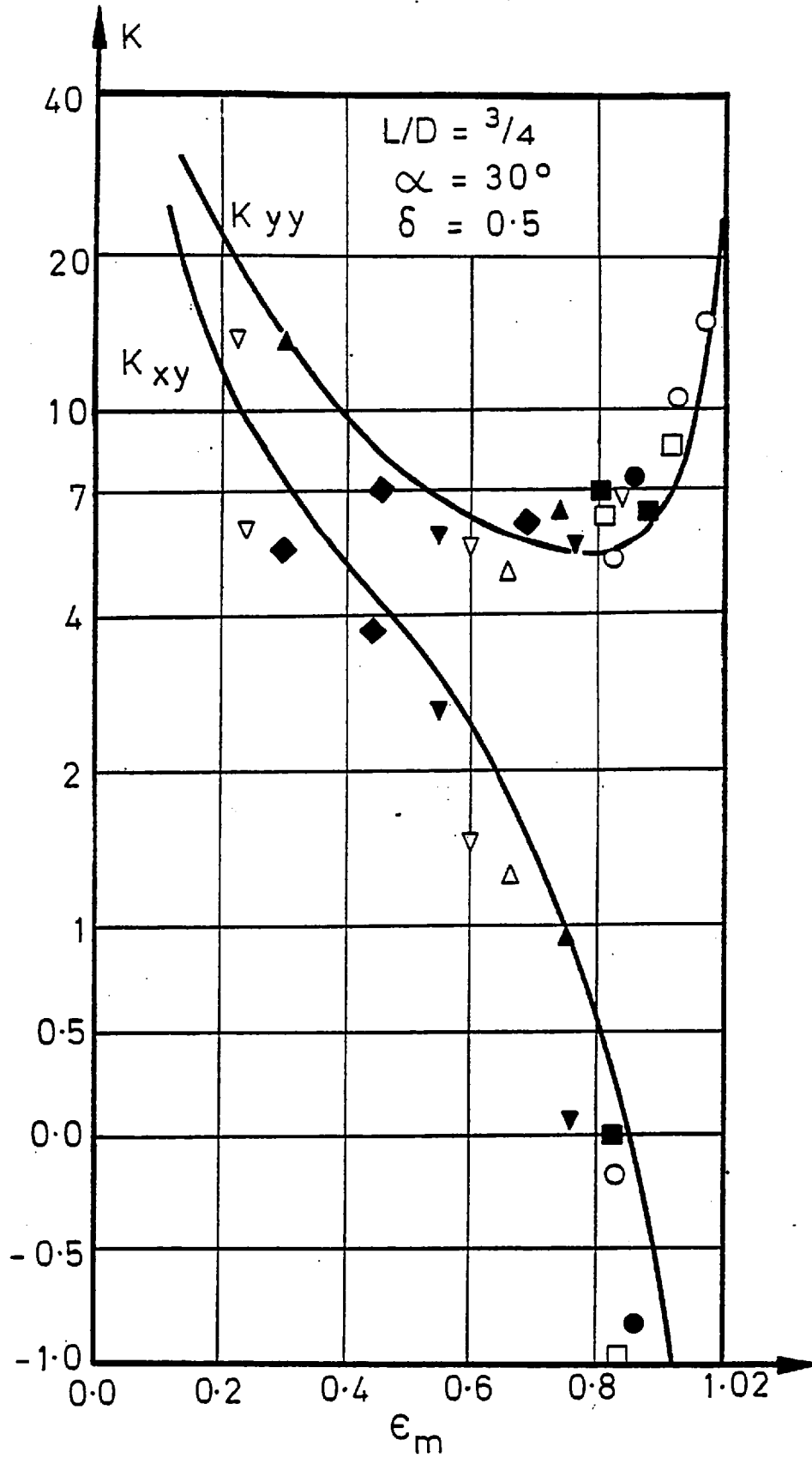
(g) 2960 RPM, $\delta = 0.4$, $d = 0.00175$ in

Figure 5.16: Whirl orbits of the elliptical bearing motion



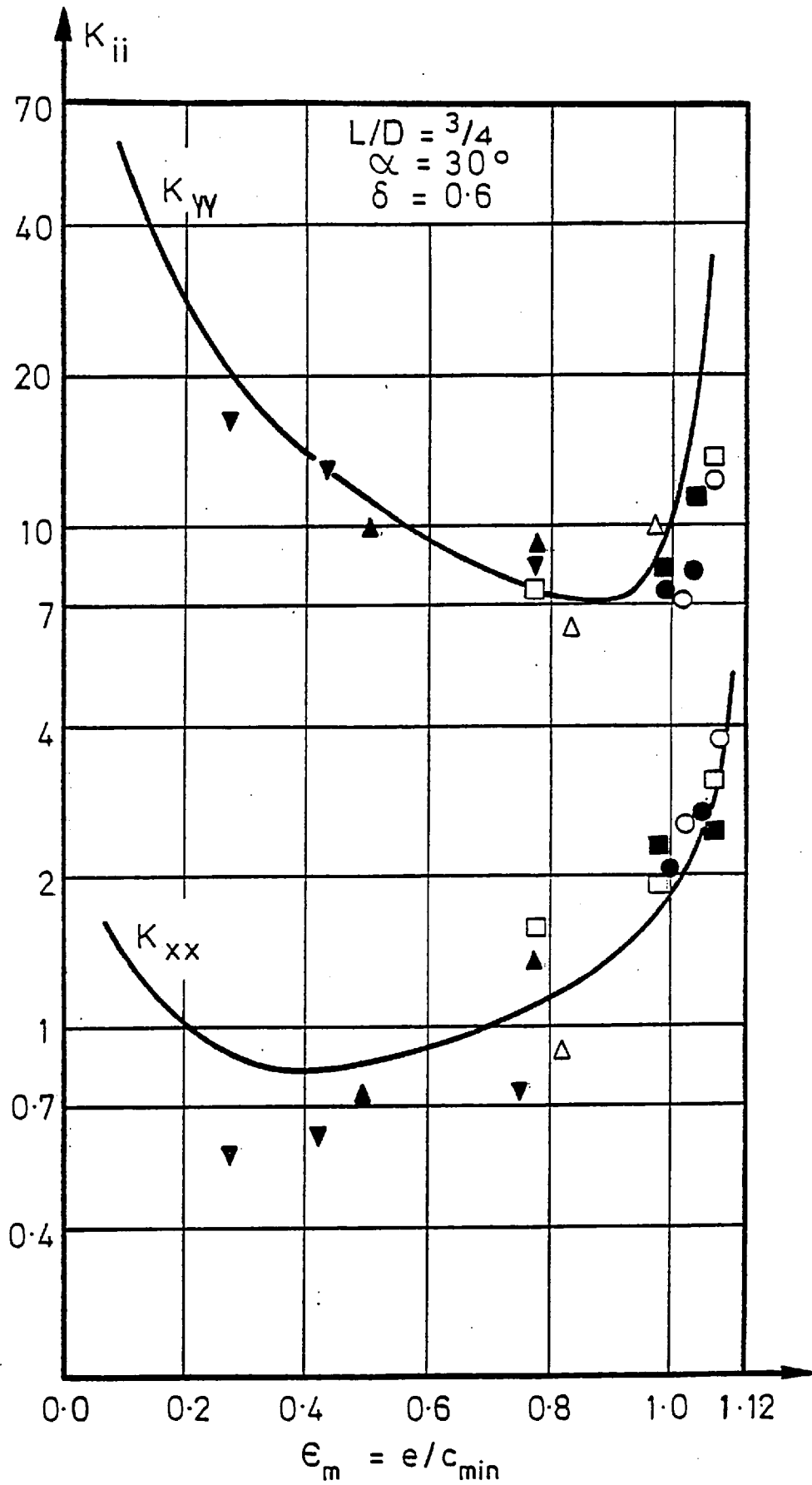
(a) Stiffness coefficients K_{xx} and K_{yx}

Figure 5.17: The variation of the stiffness coefficients for the elliptical bearing, $\delta = 0.5$



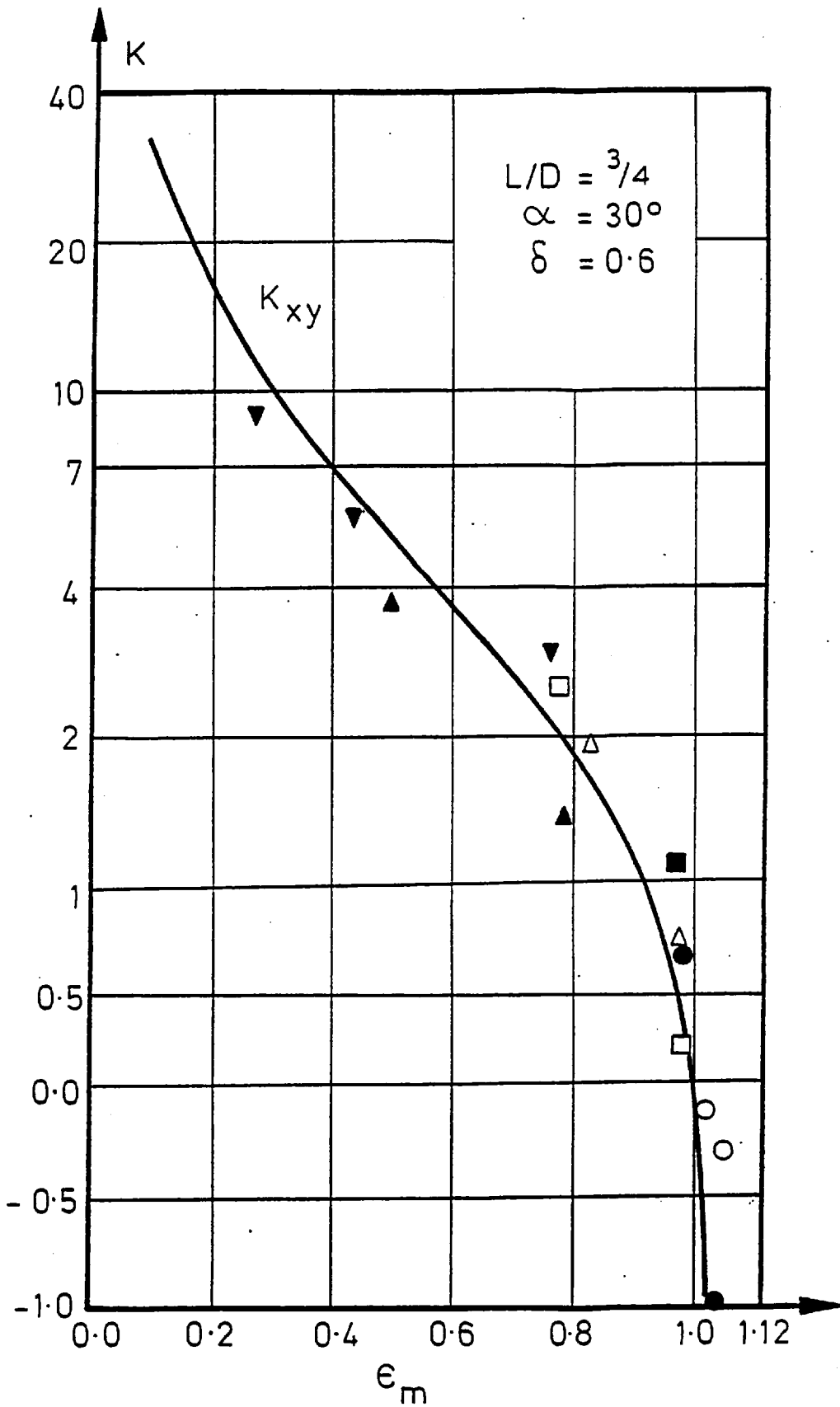
(b) Stiffness coefficients K_{XY} and K_{YY}

Figure 5.17: The variation of the stiffness coefficients for the elliptical bearing, $\delta = 0.5$



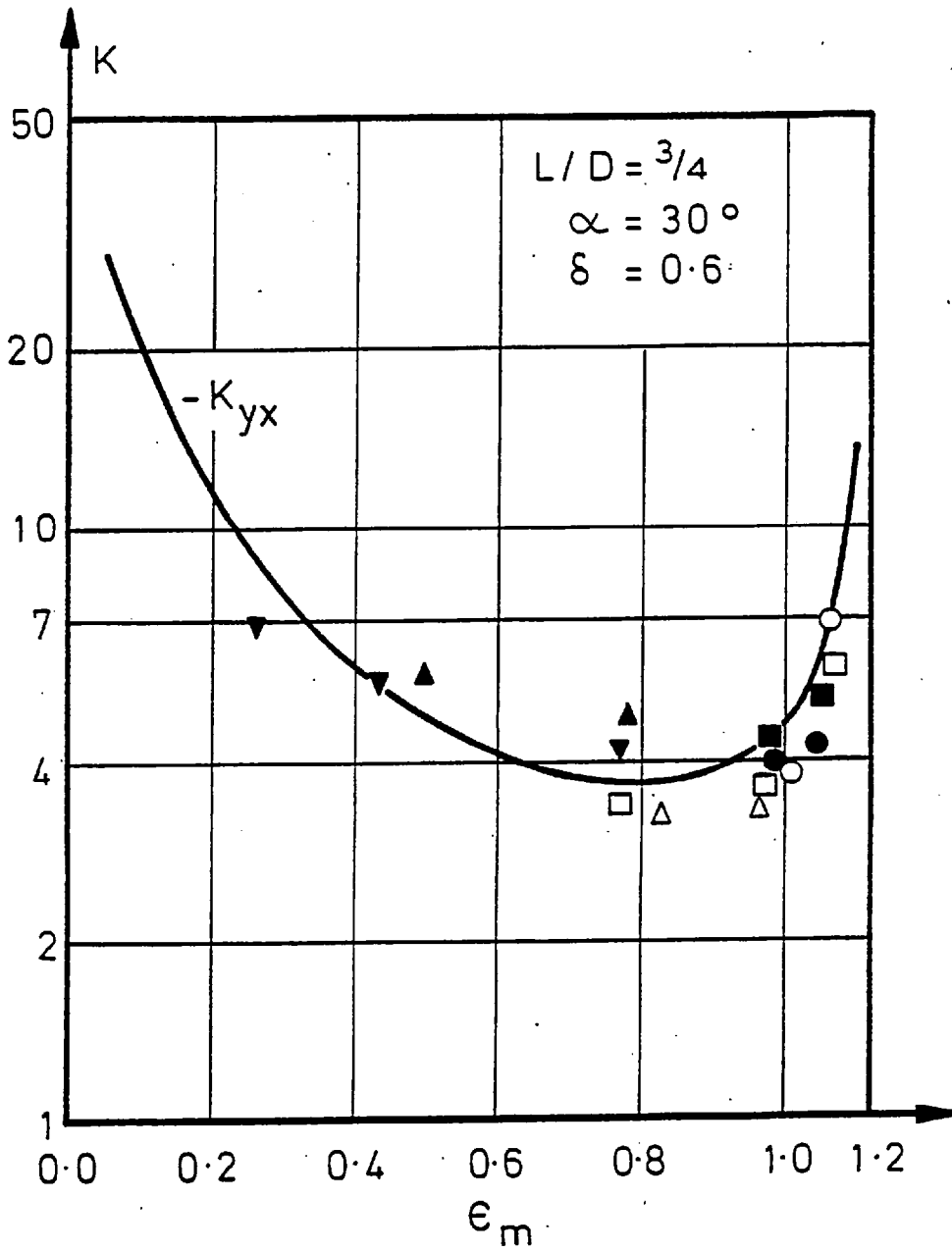
(a) Stiffness coefficients K_{XX} and K_{YY}

Figure 5.18: The variation of the stiffness coefficients for the elliptical bearing, $\delta = 0.6$



(b) Stiffness coefficient K_{XY}

Figure 5.18: The variation of stiffness coefficients for the elliptical bearing, $\delta = 0.6$



(c) Stiffness coefficient K_{YX}

Figure 5.18: The variation of the stiffness coefficients for the elliptical bearing, $\delta = 0.6$

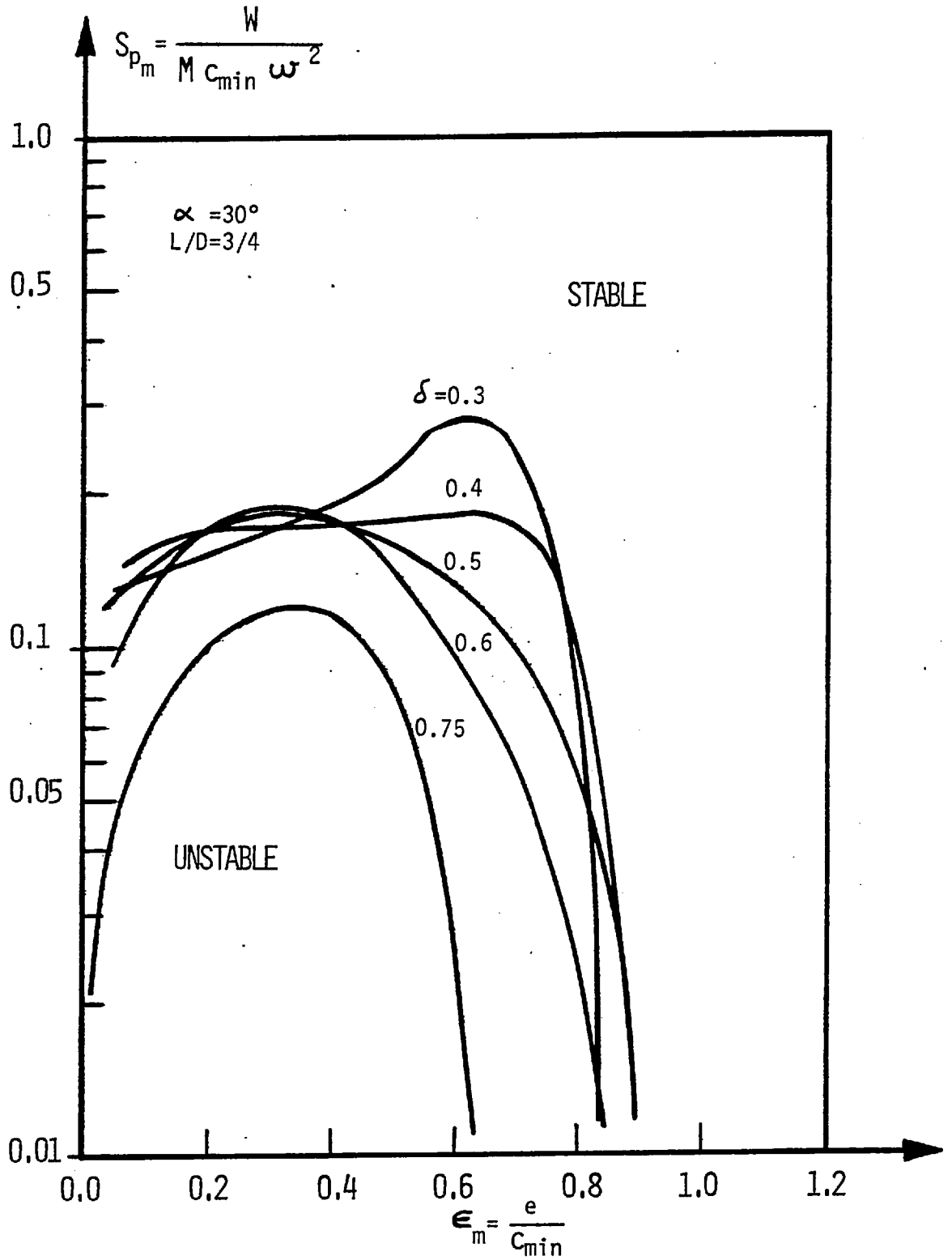


Figure 5.19: The stability threshold of the elliptical bearing based on the minimum clearance

the stability of the bearing improves, especially in the low eccentricity region.

At the stability threshold, the whirling orbit appears initially as a "figure of eight" oriented in the maximum clearance direction. Then, as the load is decreased, the whirl orbit expands into the full clearance shape.

Some of the temperature profiles are shown in Figure 5.23. The effect of preload is seen as a higher temperature increase on the bottom half of the bearing. However, on the top half, there is no observable temperature rise. This effect has also been observed on the 30° groove angle offset halves bearing.

For various operating conditions, the typical offset bearing motions are shown in Figure 5.24. In these photographs, the clearance envelopes are again seen as small points around the bearings. The equilibrium bearing centres are taken in sequence with decreasing mean bearing pressures of 100 psi, 75 psi, 50 psi and 30 psi, and at the load just prior to whirl.

In Figures 5.24(a) and 5.24(b), the effect of preload distance and arc clearance can be seen for the same preload ratio. As the preload distance decreases, the whirl amplitude decreases and it starts whirling at lower eccentricity. The onset of whirl is sudden at low eccentricity, as in Figure 5.24(b), and it is load dependent at higher eccentricity, as in Figure 5.24(a).

The decrease in load capacity with increase in preload can be seen in Figures 5.24(a) and 5.24(c). Although the arc clearance is larger for $\delta = 0.3$ (0.0085 in) than for $\delta = 0.5$ (0.0007 in), for the same loading with higher preload (Figure 5.24(c)) gives higher eccentricities.

Figure 5.24(d) shows a stable offset halves bearing even at the

no load condition due to high preload.

The stiffness coefficients are given in Figure 5.25 for the preload value of 0.5. The deviations and scattering of the measured values are quite large. This may be attributed to the peculiar shape of the shaft locus. The displacements due to incremental loading in the static load direction are very small and they directly determine the coefficients K_{XX} and K_{XY} , and can affect the other coefficients.

5.1.5 General Comments

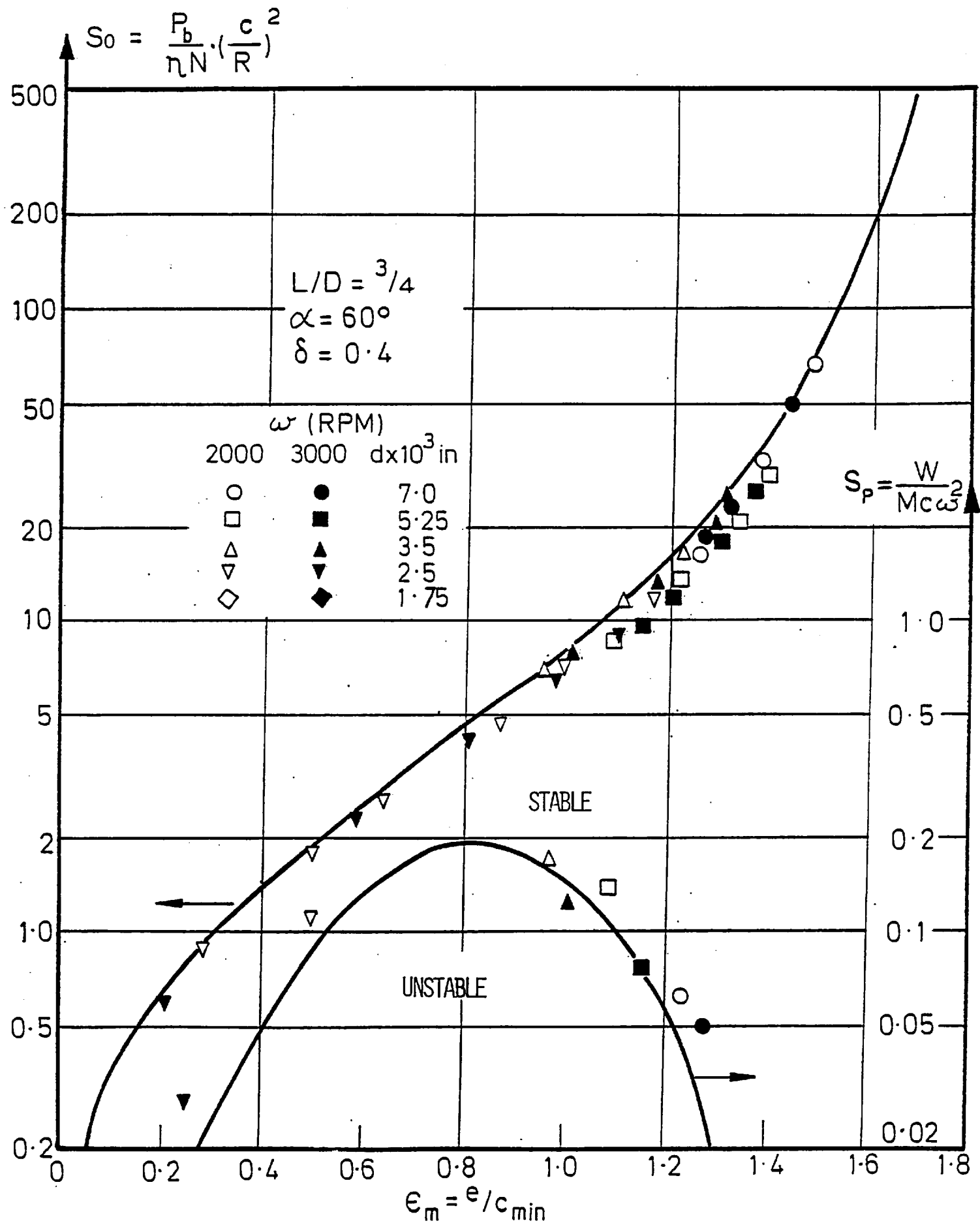
In general, although the agreement between the theoretical and experimental results is good, there are some sources of error which cause deviation from the theoretical results and scattering. Comparisons between actual measurements and calculations are based on the assumption of constant viscosity. During the experiments, the usual temperature increase of the oil was about 10°C, but at high load and low clearance conditions it could increase to 20°C. Hence, variation of the oil viscosity through the film thickness and around the circumference can affect the results. Karl [29] showed experimentally that a calculation that does not take into account the dependence of the lubricant's viscosity on temperature results in values for maximum pressures of the film higher than the experimental values. Therefore, the experimental load capacities can be lower than the theoretical values. Malcher [30] experimentally found that, due to viscosity variation at the same Sommerfeld number, the equilibrium position of the shaft can be at different positions depending on the inlet oil temperature.

From the definition of Sommerfeld number, it is clear that the viscosity can influence the operating position of the shaft in the bearing. However, the variation of viscosity around the bearing may also affect the

stiffness and damping coefficients of the bearing, and hence the instability threshold. Nikolajsen [31], by using the short bearing theory and the exponential relation between temperature and viscosity, proved that for circular bearings the instability threshold boundary can increase, especially at low eccentricity values.

In general, the experimental stability threshold values are found to be higher than the corresponding theoretical predictions. The effect of flexibility of the shaft and the bearing housing on the stability threshold was considered. The overall stiffness of the shaft bearing system was measured to be 2×10^6 lb/in. In most of the stability threshold conditions, the ratio of the deflection to the clearance was less than 0.05. Hahn [32] has shown theoretically that the effect of flexibility of the system on the stability threshold is negligibly small for flexibility ratios as small as 0.05.

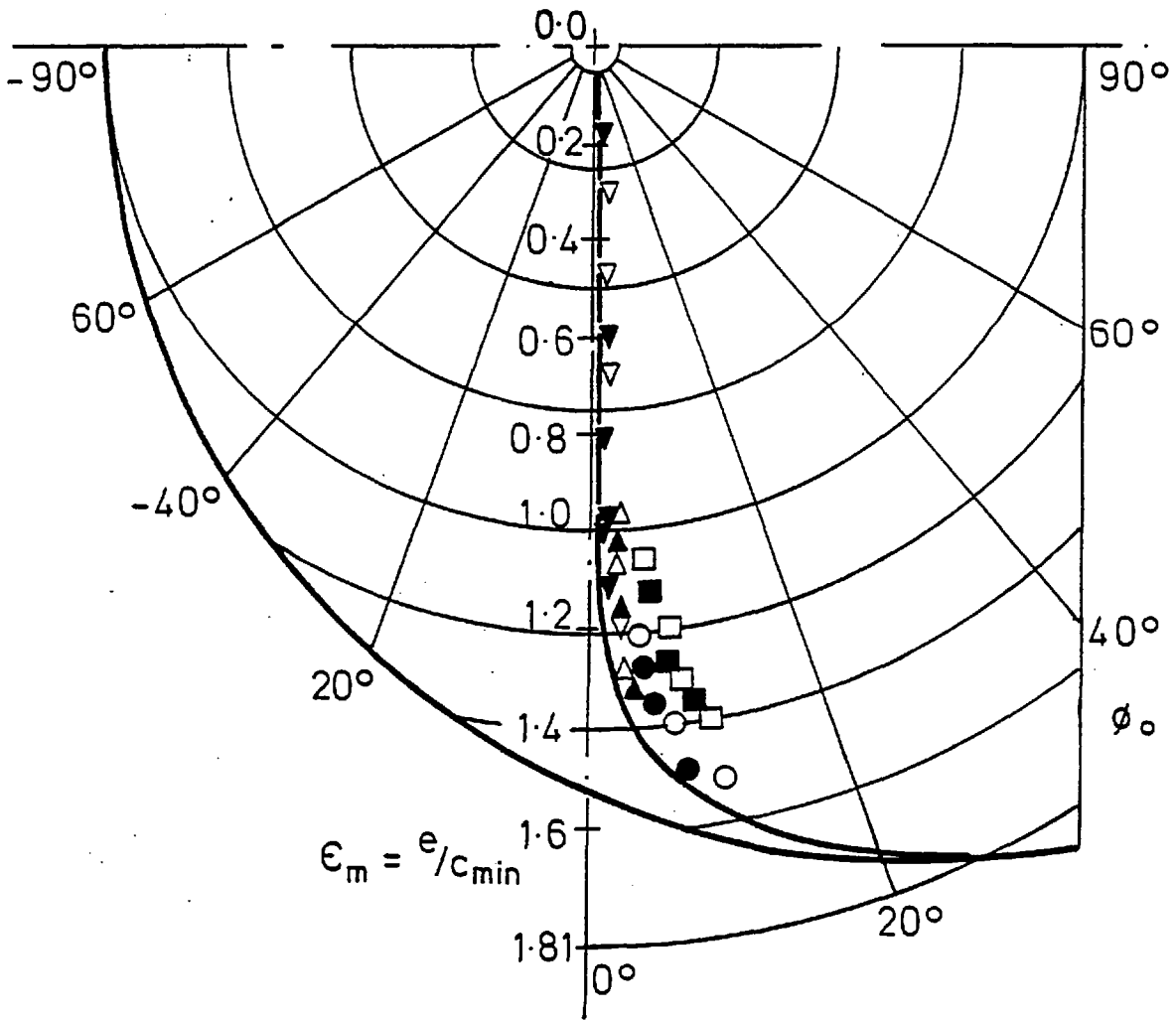
In two axial groove bearings, the experimental conditions for the lubricant supply did not match those assumed in the theory. In the experiments, the effect of the oil feed pressure on the stability of the two axial groove bearing was investigated, but no observable effect was found on the stability threshold. Therefore, it has been kept constant in all the experiments at 15 psi and in the solution of the Reynolds equation the oil feed pressure was assumed to be zero. In reality, oil is fed from the recesses at both sides of the bearing. Although the recesses are in the form of an arc, the leading edges of the oil films can be pressurised due to the velocity of the approaching lubricant film. The large and deep oil pockets can cause recirculation and turbulence in the grooves. The lands on each side of the grooves may cause additional oil film forces which were not taken into account in the calculations. These may affect the static and dynamic characteristics of the bearings.



(a) The variation of load capacity and stability threshold with journal eccentricity

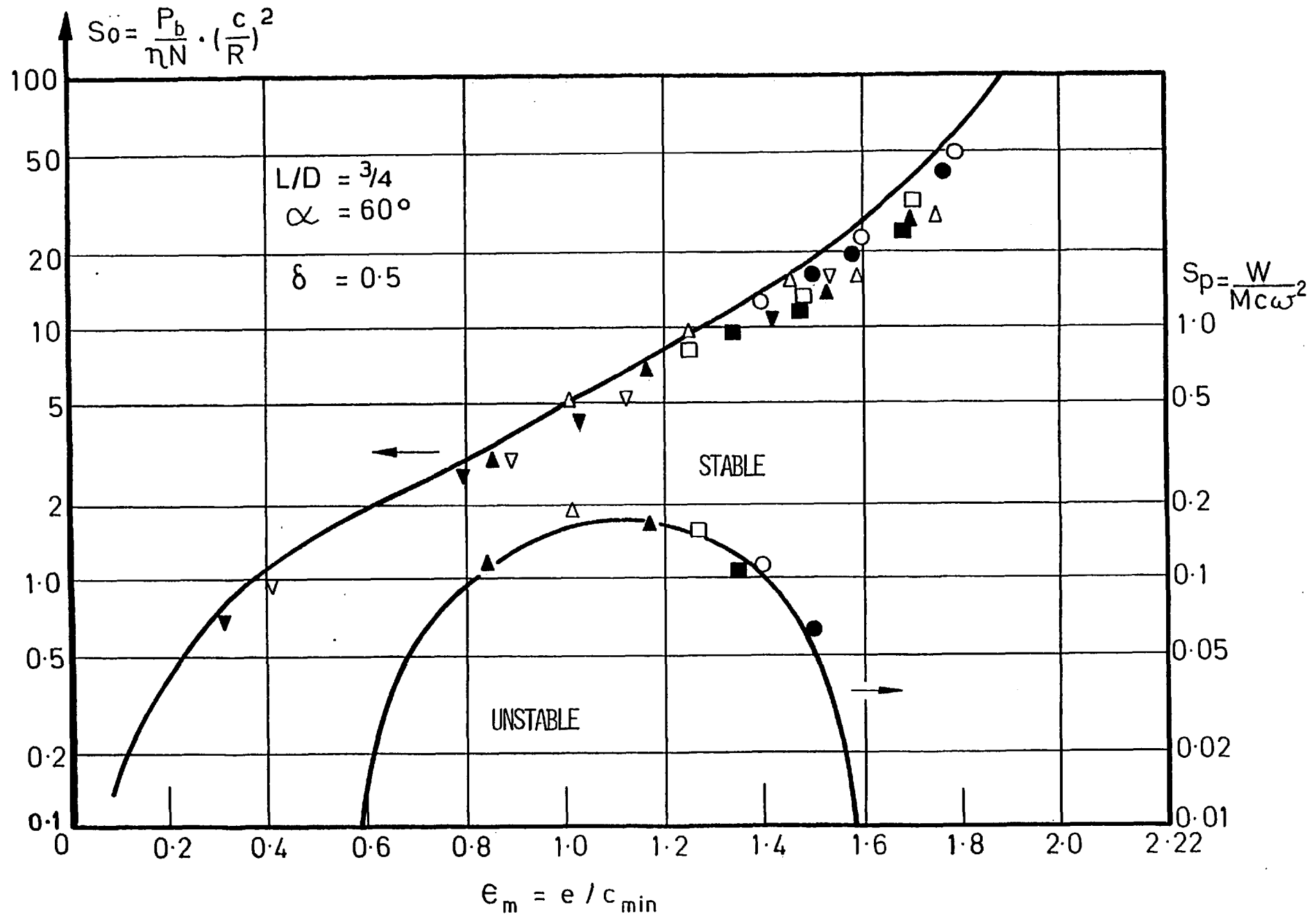
Figure 5.20: The offset halves bearing with $\delta = 0.4$

$$L/D = 3/4 \quad \alpha = 60^\circ$$
$$\delta = 0.4$$



(b) Locus of shaft centre in the clearance shape due to static loading

Figure 5.20: The offset halves bearing with $\delta = 0.4$



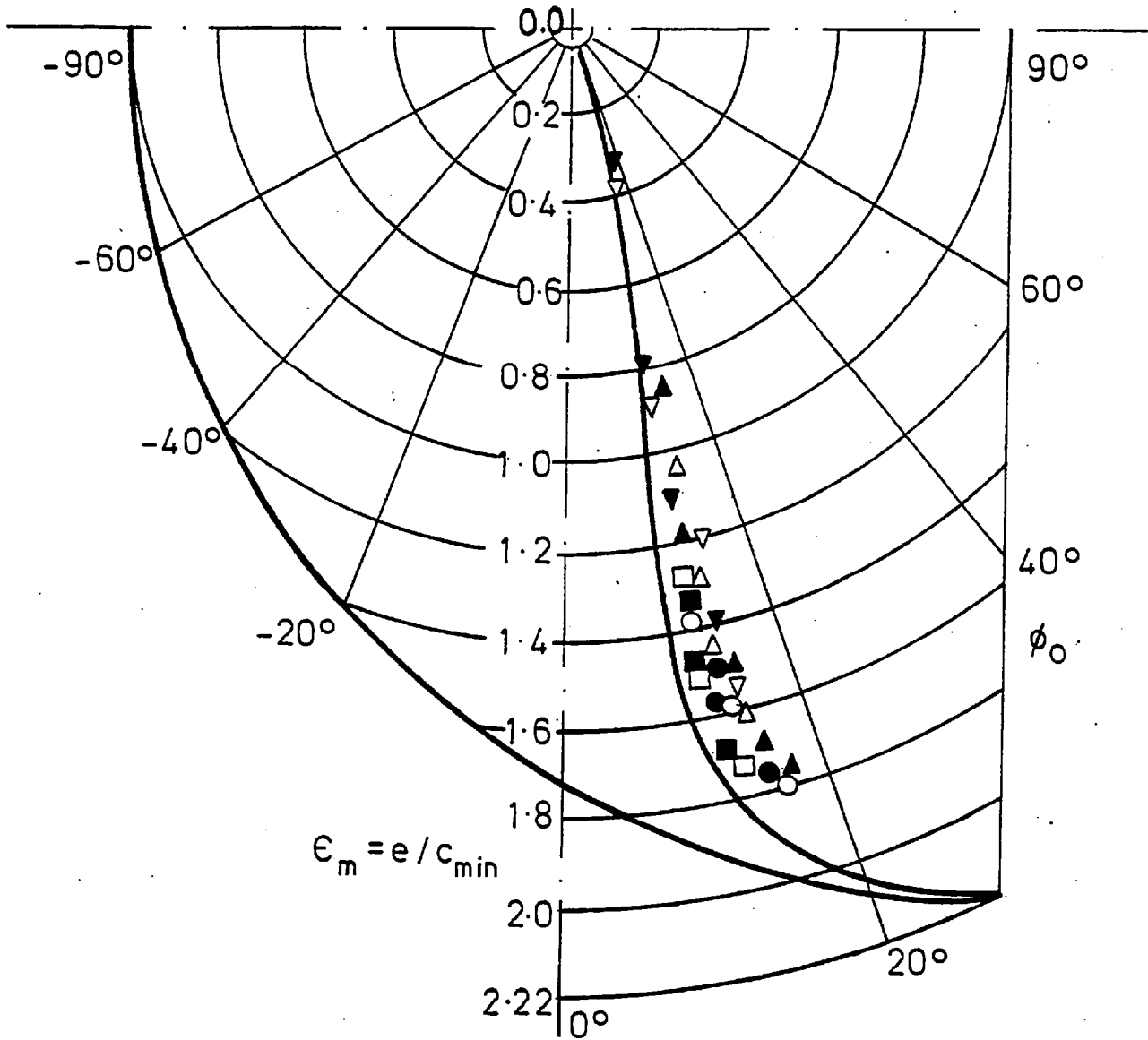
(a) The variation of load capacity and stability threshold with journal eccentricity

Figure 5.21: The offset halves bearing with $\delta = 0.5$

$$L/D = 3/4$$

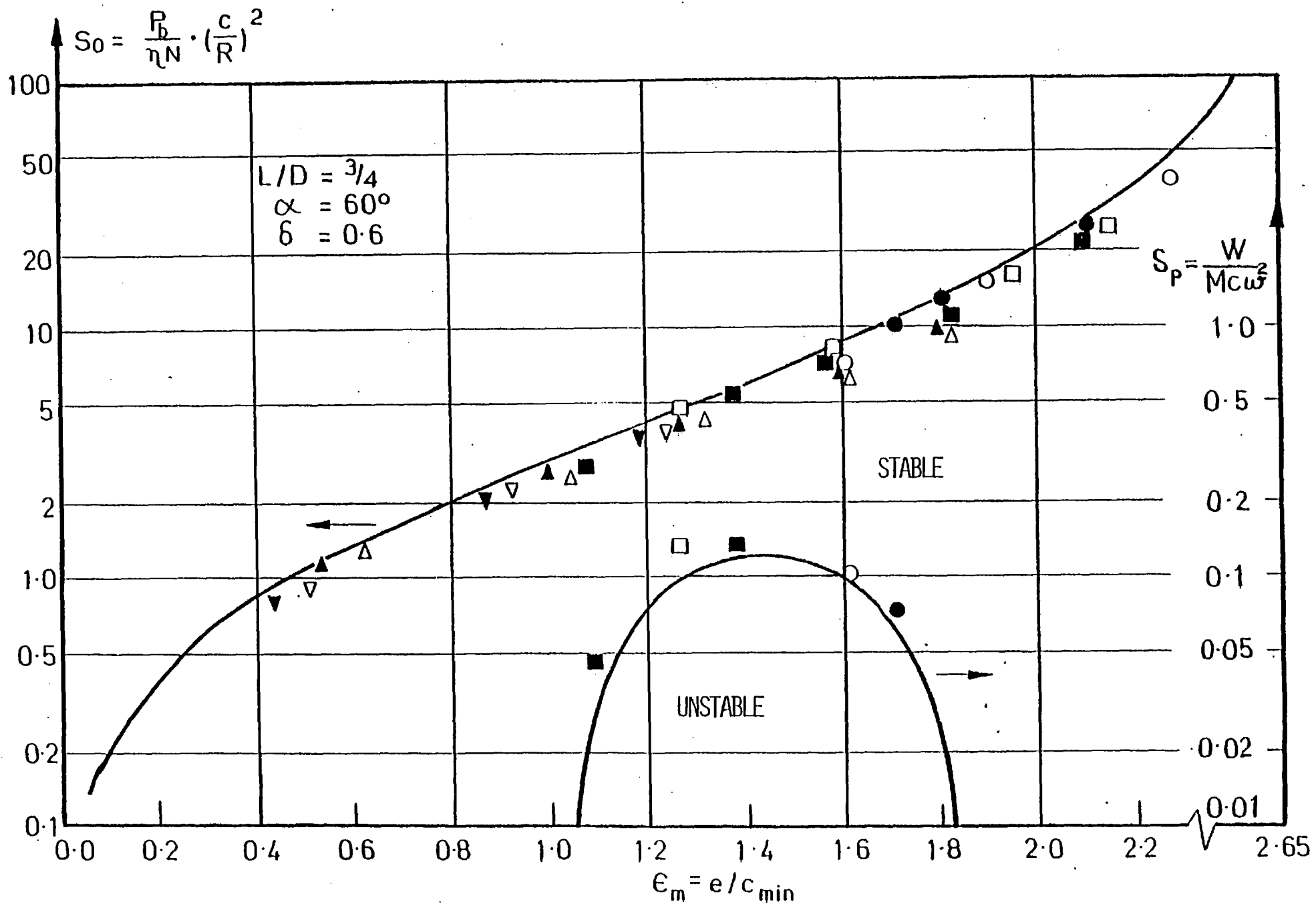
$$\alpha = 60^\circ$$

$$\delta = 0.5$$



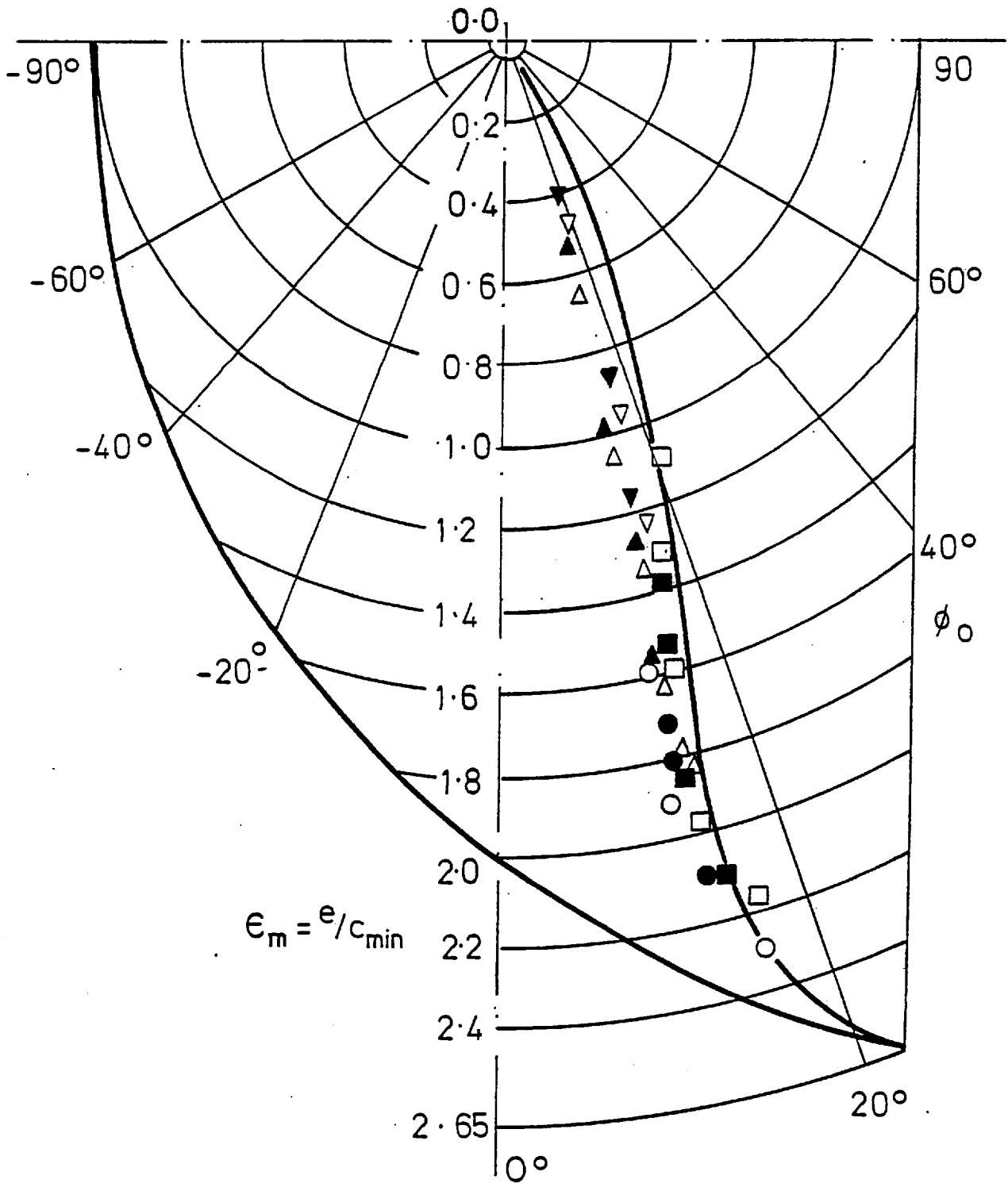
(b) Locus of shaft centre in the clearance shape due to static loading

Figure 5.21: The offset halves bearing with $\delta = 0.5$



(a) The variation of load capacity and stability threshold with journal eccentricity
 Figure 5.22: The offset halves bearing with $\delta = 0.6$

$$L/D = 3/4 \quad \alpha = 60^\circ$$
$$\delta = 0.6$$



(b) Locus of shaft centre in the clearance shape due to static loading

Figure 5.22: The offset halves bearing with $\delta = 0.6$

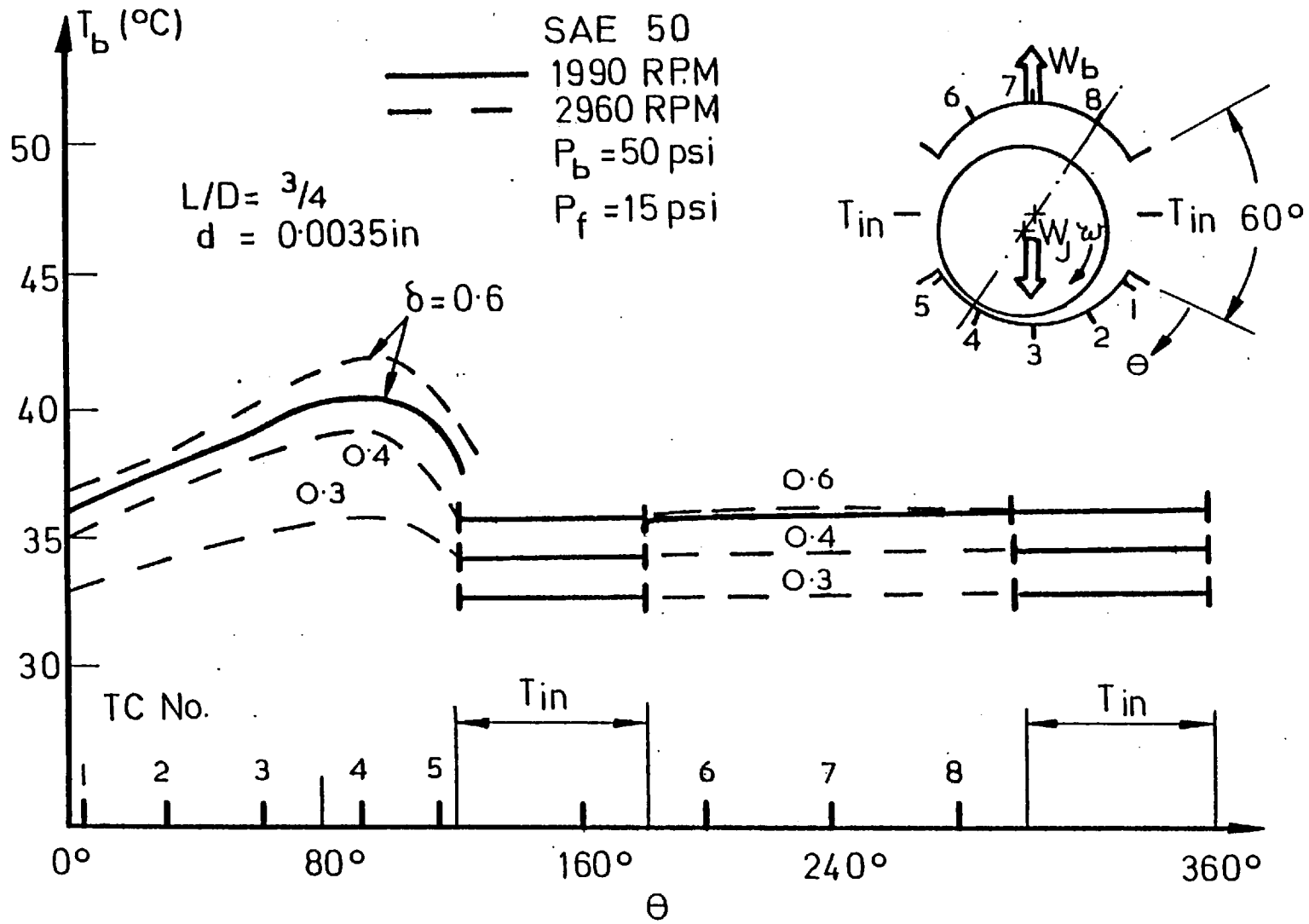
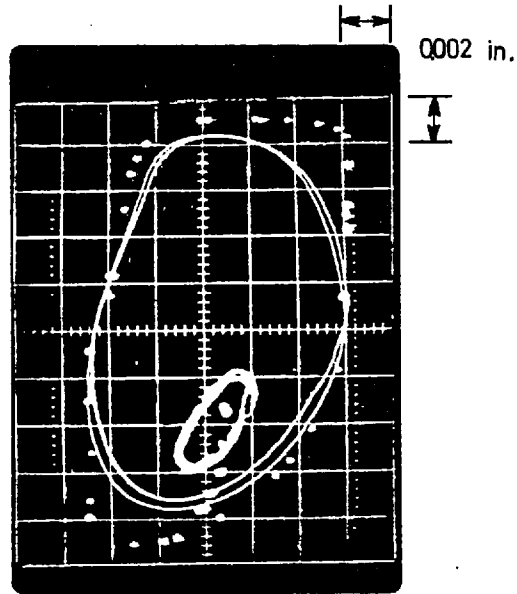
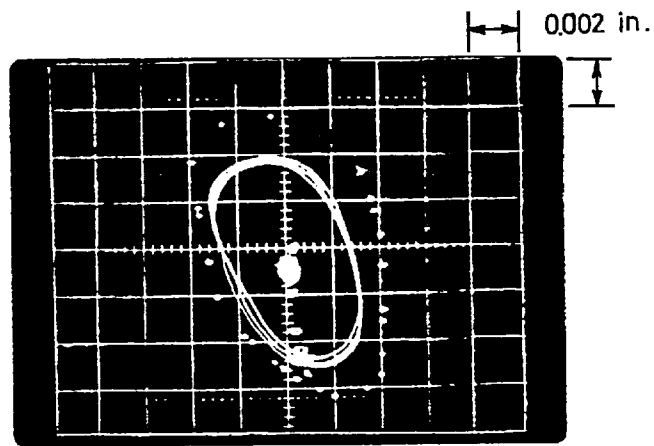


Figure 5.23: Temperature profiles around the offset halves bearing centre-line

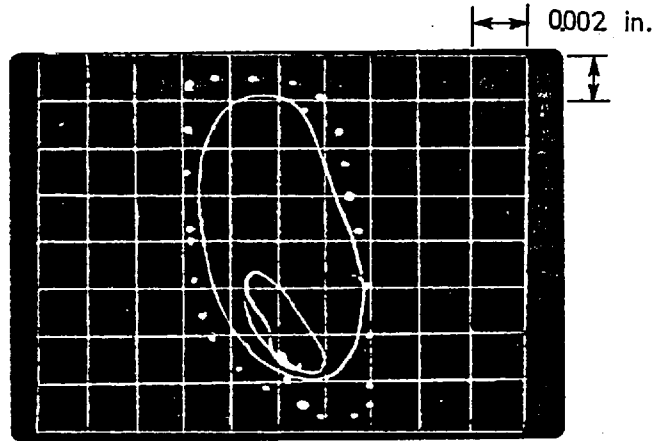


(a) 1990 RPM, $\delta = 0.3$, $d = 0.0025$ in
Shaft rotation: counter-clockwise

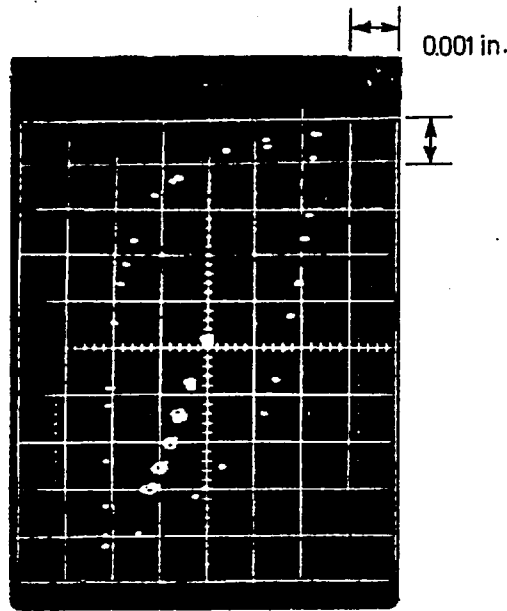


(b) 1990 RPM, $\delta = 0.3$, $d = 0.00175$ in
Shaft rotation: clockwise

Figure 5.24: Some oscilloscope photographs of the offset halves bearing whirling motion

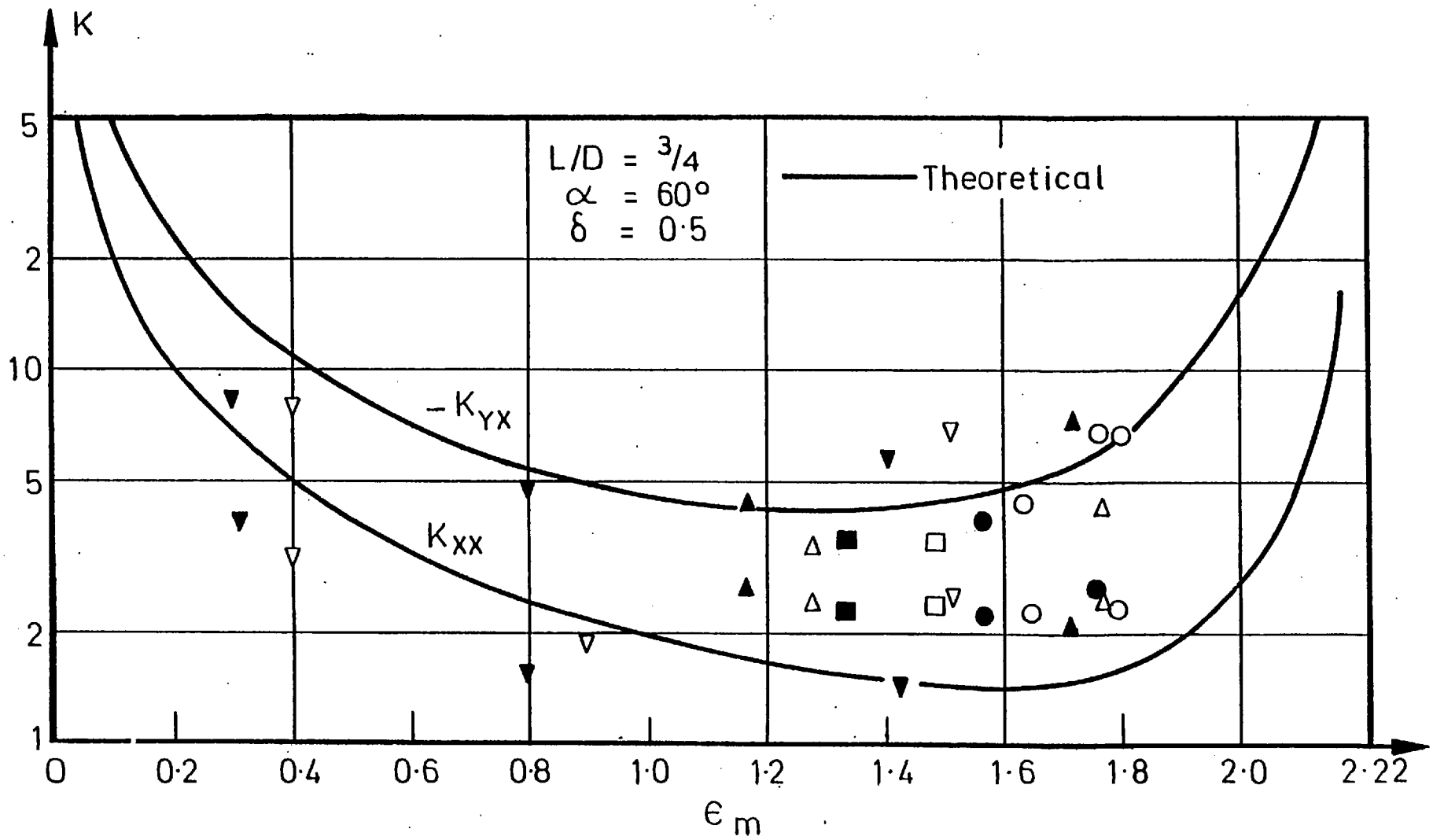


(c) 1990 RPM, $\delta = 0.5$, $d = 0.0035$ in
Shaft rotation: clockwise



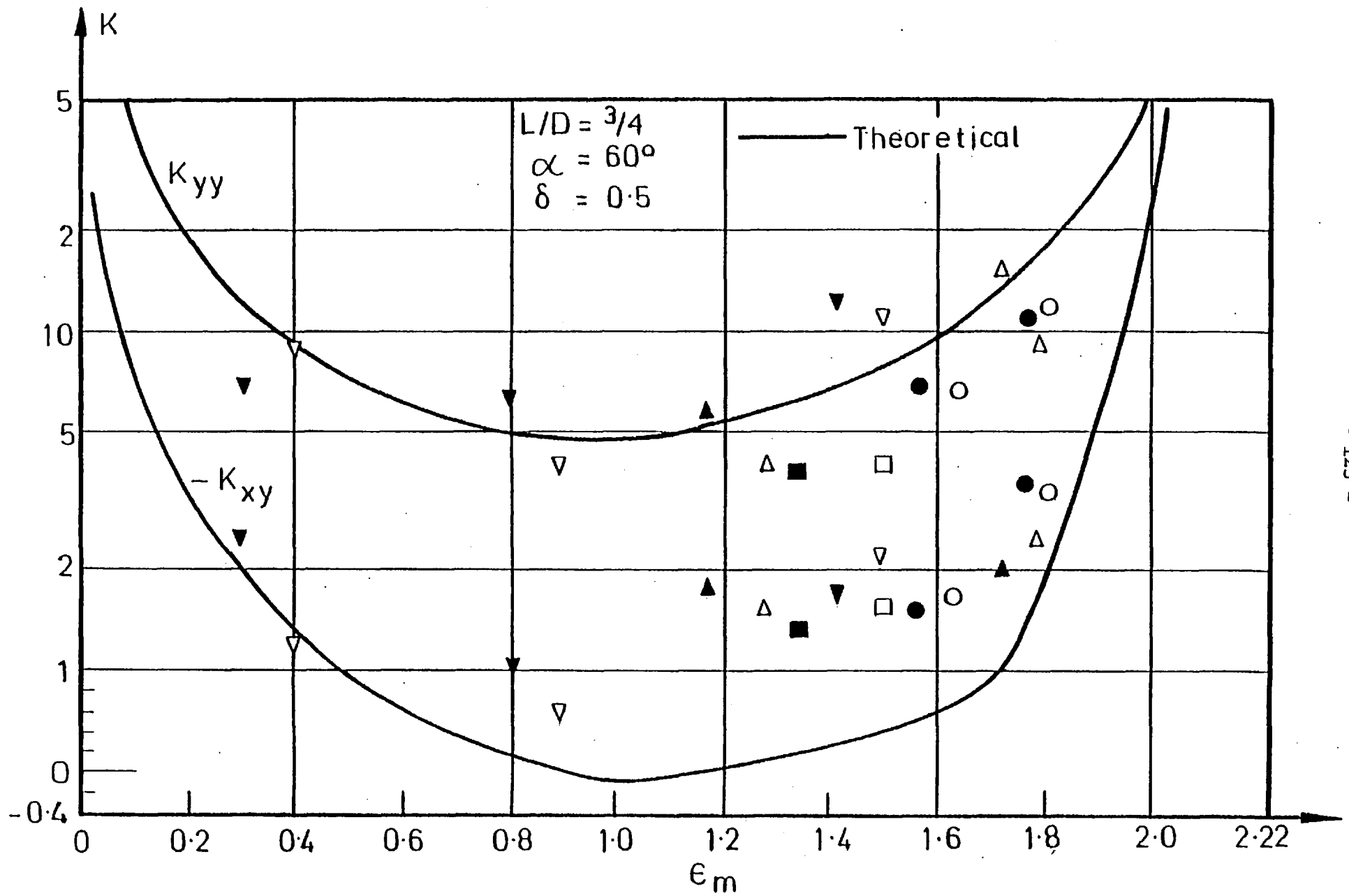
(d) 2960 RPM, $\delta = 0.6$, $d = 0.0025$ in
Shaft rotation: counter-clockwise

Figure 5.24: Some oscilloscope photographs of the offset halves bearing whirling motion



(a) Stiffness coefficients K_{XX} and K_{YX}

Figure 5.25: The variation of the stiffness coefficients for the offset halves bearing with $\delta = 0.5$



(b) Stiffness coefficients K_{yy} and K_{xy}

Figure 5.25: The variation of the stiffness coefficients for the offset halves bearing with $\delta = 0.5$

At certain operating conditions, once the temperatures around the bearing were stabilised, any small change of load (i.e. that which can cause displacements of the order of one-tenth of clearance) was observed as an immediate change in the measured temperatures. The thermocouples, which were placed about 1 mm below the bearing surface, appeared to be quite sensitive and to measure the actual oil film temperatures.

The measured temperature distribution in the centre-plane of the bearing showed that temperature increased from maximum film thickness to the minimum film thickness positions. When the oil feed pressure was kept constant, as the clearance was decreased, the temperature levels steadily increased.

5.1.6 Comparison of Bearing Bore Types

The essential feature of the non-circular bearings is that the centres of curvature of its arcs are displaced from the geometric centre of the bearing. As a result of this feature, in elliptical and offset halves bearings the hydrodynamic pressures generated in the top half at zero journal eccentricity is the same as in the bottom half. Due to their specific geometries, the locus of the journal centre is almost horizontal and vertical for elliptical and offset halves bearings, respectively. The minimum film thickness occurs on the load carrying bottom half of both the bearings. In the elliptical bearing, the oil film has another minimum value in the top half due to the lobe eccentricity. The converging part of the film is not of large extent due to the groove, and this decreases the load capacity considerably. In the offset halves bearing, the converging oil film cannot reach the minimum value due to the groove; therefore, the oil film force on the top half is not as effective as in the elliptical bearing. This causes the offset halves bearing to have a

higher load capacity than the elliptical bearing. This feature of the bearings can be shown easily by plotting the load capacity against the minimum film thickness of the bearings which occurs on the bottom half. Figure 5.26(a) shows a comparison of the load capacities of different bearing bore shapes for the same geometric parameters. Although there is a small discrepancy between the offset halves and the circular bearing, the load capacity of the elliptical bearing is much lower than these two bearings.

A comparison of the stability thresholds of the bearing bore types are shown in Figure 5.26(b) for the same geometric parameters. The elliptical and offset halves bearings have much better stability characteristics than the circular bearing. In order to see the effect of the load capacities on their stability, the load lines are shown as follows: For the same loading conditions (i.e. for the same value of S_o and S_p), the operating conditions can be at C , E and O for the circular elliptical and offset halves bearings. As the load is decreased, the stability threshold is reached at the medium eccentricity region for the circular and elliptical bearings. But for the cases shown, due to the higher load capacity and better stability characteristics of the offset halves bearing, it will always be stable.

As the speed is increased, the elliptical bearing reaches the stability threshold at higher eccentricity, while the offset halves bearing reaches the threshold in the medium eccentricity range. Therefore, the elliptical bearing is much better than the offset halves bearing under heavily loaded conditions.

This feature of the bearings can also be shown from the effect of the cross-coupling stiffness coefficients. As explained in section 3.3, the difference of the cross-coupling stiffness coefficients is important

from the stability point of view. As shown in Figures 5.17 and 5.25, although these coefficients are of the opposite sign for the elliptical bearing, except for the high values of the eccentricity, for the offset halves bearing they are of the same sign except for the medium eccentricity range in which it shows an unstable region.

For the same geometric parameters and running conditions, although the offset halves bearing is stable even at the no load condition, as seen in Figure 5.24(d), the elliptical bearing can become unstable at low loads, as seen in Figure 5.16(d). In these figures, the destabilising effect of the 60° groove angle in the offset halves bearing is to be remembered.

A further important criterion for comparison can be the bearing operating temperatures. The elliptical bearing shows a higher temperature rise than the offset halves bearing. Although the top half of the offset halves bearing shows no observable temperature rise, the elliptical bearing shows a slightly lower temperature increase in the top half than in the bottom half. This is again due to the higher lobe eccentricities of the elliptical bearing for the same operating conditions.

5.1.7 The Dynamic Test Results

Experimental curves of bearing response as a function of excitation speed for different bearing bore geometry are given in Figures 5.27, 5.28 and 5.29. The excitation force amplitudes were given on the right hand side of each graph. For each of the bearing types, the trend of the response to unbalance as the speed was varied showed common characteristics. In each case, the magnitude of vibration initially increased with increase in the excitation frequency up to the damped natural frequency of the system corresponding to the smallest damping

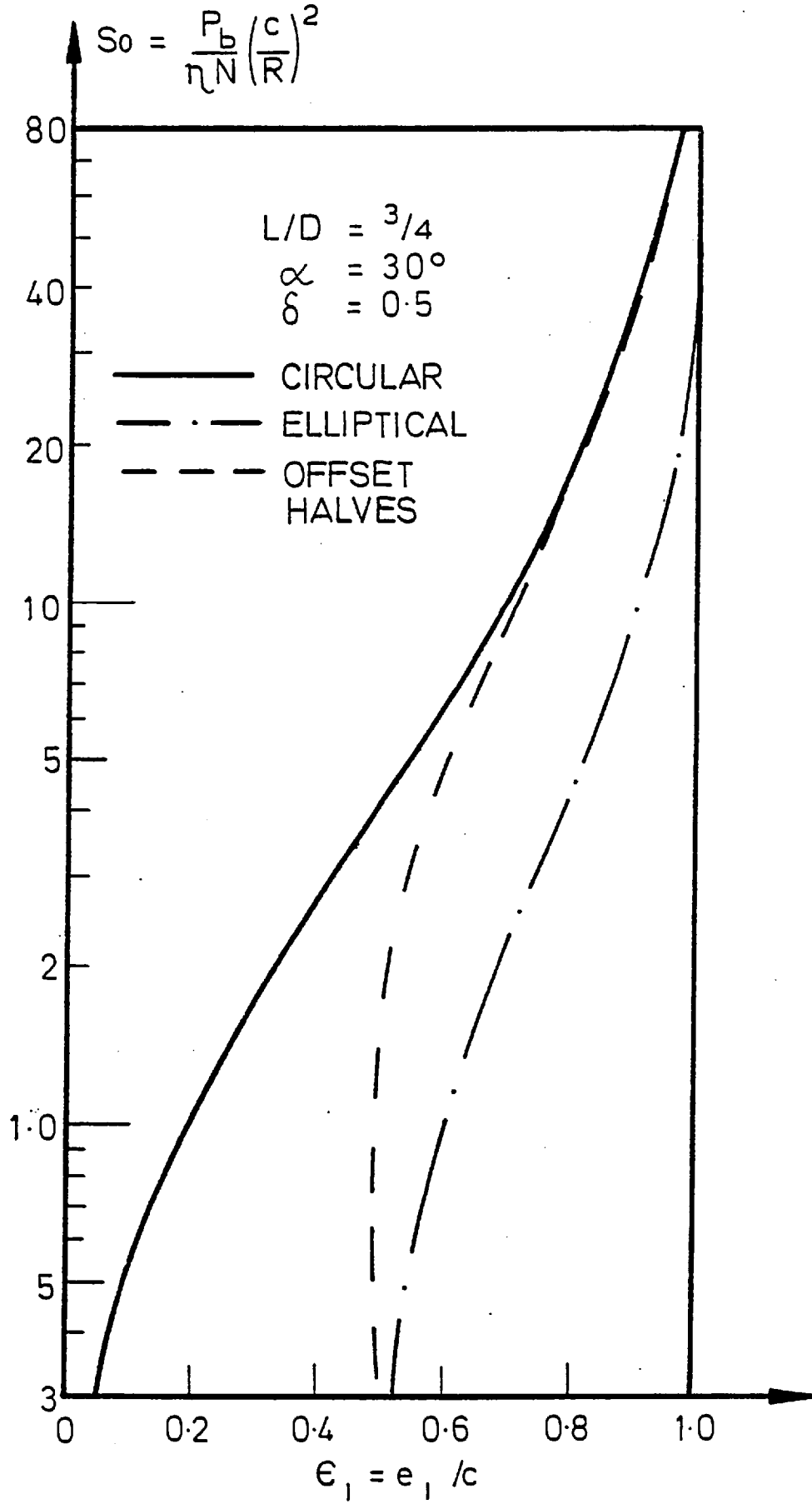


Figure 5.26: (a) Comparison of the load capacities of the bearing types

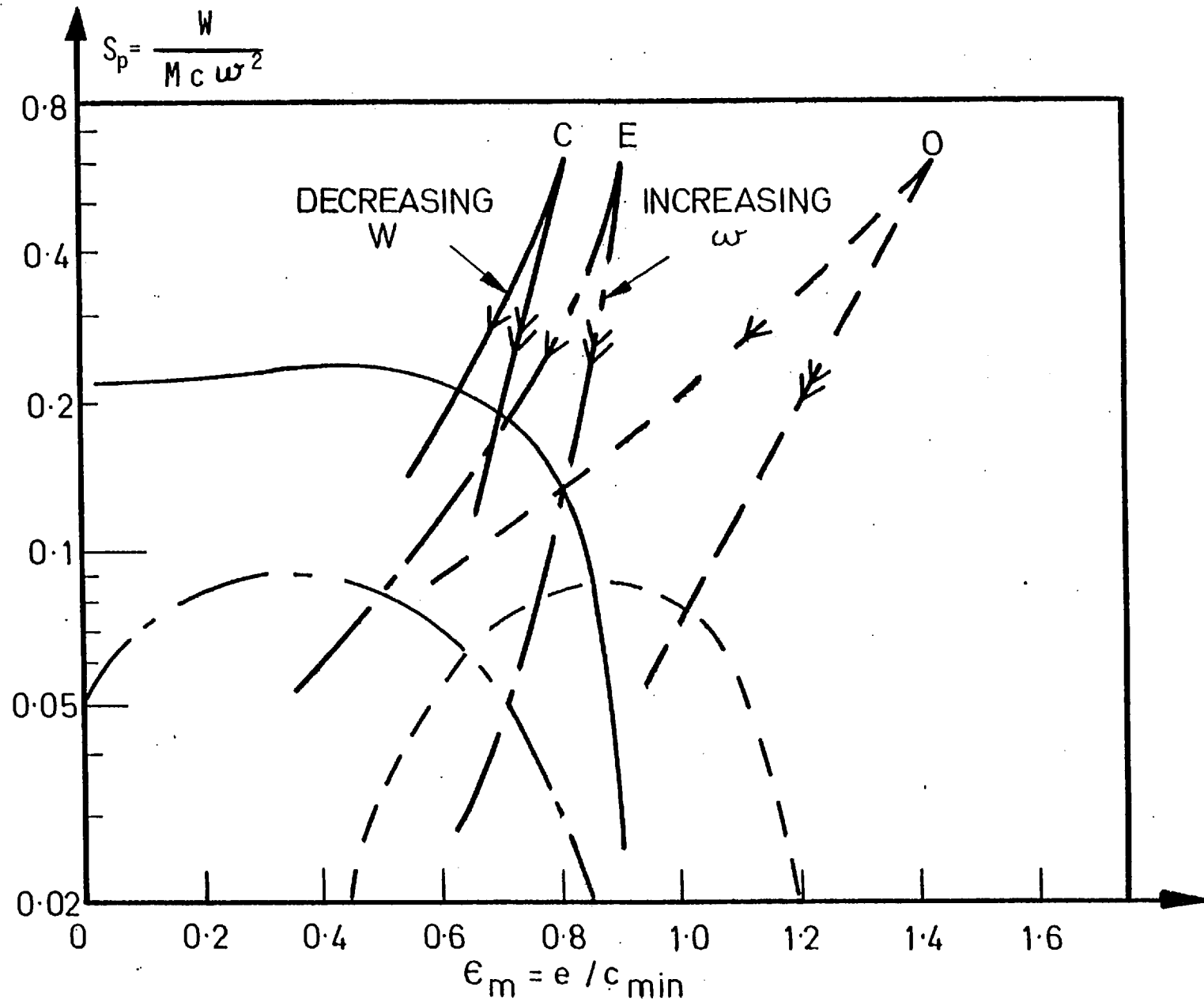


Figure 5.26: (b) Comparison of the stability thresholds of the bearing types

factor. As the excitation frequency increased, the vibration amplitudes decreased and, after reaching a minimum value, they reached higher amplitudes beyond the synchronous speed.

The response amplitudes show a rounded rather than a sharp peak, corresponding to well-damped behaviour. The amplitude and damped natural frequency are governed by the eigenvalues of the characteristic equation, as described in Appendix D. As it can be seen from equation (D.1), the eigenvalues are complicated functions of the bearing coefficients. The increase of the response at the resonant frequency is due to the decrease in the damping factor of the system.

The oscilloscope photographs which are shown in Figures 5.27, 5.28 and 5.29 were taken in sequence with increasing excitation frequency. In all these photographs, the direction of rotation is in the clockwise direction and the corresponding excitation speeds are shown above and below the photographs. Since the test shaft has a certain amount of run-out, the bearing shows a small vibration orbit around the equilibrium position. The amplitude of this vibration is small compared to that from the synchronous external excitation. At half synchronous speed, the effect of run-out on the response can be seen as a small cusp on the elliptical orbit.

The assumption of the linearisation of the dynamic oil film forces about the equilibrium position was examined during the experiments by applying different values of unbalance weights. Although the preloaded bearings have the effect of intensifying non-linearity due to higher lobe eccentricities, it was found that the limit of linearisation can be valid for maximum vibration amplitudes up to one third of the bearing clearance. Allaire et al [26] have found that the vibration characteristics are linear up to about a half to one third of the bearing clearance.

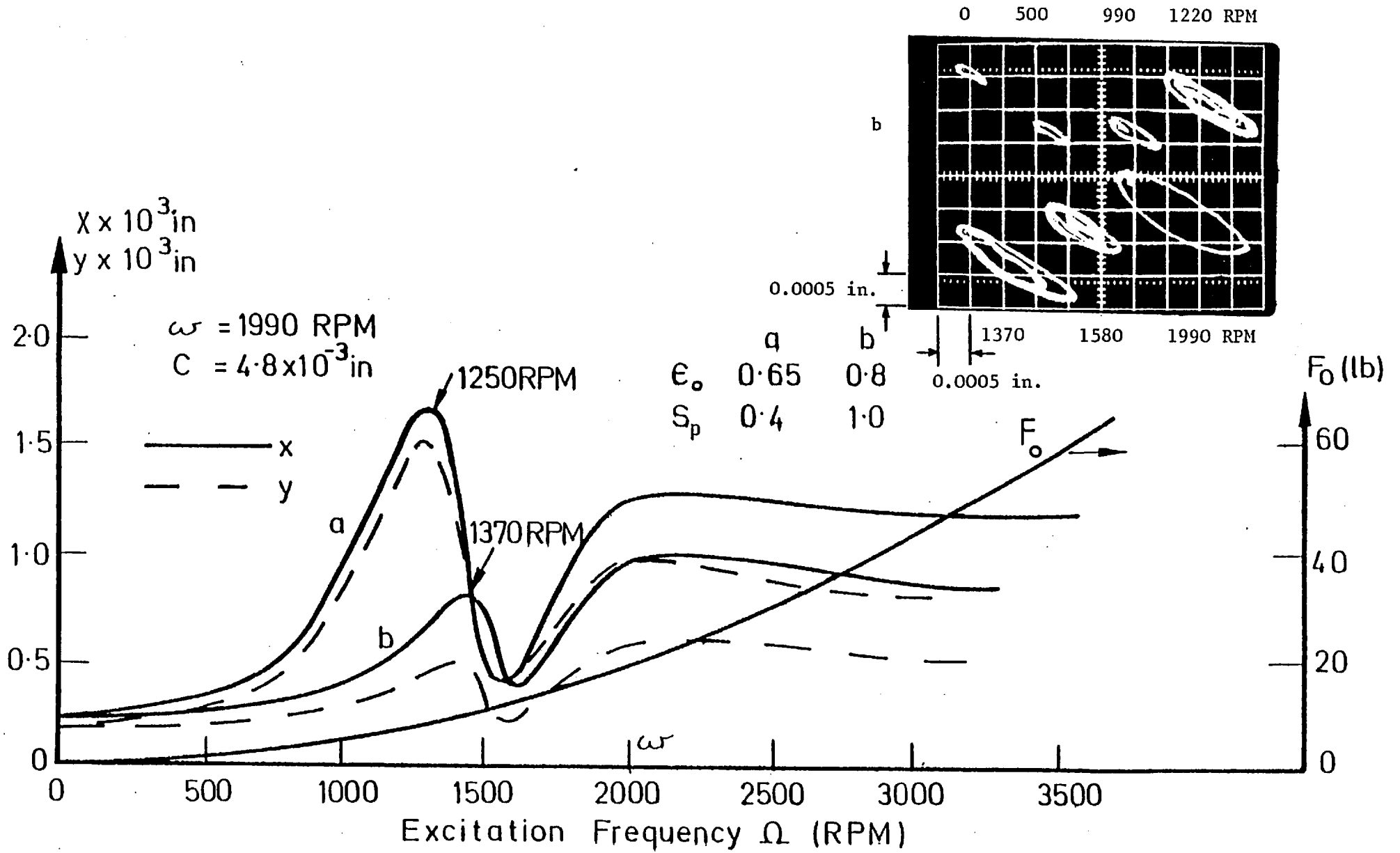
The calculations of the response to forced excitation were made by using the stiffness and damping coefficients of the bearing as described in section 3.2. As it can be seen from equation (3.6), the vibration amplitudes are linearly dependent on the unbalance force to static load ratio. Therefore, synchronous unbalance response amplitudes are presented as the product of the non-dimensional major or minor axis and the static to unbalance force ratio.

The theoretical response curves are plotted from Figures 5.30 to 5.37 for different bearing bore geometries against their load capacities. They showed fairly common characteristics. At low loads, the major axis amplitude increases with increase in the load capacity. At higher loads, for circular and offset halves bearings, the amplitudes may decrease or stay at the same level, but for elliptical bearings, it increases with the load. The minor axis amplitude increases at low loads and decreases at higher loads. But, again, for elliptical bearings it keeps increasing at a low rate. The stability parameter has a strong effect on the vibration amplitudes. It is to be noted that as the stability parameter approaches to the corresponding threshold value (i.e. as the load decreases or the shaft speed increases), the F_o/W ratio increases; therefore, the real vibration amplitudes a/c or b/c increase.

Experimentally determined response orbit axes for circumferentially grooved bearings for a feed pressure ratio $\gamma = \frac{1}{2}$ are given in Figures 5.30(a) and 5.30(b). They show good agreement with the theoretical results over a range of stability parameters.

The effect of groove angle on the response is shown for the circular bearing in Figures 5.32 and 5.33. At lightly loaded conditions, the vibration amplitude increases considerably.

The effect of preload on the vibration amplitudes are shown in



(a)

Figure 5.27: Typical dynamic response of the circumferentially grooved circular bearing to external excitation

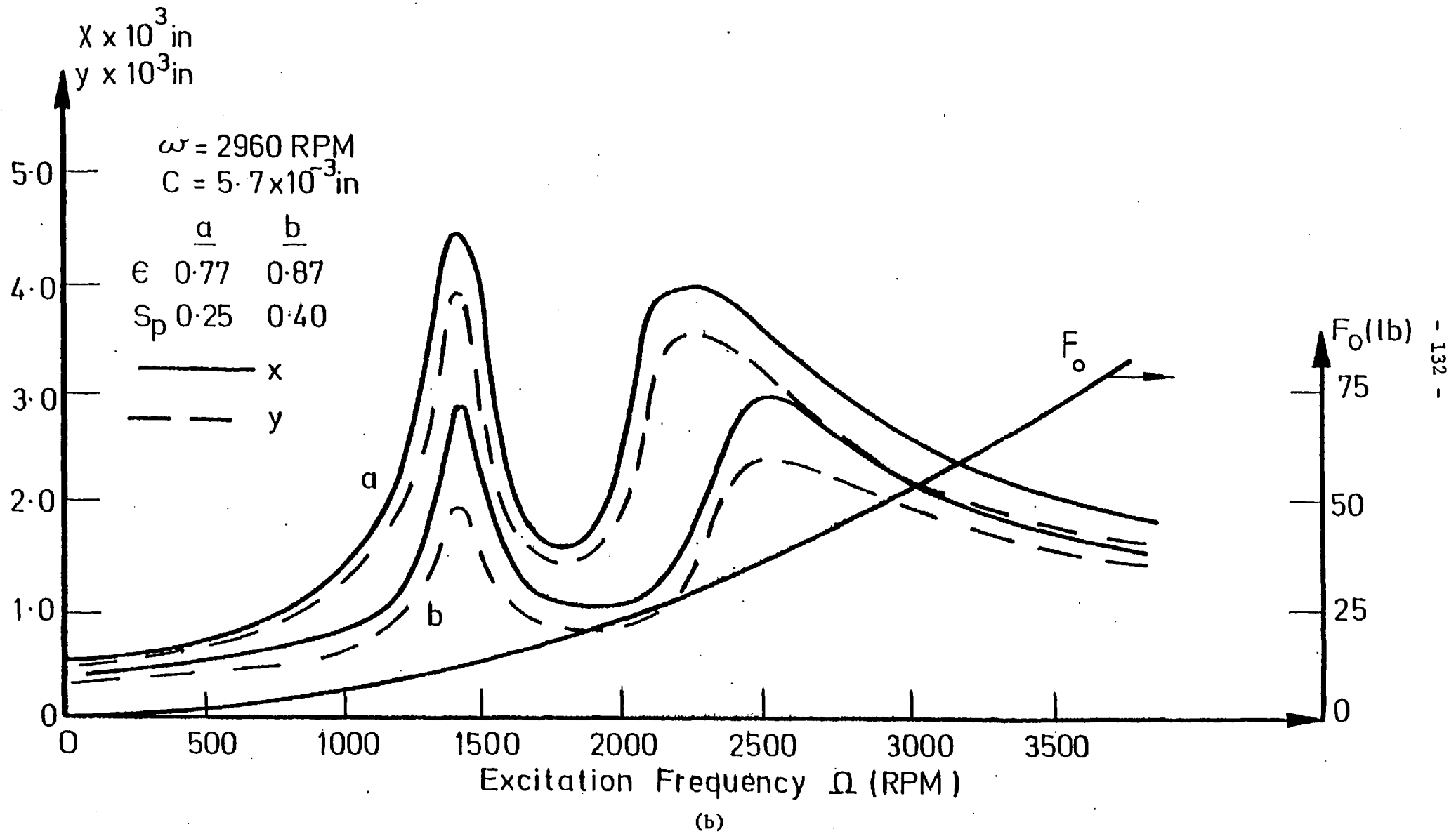


Figure 5.27: Typical dynamic response of the circumferentially grooved circular bearing to external excitation

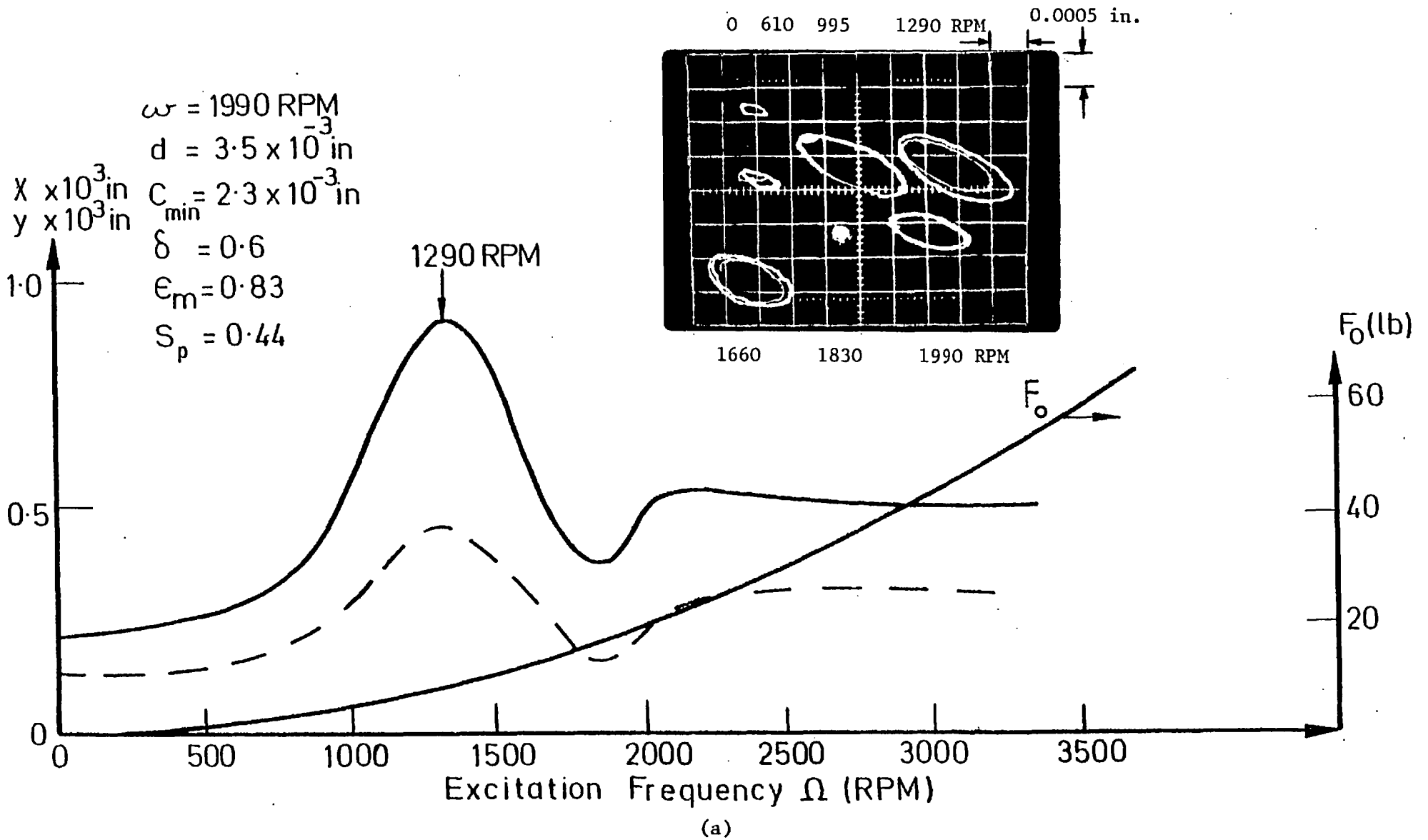
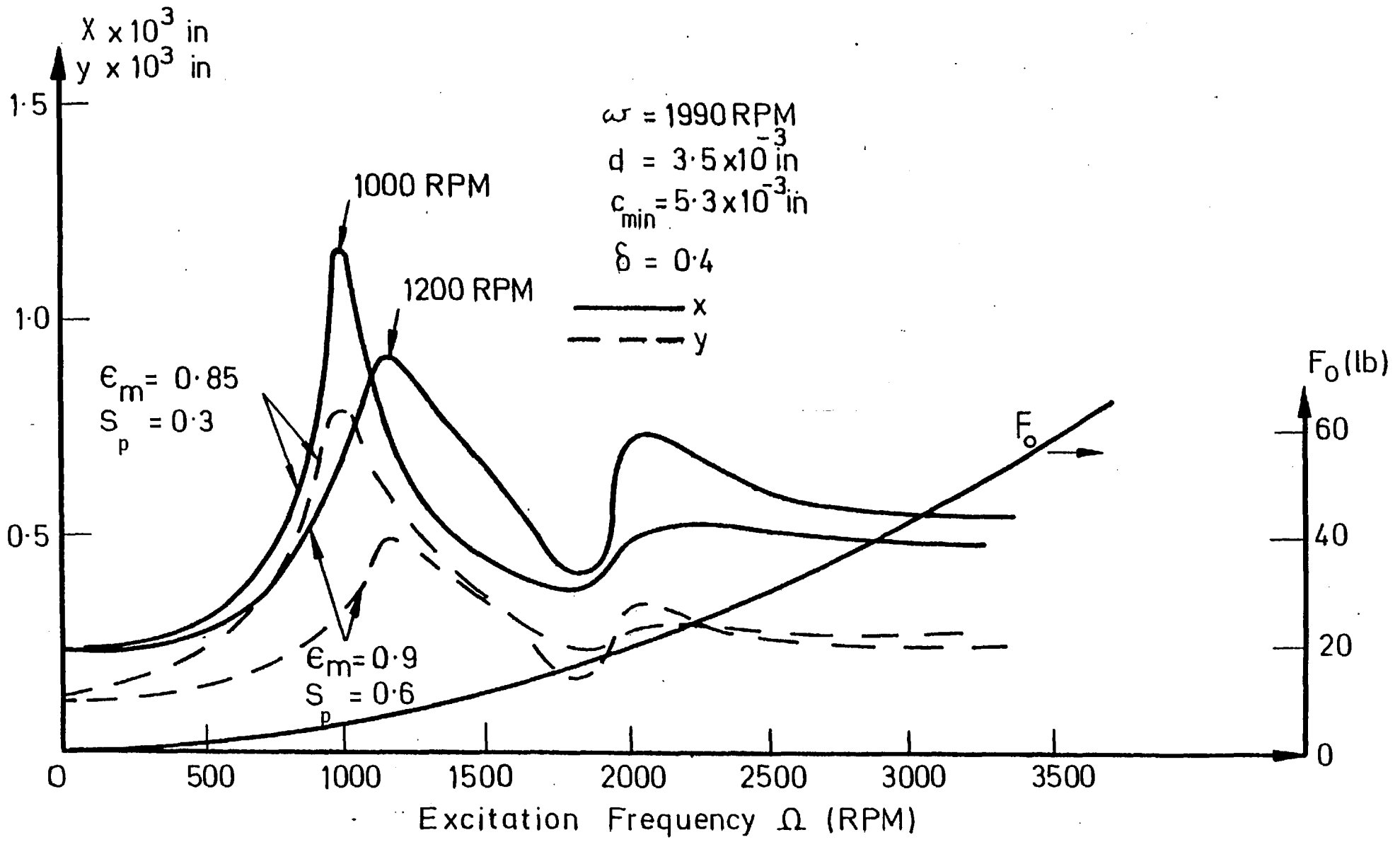
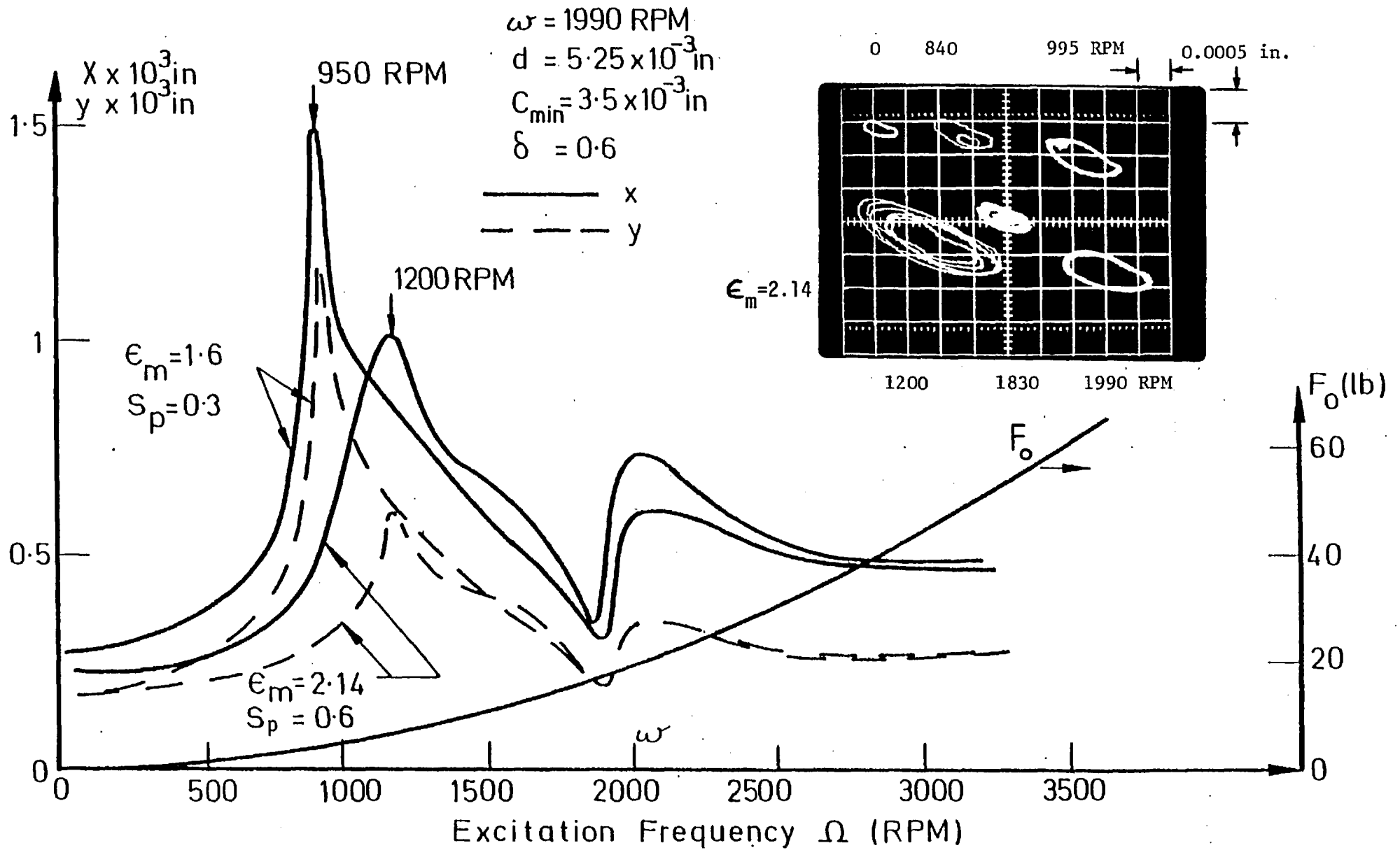


Figure 5.28: Typical dynamic response of the elliptical bearing to external excitation



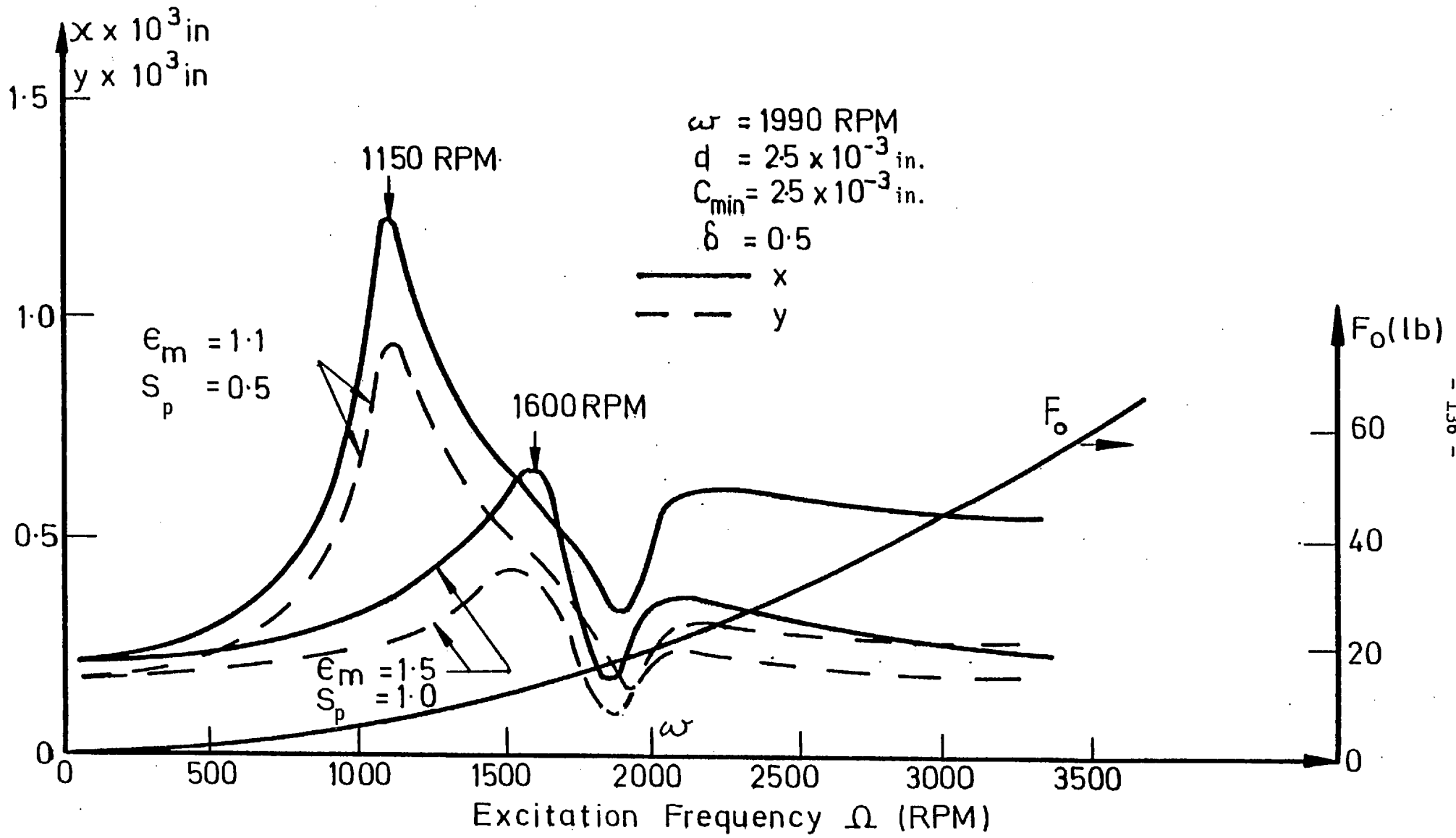
(b)

Figure 5.28: Typical dynamic response of the elliptical bearing to external excitation



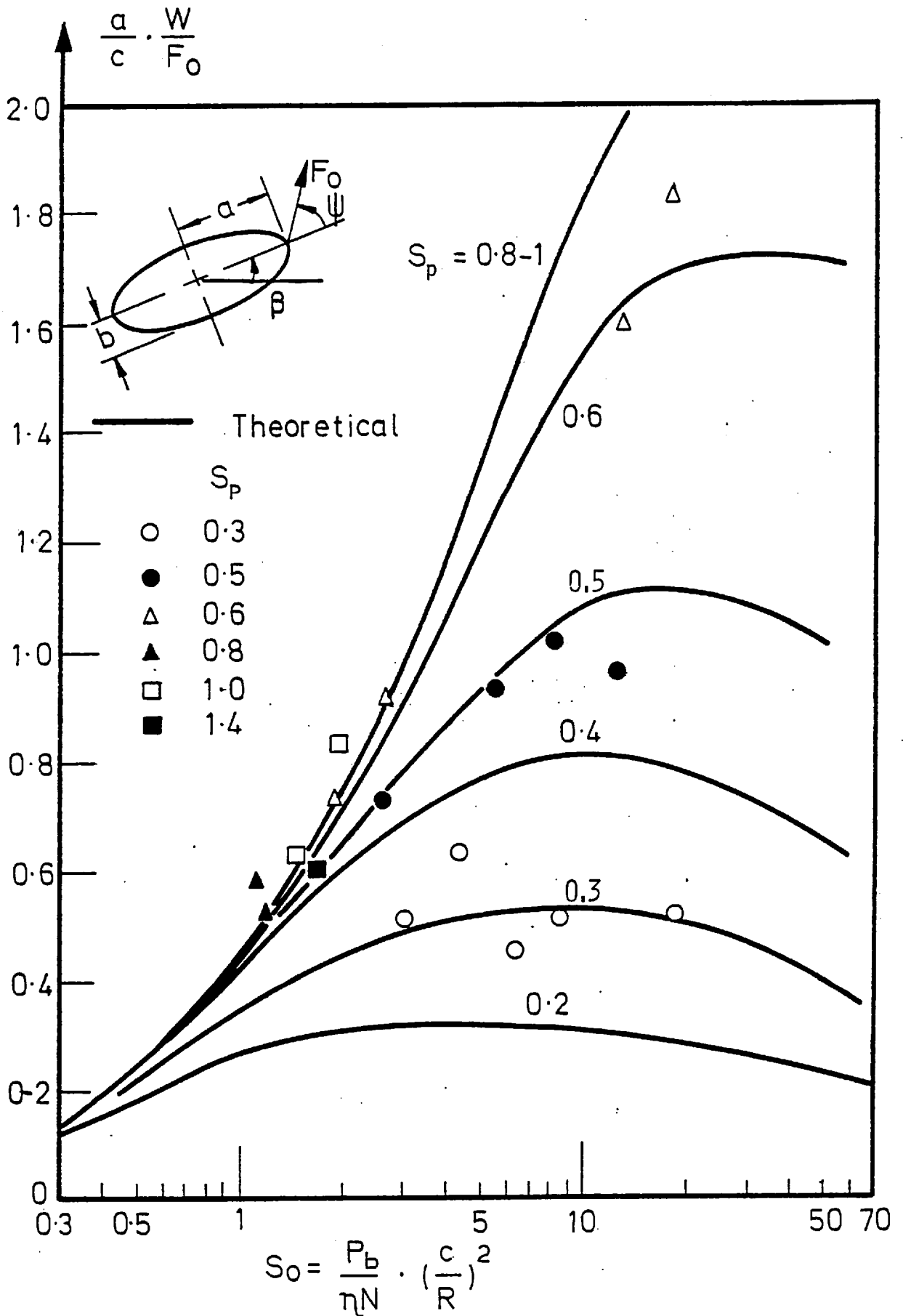
(a)

Figure 5.29: Typical dynamic response of the offset halves bearing to external excitation



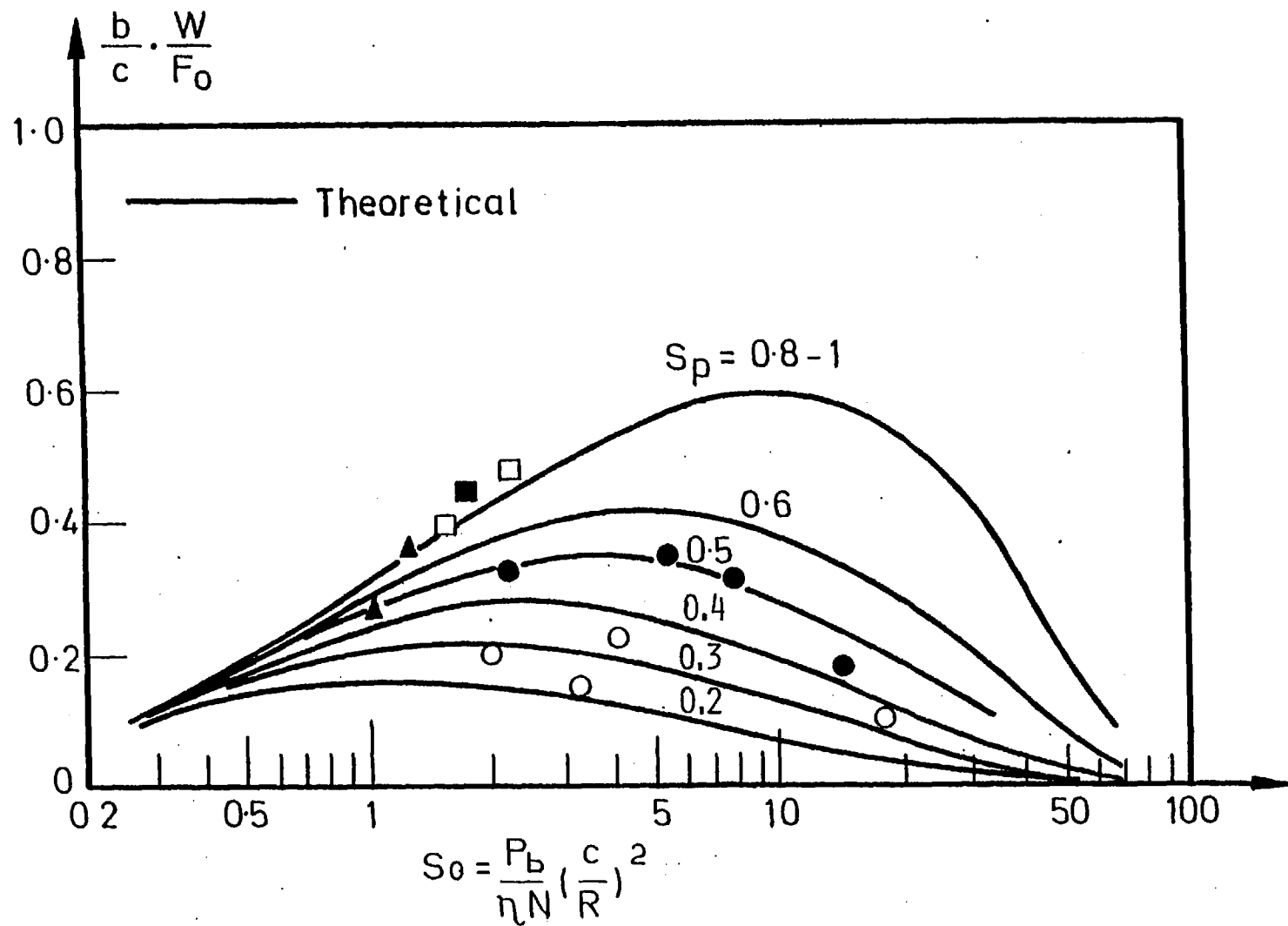
(b)

Figure 5.29: Typical dynamic response of the offset halves bearing to external excitation



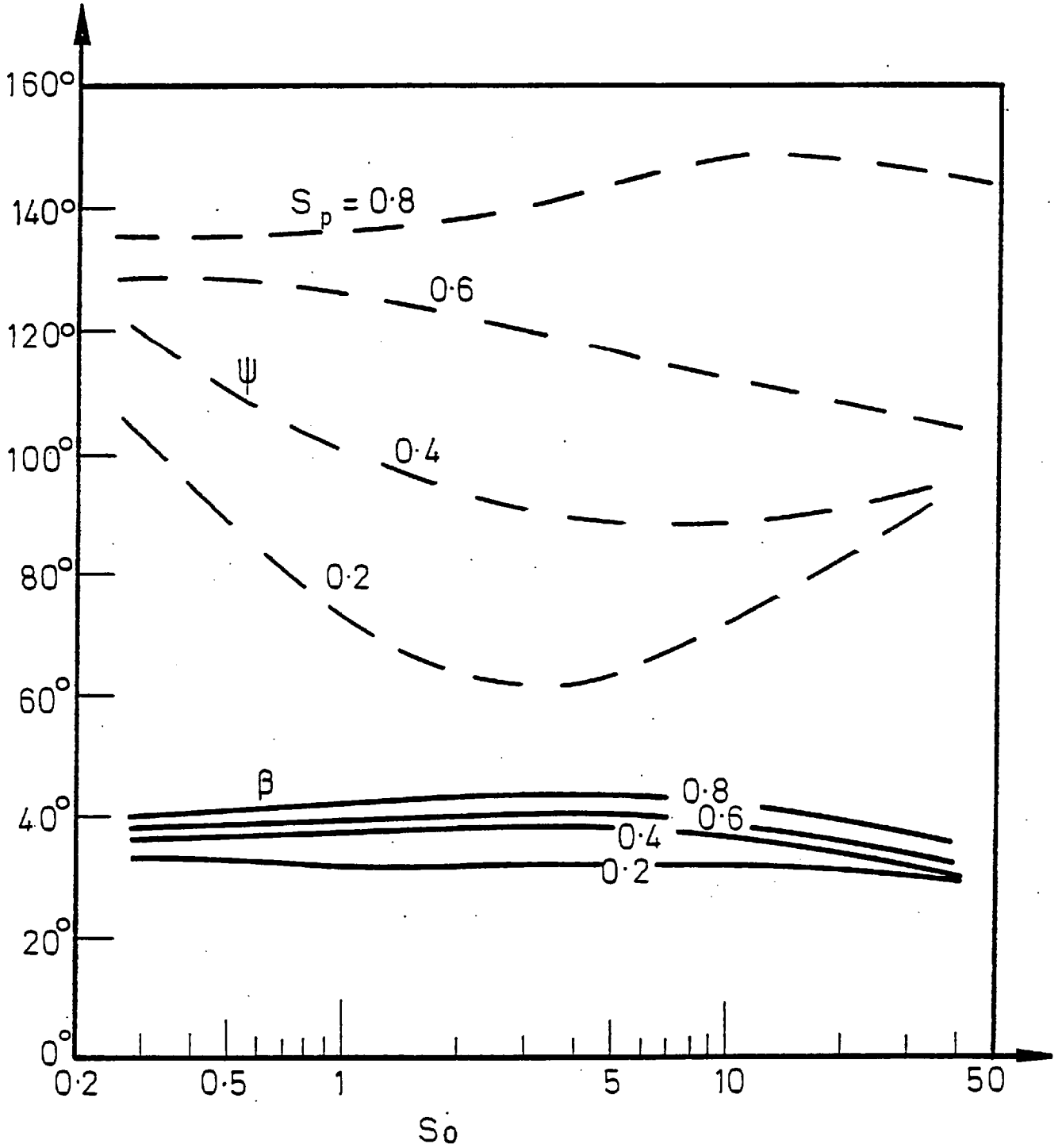
(a) The amplitude of the major semi-axis

Figure 5.30: Experimental and theoretical response of the circumferentially grooved bearing to synchronous excitation



(b) The amplitude of the minor semi-axis

Figure 5.30: Experimental and theoretical response of the circumferentially grooved bearing to synchronous excitation



(c) The theoretical phase angle and angle of inclination

Figure 5.30: Experimental and theoretical response of the circumferentially grooved bearing to synchronous excitation

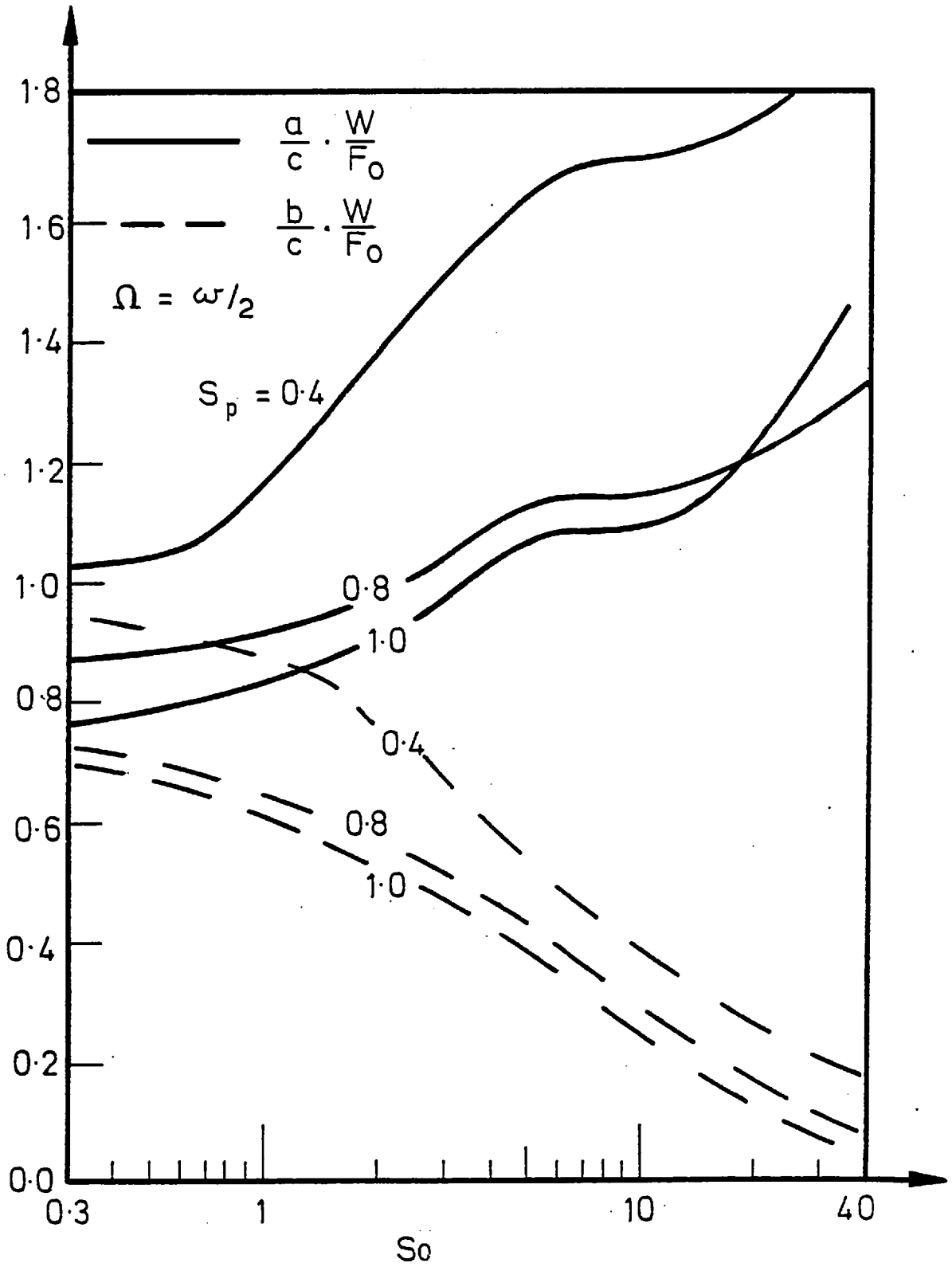
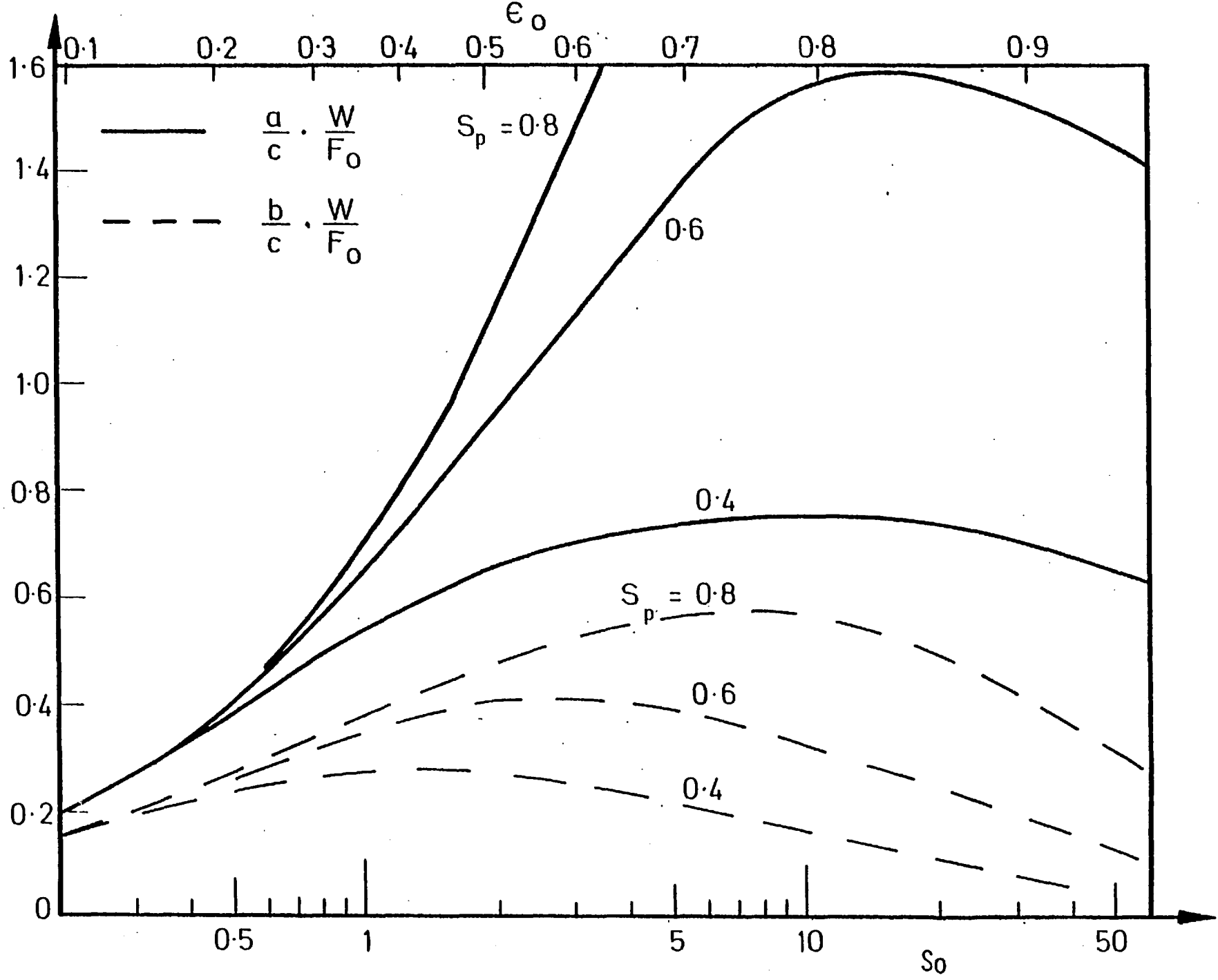
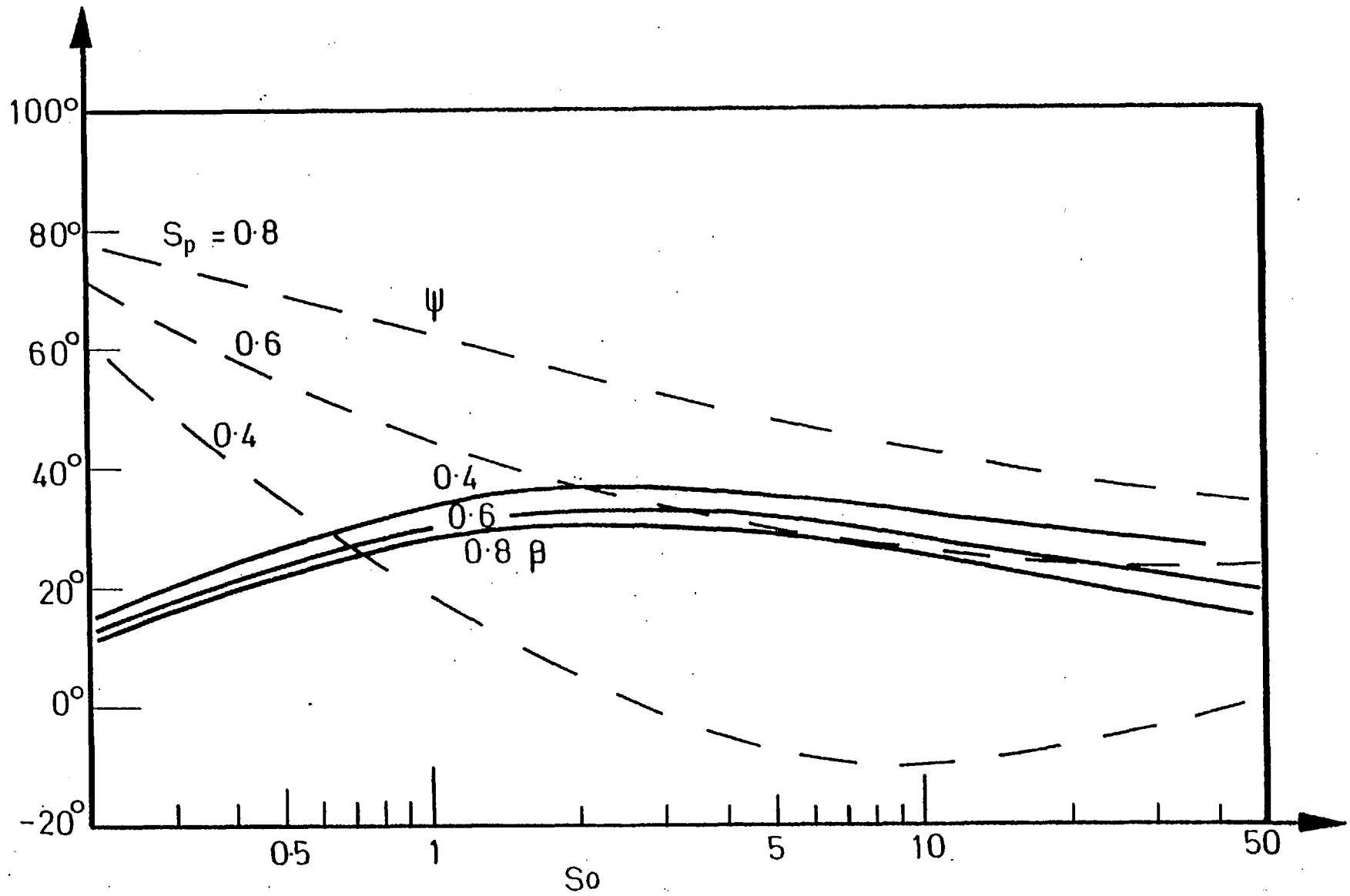


Figure 5.31: The theoretical response of the circumferentially grooved bearing to half-synchronous excitation



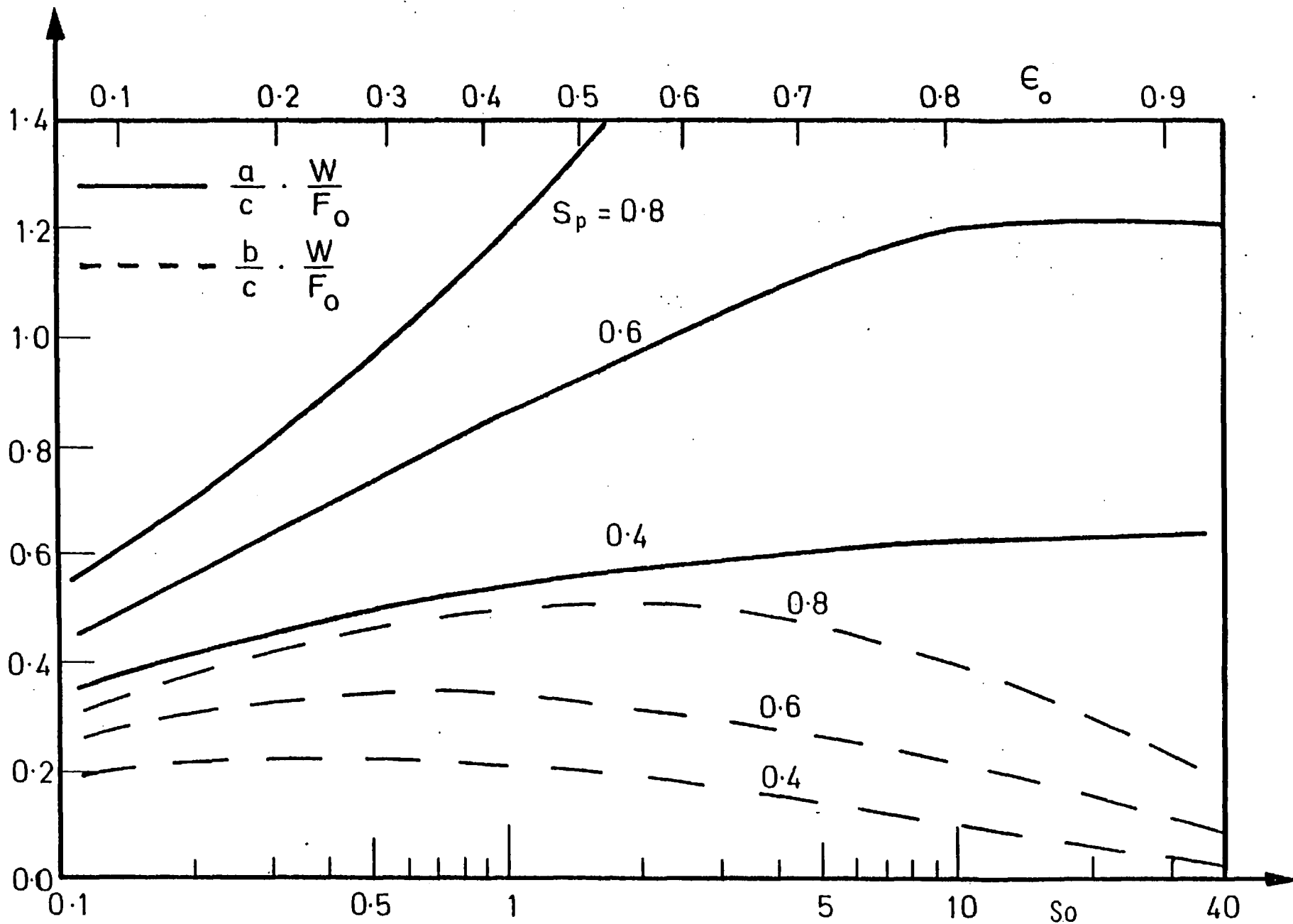
(a) The amplitudes of the major and minor semi-axes

Figure 5.32: The response of the 30° two axial groove bearing to synchronous external excitation



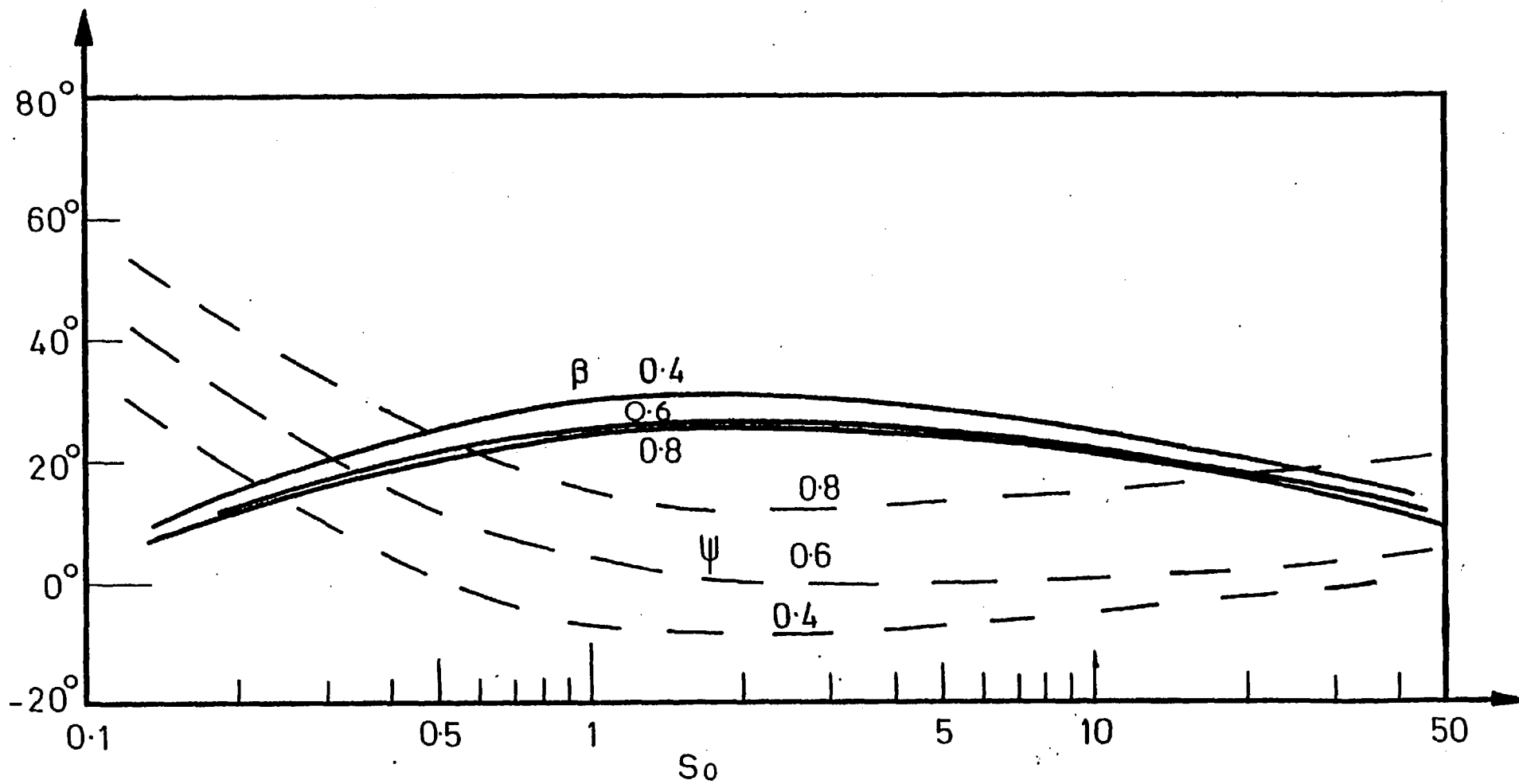
(b) The phase angle and angle of inclination

Figure 5.32 : The response of the 30° two axial groove bearing to synchronous external excitation



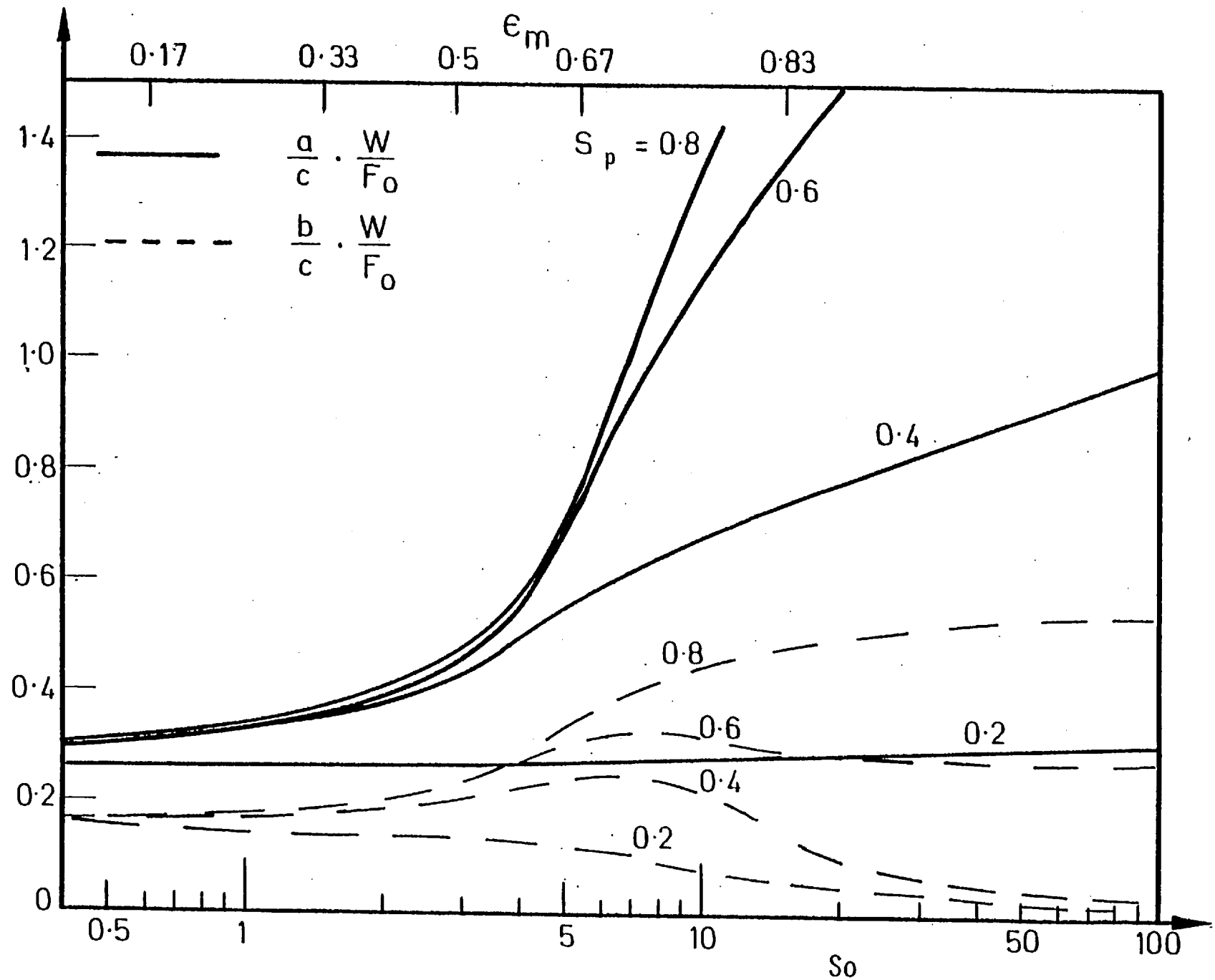
(a) The amplitudes of the major and minor semi-axes

Figure 5.33: The response of the 90° two axial groove angle bearing to synchronous external excitation

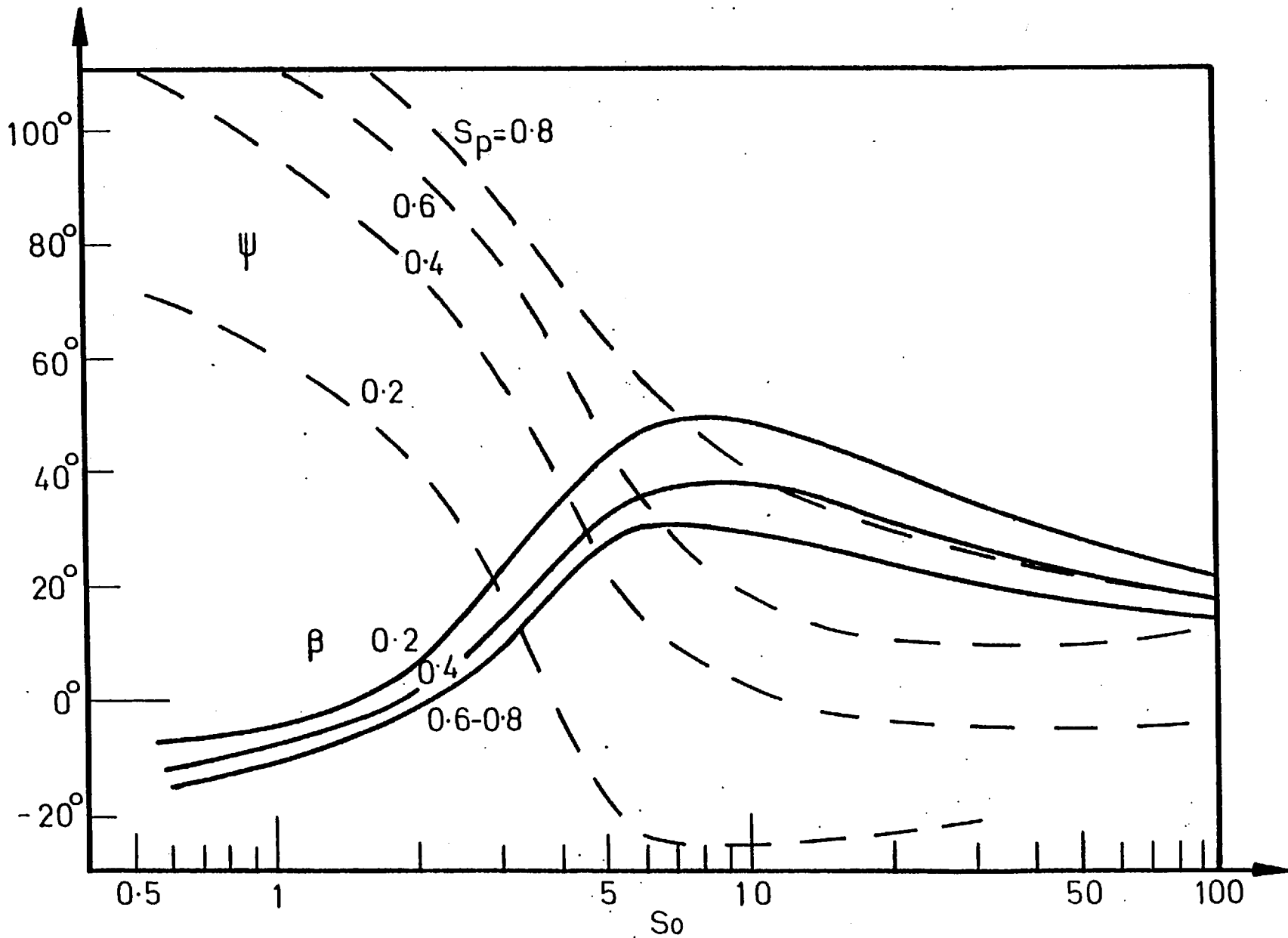


(b) The phase angle and angle of inclination

Figure 5.33: The response of the 90° two axial groove angle bearing to synchronous external excitation

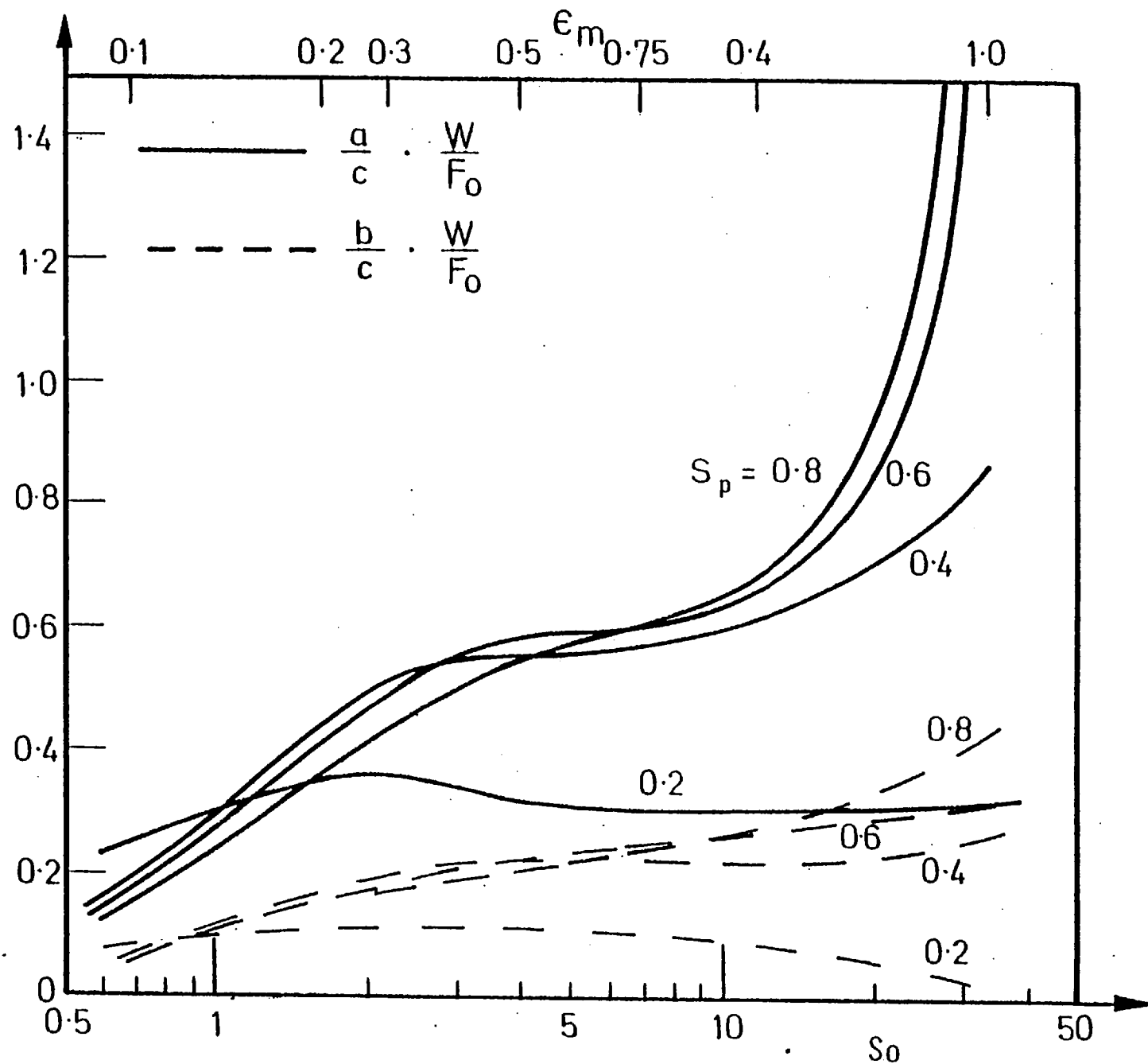


(a) The amplitudes of the major and minor semi-axes
 Figure 5.34: The response of the elliptical bearing with $\delta = 0.4$



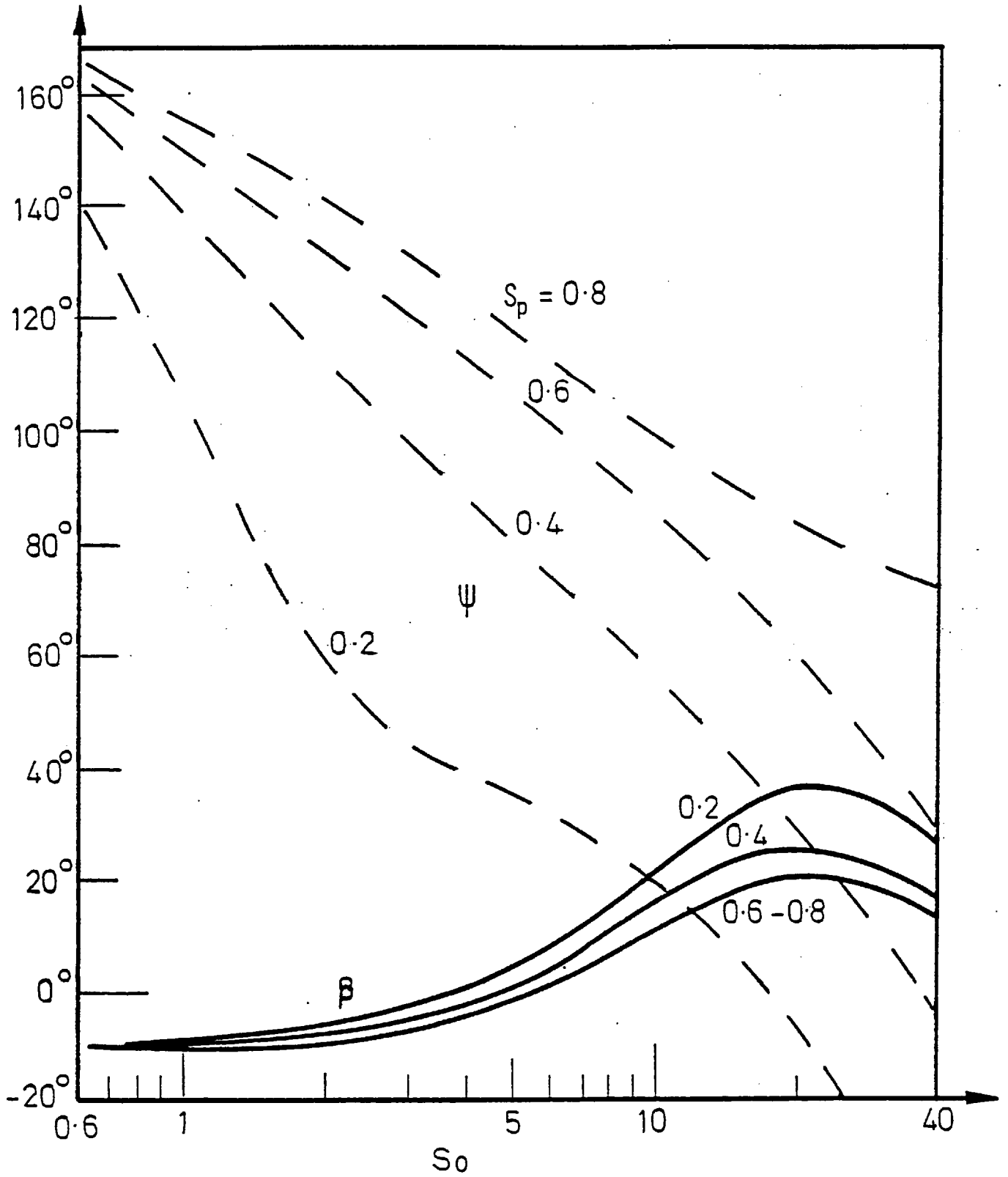
(b) The phase angle and angle of inclination

Figure 5.34: The response of the elliptical bearing with $\delta = 0.4$



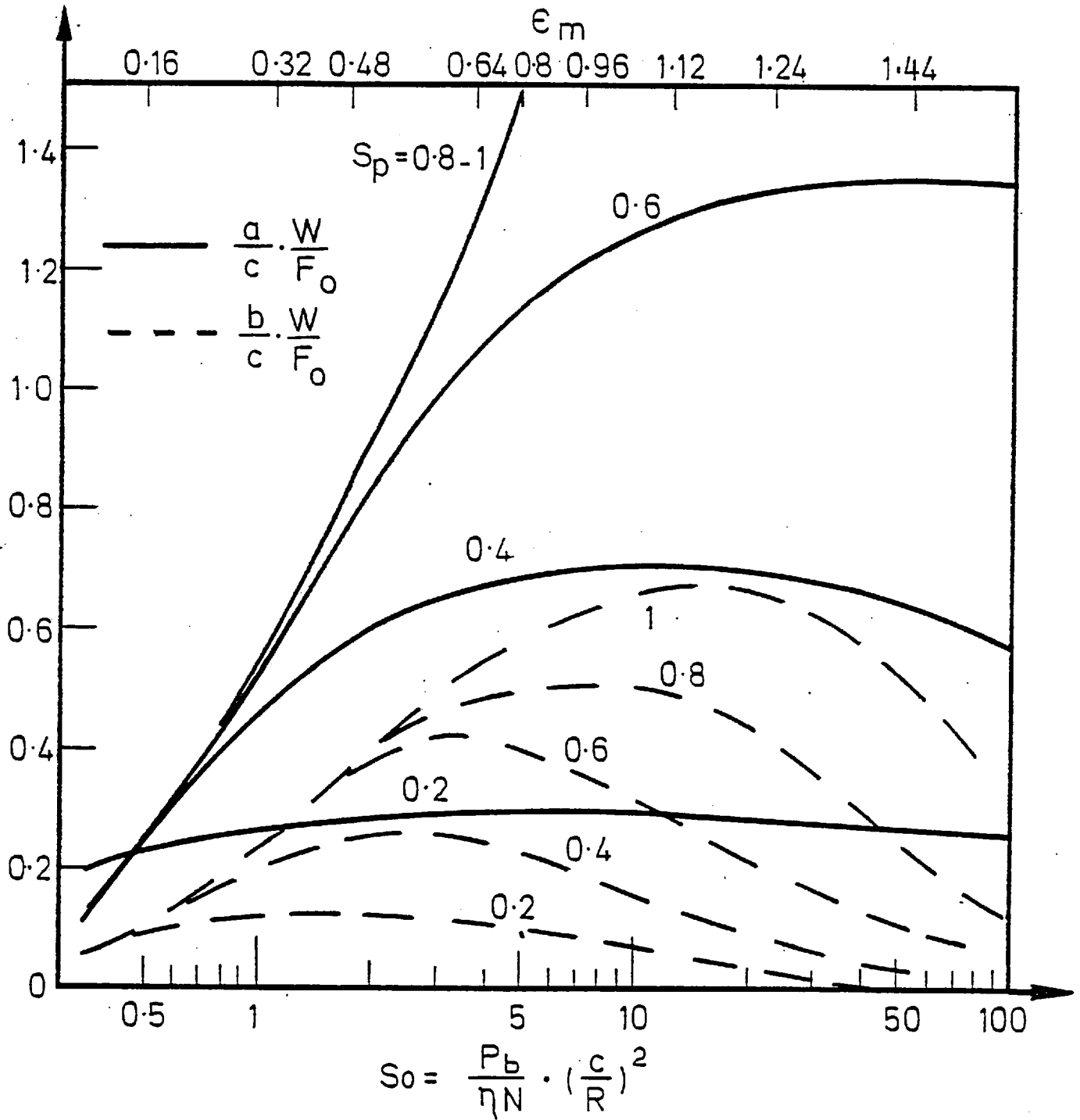
(a) The amplitudes of the major and minor semi-axes

Figure 5.35: The response of the elliptical bearing with $\delta = 0.6$



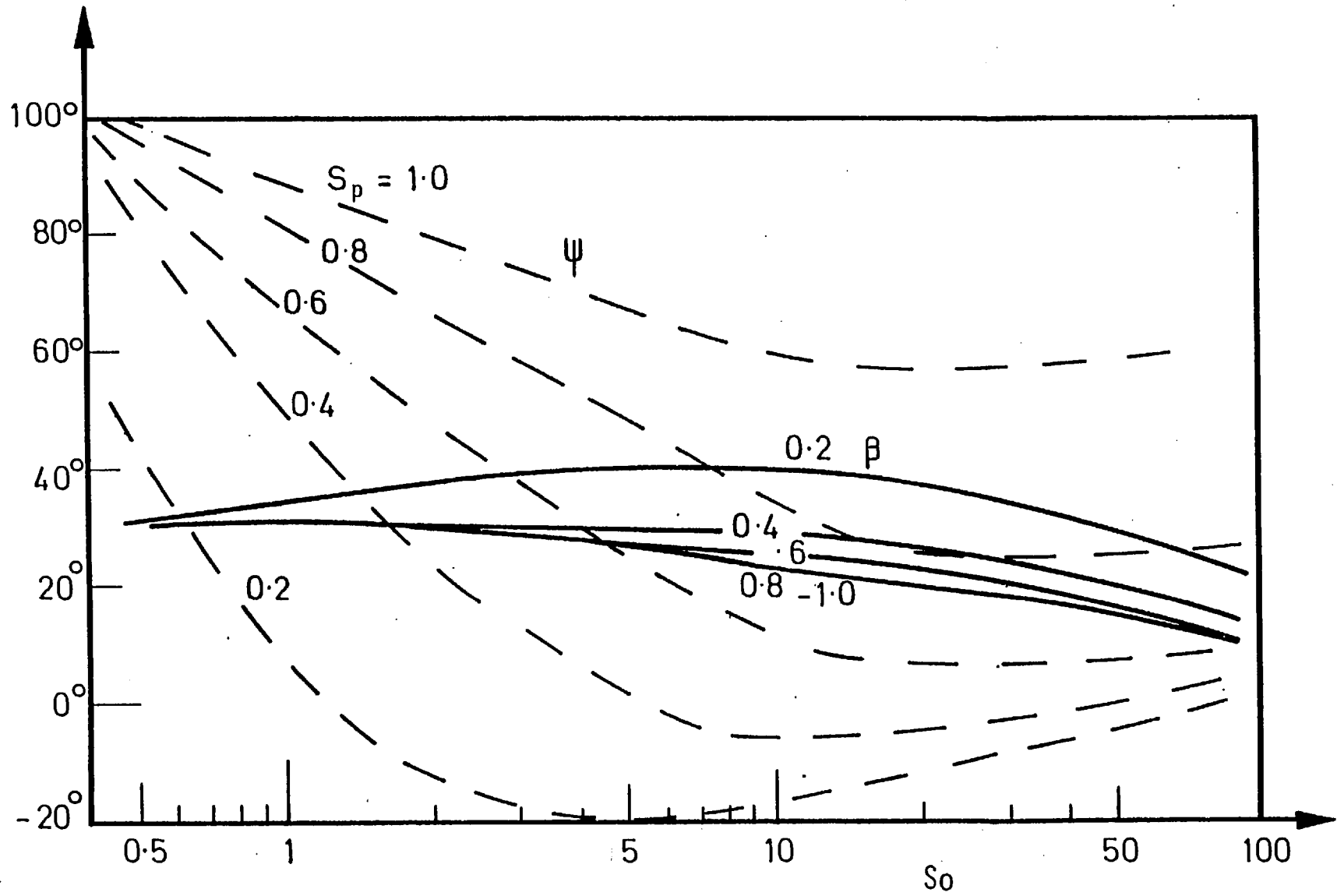
(b) The phase angle and angle of inclination

Figure 5.35: The response of the elliptical bearing with $\delta = 0.6$



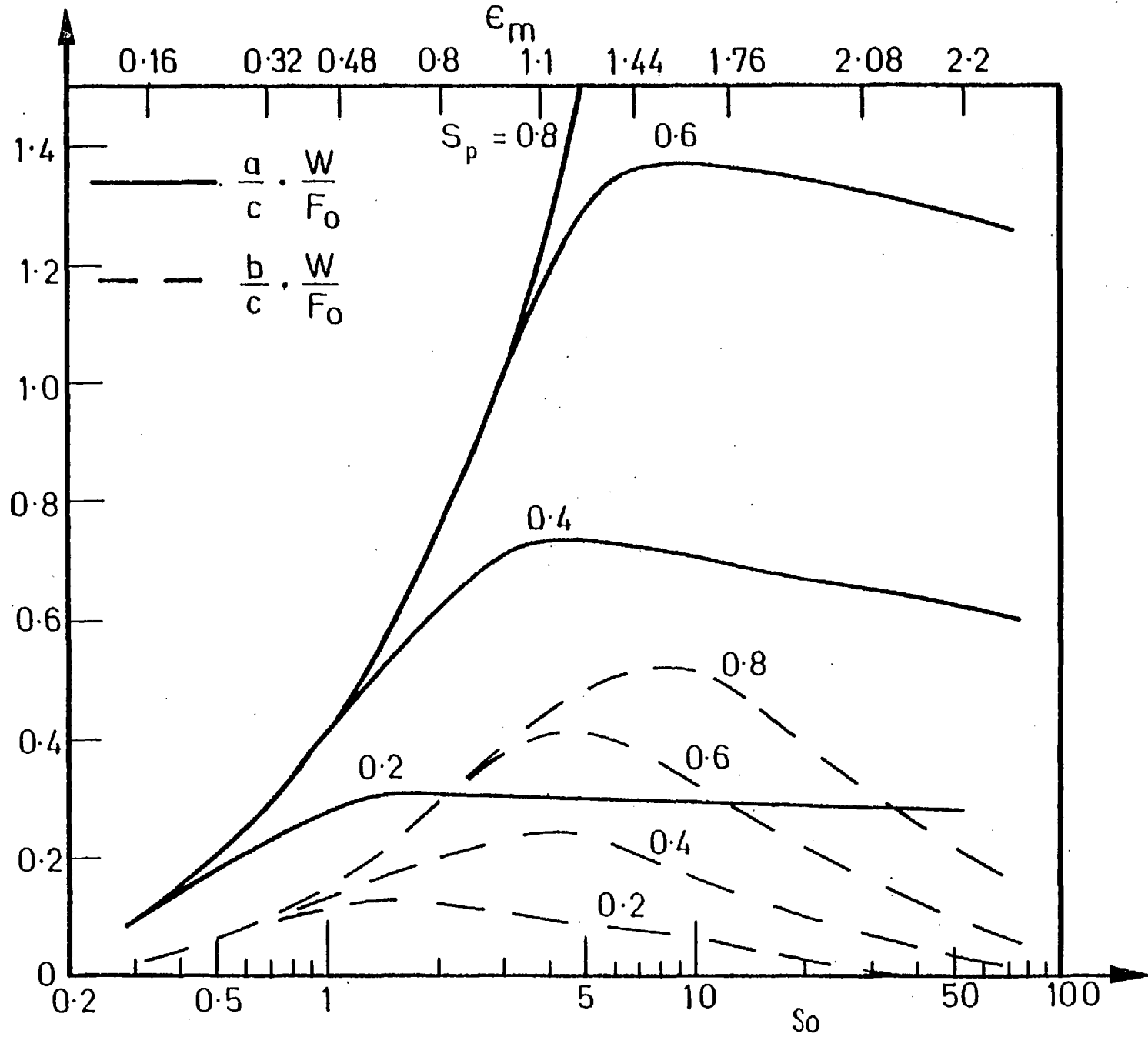
(a) The amplitudes of the major and minor semi-axes

Figure 5.36: The response of the offset halves bearing with $\delta = 0.4$



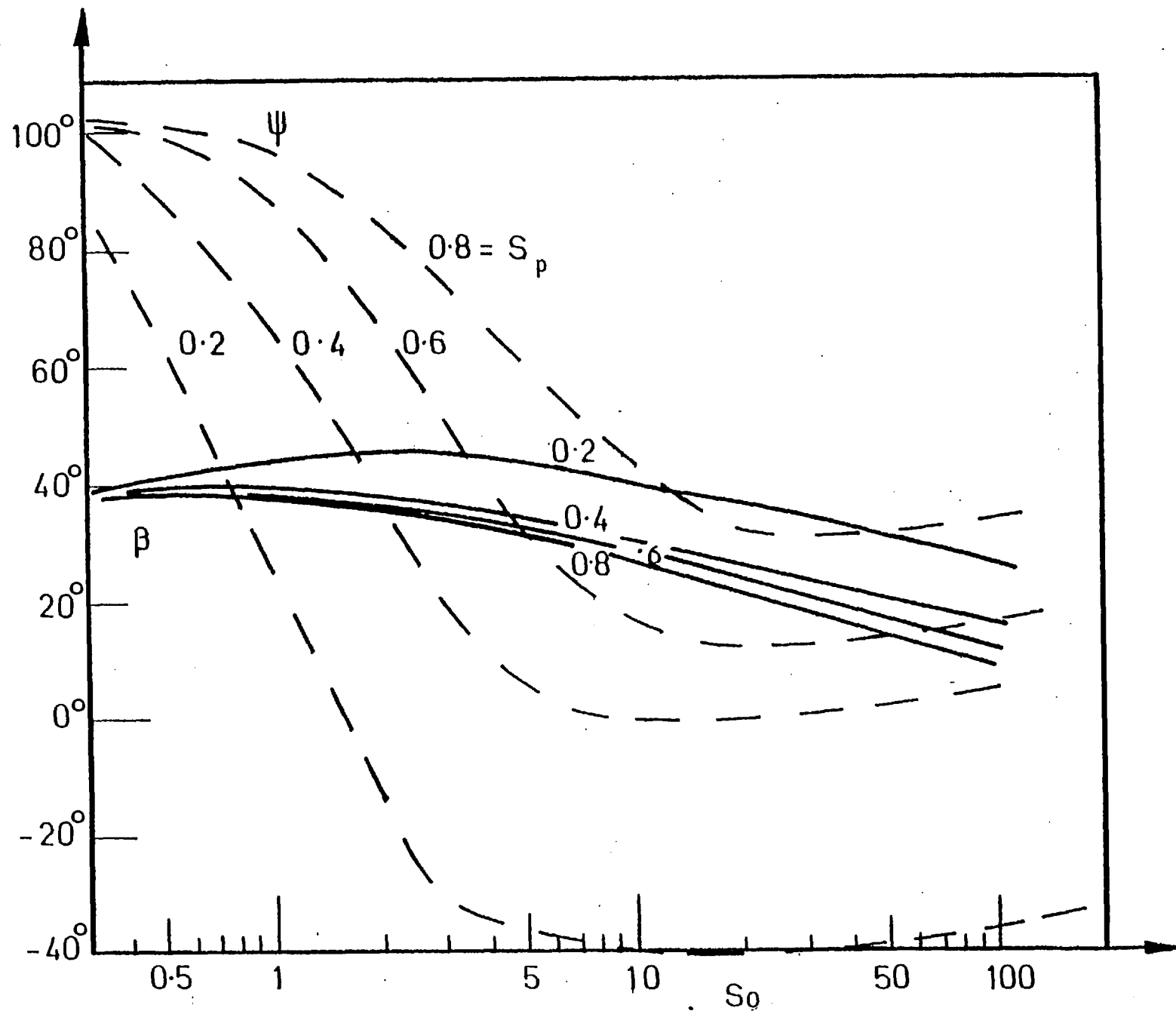
(b) The phase angle and angle of inclination

Figure 5.36: The response of the offset halves bearing with $\delta = 0.4$



(a) The amplitudes of the major and minor semi-axes

Figure 5.37: The response of the offset halves bearing with $\delta = 0.6$



(b) The phase angle and angle of inclination

Figure 5.37: The response of the offset halves bearing with $\delta = 0.6$

Figures 5.34 to 5.37 for the elliptical and offset halves bearings.

Preload decreases the vibration amplitudes of the elliptical bearing at high loads. This is due to its better stability characteristics at high preload and eccentricity.

In the offset halves bearings, preload decreases the vibration amplitudes in the lightly loaded region. This is again due to its better stability characteristics at high preload and low eccentricity.

5.2 CONCLUSIONS

The following conclusions are drawn from the results for the circumferentially grooved bearing and centrally loaded two axial groove bearings:

1. The general validity of the linearised model of the journal bearing system is confirmed experimentally for circular and non-circular bore shaped bearings.
2. The effect of oil feed pressure on the control of film extent and therefore on the stability threshold is shown experimentally for the circumferentially grooved bearing. As the cavitation region decreases due to increasing the feed pressure, the stability of the bearing decreases.
3. Although the non-circular bearings have their shortcomings with regard to the load capacity, they have better stability characteristics than conventional circular bearings.
4. The groove angle has a strong influence on stability. Improvement

in the stability performance and static load capacity can be obtained by decreasing the groove angle.

5. The load capacities of the elliptical and offset halves bearings decrease with increase in the preload.
6. The stability characteristics of these bearings progressively increase with preload.
7. In lightly loaded conditions, the offset halves bearing exhibits the best stability characteristics, while for heavily loaded conditions the best bearing is the elliptical bearing.
8. For the same operating conditions and geometric parameters, the elliptical bearing has higher temperature rise than the offset halves bearing.
9. Under stable operating conditions, the least amount of unbalance vibrations can be obtained with the elliptical bearings in heavily loaded conditions and with the offset halves bearing in lightly loaded conditions.

REFERENCES

- [1] STERNLICHT, B.
"Elastic and damping properties of cylindrical journal bearings",
Trans. ASME, J. Basic Eng., 1959, Vol. 81, No. 1, p. 101.
- [2] HOLMES, R.
"The vibration of a rigid shaft on short sleeve bearings",
J. Mech. Eng. Sci., 1960, Vol. 2, No. 4, p. 337.
- [3] MORRISON, D.
"Influence of plain journal bearings on the whirling action of an elastic rotor",
Proc. Inst. Mech. Engrs., 1962, Vol. 176, No. 22, p. 452.
- [4] LUND, J.W., & THOMSEN, K.K.
"A calculation method and data for the dynamic coefficients of oil-lubricated journal bearings",
Topics in Fluid Film Bearing and Rotor Bearing System Design and Optimisation, presented at the ASME Design Engineering Conference and Shows, Illinois, April 1978, p. 245.
- [5] LUND, J.W., & ORCUTT, F.K.
"Calculations and experiments on the unbalance response of a flexible rotor",
Trans. ASME, J. Eng. Ind., 1967, Vol. 89, p. 785.
- [6] HOLMES, R.
"Oil whirl characteristics of a rigid rotor in 360° journal bearings",
Proc. Inst. Mech. Engrs., 1963, Vol. 177, No. 11, p. 291.
- [7] KIRK, R.G., & GUNTER, E.J.
"Transient journal bearing analysis",
NASA CR-1549, June 1970.

- [8] BADGLEY, R.H., & BOOKER, J.F.
"Rigid-body rotor dynamics: Dynamic unbalance and lubricant temperature changes",
ASME Paper No. 69-Lub-14, October 1969.
- [9] SMITH, D.M.
Journal Bearings in Turbomachinery,
Chapman & Hall Limited, London, 1969.
- [10] MITCHELL, J.R., HOLMES, R., & VAN BALLYGOOYEN, H.
"Experimental determination of a bearing oil-film stiffness",
Proc. Inst. Mech. Engrs., 1965-66, Vol. 180 (3K), p. 90.
- [11] GLIENICKE, J.
"Experimental investigation of the stiffness and damping coefficients of turbine bearings and their application to instability prediction",
Proc. Inst. Mech. Engrs., 1966-67, Vol. 181 (3B), p. 116.
- [12] MORTON, P.G.
"Measurements of the dynamic characteristics of large sleeve bearings",
Trans. ASME, J. Lub. Tech., 1971, Vol. 93, p. 143.
- [13] WOODCOCK, J.S., & HOLMES, R.
"The determination of the dynamic properties of a turbo-rotor bearing oil-film",
Proc. Inst. Mech. Engrs., 1969-70, Vol. 184 (3L), p. 111.
- [14] MORTON, P.G.
"The derivation of bearing characteristics by means of transient excitation applied directly to a rotating shaft",
IUTAM Symp., Dynamics of Rotors, Lyngby, Denmark.
- [15] IWATSUBO, T.
"Error analysis of vibration of rotor-bearing system",
Conf. on Vibrations in Rotating Machinery, I.Mech.E., September 1976,
p. 87.

- [16] PINKUS, O.
"Analysis of elliptical bearings",
Trans. ASME, 1956, Vol. 78, p. 965.
- [17] PINKUS, O.
"Power losses in elliptical and three-lobe bearings",
Trans. ASME, 1956, Vol. 78, p. 899.
- [18] PINKUS, O.
"Experimental investigation of resonant whip",
Trans. ASME, 1956, Vol. 78, p. 975.
- [19] PINKUS, O.
"Analysis of journal bearings with arbitrary load vector",
Trans. ASME, 1957, Vol. 79, p. 1213.
- [20] PINKUS, O.
"Analysis and characteristics of the three-lobe bearings",
Trans. ASME, J. Basic Eng., 1959, Vol. 81, p. 49.
- [21] PINKUS, O., & STERNLICHT, B.
Theory of Hydrodynamic Lubrication,
McGraw-Hill, New York, 1961.
- [22] WILCOCK, D.F.
"Orthogonally displaced bearings - 1",
Trans. ASLE, 1961, Vol. 4, p. 117.
- [23] FALKENHAGEN, G.L., GUNTER, E.J., & SCHULLER, F.T.
"Stability and transient motion of a vertical three-lobe bearing
system",
Trans. ASME, J. Eng. Ind., 1972, Vol. 99, p. 665.
- [24] AKKOK, M., & ETTLES, C.
"The effect of grooving and bore shape on the stability of journal
bearings",
ASLE Paper No. 79-AM-6D-3, 1979.

- [25] LI, D.F., CHOY, K.C., & ALLAIRE, P.E.
"Stability and transient characteristics of four multilobe journal bearing configurations",
ASME Paper No. 79-Lub-3, 1979.
- [26] ALLAIRE, P.E., LI, D.F., & CHOY, K.C.
"Transient unbalance response of four multilobe journal bearings",
ASME Paper No. 79-Lub-26, 1979.
- [27] BARRETT, L.E., ALLAIRE, P.E., & GUNTER, E.J.
"Stability and dynamic response of pressurised journal bearings with nuclear water pump application",
Ann. Nucl. Eng., 1977, Vol. 4, No. 2, p. 115.
- [28] OLSSON, K.
"Cavitation in dynamically loaded bearings",
Trans. Chalmers University of Technology, Gothenburg, Sweden, No. 308, 1965.
- [29] KARL, T.E.
"An experimental investigation of a cylindrical journal bearing under constant and sinusoidal loading",
Proc. Inst. Mech. Engrs., 1963-64, Vol. 78 (3N), p. 100.
- [30] MALCHER, L.
"Einfluss der Ölfilmtemperatur und anderer Lagerparameter auf das statische und dynamische Verhalten von Turbinengleitlagern",
MTZ, 1974, Vol. 35, No. 6, p. 171.
- [31] NICOLAJSEN, J.L.
"The influence of variable viscosity on the stability of plain journal bearings and floating ring journal bearings",
Trans. ASME, J. Lub. Tech., 1973, Vol. 95, p. 447.

[32] HAHN, E.J.

"The excitability of flexible rotors in short sleeve bearings",
Trans. ASME, J. Lub. Tech., 1975, Vol. 97, p. 105.

APPENDIX A

GEOMETRY OF THE NON-CIRCULAR TEST BEARINGS

A.1 ELLIPTICAL BEARING

Although it is usually called the elliptical bearing, the cross-section is actually not elliptical, but is made up of two circular arcs with the same clearance, c . Their centre of curvature O_1 and O_2 , each displaced a distance, d , normal to the split surface. The preload, d , is defined as the ellipticity of the bearing. It is clear from Figure A.1 that for any given journal position, J , the eccentricities e_1 and e_2 and the attitude angles ϕ_1 and ϕ_2 of the two lobes will be different. Various geometric parameters can be mathematically related as follows.

For the lower lobe:

$$e_1 = [e^2 + d^2 - 2e d \cos (\pi - \phi)]^{\frac{1}{2}} = [e^2 + d^2 + 2e d \cos \phi]^{\frac{1}{2}}$$

and:
$$\phi_1 = \sin^{-1} \left(\frac{e \sin \phi}{e_1} \right)$$

where e is the eccentricity and ϕ is the attitude angle of the bearing.

Non-dimensionalising the above equations by the arc clearance, c , gives:

$$\varepsilon_1 = [\varepsilon^2 + \delta^2 + 2\varepsilon \delta \cos \phi]^{\frac{1}{2}}$$

and:
$$\phi_1 = \sin^{-1} \left(\frac{\varepsilon \sin \phi}{\varepsilon_1} \right)$$

The film thickness, h , for the lower lobe is given by:

$$h_1 = c + e_1 \cos \theta_1$$

where θ_1 is the coordinate measured from the line of centres along the bearing arc in the direction of rotation. Dividing the equation by the arc clearance, c , gives:

$$H_1 = 1 + \varepsilon_1 \cos \theta_1$$

Similarly, for the upper lobe:

$$\varepsilon_2 = [\varepsilon^2 + \delta^2 - 2\varepsilon \delta \cos \phi]^{\frac{1}{2}}$$

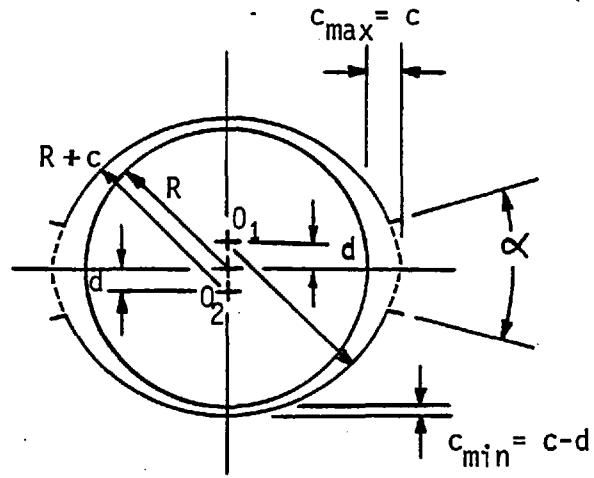
and:
$$\phi_2 = \pi - \sin^{-1} \left(\frac{\varepsilon \sin \phi}{\varepsilon_2} \right)$$

and:
$$H_2 = 1 + \varepsilon_2 \cos \theta_2$$

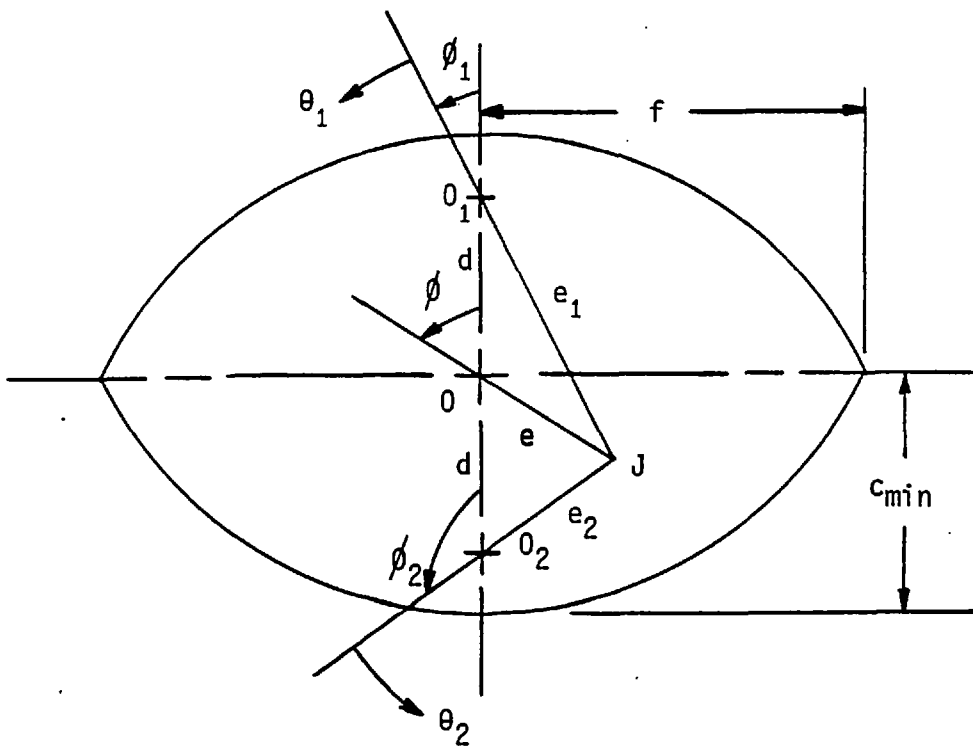
It should be noted that because of the preload in the bearing, there are two clearances in an elliptical bearing, the minimum and maximum values, as shown in Figure A.1(a). However, the journal movement is bounded in the maximum clearance direction by the circular arcs, while the centre, J , is on the split line (i.e. $\phi = \pi/2$). Therefore, $\overline{O_1 J} = \overline{O_2 J} = c$, then the maximum movement of the journal is:

$$\overline{OJ} = [\overline{O_1 J}^2 - \overline{OO_1}^2]^{\frac{1}{2}}$$

or:
$$f = [c^2 - d^2]^{\frac{1}{2}}$$



(a) Elliptical bearing



(b) Clearance shape and lobe centre geometry

Figure A.1: Elliptical bearing geometry

A.2 OFFSET HALVES BEARING

This type of bearing is obtained by the disposition of the arc centres of a two-lobe bearing orthogonally to the load line in the opposite direction. Figure A.2 shows the two circular arcs with the same clearance, c , are displaced an amount d from the geometric centre of the bearing. For any given journal position, J , the eccentricities e_1 and e_2 and the attitude angles ϕ_1 and ϕ_2 of the two lobes are determined from Figure A.2(b) as follows.

For the lower lobe:

$$e_1 = [e^2 + d^2 - 2e d \cos (\frac{\pi}{2} + \phi)]^{\frac{1}{2}}$$

and:
$$\phi_1 = \frac{\pi}{2} - \sin^{-1} \left[\frac{e \sin ((\pi/2) + \phi)}{e_1} \right]$$

where e and ϕ are the eccentricity and the attitude angle of the bearing, respectively. Non-dimensionalising by the arc clearance, c , gives:

$$\epsilon_1 = [\epsilon^2 + \delta^2 - 2\epsilon \delta \cos (\frac{\pi}{2} + \phi)]^{\frac{1}{2}}$$

and:
$$\phi_1 = \frac{\pi}{2} - \sin^{-1} \left[\frac{\epsilon \sin ((\pi/2) + \phi)}{\epsilon_1} \right]$$

Similarly, for the upper lobe:

$$\epsilon_2 = [\epsilon^2 + \delta^2 - 2\epsilon \delta \cos (\frac{\pi}{2} - \phi)]^{\frac{1}{2}}$$

and:
$$\phi_2 = - \left[\frac{\pi}{2} - \sin^{-1} \left(\frac{\epsilon \sin ((\pi/2) - \phi)}{\epsilon_2} \right) \right]$$

And the non-dimensional film thicknesses are:

$$H_1 = 1 + \varepsilon_1 \cos \theta_1$$

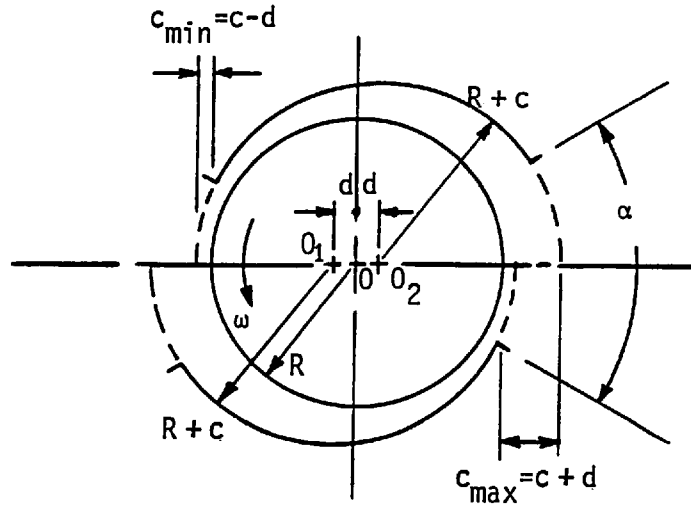
$$H_2 = 1 + \varepsilon_2 \cos \theta_2$$

where θ_1 and θ_2 are the coordinates measured from the lines of centres in the direction of rotation along the lower and upper arcs, respectively.

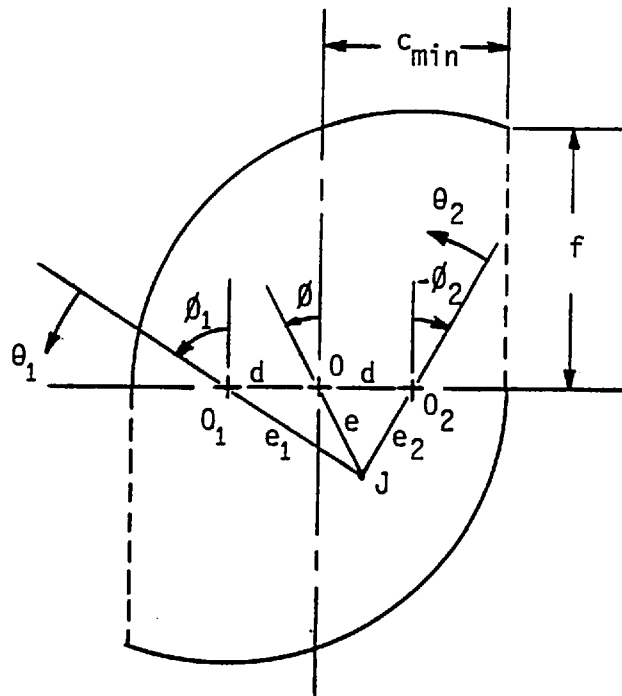
It should be noted that offset halves bearing is not symmetric about any axial plane; therefore, the direction of rotation is to be specified for the given disposition of the halves. In Figure A.2, the direction of rotation is in the counter-clockwise direction.

If the preload, δ , is less than 0.5, the maximum journal movement is equal to the arc clearance and, if it is greater than 0.5, the maximum journal movement is bounded by the circular arc of the lobe and the vertical line drawn from the edge of the other lobe. Figure A.2(b) shows the free clearance space of the bearing within which the journal is able to move without being in contact with the bearing surface. From the geometry of the clearance shape:

$$f = [c^2 - c_{min}^2]^{\frac{1}{2}} = [2c d - d^2]^{\frac{1}{2}}$$



(a) Offset halves bearing



(b) Clearance shape and lobe centre geometry

Figure A.2: Offset halves bearing geometry

APPENDIX B

ANALYTICAL DESCRIPTION OF AN ELLIPTICAL ORBIT

An elliptical whirl orbit, in general, can be expressed in terms of complex variables as:

$$X = \operatorname{Re} \{ \bar{X} e^{i(T - \bar{\phi}_X)} \} = \operatorname{Re} \{ (X_c - iX_s) e^{iT} \}$$

$$Y = \operatorname{Re} \{ \bar{Y} e^{i(T - \bar{\phi}_Y)} \} = \operatorname{Re} \{ (Y_c - iY_s) e^{iT} \}$$

or in terms of real variables as:

$$X = \bar{X} \cos (T - \bar{\phi}_X) = X_s \sin T + X_c \cos T$$

$$Y = \bar{Y} \cos (T - \bar{\phi}_Y) = Y_s \sin T + Y_c \cos T$$

(B.1)

where:

$$\bar{X} = (X_c^2 + X_s^2)^{\frac{1}{2}}$$

$$\bar{Y} = (Y_c^2 + Y_s^2)^{\frac{1}{2}}$$

$$\bar{\phi}_X = \tan^{-1} \left(\frac{X_s}{X_c} \right)$$

$$\bar{\phi}_Y = \tan^{-1} \left(\frac{Y_s}{Y_c} \right)$$

If the X-Y coordinate is rotated such that it coincides with the major and minor semi-axes of the ellipse, as in Figure B.1, then the motion can be expressed as:

$$X' = A \cos (T + \psi)$$

$$Y' = B \sin (T + \psi)$$

(B.2)

where A and B are non-dimensional major and minor semi-axes, respectively, and ψ is the phase angle between the exciting force and the major semi-axis.

If β is the angle between the major semi-axis and the X axis, then using the following transformation equations:

$$\begin{bmatrix} X' \\ Y' \end{bmatrix} = \begin{bmatrix} \cos \beta & \sin \beta \\ -\sin \beta & \cos \beta \end{bmatrix} \begin{bmatrix} X \\ Y \end{bmatrix}$$

and equating the coefficients of $\sin T$ and $\cos T$ terms by the use of equations (B.1) and (B.2) gives:

$$A \cos \psi = X_c \cos \beta + Y_c \sin \beta \quad (\text{B.3a})$$

$$-A \sin \psi = X_s \cos \beta + Y_s \sin \beta \quad (\text{B.3b})$$

$$B \sin \psi = -X_c \sin \beta + Y_c \cos \beta \quad (\text{B.3c})$$

$$B \cos \psi = -X_s \sin \beta + Y_s \cos \beta \quad (\text{B.3d})$$

Eliminating ψ and β between the equations in two ways gives:

$$A^2 + B^2 = X_c^2 + Y_c^2 + X_s^2 + Y_s^2 \quad (\text{B.4})$$

and:
$$(A+B)^2 = (X_c + Y_s)^2 + (Y_c - X_s)^2 \quad (\text{B.5})$$

From equations (B.4) and (B.5), one can deduce that:

$$B = \frac{X_c Y_s - Y_c X_s}{A} \quad (\text{B.6})$$

Substituting equation (B.6) into equation (B.4) gives:

$$A^4 - (X_c^2 + X_s^2 + Y_c^2 + Y_s^2) A^2 + (X_c Y_s - Y_c X_s)^2 = 0$$

then:

$$A = \left\{ \frac{1}{2}(X_c^2 + X_s^2 + Y_c^2 + Y_s^2) + \sqrt{\frac{1}{4}(X_c^2 + X_s^2 + Y_c^2 + Y_s^2)^2 - (X_c Y_s - Y_c X_s)^2} \right\}^{\frac{1}{2}}$$

The attitude angle of the elliptical orbit, β , can be obtained by eliminating A and B and ψ between the equations (B.3) and gives:

$$\beta = \frac{1}{2} \tan^{-1} \left[\frac{2 (X_c Y_c + X_s Y_s)}{X_c^2 + X_s^2 - (Y_s^2 + Y_c^2)} \right]$$

Then, the phase angle between the excitation force and the major semi-axis can be solved by using any one of equations (B.3).

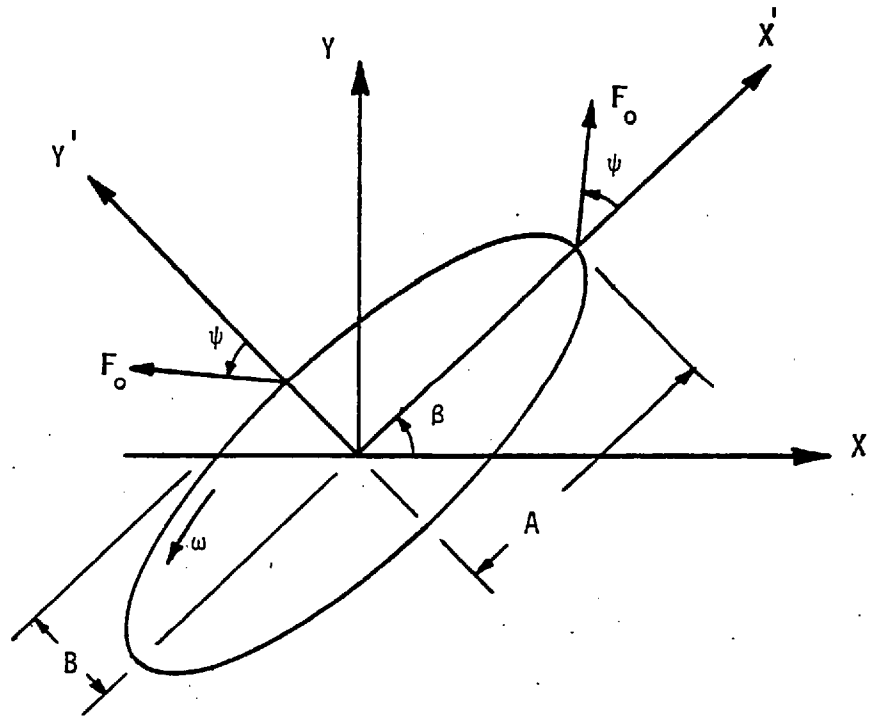


Figure B.1: Dynamic load orbit

APPENDIX C

THE INCREMENTAL LOADING METHOD

The stiffness coefficients of an oil film are calculated from the experimentally determined influence coefficients as follows.

Consider the static load locus of a journal as shown in Figure C.1. If the point J_1 represents the static position of the journal centre due to the application of a vertical static load, W . When an extra incremental load, Δf_x , is added in the x -direction, let the journal centre move to the new static position, J_2 , as shown in Figure C.1(a).

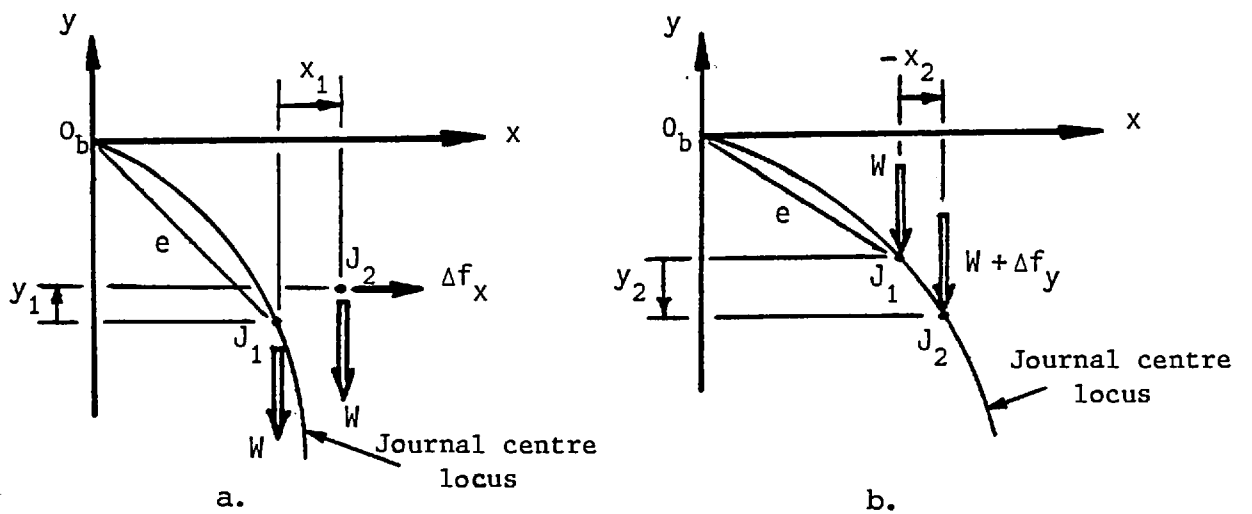


Figure C.1: Method of determining the stiffness coefficients

The influence coefficients, r_{xx} and r_{yx} , are given by:

$$r_{xx} = \frac{x_1}{\Delta f_x}, \quad r_{yx} = \frac{y_1}{\Delta f_x}$$

Similarly, upon the application of a static load, Δf_y , in the y -direction, as shown in Figure C.1(b), gives:

$$r_{yy} = \frac{y_2}{\Delta f_y}, \quad r_{xy} = \frac{x_2}{\Delta f_y}$$

If Δf_x and Δf_y are now applied simultaneously, then the total displacements are:

$$\left. \begin{aligned} x &= x_1 + x_2 = \Delta f_x r_{xx} + \Delta f_y r_{xy} \\ y &= y_1 + y_2 = \Delta f_x r_{yx} + \Delta f_y r_{yy} \end{aligned} \right\} \quad (C.1)$$

Equation (C.1) can be inverted to give:

$$\begin{vmatrix} \Delta f_x \\ \Delta f_y \end{vmatrix} = \frac{1}{\text{Det } [r_{ij}]} \begin{bmatrix} r_{yy} & -r_{xy} \\ -r_{yx} & r_{xx} \end{bmatrix} \begin{vmatrix} x \\ y \end{vmatrix} \quad (C.2)$$

where $\text{Det } [r_{ij}] = r_{xx} r_{yy} - r_{xy} r_{yx}$.

The oil film forces are defined in terms of stiffness coefficients as in equation (C.2):

$$\begin{vmatrix} \Delta f_x \\ \Delta f_y \end{vmatrix} = \begin{bmatrix} k_{xx} & k_{xy} \\ k_{yx} & k_{yy} \end{bmatrix} \begin{vmatrix} x \\ y \end{vmatrix} \quad (C.3)$$

From equations (C.2) and (C.3), one can deduce that the stiffness coefficients are:

$$\begin{bmatrix} k_{xx} & k_{xy} \\ k_{yx} & k_{yy} \end{bmatrix} = \frac{1}{r_{xx} r_{yy} - r_{xy} r_{yx}} \begin{bmatrix} r_{yy} & -r_{xy} \\ -r_{yx} & r_{xx} \end{bmatrix}$$

APPENDIX D

THE STABILITY THRESHOLD CONDITION

Substituting equation (3.11) into equation (3.10) gives the following system of equations:

$$\begin{bmatrix} \lambda^2 + S_p (\lambda C_{XX} + K_{XX}) & S_p (\lambda C_{XY} + K_{XY}) \\ S_p (\lambda C_{YX} + K_{YX}) & \lambda^2 + S_p (\lambda C_{YY} + K_{YY}) \end{bmatrix} \begin{bmatrix} X_0 \\ Y_0 \end{bmatrix} = \begin{bmatrix} 0 \\ 0 \end{bmatrix}$$

For a non-trivial solution to exist, the characteristic determinant must vanish. Thus, for a rigid journal bearing system, the characteristic equation is a polynomial of the order four with respect to λ :

$$\lambda^4 + A_1 \lambda^3 + A_2 \lambda^2 + A_3 \lambda + A_4 = 0 \quad (D.1)$$

where:

$$\begin{aligned} A_1 &= S_p a_1 = S_p (C_{XX} + C_{YY}) \\ A_{21} &= S_p a_{21} = S_p (K_{XX} + K_{YY}) \\ A_{22} &= S_p^2 a_{22} = S_p^2 (C_{XX} C_{YY} - C_{XY} C_{YX}) \\ A_2 &= A_{21} + A_{22} \\ A_3 &= S_p^2 a_3 = S_p^2 [K_{XX} C_{YY} + C_{XX} K_{YY} - K_{XY} C_{YX} - K_{YX} C_{XY}] \\ A_4 &= S_p^2 a_4 = S_p^2 [K_{XX} K_{YY} - K_{XY} K_{YX}] \end{aligned} \quad (D.2)$$

The eigenvalues of the characteristic equation (D.1) can be expressed as:

$$\lambda_k = \sigma_k + i \nu_k$$

where σ_k is the real part of the λ_k and denoted as the growth ($\sigma_k > 0$) or decay ($\sigma_k < 0$) factor; and

ν_k is the imaginary part of λ_k and denoted as the damped natural frequency of the system.

The condition for stability is that the real part must have a negative value. The instability threshold is defined to be the condition at which the growth factor is zero. Then, by substituting $\lambda = i \nu_0$ into equation (D.1), where ν_0 is the instability threshold frequency, gives:

$$\nu_0^4 - i A_1 \nu_0^3 - A_2 \nu_0^2 + i A_3 \nu_0 + A_4 = 0 \quad (D.3)$$

In order that the above equation is satisfied, the real and imaginary parts must vanish. By considering the imaginary part to be zero, one gets:

$$\nu_0^2 = \frac{A_3}{A_1} = \frac{a_3}{a_1} S_p \quad (D.4)$$

which is known as the whirl frequency ratio, and by equating the real part to zero and substituting equation (D.4) gives:

$$\left(\frac{A_3}{A_1}\right)^2 - A_2 \frac{A_3}{A_1} + A_4 = 0$$

Substituting the coefficients from equations (D.2) and solving for the stability parameter gives:

$$S_p = \left[\frac{a_3^2 + a_1^2 a_4}{a_1 a_3} - a_{21} \right] / a_{22} \quad (D.5)$$

This is the stability threshold parameter at which the journal becomes unstable at the particular equilibrium eccentricity.

The system behaviour above the stability borderline may be investigated from the behaviour of the roots of the characteristic equation. For a given stability parameter above the threshold value, the characteristic equation (D.1) has, in general, two negative real roots and a pair of complex roots. As S_p approaches the threshold value, two negative roots change into a pair of complex roots, whose real part is a negative value. The other pair of roots, whose imaginary part is slightly less than 0.5, and that real part of it changes from a negative to a positive value on the stability borderline. Therefore, this mode of natural vibration becomes self-excited at the threshold.

COMPUTER PROGRAM

```
COMMON SXX, SXY, SYX, SYY, CXX, CXY, CYX, CYY, XD, YD, DX1, DY1, FR, SP, F0WC
COMMON FX(3,3,3), FY(3,3,3), H(80), EB, DE, LG(80,11), JG, KG, REC, F, PI1
COMMON YLD, DT, DY, JT, KT, FI, PS, PC, NX, NY, IS, RP, EP, LMAX, NBTYP
COMMON P(80,11), WS, WT, G(80), CE(80), CW(80), CNS(80), EPS1, EPS2
DIMENSION X(10), XA(10), QA(80)
DIMENSION KK(11)
PI1=400*DATAN(100)
GRAV=9800.
```

C SHIFTS FOR BEARING COEFFICIENTS

```
XD=.001
YD=.001
DX1=.001
DY1=.001
```

C MESH SIZE

```
JT=37
KT=7
DT=2.*PI1/FLOAT(JT-1)
DY=1./FLOAT(KT-1)
```

C PRINT OUT FLAGS

```
NVISC=0
NPRGR=0
NPRES=0
NCONT=1
```

C BEARING OPERATING VARIABLES

```
NBTYP=3
D=355.8
YL=266.85
GY=166.
FA=42.
ANL=0.0
CL=0.3556
RPM=3000.
EU=0.01
PC=.0
PSUP=1.E+5
IREF=1
TIN=25.
REC=1000.
CP=1880.
```

C

```
YLD=YL/D
CR=2.*CL/D
OM=2.*PI1*RPM/60.
U=OM*D/2.
NCASES=15
DE=0.6
IF(NBTYP.EQ.1) DE=0.0
FR=1.
SP=GRAV/CL/OM**2
F0WC=GRAV/CL/EU/OM**2
```

C ATTITUDE ANGLE ITERATION VARIABLES

```
FI=1.594
LF=20
FCC=1.
RF=1.
```

C TEMPERATURE INCREASE ITERATION VARIABLES

```
DELT=18.
LTC=10
TCC=1.
RT=0.5
TK=0.8
TF=0.8
RTMAX=1.5
```

C PRESSURE DISTRIBUTION ITERATION VARIABLES

RP=1.5
EP=1.E-4
LMAX=JT*KT

C GROOVE GEOMETRY
C

JB1=(JT-1)/2+1
TA=FA*PI1/180./2.
JG=FIX(TA/DT)
KG=FIX((YL-GY)/YL/DY)+1
GL=YL-FL0AT(KG-1)*DY*YL
JG1=JG+1
JG2=JB1-JG
JG3=JB1+JG
JG4=JT-JG

C SET GROOVE POSITION

D0 31 K=1,KT
D0 31 J=1,JT
LG(J,K)=1

C USER SHOULD SET NON-STANDART GROOVE HERE

31 IF<(J.LE.JG1.OR.(J.GE.JG2.AND.J.LE.JG3).OR.J.GE.JG4).AND.K.GE.KG)
1 LG(J,K)=0
FAA=DT*FL0AT(JG)*180./PI1*2.

***** TEMPERATURE-VISCOSITY CHARACTERISTICS*****

C SUPPLY VREF1,VREF2,VREF3, AT TEMPS TREF1,TREF2,TREF3

C SET NUNITS PARAMETER AS FOLLOWS

TEMPERATURE	UNITS	VISC UNITS	NUNITS
DEG FAH		REYNS	1
DEG FAH		C-POISE	2
DEG C		C-POISE	3
DEG C		C-STOKE	4

TREF1=38.

TREF2=93.

TREF3=10.

NUNITS=4

G0 T0 (51,52,53,54,55) , IREF

C IREF=1

51 DEN=870.
VREF1=25.
VREF2=5.
VREF3=126.
G0 T0 56

C IREF=2

52 DEN=870.
VREF1=35.
VREF2=6.2
VREF3=184.
G0 T0 56

C IREF=3

53 DEN=873.
VREF1=49.5
VREF2=7.7
VREF3=321.
G0 T0 56

C IREF=4

54 DEN=880.
VREF1=59.
VREF2=8.4
VREF3=432.
G0 T0 56

C IREF=5

55 READ(6,103) TREF1,TREF2,TREF3,VREF1,VREF2,VREF3,DEN

103 FORMAT(7F10.0)

56 CALL VISC05(NUNITS,DEN,TREF1,TREF2,TREF3,VREF1,VREF2,VREF3,VK,BV,
1CONN,NVISC)


```

FX(NX,NY,IS)=2.*(WS* SIN(FI)+WT* COS(FI))
FY(NX,NY,IS)=2.*(-WS* COS(FI)+WT* SIN(FI))
F=ATAN(-WT/WS)+ANL*PI/180.
IF(NBTYP.NE.3.AND.F.LT.0.0)F=F+PI
WRITE(6,101) F,FI
101 FORMAT(2X,10(1PE12.4))
IF(ABS(F-FI).LE.FCC*PI/180.) GO TO 3612
FI=FI+RF*(F-FI)
L=L+1
GO TO 2222
C          END OF ATTITUDE ANGLE LOOP
3612 HMIN=(1.-EPS1)*CL
IF(EPS2.GT.EPS1) HMIN=(1.-EPS2)*CL
FIO=FI*180./PI
FX1=FX(NX,NY,1)
FY1=FY(NX,NY,1)
C          LOAD CAPACITY
S=PI*SQRT(FX1**2+FY1**2)*3.
C
C          OIL FLOW RATE
DO 6 J=1,JT
RE=REC*H(J)
YK=1.+0.0198*RE**0.741/12.
6  QA(J)=H(J)**3*(-3.*P(J,1)+P(J,2)*4.-P(J,3))/(2.*DY)/YK
CALL SIMP(QA,DT,JT,AR)
Q=AR
QF=Q*U*CL*YL/2./YLD**2*3.6E-3
C          CIRCUMFERENTIAL FLOW AT THE MAX. PRESSURE
JM1=1
JM2=1
DO 63 J=2,JT
IF(JM1.GT.1.AND.J.LT.JB1) GO TO 63
IF(JM2.GT.1) GO TO 63
IF(P(J,KT).GE.P(J-1,KT)) GO TO 63
IF(J.GT.JG1.AND.J.LT.JG2) JM1=J-1
IF(J.GT.JG3.AND.J.LT.JG4) JM2=J-1
63 CONTINUE
RE=REC*H(JM1)
YK=1.+0.0198*RE**0.741/12.
DO 64 K=1,KT
64  QA(K)=H(JM1)-H(JM1)**3/YK*(P(JM1+1,K)-P(JM1-1,K))/2./DT
CALL SIMP(QA,DY,KT,AR)
QM1=AR
RE=REC*H(JM2)
YK=1.+0.0198*RE**0.741/12.
DO 65 K=1,KT
65  QA(K)=H(JM2)-H(JM2)**3/YK*(P(JM2+1,K)-P(JM2-1,K))/2./DT
CALL SIMP(QA,DY,KT,AR)
QM2=AR
Q=QM1+QM2
C
C          FRICTION FORCE
CALL FRICF
C          TEMPERATURE INCREASE
TN=VIS*U*D/DEN/CP/CL**2*YLD**2*1.E-3
DT1=TN*F/Q*TK
IF(ABS(DT1-DELT).LE.TCC) GO TO 57
DELT=(DT1-DELT)*RT+DELT
REC=DEN*U*CL/VIS*1.E-3
LT=LT+1
GO TO 58
C          END OF TEMP. INCREASE LOOP
57  PB=S*VIS*RPM/60./CR**2*1.E-6
WL=PB*YL*D*1.E-6

```

```

T0=TIN+DELT/1.8
TMAX=TIN+RTMAX*DELT/1.8
C          POWER LOSS
PL=VIS*U**2*YL*D/2./CL*F*1.E-12
WRITE (6,303) YLD,CR,DE,PC,PSUP,EB,S,WL,PB,FIO,HMIN,TIN,T0,TMAX,QF,
1PL
303  FORMAT(///10X,26HLENGTH/DIAMETER RATIO    =,F8.2,
A/10X,26HARC CLEARANCE RATIO    =,F8.4,
1/10X,26HPRELOAD                =,F8.2,
2/10X,26HCAVITATION PRESSURE    =,F8.2,2X,7HKN/M**2,
3/10X,26HFEED PRESSURE          =,G8.2,2X,7HKN/M**2,
C///42X,25HSTATIC CHARACTERISTICS/,37X,35(1H-),
1///10X,26HBEARING ECCENTR. RATIO =,F8.2,
2/10X,26HSOMMERFELD NUMBER      =,F8.2
A/10X,26HSTATIC LOAD              =,F8.2,2X,2HKN,
B/10X,26HMEAN BEARING PRESSURE   =,F8.2,2X,7HKN/M**2,
3/10X,26HATTITUDE ANGLE          =,F8.2,2X,6HDEGREE,
4/10X,26HMINIMUM FILM THICKNESS  =,F8.2,2X,2HMM,
5///,
6/10X,26HOIL INLET TEMPERATURE  =,F8.2,2X,5HDEG C,
7/10X,26HOIL OUTLET TEMPERATURE =,F8.2,2X,5HDEG C,
8/10X,26HMAX.BEARING TEMPERATURE =,F8.2,2X,5HDEG C,
4/10X,26HOIL FLOW RATE           =,F8.1,2X,10HL/HR,
9/10X,26HPOWER LOSS              =,G8.2,2X,5HW ,
6//)
FMU=F*CL*PI1/(D/2.)/S
WRITE (6,308) FMU,REC
308  FORMAT(/10X,26HFRICTION COEFFICIENT =,F8.4,2X,
5/10X,26HREYNOLDS NUMBER            =,F8.2,
1//)
IF (NPRES.NE.1) GO TO 60
WRITE (6,202) (K,K=1,KT)
202  FORMAT(30X,39HNON-DIMENSIONAL PRESSURE DISTRIBUTION,//10X,7(3HK
1=,I2,8X),11HFILM THICK./)
DO 59 J=1,JT
59  WRITE (6,201) J, (P(J,K),K=1,KT),H(J)
201  FORMAT(2HJ=,I3,8(1X,1PE12.3))
60  TT=10.
C          VELOCITY PERTURBATION IN X-DIRECTION
IS=2
CALL      SOL
CALL      FILMF
FX(NX,NY,IS)=2.*(WS*SIN(FI)+WT*COS(FI))
FY(NX,NY,IS)=2.*(-WS*COS(FI)+WT*SIN(FI))
C          VELOCITY PERTURBATION IN Y-DIRECTION
IS=3
CALL      SOL
CALL      FILMF
FX(NX,NY,IS)=2.*(WS*SIN(FI)+WT*COS(FI))
FY(NX,NY,IS)=2.*(-WS*COS(FI)+WT*SIN(FI))
C          DISPLACEMENT PERTURBATIONS
IS=1
X(1)=EB*SIN(FI)
X(3)=-EB*COS(FI)
XA(1)=X(1)-2.*DX1
XA(3)=X(3)-2.*DY1
Y1=XA(3)

DO 20 NX=1,3
XA(3)=Y1
XA(1)=XA(1)+DX1
DO 20 NY=1,3
XA(3)=XA(3)+DY1
IF (NX.EQ.2.AND.NY.EQ.2) GO TO 20

```

```

IF (NX.NE.2.AND.NY.NE.2) GO TO 20
EB=SQRT (XA (1) **2+XA (3) **2)
FI=ATAN (-XA (1) /XA (3) )
IF (FI.LE.0.0) FI=FI+PI1
CALL      SOL
CALL      FILMF
FX (NX, NY, IS) =2. * (WS * SIN (FI) +WT * COS (FI) )
FY (NX, NY, IS) =2. * (-WS * COS (FI) +WT * SIN (FI) )
20 CONTINUE
CALL      SC
FC=-3. PI1 /S
SXX=SXX *FC
SXY=SXY *FC
SYX=SYX *FC
SYY=SYY *FC
CXX=CXX *FC
CXY=CXY *FC
CYX=CYX *FC
CYY=CYY *FC
C DIMENSIONALIZATION OF THE DYNAMIC COEFFICIENTS
SXX1=SXX *WL /CL
SXY1=SXY *WL /CL
SYX1=SYX *WL /CL
SYY1=SYY *WL /CL
CXX1=CXX *WL /CL /OM
CXY1=CXY *WL /CL /OM
CYX1=CYX *WL /CL /OM
CYY1=CYY *WL /CL /OM
WRITE (6, 301) SXX, SXX1, CXX, CXX1, SXY, SXY1, CXY, CXY1, SYX, SYX1, CYX, CYX1,
301 ASYY, SYY1, CYY, CYY1
FORMAT (1H1, //45X, 24HDYNAMIC CHARACTERISTICS, /43X, 28 (1H-) /15X,
A25HSTIFFNESS COEFFICIENTS, 38X, 24HDAMPING COEFFICIENTS,
1 //20X, 8HNON-DIM., 8X, 5HKN/MM, 43X, 8HNON-DIM., 7X, 7HKN-S/MM/10X,
23HKXX, 2 (1X, F14.3) , 30X, 3HCXX, 2 (1X, F14.3) /10X,
33HKXY, 2 (1X, F14.3) , 30X, 3HCXY, 2 (1X, F14.3) /10X,
43HKYX, 2 (1X, F14.3) , 30X, 3HCYX, 2 (1X, F14.3) /10X,
53HKYY, 2 (1X, F14.3) , 30X, 3HCYY, 2 (1X, F14.3) /
C STABILITY THRESHOLD
A1=CXX+CYY
A21=SXX+SYY
A22=CXX *CYY -CYX *CXY
A3=SYY *CXX +SXX *CYY -CXY *SYX -CYX *SXY
A4=SXX *SYY -SXY *SYX
IF (A1.GT.0.0.AND.A3.GT.0.0.AND.A4.GT.0.0) GO TO 23
WRITE (6, 304) A1, A3, A4
304 FORMAT (//78H### COEFFICIENT OF THE CHARACTERISTIC POLYNOMIAL
1 IS NEGATIVE #####/10X, 3HA1=, G14.4/10X, 3HA3=, G14.4, /10X,
23HA4=, G14.4)
23 SPO= ((A3 **2 +A1 **2 *A4) /A1 /A3 -A21) /A22
C WHIRL FREQUENCY RATIO
SBO=A3 /A1
IF (SPO.LE.0.0) GO TO 22
WFR=SQRT (SPO *SBO)
WRITE (6, 305) SPO, WFR
305 FORMAT (//10X, 26HSTABILITY THRESHOLD =, F8.4,
1 /10X, 26HWHIRL FREQ. RATIO =, F8.4 //)
SP=GRAV /CL /OM **2
FOWC=GRAV /CL /EU /OM **2
FR=1.
CALL      EIGEN
CALL      RESPON

```

```

JA=JT
KA=KT
IF (NCONT.EQ.1) CALL CONTOR(P,JA,KA)
STOP
END
SUBROUTINE COF
COMMON SXX,SXY,SYX,SYX,CXX,CXY,CYX,CYY,XD,YD,DX1,DY1,FR,SP,FQWC
COMMON FX(3,3,3),FY(3,3,3),H(80),EB,DE,LG(80,11),JG,KG,REC,F,PI1
COMMON YLD,DT,DY,JT,KT,FI,PS,PC,NX,NY,IS,RP,EP,LMAX,NBTYP
COMMON P(80,11),WS,WT,G(80),CE(80),CW(80),CNS(80),EPS1,EPS2
DIMENSION DHT(80)
C          BEARING      GEOMETRY
JB1=(JT-1)/2+1
DO 33 M=1,2
IF (M-1) 33 , 40 , 41
C
C          BOTTOM      HALF
C
40 GO TO (34, 34 , 31), NBTYP
C$$$$$$$$$$$$$$$$$$$$ FOR OFFSET HALVES BEARING $$$$$$$$$$$$$$$$$$$$$
31 EPS=SQRT(EB**2+DE**2-2.*DE*EB*COS(PI1/2.+FI))
IF (EPS.GE.1.0) WRITE (6,51)
A1=PI1/2.-ASIN(EB*SIN(PI1/2.+FI)/EPS)
X=PI1/2.-A1
GO TO 52
CXXXXXXXXXXXXXXXXX FOR ELLIPTICAL BEARING XXXXXXXXXXXXXXXXXXXXXXXXXXXXXXXX

```

```

34 EPS=SQRT (EB**2+DE**2+2.*DE*EB*COS (F I )
A1=ASIN (EB*SIN (F I ) /EPS)
X=PI1/2.-A1
52 EPS1=EPS
IF (EPS.LE.1.0) GO TO 38
WRITE (6,51)
51 FORMAT (//53H$$$ BOTTOM HALF ECCENTRICITY GREATER THAN 1.0 $$)
STOP
38 IT=1
JI=JB1-1
GO TO 36
C TOP HALF
C
41 GO TO (35 , 35 , 32 ) , NBTP
C $$$$$$$$$$$$ FOR OFFSET HALVES BEARING $$$$$$$$$$$$$$$$$$$$$$$$$$$$$$$$$$$$
32 EPS=SQRT (EB**2+DE**2-2.*EB*DE*COS (PI1/2.-F I )
A2=-(PI1/2.-ASIN (EB*SIN (PI1/2.-F I ) /EPS))
X=3.*PI1/2.-A2
GO TO 53
CXXXXXXXXXXXXXXXXXXXXXXXXXXXXXXXXXXXXXXXXXXXXXXXXXXXXXXXXXXXXXXXXXXXXXXXXXXXX
35 EPS=SQRT (EB**2+DE**2-2.*EB*DE*COS (F I )
A2=PI1-ASIN (EB*SIN (F I ) /EPS)
IF (NBTP.EQ.1) A2=PI1-A2
X=3.*PI1/2.-A2
53 EPS2=EPS
IF (EPS.LE.1.0) GO TO 37
WRITE (6,50)
50 FORMAT (//53H$$$ TOP HALF ECCENTRICITY GREATER THAN 1.0 $$)
STOP
37 IT=JB1
JI=JT
36 ED=0.0
FD=0.0
A=A1
IF (M.EQ.2) A=A2
IF (IS-2) 42 , 2 , 17
2 FD=XD*COS (A) /EPS
ED=XD*SIN (A)
GO TO 42
17 FD=YD*SIN (A) /EPS
ED=-YD*COS (A)
42 X1=X
C FILM THICKNESS AND ITS DERIVATIVE
DO 4 J=IT,JI
H (J) =1.+EPS*COS (X)
DHT (J) =-EPS*SIN (X)
4 X=X+DT
IF (NBTP-1) 5 , 60, 60
C DISCONTINUITY OF FILM THICKNESS DERIVATIVE
60 IF (IT.NE.JB1) GO TO 5
DHT (JB1) = (DHT (JB1-1) +DHT (JB1+1)) /2.
DHT (JT) = (DHT (JT-1) +DHT (2)) /2.
DHT (1) =DHT (JT)
H (JT+1) =H (2)
DHT (JT+1) =DHT (2)
5 X=X1
C COMPUTING COEFFICIENTS
DO 1 J=IT,JI
RE=REC*H (J)
TK=1.+0.026/12.*RE**0.8265
YK=1.+0.0198*RE**0.741/12.
DTK=1.791E-3*REC**0.8265*DHT (J) /H (J) **0.1735
D=-DTK/TK
ALD=SQRT (YK/TK) *YLD

```

```

        IF (J.EQ.JB1.OR.J.EQ.JT) GO TO 6
        GO TO 7
6      DH2=(H(J+1)-2.*H(J)+H(J-1))/DT**2
        F=3.*(D*DHT(J)/H(J)+(DHT(J)**2/2./H(J)+DH2))/2.
        GO TO 8
7      F=3.*EPS*(EPS*SIN(X)**2/H(J)/2.-COS(X)-SIN(X)*D)/2./H(J)
8      C=2./DT**2+2./(ALD*DY)**2+F
        CE(J)=(1./DT**2+D/2./DT)/C
        CW(J)=(1./DT**2-D/2./DT)/C
        CNS(J)=1./(DY*ALD)**2/C
        G1=(1.-2.*FD)*DHT(J)+2.*ED*COS(X)
        G(J)=-G1/(SQRT(H(J)))**3/C*TK
1      X=X+DT
33     CONTINUE
        RETURN
        END
        SUBROUTINE SOL
        COMMON SXX,SXY,SYX,SYX,CXX,CXY,CYX,CYY,XD,YD,DX1,DY1,FR,SP,FBWC
        COMMON FX(3,3,3),FY(3,3,3),H(80),EB,DE,LG(80,11),JG,KG,REC,F,PI1
        COMMON YLD,DT,DY,JT,KT,FI,PS,PC,NX,NY,IS,RP,EP,LMAX,NBTYP
        COMMON P(80,11),WS,WT,G(80),CE(80),CW(80),CNS(80),EPS1,EPS2
        CALL CCF
        L=0
115    L=L+1
        RS=.0
        XS=.0
        DO 7 K=2,KT
        P(1,K)=PS*SQRT(H(1))**3
        DO 7 J=2,JT
        Z=P(J,K)
        IF(LG(J,K).EQ.0) GO TO 70
        P(J,K)=CW(J)*P(J-1,K)+CE(J)*P(J+1,K)+CNS(J)*(P(J,K-1)+P(J,K+1))
        2+G(J)
        DP=P(J,K)-Z
        P(J,K)=Z+RP*DP
        IF(P(J,K)-PC) 9,19,19
9      P(J,K)=PC
19     IF(P(J,K)) 1,7,1
1      RA=ABS(1.-Z/P(J,K))
        XS=XS+ABS(P(J,K))
        RS=RS+RA*ABS(P(J,K))
        GO TO 7
70    P(J,K)=PS*SQRT(H(J))**3
7      CONTINUE
        DO 2 K=1,KT
        P(JT+1,K)=P(2,K)
2      P(1,K)=P(JT,K)
        DO 5 J=1,JT
5      P(J,KT+1)=P(J,KT-1)
        WR=RS/XS
        IF(L-LMAX) 8,8,21
8      IF(WR-EP) 11,11,115
21     WRITE(6,102)
102    FORMAT(/95H$$$$$$ PRESSURE DOES NOT CONVERGE WITHIN THE
1      ITERATION LIMITS $$$$$$$$$$$$$$$$ )
        STOP
11     DO 81 J=1,JT
        DO 181K=1,KT+1
        P(J,K)=P(J,K)/(SQRT(H(J)))**3
181    CONTINUE
81     CONTINUE
        RETURN
        END
        SUBROUTINE FILMF

```



```

COMMON SXX,SXY,SYX,SY,Y,CXX,CXY,CYX,CYY,XD,YD,DX1,DY1,FR,SP,F0WC
COMMON FX(3,3,3),FY(3,3,3),H(80),EB,DE,LG(80,11),JG,KG,REC,F,PI1
COMMON YLD,DT,DY,JT,KT,FI,PS,PC,NX,NY,IS,RP,EP,LMAX,NBTYP
COMMON P(80,11),WS,WT,G(80),CE(80),CW(80),CNS(80),EPS1,EPS2
DIMENSION A(19),PM(90),PT(90)
X=PI1/2.-FI
DO 30 J=1,JT
DO 31 K=1,KT
31 A(K)=P(J,K)
CALL SIMP(A,DY,KT,AR)
PM(J)=AR*COS(X)
PT(J)=AR*SIN(X)
30 X=X+DT
CALL SIMP(PM,DT,JT,AR)
WS=AR
CALL SIMP(PT,DT,JT,AR)
WT=AR
RETURN
END
SUBROUTINE SIMP(A,H,NT,AR)
DIMENSION A(90)
A2=0.
A4=0.
N1=NT-1
N2=NT-2
DO 23 N=2,N1,2
23 A4=A4+4.*A(N)
DO 24 N=3,N2,2
24 A2=A2+2.*A(N)
AR=(A2+A4+A(1)+A(NT))*H/3.
RETURN
END
SUBROUTINE FRICF
COMMON SXX,SXY,SYX,SY,Y,CXX,CXY,CYX,CYY,XD,YD,DX1,DY1,FR,SP,F0WC
COMMON FX(3,3,3),FY(3,3,3),H(80),EB,DE,LG(80,11),JG,KG,REC,F,PI1
COMMON YLD,DT,DY,JT,KT,FI,PS,PC,NX,NY,IS,RP,EP,LMAX,NBTYP
COMMON P(80,11),WS,WT,G(80),CE(80),CW(80),CNS(80),EPS1,EPS2
DIMENSION A(80,11),AO(80),D(11)
DO 40 K=1,KT
P(JT+1,K)=P(2,K)
DO 41 J=2,JT
DPDT=(P(J+1,K)-P(J-1,K))/2./DT
RE=REC*H(J)
TK=1.+0.026/12.*RE**0.8265
IF(LG(J,K).EQ.0) GO TO 46
IF(K.EQ.1.AND.P(J,K+1).GT.PC) GO TO 45
IF(K.EQ.1.AND.P(J,K+1).LE.PC) GO TO 47
IF(P(J-1,K).LE.PC.AND.P(J,K).LE.PC) GO TO 44
IF(P(J-1,K).GT.PC.AND.P(J,K).LE.PC) GO TO 42
FRAC=1.0
GO TO 43
42 HC=H(J)
44 FRAC=HC/H(J)
GO TO 43
47 TK=0.0
45 DPDT=0.0
FRAC=1.
43 A(J,K)=FRAC*(-3.*H(J)*DPDT+TK/H(J))
GO TO 41
46 A(J,K)=0.0
41 AO(J)=A(J,K)
AO(1)=AO(JT)
A(1,K)=A(JT,K)
CALL SIMP(AO,DT,JT,AR)

```

```

40  D(K)=AR
    CALL SIMP(D,DY,KT,AR)
    F=AR
    RETURN
    END
    SUBROUTINE VISCOS(N,DE,T1,T2,T3,V1,V2,V3,VK,BV,C0NN,NPRINT)
    IF(N.LT.3) GO TO 1
    T1=T1*1.8+32.
    T2=T2*1.8+32.
    T3=T3*1.8+32.
1   IF(N.EQ.1) GO TO 2
    V1=V1*1.4503E-7
    V2=V2*1.4503E-7
    V3=V3*1.4503E-7
    IF(N.EQ.4) GO TO 2
    V1=V1*DE/1000.
    V2=V2*DE/1000.
    V3=V3*DE/1000.
C
2   AAV=ALOG(V1/V2)
    BBV=ALOG(V1/V3)
    TEST=AAV/BBV
    C0NN=-T1
5   C0NN=C0NN+1.
    GR=(1.-(T1+C0NN)/(T2+C0NN))/(1.-(T1+C0NN)/(T3+C0NN))
    IF(TEST-GR) 5,5,6
6   AV=1./(T1+C0NN)-1./(T2+C0NN)
    BV=AAV/AV
    VK=V1*EXP(-BV/(T1+C0NN))
C
    D0NN=C0NN*0.1
    IF(NPRINT.EQ.1) WRITE(6,50) VK,BV,D0NN
    IF(NPRINT.EQ.1) WRITE(6,101)
    DO 150 JFAH=80,230,10
    T=JFAH
    VREYN=VK*EXP(BV/(T+C0NN))*1.E6
    VCP=VREYN/0.14503
    VCS=VCP*1000./DE
    IF(NPRINT.EQ.1) WRITE(6,201) JFAH,VREYN,VCP,VCS
150  CONTINUE
    IF(NPRINT.EQ.1) WRITE(6,102)
    DO 151 JDEGC=20,120,10
    T=FLOAT(JDEGC)*1.8+32.
    VREYN=VK*EXP(BV/(T+C0NN))*1.E6
    VCP=VREYN/0.14503
    VCS=VCP*1000./DE
    IF(NPRINT.EQ.1) WRITE(6,201) JDEGC,VREYN,VCP,VCS
151  CONTINUE
    RETURN
50  FORMAT(1H1,28X,46HCONSTANTS IN VOGEL'S VISCOSITY TEMPERATURE LAW/
1/,30X,39H VISCOSITY (REYNS)=K*EXP(B/T DEG F + C ),/,
246X,2HK=,1PE10.3,/,46X,2HB=,1PE10.3,/,46X,2HC=,F5.1)
101  FORMAT(1H0,30X,10HTEMP DEG F,6X,10HMICROREYNS,3X,10H C-POISE ,4X,
110H C-STOKE )
102  FORMAT(1H0,30X,10HTEMP DEG C,6X,10HMICROREYNS,3X,10H C-POISE ,4X,
110H C-STOKE )
201  FORMAT(1H ,34X, I3,10X,3(F6.2,8X) )
    END
    SUBROUTINE CONTOR(P,JT,KT)
    DIMENSION P(80,11)
    DIMENSION NR(111),LINE(111,30)
    INTEGER BLANK,STAR,LINE
    READ(5,100) BLANK,STAR
100  FORMAT(2A1)

```

```

GR=0.
DO 11 I=1,KT
DO 12 J=1,JT
IF (P(J,I).GT.GR) GR=P(J,I)
12 CONTINUE
11 CONTINUE
    IR=1
    IN=20/(KT-1)*IR
    JN=110/(JT-1)
    FJ=FLOAT(JN)
    FI=FLOAT(IN)
    MT=JN*(JT-1)+1
    INV=IN+1
    DO 1 L=1,KT-1
    DO 3 I=1,MT
    JM=(I-1)/JN+1
    IF (JM.EQ.JT) GO TO 10
    P1=P(JM,L)
    P2=P(JM+1,L)
    P3=P(JM,L+1)
    P4=P(JM+1,L+1)
    P3=P(JM,L+1)
    LM=(JM-1)*JN+1
    F2=I-LM
    F1=FJ-F2
    X=(P1*F1+P2*F2)/FJ
    Y=(P3*F1+P4*F2)/FJ
    GO TO 201
10  X=P(JM,KT)
    Y=P(JM,KT+1)
201 RED=1.
    DO 2 K=1,INV
    F3=INV-K
    F4=K-1
    NR(I)=(X*F3+Y*F4)/FI/GR*10.+5
    L1=K+(L-1)*INV
    IF ((NR(I)+1)/2-NR(I)/2) 8,9,8
9  LINE(I,L1)=STAR
    GO TO 2
8  LINE(I,L1)=BLANK
2  CONTINUE
3  CONTINUE
1  CONTINUE
    WR_TE(6,200)((LINE(I,L),I=1,MT),L=1,INV*(KT-1))
200 FORMAT(5X,/109(A1))
RETURN
END

```

```

SUBROUTINE SC
COMMON SXX,SXY,SYX,SY,Y,CXX,CXY,CYX,CYY,XD,YD,DX1,DY1,FR,SP,F0WC
COMMON FX(3,3,3),FY(3,3,3),H(80),EB,DE,LG(80,11),JG,KG,REC,F,PI1
C          STIFFNESS AND DAMPING COEFFICIENTS
NX=2
NY=2
SXX=(FX(NX+1,NY,1)-FX(NX-1,NY,1))/2./DX1
SXY=(FX(NX,NY+1,1)-FX(NX,NY-1,1))/2./DY1
SYX=(FY(NX+1,NY,1)-FY(NX-1,NY,1))/2./DX1
SYY=(FY(NX,NY+1,1)-FY(NX,NY-1,1))/2./DY1
CXX=(FX(NX,NY,2)-FX(NX,NY,1))/XD
CXY=(FX(NX,NY,3)-FX(NX,NY,1))/YD
CYX=(FY(NX,NY,2)-FY(NX,NY,1))/XD
CYY=(FY(NX,NY,3)-FY(NX,NY,1))/YD
RETURN
END
SUBROUTINE EIGEN
COMMON SXX,SXY,SYX,SY,Y,CXX,CXY,CYX,CYY,XD,YD,DX1,DY1,FR,SP,F0WC
REAL AK(4,4),RR(4),RI(4),WK(8),AX(10)
INTEGER IN(4)
C          ELEMENTS OF THE COEFFICIENT MATRIX
DO 21 IJ=1,4
DO 21 K=1,4
21 AK(IJ,K)=0.0
AK(1,1)=-SP*CXX
AK(1,2)=-SP*CXY
AK(1,3)=-SP*SXX
AK(1,4)=-SP*SXY
AK(2,1)=-SP*CYX
AK(2,2)=-SP*CYY
AK(2,3)=-SP*SYX
AK(2,4)=-SP*SYY
AK(3,1)=1.0
AK(4,2)=1.0
C          EIGENVALUES OF THE COEFFICIENT MATRIX
IA=4
N=4
IF=1
CALL F02AFF(AK,IA,N,RR,RI,IN,IF)
IF(IF.EQ.0) GO TO 120.
WRITE(6,99) IF
99  FORMAT(2X,10I5)
STOP
120 WRITE(6,302) (RR(K),RI(K),K=1,N)
302  FORMAT(///32X,*RESPONSE TO STEP INPUT*//33X,*DECAY RATE*,6X,
1*DAMPED NAT. FREQ.*//15X,*ROOT 1*,2X,2(5X,F15.3)/15X,
2*ROOT 2*,2X,2(5X,F15.3)/15X,*ROOT 3*,2X,2(5X,F15.3)/15X,
3*ROOT 4*,2X,2(5X,F15.3) //)
RETURN
END
SUBROUTINE RESPON
COMMON SXX,SXY,SYX,SY,Y,CXX,CXY,CYX,CYY,XD,YD,DX1,DY1,FR,SP,F0WC
COMPLEX ZA(2,2),ZB(2,1),ZC(2,1),XJ,YJ
DIMENSION WK(5),FE(2),WD(5)

```

```

PI1=4D0*DATAN(1D0)
ZA(1,1)=CMPLX(SXX-FR**2/SP,CXX*FR)
ZA(1,2)=CMPLX(SXY,CXY*FR)
ZA(2,1)=CMPLX(SYX,CYX*FR)
ZA(2,2)=CMPLX(SYY-FR**2/SP,CXX*FR)
C      RIGHT HAND SIDE
ZB(1,1)=CMPLX(1.,0.)
ZB(2,1)=CMPLX(0.,-1.)
IF=0
CALL F04ADF(ZA,2,ZB,2,2,1,ZC,2,WK,IF)
WK(1)=CABS(ZC(1,1))
WK(2)=CABS(ZC(2,1))
WRITE(6,303)FR
303  FORMAT(40X,*RESPONSE TO EXTERNAL EXITATION*//5X,
1*EXCITATION FREQ. RATIO*5X,F5.2//)
WRITE(6,11)(ZC(I2,1),WK(I2),I2=1,2)
11  FORMAT(/3(2X,1PE13.4))
XC=REAL(ZC(1,1))
XS=-AIMAG(ZC(1,1))
YC=REAL(ZC(2,1))
YS=-AIMAG(ZC(2,1))
C      DESCRIPTION OF ELLIPTICAL ORBIT
AMAJ=SQRT(0.5*(XC**2+XS**2+YC**2+YS**2)+SQRT(0.25*(XC**2+XS**2
1-YC**2-YS**2)**2+(XC*YC+XS*YS)**2))
BMIN=(XC*YS-XS*YC)/AMAJ
FAXIS=0.5*(ATAN(2.*(XC*YC+XS*YS)/(XC**2+XS**2-YC**2-YS**2))
FPHASE=0.5*(ATAN(2.*(-XC*XS-YC*YS)/(XC**2-XS**2+YC**2-YS**2))
FAXIS=FAXIS*180./PI1
FPHASE=FPHASE*180./PI1
WRITE(6,102)AMAJ,BMIN,FAXIS,FPHASE,SP
102  FORMAT(8X,9(1PE13.5))
RETURN
END

```

PUBLICATIONS

LOAD AND FEED PRESSURE ON

WHIRL IN A

GROOVED JOURNAL BEARING

M. Akkok*

C. M. M. Ettles**

March 1978

ASLE Paper 78 LC6B3

* Research Student, Mechanical Engineering Department, Imperial College
London SW7 2BX

** Lecturer, Mechanical Engineering Department, Imperial College
London SW7 2BX

SYNOPSIS

An experimental investigation is described of the whirl stability of a circumferentially grooved journal bearing carrying a stiff rotor. The shaft and bearing were made with a slight taper so that the clearance could be infinitely varied, and the assembly could be tilted to any angle between the horizontal and vertical directions to vary the load on the bearing. These features allowed a wide range of running conditions.

Experimental results imply that sub-ambient film pressures are negligible, regardless of load, and that Reynolds boundary conditions apply with cavitation at ambient pressure. This has an important effect on film extent and consequently on promoting stability. The influence of feed pressure on the control of film extent, and hence on stability, is shown by analysis and experiment.

NOTATION

- a_{xx} , etc : stiffness coefficients of film per land of bearing
- b_{xx} , etc : damping coefficients of film per land of bearing
- c_r : bearing radial clearance
- D : bearing diameter
- F : total oil film force on one land
- k : polar radius of gyration (equations (2))
- L_o : axial length of one land
- ℓ : axial radius of gyration (equations (2))
- M : effective mass of rotor at test bearing
- M_t : mass of whole rotor
- P : specific loading, $F/L D$
- p : pressure
- S : stability parameter, $2F/M c_r \omega^2$
-
- β : cavitation parameter, $- p_{cav}/p$
- γ : feed pressure parameter, p_{feed}/p
- ϵ_b : non-dimensional unbalance
- ϵ_o : equilibrium eccentricity ratio of bearing
- θ : angle of inclination of shaft from horizontal
- λ_n : roots of perturbed motion (equations (8), (9))
- ω : spin velocity of shaft, rad/s

INTRODUCTION

The extent of the fluid film in a journal bearing is known to have a moderate effect on load capacity and a more marked effect on the dynamic characteristics. A bearing running under full Sommerfeld conditions can be shown theoretically to be completely unstable at all speeds, whereas if the Reynolds boundary condition is applied to allow for cavitation, the stability boundary becomes well defined.

The full Sommerfeld and Reynolds conditions represent the extreme ends of a range in which practical bearings operate. A lightly loaded bearing with a loading intensity of less than 0.1 bar could be expected to run under full Sommerfeld conditions since the peak pressures would be of the order ± 0.3 bar (depending on eccentricity ratio) and it is likely that the film could withstand such a relatively small negative pressure relative to atmospheric conditions. Conversely, a heavily loaded bearing at 100 bar tends closely to the Reynolds condition, which assumes the cavitation pressure to be ambient. The intermediate case is of great practical interest since some sub-ambient pressure may occur within the cavitated zone or upstream of it.

Dyer and Reason [1] have presented an experimental study of a steadily loaded bearing using a pressure transducer rotating with the shaft, showing that tensile stresses of up to 3 bar without cavitation could occur during a single shaft revolution, followed by cavitation at an irregular sub-ambient pressure during the next revolution. This behaviour was attributed to the random occurrence of asperities or air bubbles from which cavities could grow.

For lightly loaded bearings (in the range 0.5 - 4.0 bar) cavitation at less than atmospheric pressure would have a considerable destabilising effect since the film extent and attitude angle would be affected. This range of loading is of practical interest since many test machines to investigate rotor behaviour are run lightly loaded. Some pump bearings (which are large for reasons of shaft strength) are run at similar loading..

A second factor which can control film extent is the feed pressure to the bearing. Of the various practical grooving designs, a full central circumferential groove gives the greatest control on film extent since by using very high feed pressures it is possible to approach full Sommerfeld conditions, regardless of loading intensity.

This work was undertaken to find the individual and combined effects of loading intensity and feed pressure on the half-frequency whirl stability of a circumferentially grooved bearing.

APPARATUS

A general arrangement of the shaft and bearing is shown in Figure 1. The first test bearing was of 12.7mm (0.50 in.) nominal diameter with two lands formed by a circumferential groove 2.5mm (0.10) wide and of the same depth. Each land was of $L = 3.2\text{mm}$ (0.125in) axial length, giving a ratio $L/D = 0.25$ per land. A second test bearing for the same specific loading was made of 8.2mm (0.323 in.) nominal diameter and 5.5mm (0.217 in.) land length to give $L/D = 0.671$ per land.

The rotor was supported on two bearings as shown, one being the oil film bearing under test and the other a self-aligning double row spherical track ball bearing with collet fixing to the shaft. The ball bearing was assumed to act as a hinge when considering the dynamics of the shaft.

The bore and journal of the test bearings were tapered with an included angle of 2.43 degrees to allow the clearance to be infinitely varied. This was achieved by loosening the collet of the ball bearing and sliding the shaft forward to give zero film thickness in the journal bearing. The shaft was then moved back a known distance (measured using a clock gauge) so that, knowing the taper angle, the running clearance could then be found, nominally to within three significant figures.

The same taper on shaft and bearing was achieved by finish machining on the same lathe with an unaltered skew cross slide setting. The alignment of the assembly was achieved by *in situ* lapping and checked using thin applications of engineering blue. To assist the small amount of lapping necessary, the journal was of hardened steel and the bearing of brass.

The calculated first critical speed of the shaft when assumed pinned at the bearings was more than twice the maximum speed available on the test machine. For analysis purposes the rotor was considered to be stiff. The drive was applied by a simple coupling consisting of a piece of slack cord passing through an axial groove on the free end of the shaft.

The dimensions were such that the specific loading on both test bearings was 0.345 MPa (50 psi) when the assembly was horizontal. The unit and motor were mounted on a base plate of 225kg mass (500 lbm). The whole assembly could be tilted (with the test bearing downwards) to allow the bearing load to be infinitely varied from 0.345 MPa to nil.

The lubricant used was a mineral oil of 365 cS at 30°C and 17.9 cS at 100°C. The effective temperature for the determination of viscosity was measured by a single thermocouple close to the film. For the great majority of running conditions, the temperature rise of the bearing over inlet was less than 2°C.

The static reaction at the test bearing when the assembly was horizontal was 2.835kgf, however, considering the ball bearing to be a hinge, the effective mass of the rotor viewed from the test bearing was 2.585kg, or 8.8 per cent less than the static reaction. (Had the rotor been a uniform rod, this reduction would have been 33.3%.) In the stability analysis (to be described), this shaft assembly was balanced without the collet (which it was necessary to remove) to a nominal error of 0.5gm cm.

The range of operation variables for the test machine were:

Speed	: 0 - 130 rev/s
Load	: 0 - 0.345 MPa (50 psi)
Radial Clearance	: 0 - 0.23mm (0.009 in.)
Feed Pressure	: 0 - 0.621 MPa (93 psi)

THEORETICAL ANALYSIS

The pressure field within the film was calculated using a finite-difference iterative solution of the Reynolds equation. The boundary pressure at the outer edge of the land was set to ambient (zero). At the inner edge the feed pressure was set according to an independent parameter γ , where $\gamma = (\text{feed pressure}/\text{bearing specific loading}) = P_{\text{feed}}/P$. For any fixed value of ϵ the feed pressure was found to affect the pressure fluid in the film and the film extent. The oil film force F was therefore slightly affected by feed pressure. To obtain a fixed value of γ the value of P_{feed} was adjusted according to the current value of F as the convergence of the iterative solution proceeded.

To allow for sub-ambient cavitation, a floating boundary condition was applied such that if the pressure at any node during an iterative sweep was found to be less than $-\beta P$, the pressure was set immediately to that limiting value. A value of $\beta = 0$ corresponds to the Reynolds boundary condition. The pressure in the cavitated zone was assumed to be zero absolute or minus 0.101 MPa gauge (one atmosphere = 0.101 MPa). The loading P changes with the angle of inclination θ of the shaft from the horizontal and is equal to $P_{\theta=0} \cos \theta$. The ratio β is therefore $0.101/P_{\theta=0} \cos \theta$ and, for this apparatus, has the following values.

θ	P (MPa)	(psi)	β
80	0.060	8.7	1.67
70	0.118	17.1	0.85
60	0.173	25.0	0.58
45	0.244	35.4	0.41
0	0.345	50.0	0.29

The choice of zero absolute as the pressure in the cavitated zone was arbitrary but corresponds approximately to Dyer's experiments [1] for a fractured or striated film. The occurrence of tensile stresses within the film, as found for some conditions by Dyer, could be accommodated within the solution by using higher values of β , but for the purposes of this paper this is later shown to be unnecessary. For each value of β , solutions were obtained for values of $\gamma = 0, 0.25, 0.5, 1, 2$. An illustration of the effect of γ on film extent is shown in Figure 2 for a typical value of $\beta = 0.5$. At a value of $\gamma = 2$, cavitation is avoided although a small area of the film is at sub-ambient pressure.

Stability Analysis

Assuming that the rotor is hinged at the ball bearing and taking moments about the hinge, the equations of motion about the equilibrium running position in the x and y directions are as follows:

$$\left. \begin{array}{l} \frac{I}{L_o^2} \ddot{x} - \frac{J \omega}{L_o^2} \dot{y} \\ \frac{I}{L_o^2} \ddot{y} + \frac{J \omega}{L_o^2} \dot{x} \end{array} \right\} + 2 \begin{bmatrix} a_{xx} & a_{xy} \\ a_{yx} & a_{yy} \end{bmatrix} \begin{bmatrix} x \\ y \end{bmatrix} + 2 \begin{bmatrix} b_{xx} & b_{xy} \\ b_{yx} & b_{yy} \end{bmatrix} \begin{bmatrix} \dot{x} \\ \dot{y} \end{bmatrix} = 0 \quad (1)$$

- where I = moment of inertia of rotor about hinge
- J = polar moment of inertia of rotor
- L_o = distance between bearings
- x = horizontal coordinate at bearing from equilibrium running position
- y = vertical coordinate at bearing from equilibrium running position

The setting up of such equations has been demonstrated by Woodcock and Holmes [2] for a similar but more complex system where the rotor was supported on

two oil film bearings. The concept of linearised spring and damping coefficients relating to small displacements of a journal bearing from the equilibrium running position is well established and is described in detail in, for example, [3] by Holmes. The coefficients were determined in the oil film analysis by imposing small perturbations of displacement or velocity in the x or y directions and observing the change in oil film force.

The equations of motion are set in non-dimensional form by the substitutions:

$$\begin{aligned}
 I &= M_t \ell^2 \\
 J &= M_t k^2 \\
 x &= X c_r \\
 y &= Y c_r \\
 t &= T/\omega \\
 a_{xx} &= A_{xx} \cdot F/c_r, \text{ etc.} \\
 b_{xx} &= B_{xx} \cdot F/\omega c_r, \text{ etc.}
 \end{aligned}
 \tag{2}$$

After some manipulation, the equations of motion become:

$$\left. \begin{array}{l} \ddot{X} - \dot{Y}_n \\ \ddot{Y} + \dot{X}_n \end{array} \right\} + S \begin{bmatrix} A_{xx} & A_{xy} \\ A_{yx} & A_{yy} \end{bmatrix} \begin{bmatrix} X \\ Y \end{bmatrix} + S \begin{bmatrix} B_{xx} & B_{xy} \\ B_{yx} & B_{yy} \end{bmatrix} \begin{bmatrix} \dot{X} \\ \dot{Y} \end{bmatrix} = 0 \tag{3}$$

where:

$$S = \frac{2F}{c_r \omega^2 M_t (\ell/L_o)^2} \tag{4}$$

and:
$$n = (k/\ell)^2$$

The form of the stability parameter (4) can be further reduced to include the effective mass, M , at the bearing as follows. Considering the equations (1) and writing the oil film forces from both lands as F_x, F_y , then the equation can be written:

$$\frac{I}{L_o} \ddot{x} - \frac{J \omega}{L_o} \dot{y} + F_x L_o = 0 \quad \text{_____ (5)}$$

$$\frac{I}{L_o} \ddot{y} + \frac{J \omega}{L_o} \dot{x} + F_y L_o = 0 \quad \text{_____ (6)}$$

If the system is at rest, $\dot{x} = \dot{y} = 0$ and using the identities $F_x \equiv M \ddot{x}$, $F_y \equiv M \ddot{y}$, then both (5) and (6) yield the same result:

$$M = I/L_o^2 = M_t \ell^2 / L_o^2 \quad \text{_____ (7)}$$

As an example, for a uniform rod $I = M_t L_o^2 / 3$ so that $M = M_t / 3$ compared to the static reaction $F = M_t g / 2$. As a consequence of equation (7), the stability parameter in equation (4) becomes the commonly used parameter $S = 2F / M c_r \omega^2$.

The stability of the equation of motion (1) is assessed as in [4,5] by assuming a solution:

$$x = A e^{\lambda T}, \quad y = B e^{\lambda T} \quad \text{_____ (8)}$$

If equation (8) is substituted in the equations of motion, the result can be expressed as:

$$\begin{bmatrix} Z \end{bmatrix} \begin{bmatrix} A \\ B \end{bmatrix} = \begin{bmatrix} 0 \\ 0 \end{bmatrix}$$

where $[Z]$ is a 2×2 matrix, made up of S, λ and the spring and damping coefficients. From conventional vibration theory, the determinant of $[Z]$ must be zero for a solution to exist. Expansion of the determinant gives a fourth order equation for λ . The four roots are usually arranged as conjugate pairs:

$$\lambda_{1,2} = \alpha_1 \pm i \beta_1 \quad \lambda_{3,4} = \alpha_2 \pm i \beta_2 \quad \text{--- (9)}$$

If a value of S is assumed, the numerical values of the roots can be found. All real parts of the roots must be negative for stability. The solution of the determinantal equation for the roots can be avoided by applying Routh's stability criterion [4, 5]. This locates the threshold of stability corresponding to a zero value of the largest real part α (all other real parts being negative). Applying the criterion gives a particular value of S (the threshold value) at which the stability is neutral. For values of S less than the critical value, the system is unstable.

Solutions are presented in the form of stability profile maps according to the Routh criterion. Extreme examples are shown in Figure 3 for angles of inclination of 80° and zero, where the stability parameter $S = 2F/M c_r \omega^2$ is plotted against the equilibrium eccentricity ratio ϵ_0 . It appears that the low loading for $\theta = 80^\circ$ ($P = 0.59$ bar) gives almost complete Sommerfeld conditions and the bearing is unstable for all conditions for ϵ_0 less than 0.6. In Figure 3(a) for $\theta = 0$ ($P = 3.40$ bar), the conditions are intermediate between pure Sommerfeld and Reynolds. The effect of increased feed pressure in lowering the stability is apparent.

As a matter of interest, the classical solution for stability assuming a point mass concentrated at the bearing, is shown in Figure 3(a)

for $\gamma = 0$ as a dashed line. This should be compared with the full line which represents the stability of the test system and includes gyroscopic effects. The two characteristics are not greatly different.

The case of vertical rotors ($\theta = 90^\circ$) is of practical interest. The force F applied to the bearing is then zero and the stability parameter is also zero. Theoretically the rotor is unstable at all speeds. This was verified experimentally. Capone [7] has shown experimentally that the amplitude of whirl can be controlled in an unloaded journal bearing although whirl always occurs.

Vertical axis machines are usually provided with pivoted pad guide bearings. If the circular bore bearings are used several factors could operate fortuitously to prevent whirl. These include misalignment, unbalance magnetic pull (to give a finite value of F), coupling forces and thermal distortion of the bore.

EXPERIMENTAL RESULTS AND DISCUSSION

Results were taken for both test bearings at six angles of tilt between 0 and 80 degrees and for five values of radial clearance at each tilt setting. For a standard test run, the feed pressure was set to give a γ value of $\frac{1}{4}$, $\frac{1}{2}$, 1 or 2 and the speed gradually increased until whirl began. Due to the asymmetry of the collet, it proved difficult to eliminate all unbalance from the rotor and, although the residual unbalance did not materially affect the whirl onset speed, it modified the way in which whirl appeared according to the clearance setting.

In theoretical studies, a convenient general form to indicate the extent of unbalance is given by ϵ_b in which the distance of the mass centre from the geometric centre is normalised with respect to the radial clearance. A value of $\epsilon_b > 0.3$ is sufficient to suppress all sub-synchronous frequencies, but for $\epsilon_b < 0.3$ half speed whirl occurs at approximately the same speed as for a perfectly balanced shaft together with synchronous whirl.


Figure 4, taken from A.G. Holmes (8), shows the amplitude of the half speed whirl component for an unbalance of $\epsilon_b = 0.2$. The data was derived from a Fourier analysis of the limit cycle motion found using short bearing theory. An inspection of Figure 4 shows that, as the stability threshold is approached, a small component of half speed motion arises, which appears on the orbit initially as a double loop and then as a cusp as the half speed component increases (9).

In the present work, the variation of clearance by a factor of four, together with a small and fixed value of residual unbalance gave a variation of ϵ_b over a range which was estimated to be 0.02 to 0.08. For large clearances, the onset of whirl was sudden and well defined, whereas for small clearances, whirl appeared initially as a double loop and then as a cusp as the speed was slightly increased, together with a general increase in size of the orbit. Figure 4 shows, for the comparatively large unbalance of $\epsilon_b = 0.2$, that the growth of a cusped orbit

becomes clear over the stability parameter range 0.16 to 0.14 which corresponds to a speed increase of 7%. It is interesting that Tondl (10) found in a comprehensive series of tests with different bearing types that unbalance did not affect the instability threshold.

All whirl conditions showed hysteresis in that once whirl was established it was possible to reduce the speed by about 30% below the onset speed before whirl ceased. The same effect was found by Tondl.

The experimental points for whirl onset conditions are shown in Figure 5.

 Groups of points run at the same clearance ratio c_r/R and are joined with dashed lines. The influence of feed pressure is clear for a line of points such as aa'. The solid lines attempt to join experimental points of constant γ regardless of clearance and loading intensity. The most interesting result is that loading intensity has no clear effect on stability.

The theoretical results in Figure 3 which assume cavitation at zero absolute pressure will now be reviewed. Comparing the two cases (a, $\theta = 0^\circ$, $P = 3.40$ bar; b, $\theta = 80^\circ$, $P = 0.59$ bar) it can be seen that effect of P is totally dominant. The experimental results do not show this trend, indeed there appears to be no effect of P on stability.

This implies that sub-ambient pressures were not present as assumed in the data of Figure 3, but that the cavitated area vented at atmospheric pressure as assumed in the Reynolds boundary condition.

To verify this conclusion the stability profile map for $\beta = 0$ was obtained and appears in Figure 6. This corresponds to the Reynolds boundary condition and is independent of P . Figure 6 gives fair correlation with the experimental results. The agreement between analysis and experiment on the effect of feed pressure is good.

On the phenomenon of cavitation in journal bearings, a number of questions are raised which, if examined in detail, must lie outside the scope of this paper. However, it is possible to reach some tentative conclusions. Dyer (1) has argued

that the occurrence of cavitation is initiated by a disturbance or discontinuity, such as an asperity or entrained bubble. It could be surmised that small fluctuations due to run out from out-of-round or unbalance effects could give a cyclically varying cavitation position which, by reason of its unsettled nature, promotes cavitation at ambient pressure. This hypothesis can be reinforced in the case of incipient whirl even if no run out or out-of-balance exists. Supposing that negative pressures and a large film extent do occur, the bearing would be temporarily unstable. The resulting growth of the orbit could provide the necessary disturbance to promote ambient cavitation and a return to steady running.

It is significant that in the experiments reported by Dyer (1) tensile pressures occurred during single individual revolutions of the shaft. Subsequent revolutions gave a cavitated film until conditions settled and the tensile pressures were repeated.

The hypothesis can also be supported weakly from minimum energy considerations in that more energy is absorbed in whirl than in steady running, so that the film will self-adjust to promote minimum dissipation.

An interesting situation would arise if the temporary instability referred to above was strong rather than slight. This could give large initial displacements (equivalent to shock loading) which might grow rather than damp out. This effect, which is illustrated by the hysteresis or continuation of whirl in stable regions once initiated, is due to non-linear effects within the film and could be an explanation for the scatter of experimental results seen in part of Figure 5.

The effect of system damping to restore stability has been considered in recent publications (e.g. 11, 12). A quantitative assessment of damping is given by the real parts α of the eigenvalues $\lambda = \alpha \mp i\beta$ defined in equation (9). The largest value of α is taken as α_c and indicates the reserve of system damping. For example if $\alpha_1 = -1, \alpha_2 = -2$ then $\alpha_c = \alpha_1 = -1$. If α is strongly negative, then the damping is correspondingly strong.

Figure 7 shows a plot of α_c for $L/D = 0.25$ and $\gamma = \beta = 0$. The curve for $\alpha_c = 0$ corresponds to the stability threshold found using the Routh criterion. Of

particular interest are the regions for high and low eccentricity ratio where the system damping is low. Figure 8 shows a further peculiarity at high eccentricity ratios. This figure, which is similar to data in [3], shows the response to unbalance in the direction of loading as a proportion of the unbalance ratio. The area of irregularly spaced contours at high values of eccentricity show that large amplitude aperiodic behaviour is likely, as found by A.G. Holmes in Figure 4 using non-linear methods.

Figure 7 and 8 are offered as further possible explanations for the scatter of experimental results which, for $L/D = 0.67$, is more pronounced at high and low eccentricity ratios.

A general conclusion of this paper is that, contrary to expectations, light loading does not affect the stability of a journal bearing. This is supported by the successful running of flexible test rotors in several reported cases, e.g. [2], [13], [14], [15], [16], where the bearing loading varied from 0.5 to 1.7 bar. In three of the references quoted [2,13,16], the loading was in the region 0.6 bar or less, under which almost pure Sommerfeld conditions could be expected, leading to strong instability over almost the whole speed range as shown in Figure 3(b), which corresponds to a loading of 0.59 bar. However, in none of these cases was half frequency whirl reported, although its possible occurrence was realised.

The previous work most relevant to the hypothesis outlined in this paper is a short discussion by Cole and Hughes (17) which is reproduced here in full.

"During the course of some film extent experiments on a transparent sleeve bearing (25 x 25 x 0.05 mm) with a single-hole entry, we have observed that whirl at a frequency near to half shaft speed may occur over a wide speed range but only while the film remains complete. As soon as the film breaks, as a result of increased eccentricity ratio or changed oil-supply conditions, whirl ceases.

A cyclic effect which probably is associated with the construction of the test machine has been noticed. Whirl gradually builds up, then the film breaks down, whereupon whirl ceases and the complete film is formed again, permitting

the whole cycle to repeat. If the oil supply is shut off, this state of affairs continues until insufficient oil remains in, or near, the bearing to maintain a complete film."

The discussion offers further explanation for the experimental scatter seen in Figure 5. The work by Cole and Hughes was subsequently published in more detail [18] but their earlier discussion describes the bearing behaviour more succinctly. In [18] it is further reported that control of the oil film extent by alteration of the inlet oil position increased the tendency to whirl if the film extent was increased and vice versa.

CONCLUSIONS

1. Within the context of the paper, the effect of leading intensity on film extent and the subsequent stability is small. The Reynolds boundary condition implying cavitation at ambient pressure appears to apply, regardless of load, for conditions close to the instability threshold.
2. It has been demonstrated that feed pressure exerts an influence on stability, most probably by its effect on film extent. Lower feed pressure enhanced stability.
3. For horizontal rotors where $F = \frac{1}{2}mg$ the stability parameter S reduces to $S = g/c_r \omega^2$. For a light feed pressure an approximate threshold value is $S = 0.2$. This gives the maximum allowable clearance as $C_r \approx 5g/\omega^2$ for horizontal rotors.
4. Slight unbalance has little effect on the stability threshold but can affect the manner in which whirl appears.

REFERENCES

1. DYER, D., and REASON, B. R.
"A study of tensile stresses in a journal bearing oil film",
J.M.E.S., 18, 1976, pp. 46-52.
2. WOODCOCK, J. S., and HOLMES, R.
"Determination and application of the dynamic properties of a turbo-rotor bearing oil film",
I. M. E. Tribology Conv., Brighton, 184, 3L, 1970, pp. 111-119.
3. HOLMES, R.
"The vibration of a rigid shaft in short sleeve bearings",
J.M.E.S., 2, No. 4, 1970, p.337.
4. HOLMES, R.
"Instability phenomena due to circular bearing oil films",
J.M.E.S., 8, No. 4., 1966, p. 419.
5. GUNTER, E. J.
"Dynamic stability of rotor bearing systems",
NASA, SP-113, 1966, p. 55.
6. STERNLICHT, B.
"Rotor stability",
I. M. E. Proc., 182, 3A, 1967-68, p. 82.
7. CAPONE, E.
"Oil whirl in Journal Bearings under no load conditions",
Wear 26, 1973, p. 207
8. HOLMES, A. G., ETTLES, C. M. M., and MAYES, I. W.
"Aperiodic behaviour of a rigid shaft in short journal bearings",
Int. J. for Num. Methods in Eng., 12, 1978, p. 695.
9. Gunter E. J.
op. cit. (5), p.135
10. TONDL, A.
Some problems of rotor dynamics,
Chapman and Hall, London, 1965, p.166

11. POLLMANN, E., and SCHWERTFEGER, H.
"Characteristic vibrations of flexural rotors in journal bearings",
I. M. E. Conf. on Vibrations in Rotating Machinery, 1976, p.21.
12. HAHN, E. J.
"The excitability of flexible rotors in short sleeve bearings",
ASME, J. Lubn. Tech. January 1975, p.105.
13. MAYES, I. W., and DAVIES, W. G. R.
"The vibrational behaviour of a rotating shaft system containing a
transverse crack",
I. M. E. Conf. on Vibration in Rotating Machinery, 1976, p. 53.
14. POPE, A. W., and HEALY, S. P.
"Anti-vibration journal bearings",
Proc. Inst. Mech, Engrs., 181, 3B, 1966-67.
15. TONDL, A.
op cit (9), p. 156.
16. PINKUS, O.
"Experimental investigation of resonant whip ",
Trans. ASME, 78, 1956, p. 975.
17. COLE, J. A. and HUGHES, C. J.
Discussion to "Investigation of translatory fluid whirl in vertical
machines" by Boeker, G. F. and Sternlicht, B.
Trans. ASME, 78, 1956, p.13.
18. COLE, J. A.
"Film extent and whirl in complete journal bearings",
I. M. E. Conference of LUBrication and Wear, 1957.

LIST OF FIGURES

- Figure 1 : Rotor and bearing assembly
- Figure 2 : Contours of film pressure showing the influence of feed pressure on the film extent for $\epsilon_0 = 0.4$, $\beta = 0.5$, $\gamma = 0, \frac{1}{2}, 1, 2$
- Figure 3 : Profile stability map for:
(a) $\theta = 0^\circ$, $L/D = 0.67$
(b) $\theta = 80^\circ$, $L/D = 0.67$
- Figure 4 : The amplitude of half frequency whirl motion of a stiff rotor with unbalance of $\epsilon_b = 0.2$ (from A. G. Holmes for short bearing theory)
- Figure 5 : Experimental stability points for bearing with:
(a) $L/D = 0.25$
(b) $L/D = 0.67$
- Figure 6 : Stability profile map assuming Reynolds conditions of cavitation, $L/D = 0.67$
- Figure 7 : The system damping for a circular journal bearing where $L/D=0.67$ $\gamma = \beta = 0$, The values on the curves are the largest real part α_c of the eigenvalues (Equation 9)
- Figure 8 : The forced response to unbalance in the direction of loading shown as a proportion of the unbalance eccentricity ratio ϵ_b , for a circular bearing where $L/D = 0.25$, $\gamma = \beta = 0$. The values on the curves show response amplitude.

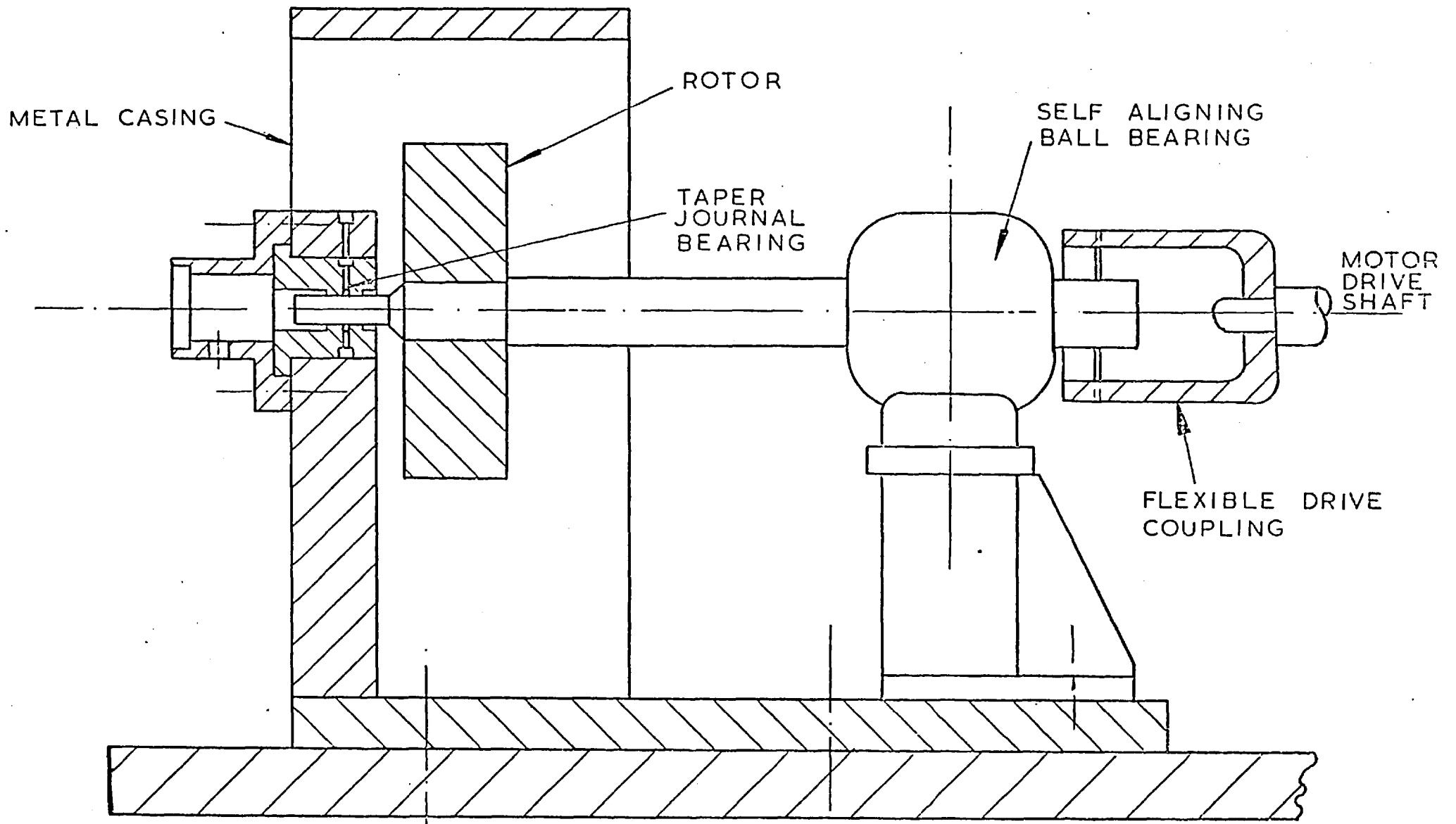


FIG.1

GENERAL ARRANGEMENT OF SHAFT AND ROTOR SYSTEM

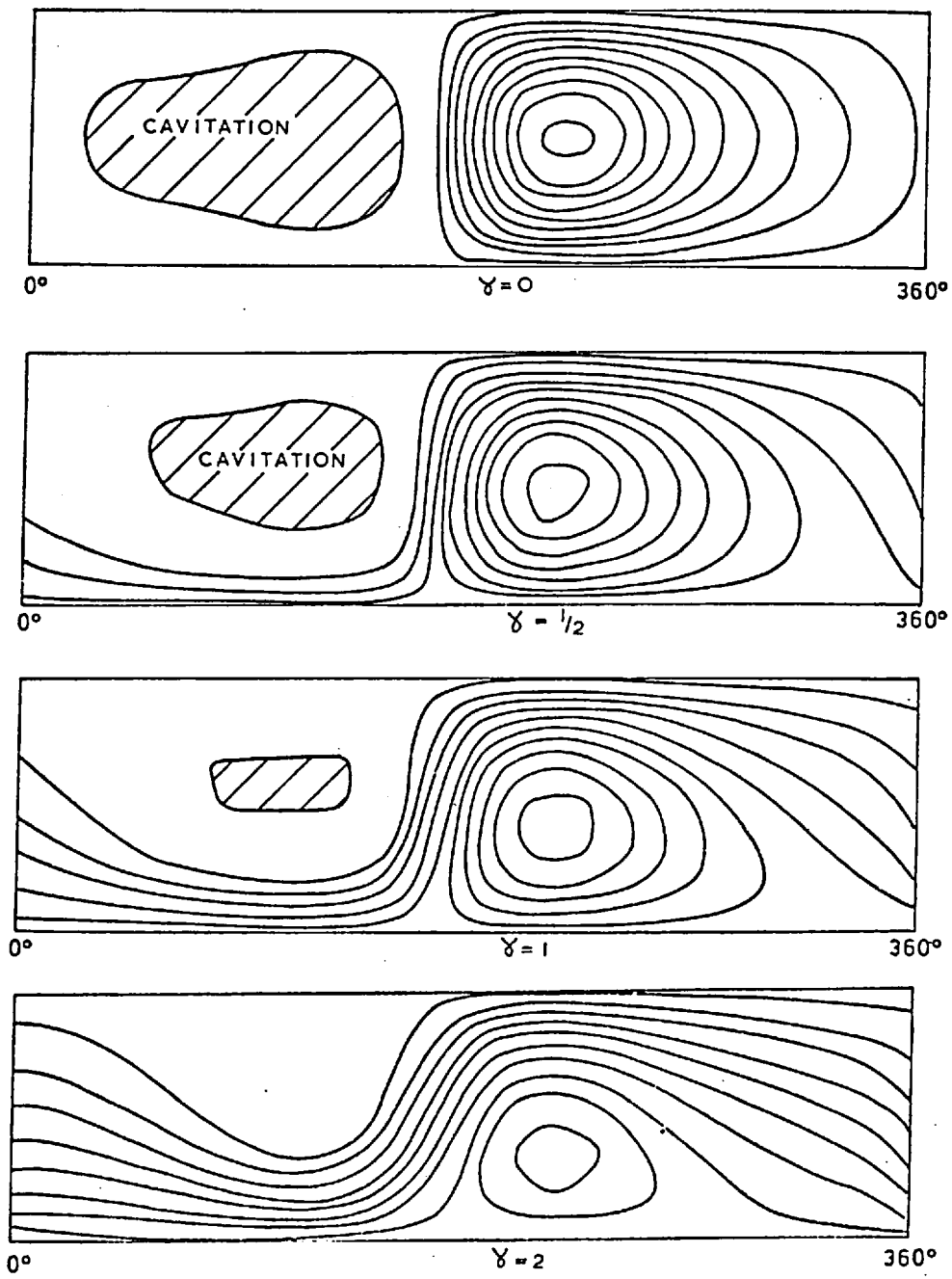


FIG. 2

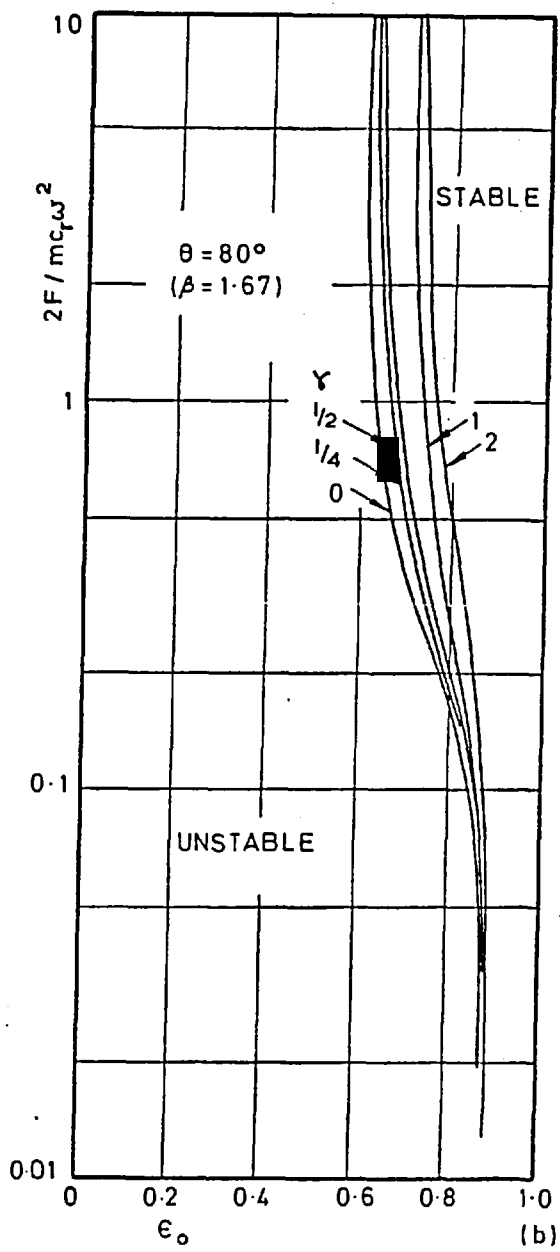
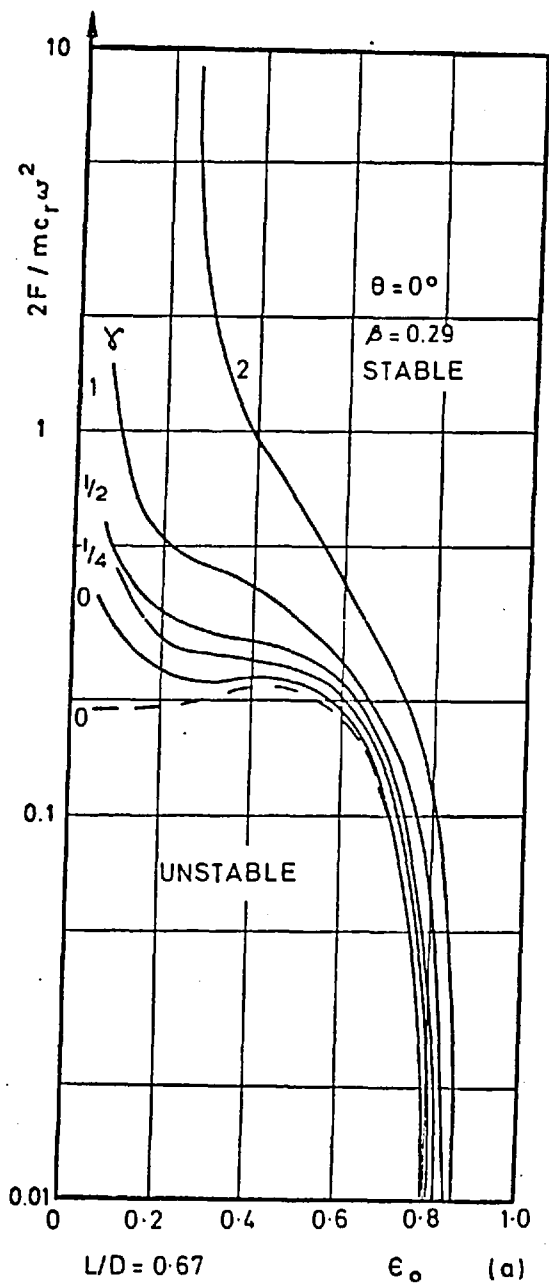


FIG. 3.

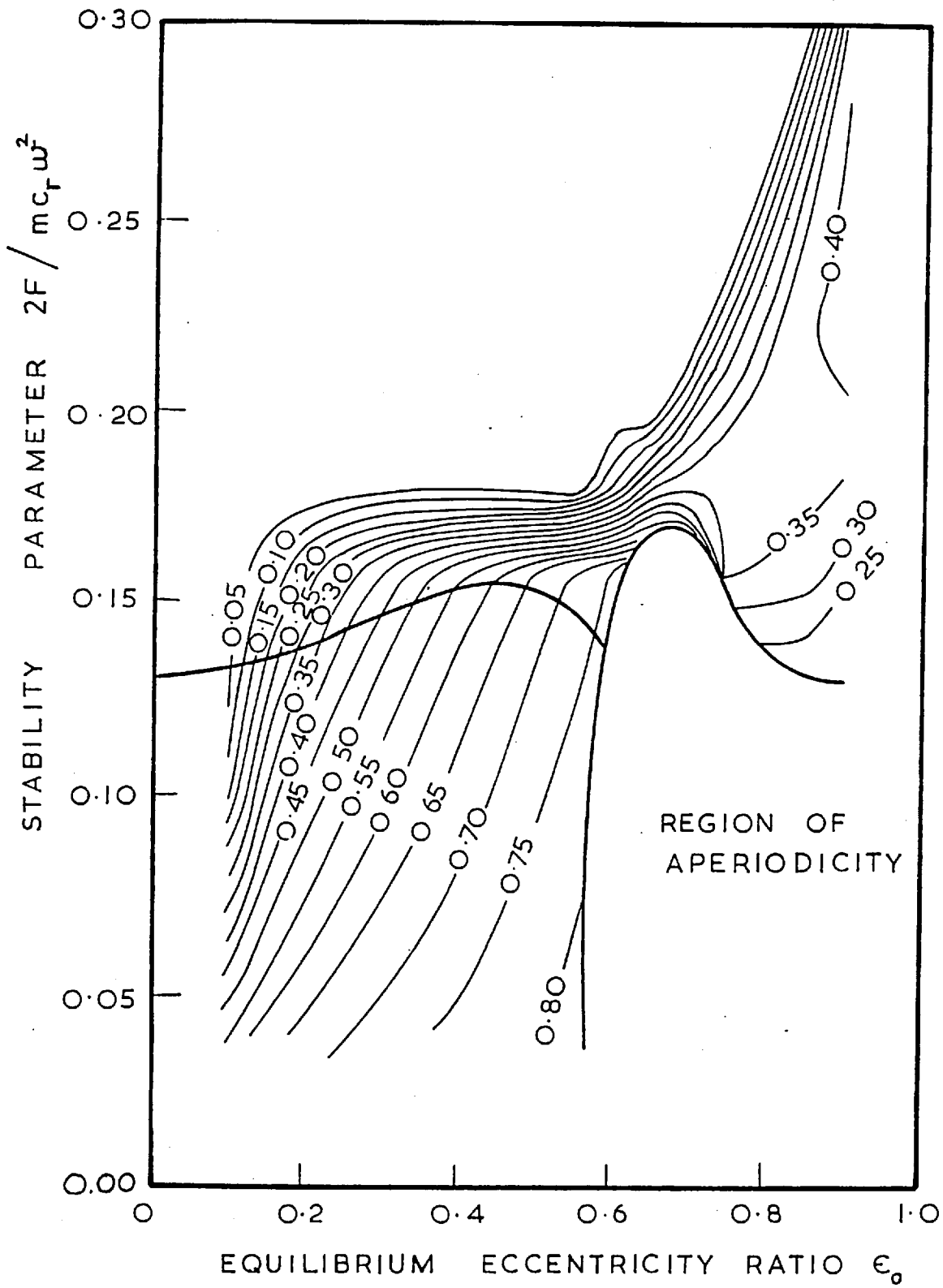


FIG. 4

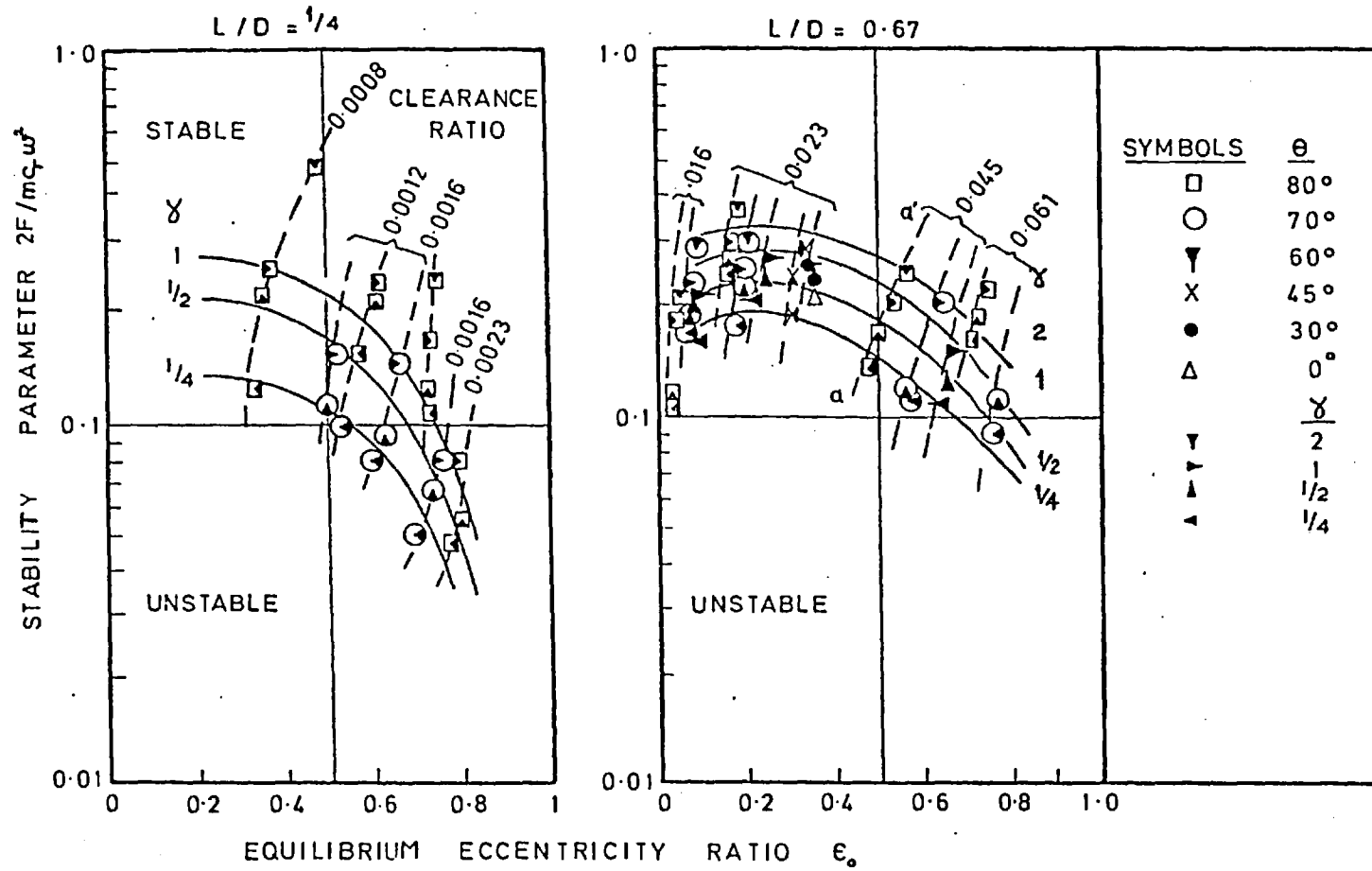


FIG. 5

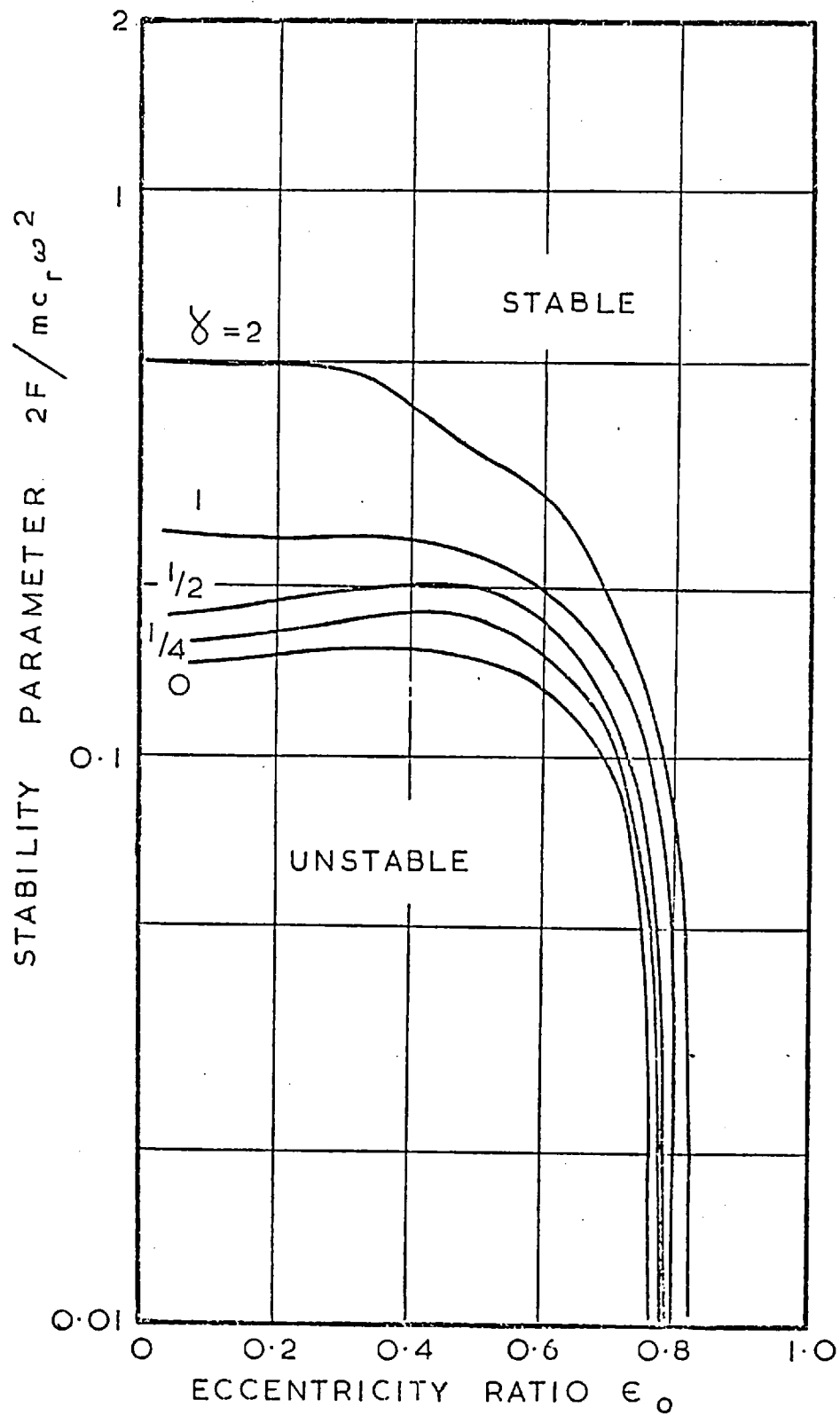


FIG.6

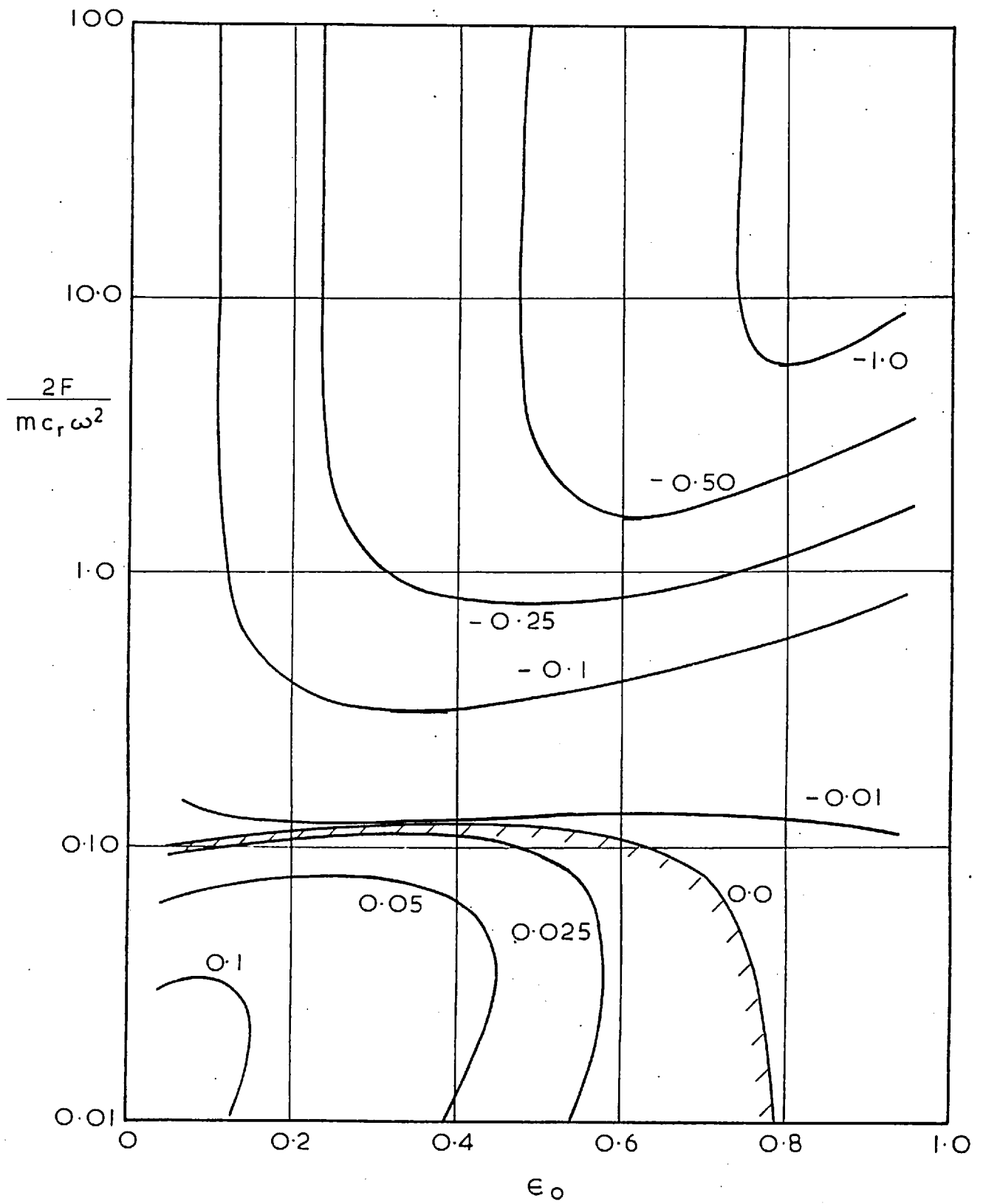


FIG.7.

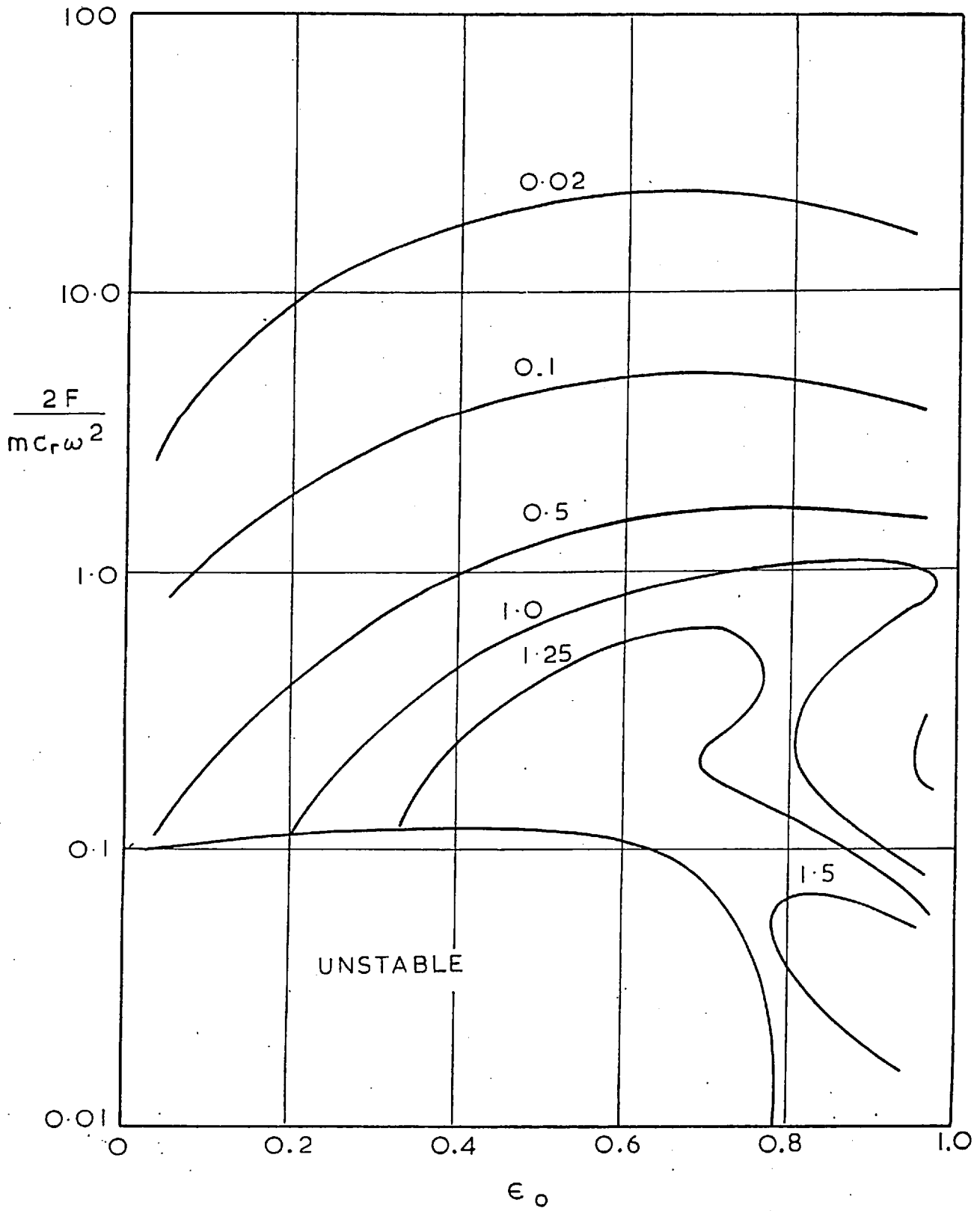


FIG.8



The Effect of Grooving and Bore Shape on the Stability of Journal Bearings

M. AKKOK and C. M. McC. ETTLES
Imperial College of Science and Technology
London SW7 2BX, England

The stability thresholds of four basic journal bearing types are found. Increasing groove size (up to 90°) is found to exert a strong destabilizing effect. Increasing aspect ratio (L/D) also has a destabilizing effect. The stability of each type was found to improve progressively with preload.

The influence of bore shape was found to be less important than groove size, α , or preload, δ . For fixed values of α , δ and L/D, the bore shapes in increasing order of stability were found to be: circular, lemon bore, offset halves, three-lobe. Some variations on the three-lobe design are investigated.

INTRODUCTION

The whirling of a rotor usually originates from two different classes of vibrations; self-excited vibrations and forced vibrations.

Examples of self-excited or free vibrations include the "oil whip" of a rotor supported on fluid film journal bear-

ings and the unstable motion of a rotor carrying components with a light shrink fit. Forced vibration can be caused by noncircularity of the shaft, unbalance or excitation from steam or coupling forces.

In the past decade, much effort has been spent on the development of analytical techniques to predict rotor behavior. It has been demonstrated analytically and by experiment [e.g. (1)] that, as a flexible rotor is brought to speed, the system passes through one, two or even three resonances associated with the bending modes.

The upper limit of operation is given by self-excited oil whip originating from the bearings. Recent experimental work by Leader and others (2) with a single-mass, flexible rotor clearly demonstrates the sequence of events. In (2), it is also shown that bearing type (or bore shape) exerts a strong influence on the threshold of oil whip.

There are several journal bearing bore shapes in common use. These include, apart from the classic circular bore bearing, the lemon bore, three-lobe, offset halves, and pivoted pad. Within each type, there is a range of further parameters which are thought or known to affect stability. These include preload, groove extent, feed pressure, inertia effects, and top-half relief. Little is known of the stability

Presented at the 34th Annual Meeting
in St. Louis, Missouri,
April 30-May 3, 1979

NOMENCLATURE

a_{xx} , etc. = damping coefficient of bearing
 c = radial clearance between arcs and shaft before preload is applied
 c_m = minimum local clearance when bearing and shaft are concentric (Fig. 1)
 D = bearing diameter
 e = eccentricity of shaft center from bearing center
 e_p = preload of bearing arc (Fig. 1)
 e_m = distance of rotor mass center from geometric center
 F = load on bearing
 k_{xx} , etc. = stiffness coefficient of bearing
 L = axial length of bearing
 M = mass of rotor associated with bearing

N = shaft speed (rev/s)
 P = projected loading, F/LD
 R = shaft radius
 Re = Reynolds number, $\rho U c / \eta$
 S = Sommerfeld number, $P c^2 / N \eta R^2$
 S_o = stability parameter, $F / M c \omega^2$
 α = groove size (degrees) (Fig. 1)
 γ = damping
 δ = preload, e_p / c
 ϵ = eccentricity ratio, e / c_m
 η = viscosity
 λ = stability root
 ρ = lubricant density
 ω = shaft spin velocity, $2\pi N$, (rad/s)
 ω_{n1} , ω_{n2} = natural frequencies of bearing

characteristics of each basic type, and very little for variations on each type.

The development of bearings for turbomachinery has, until recently, proceeded on an *ad hoc* basis. For example, it has long been industrial practice to use top-half relief and large "scallop" feed grooves which subtend angles of up to 90°. The purpose in using such "cutaway" bearings has been to reduce friction and temperature rise. The effect on stability of these departures from the basic bore shape is largely unknown. In this connection, recent suggestions (3) that, for conservation of energy, the losses in turboset journal bearings be further reduced seem fraught with undesirable consequences for rotor behavior. The bearing losses in machines of about 500 MW are in the region of 0.5 percent or less, giving little room for improvement.

This paper attempts to supply basic information on the effect of grooving and bore shape on stability. The relevance of the results presented is discussed in the light of the small amount of published experimental work carried out in this area.

ANALYSIS

The very simplest linearized analysis is used, assuming a stiff symmetric rotor of mass $2M$ on identical bearings. The translatory rather than conical mode of motion is considered. Given the eight linearized coefficients of a bearing, it is possible to carry out the most sophisticated analysis of rotor behavior [e.g. (4)]. However, this is not the purpose of this work which is to concentrate specifically on bearings.

The stability analysis, which is detailed in Appendix 1, produces a variable, $S_0 = F/Mc\omega^2$, where F is the bearing load, M is the associated mass, c is a reference clearance (to be described), and ω the rotational speed of the shaft (rad/s). This variable has appeared in various forms in other treatments, where it is often called the critical mass. Other forms include its inverse, square root (or both), or the substitution of $LD\eta N(R/c)^2 \propto F$ for the load term. The basic form S_0 is used in this work.

For any given bearing, the linearized analysis produces a threshold value of S_0 below which the bearing is unstable. Concerning this type of analysis, Lund and Thomsen (5) write: "The critical mass may be considered as a measure of a particular bearing type's sensitivity to instability." This implication will now be examined in detail to justify the analysis and also to show its shortcomings.

RELEVANCE OF THE ANALYSIS

The theoretical aspects of rotor dynamics have provided pleasure and employment for many years. There has been a strong imbalance between theoretical work and its experimental verification, particularly in practical situations.

A weak justification for the linearized analysis method is that the alternative nonlinear approach gives the same stability threshold. The nonlinear analysis method assumes a small initial perturbation and the subsequent orbit path is found by solving the equations of motion over small discrete time intervals. That the same *threshold* value is found has been demonstrated in, for example, (6), (7) and (8). The nonlinear method can yield more information than the

linearized approach, particularly on the existence of limit cycles beyond the threshold and on the effect of unbalance.

Experimental Verification

In (9), the stability of a 500 MW turboset is considered. The rotor system consisted of seven solid-coupled rotors on fourteen bearings. The presence of steam piping caused uneven thermal distortion of the foundation, changing the load distribution (F) among the bearings. However, the mass (M) associated with each bearing remained unchanged. Severe whirl occurred.

The form of stability parameter preferred by the authors, $S_0 = F/Mc\omega^2$, is particularly relevant in this case, since F varies while $Mc\omega^2$ does not (at constant speed).

By considering the elasticity of the shaft and the disturbed catenary, it was possible to calculate the new values of S_0 at each bearing and to demonstrate that, at some bearings, the value of S_0 was beyond the stability threshold.

The problem was rectified by misaligning the catenary in the cold condition so that, when hot, the bearings ran in a stable condition. The theoretical basis of this action was later treated in detail (10).

Some excellent experimental work with a stiff rotor is reported by Lundholm for circumferentially grooved bearings (11) and bearings with one or two narrow axial grooves (12). For both bearing types, Lundholm found good agreement for the onset of whirl at calculated critical mass values.

Stability experiments at zero load are widely reported by Schuller and others (6), (13) for lobed bearings with preload and offset. Comparison with theoretical results in (13) was poor and was attributed to a departure of the actual geometry to that assumed. However, in (6), agreement between theoretical and experimental stability thresholds was good. In this work, it was shown that the three-lobed bearing can operate above the threshold by forming a limit cycle. This has also been experimentally confirmed by Capone (14) for circular bearings under zero load.

The experimental work of Edwards and others (15) is unusual and concerned with the natural frequencies of a bearing carrying a stiff rotor. The frequencies, ω_n , can be obtained from the roots of the perturbed motion, $\lambda = \gamma \pm i\omega_n$ (see Appendix 1). Agreement with experiment was fair.

A recent experimental study by the authors (16) was concerned with the effect of load intensity and feed pressure on the whirl threshold. At very light loading, a bearing could be expected to operate at near Sommerfeld conditions and to be very unstable. It was shown that, even under loads of $P = F/LD = 0.5$ bar, cavitation appeared to take place at atmospheric pressure which had a stabilizing effect.

To account for this, a "continuous agitation" hypothesis was formed in which unbalance or out of round caused agitation of the cavitation boundary and allowed the film to vent at atmospheric pressure. In the absence of such synchronous forcing, it appeared that the bearing *would* begin to whirl, giving the necessary disturbance of the cavitation boundary and a return to steady running. Further evidence to support this is given by Lundholm (11) for $P = 1.67$ bar, who writes (page 70): "When the speed approached critical, very small vibrations occurred. The onset speed of these

small vibrations was too diffuse to be determined. At that speed which was taken as critical the vibrations suddenly changed to very large."

Unbalance Response

A limited amount of experimental work has been cited to demonstrate the effectiveness of simple stability analyses. It is worth mentioning that the agreement of response calculations with experiment is less good. Orcutt and Arwas (17) show fair agreement with predicted and test orbits. An attempt by Morton (18) to derive linear coefficients from excitation showed fairly poor agreement with analysis.

It might be expected that the onset of whirl stability could be more accurately predicted than response, since the analysis is concerned with infinitesimally small excursions about the equilibrium position which either grow or decay. In contrast to this, experiments by Tondl (19) have shown that the stability threshold is not greatly affected by unbalance. The authors reached the same conclusion in (16).

The nonlinear analysis in (8) showed that, with an unbalanced rotor, an increasing proportion of half-synchronous motion appears as the stability threshold is approached, causing a more gradual onset of whirl than the sudden large amplitude motion observed by Lundholm (11).

ANALYSIS RESULTS

Range of Results

The six basic types considered are shown in Fig. 1. All except for the circular bearing are geometrically "preloaded," which is defined by the parameter $\delta = e_p/c$. The reference clearance, c , is defined as the radial clearance before preload. The effect of varying groove size, α , on stability has not been investigated previously, and this, together with the preload, δ , form the main variables within each type.

The effect of aspect ratio (L/D) is found for some cases and for the lemon bore bearing only the effect of Reynolds numbers up to 10 000 is found. This is defined as $Re = \rho U c / \eta$, and is based on the reference clearance. The effective turbulent viscosity relationships proposed by Constantinescu (20) were used for this section of the work.

The feed grooves were considered to extend for the whole axial length of the bearing and to be at zero pressure. In (11) and (16), both concerned with circumferentially grooved bearings, it was shown that feed pressure below about $0.25 P$ has a marginal effect on stability. The feed pressures used in practice are usually far below this figure.

In all cases, the load is assumed to be vertically downwards (Fig. 1). This is probably a serious departure from practice since horizontal as well as vertical misalignment of rotor systems can occur. Although the effect of nonvertical loads could be found without extra difficulty, the volume of data would be excessive for a single paper.

Presentation and Discussion of Results

The majority of results are presented as stability maps of the threshold value of $F/Mc\omega^2$ against the dual (horizontal) scales of $\epsilon = e/c_m$ and Sommerfeld capacity, $S = Pc^2/N\eta R^2$. The eccentricity ratio is defined from e , the distance of the shaft center from the bearing center when the bearing is

supporting a downwards load, and c_m the minimum clearance of the bearing when the shaft and bearing are concentric (see Fig. 1).

The Circular Bore Bearing

The effect of groove size, α , on stability is shown in Fig. 2 for $L/D = 1/2$. The full line for $\alpha = 0^\circ$ is close to the classical result for a bearing with no grooves. For this bearing and others, $\alpha = 0^\circ$ denotes a line groove at zero feed pressure. The groove sizes in common use, $\alpha = 60^\circ$ to 90° , have a considerable destabilizing effect.

A single case for $L/D = 1$, $\alpha = 60^\circ$, is given in Fig. 2 and should be compared with $L/D = 1/2$, $\alpha = 60^\circ$. It can be seen that increasing L/D also has a destabilizing effect.

In general, the same effects for increasing groove size and increasing L/D are followed for other bearing types.

The Lemon Bore Bearing

The effects of preload (for $\alpha = 60^\circ$) and groove size (for $\delta = 0.6$) are shown in Figs. 3(a) and 3(b). This type of bearing is widely used and comparison with Fig. 2 shows a considerable advantage over the circular type. Stability increases progressively with preload, although it must be taken into account that, in practice, as the preload is increased so is the reference clearance, c .

The effects of turbulence are shown in Fig. 3(a) for the case $\alpha = 60^\circ$, $\delta = 0.6$, $L/D = 1/2$. Increasing turbulence has only a mild destabilizing effect, the effects of preload or groove size being much stronger.

The introduction of an effective turbulent viscosity (based on local Reynolds number) gives a variation of viscosity around the bore. In (21), a study is made of the effect of varying local viscosity due to heating. A similar conclusion is reached, in that there is only a moderate decrease of stability with decreasing viscosity index.

Figure 4(a) confirms the destabilizing effect of L/D ratio for $\alpha = 0^\circ$. Figure 4 (b) gives the Sommerfeld capacity for $L/D = 1/2$, $\alpha = 60^\circ$ and varying Reynolds number.

The Offset Halves Bearing

This type of bearing is not widely used in practice and little is known of its stability characteristics, although it is classed as an "antiwhirl" bearing. Figure 5(a) shows the ef-

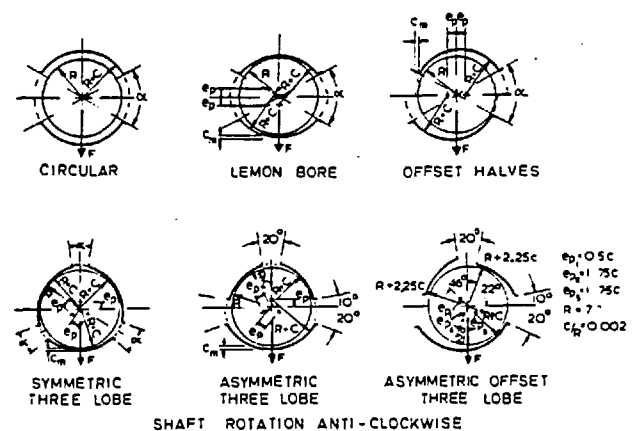


Fig. 1—Bearing types considered

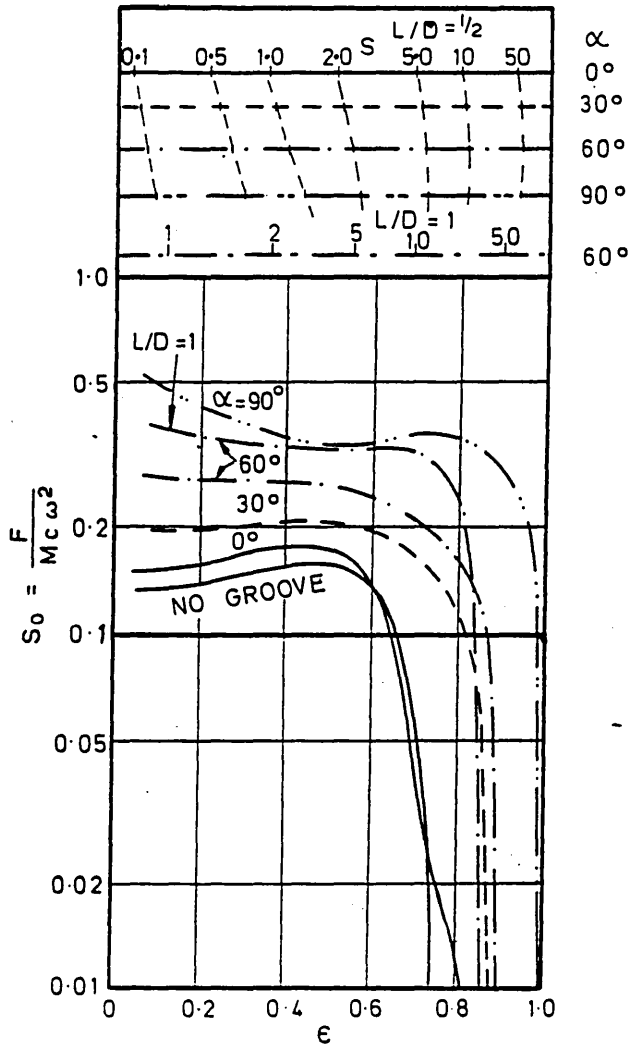


Fig. 2—Circular bore bearings. The effect of groove size and L/D ratio on stability.

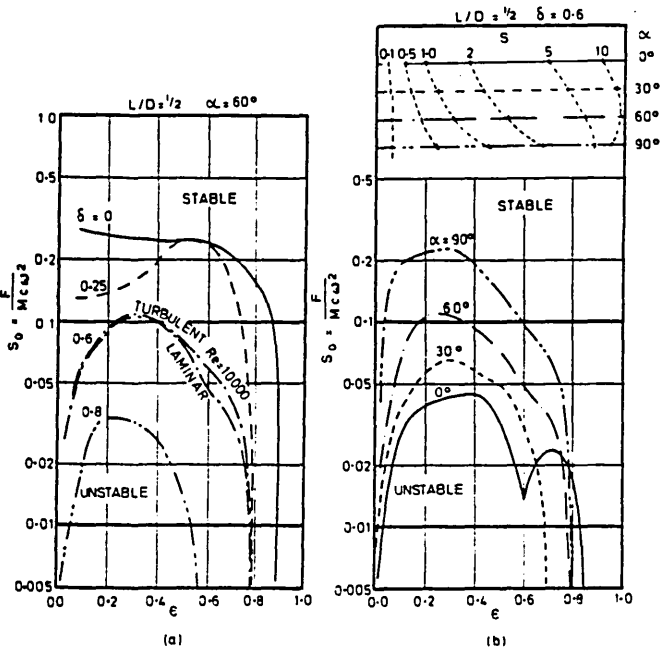


Fig. 3—The lemon bore bearing
 (a) The effect of preload and Reynolds number on stability, $\alpha = 60^\circ$
 (b) The effect of groove size on stability, $\delta = 0.6$

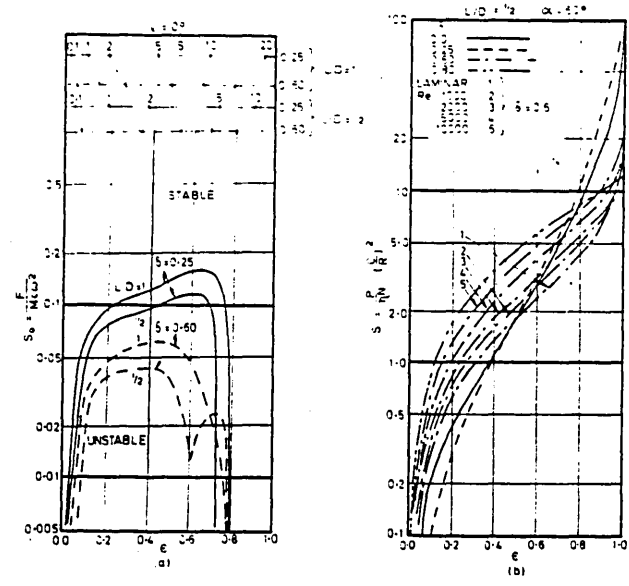


Fig. 4—The lemon bore bearing
 (a) The effect of L/D and preload on stability, $\alpha = 0^\circ$
 (b) Sommerfeld capacity, $L/D = 1/2$, $\alpha = 60^\circ$, varying preload and Reynolds number.

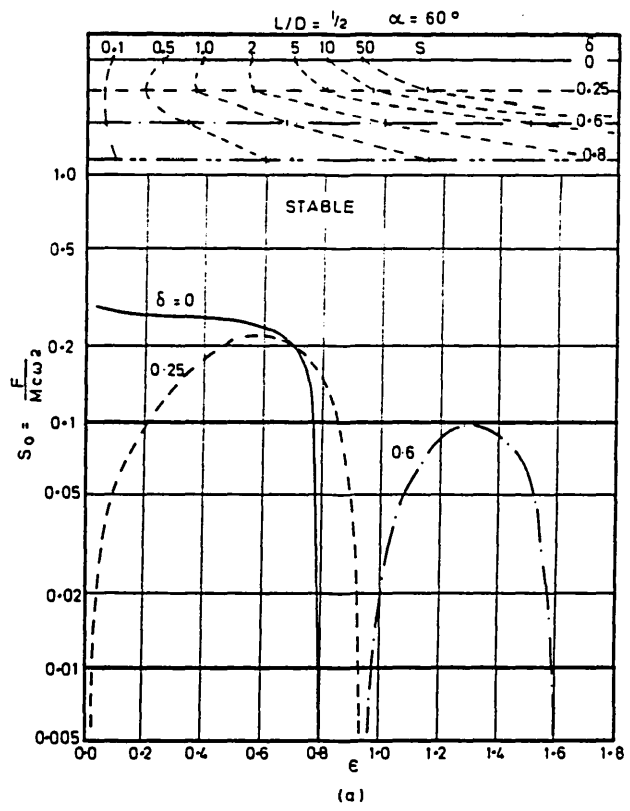


Fig. 5—The offset halves bearing
 (a) The effect of preload and L/D on stability, $\alpha = 60^\circ$

fect of preload for $\alpha = 60^\circ$, $L/D = 1/2$. The effect of increasing preload is more marked than for the lemon bearing, particularly at eccentricities of up to 0.5. For $\delta = 0.6$, a single case for $L/D = 1$ is plotted, which again shows the destabilizing effect of increasing aspect ratio.

The effect of increasing groove size [Fig. 5(b)] is to give increased stability. This trend is contrary to the circular and offset types.

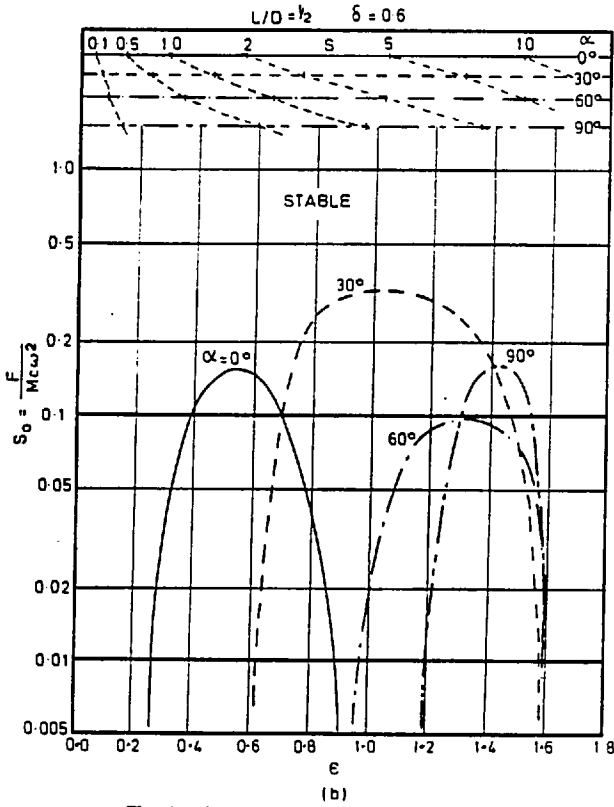


Fig. 5—The offset halves bearing
(b) The effect of groove size on stability, $L/D = 1/2$, $\delta = 0.6$

The Symmetric Three-Lobe Bearing

In this basic type of bearing, the three arcs are of equal size and have equal preload. The effect of preload is particularly marked, as shown in Figs. 6(a) and 6(b), where $\alpha = 0^\circ$ for both cases. One case where $\alpha = 20^\circ$ is also shown.

The Asymmetric Three-Lobe Bearing

Although the symmetric three-lobe bearing is known to have satisfactory stability properties, the Sommerfeld capacity can be improved by increasing the size of the bottom arc. In turbines, this also gives advantages in disassembly of the top casing for inspection. The example considered (see Fig. 1) has a bottom arc of 140° and two top arcs of 70° , giving two 30° grooves near the horizontal split line and a 20° groove at the top of the bearing. The same preload is applied on each arc. The attitude angle curve in Fig. 7(a) shows that the minimum film thicknesses occur in the top arc for higher preloads. Figure 7(b) shows that the stability characteristics are good, although strongly dependent on preload.

The Asymmetric Offset Three-Lobe Bearing

This is a progression of the previous type in which the arcs are tilted as well as preloaded to give an offset film. The offsetting of the lobes in this way is reported by Falkenhagen (6) to have beneficial effects.

The design analyzed was that proposed by McGuire* in which the bottom arc is preloaded by 0.5 and the top arcs

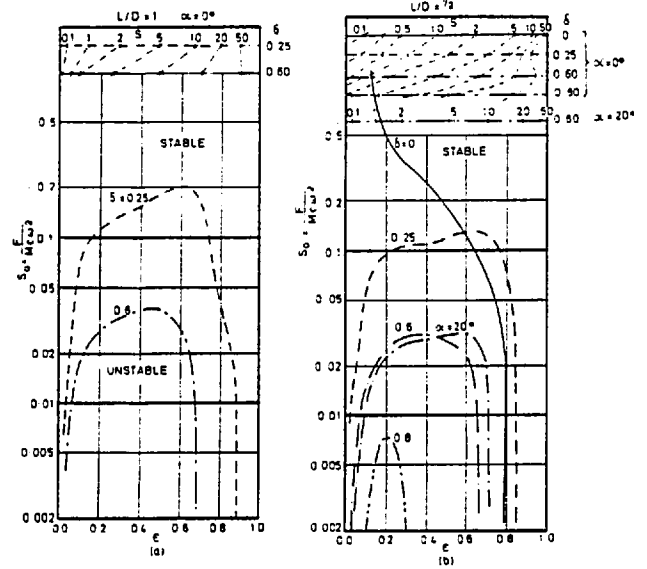


Fig. 6—The symmetric three-lobe bearing
(a) The effect of preload on stability, $\alpha = 0^\circ, 20^\circ$, $L/D = 1/2$
(b) The effect of preload on stability, $\alpha = 0^\circ, 20^\circ$, $L/D = 1$

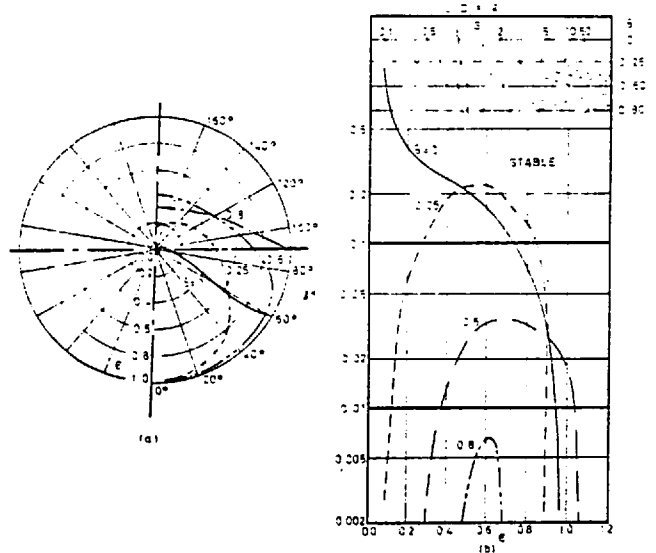


Fig. 7—The asymmetric three-lobe bearing (no offset)
 $L/D = 1/2$, $\alpha = 30^\circ$ at $\pm 90^\circ$ to load, $\alpha = 20^\circ$ at top of bearing (see Fig. 1)
(a) Locus paths due to static loading
(b) Effect of preload on stability

by 0.778. The top arcs are also offset by approximately 0.3.

The locus paths and stability threshold for certain variations of the geometry are shown in Figs. 8(a) and 8(b). In this instance, there appears to be little advantage produced by the offset but the stability characteristics are better than the lemon bore or offset halves bearings.

As a matter of interest, the stability characteristics were found of the HP turbine circular bearings in Ref. (9) which it is intended to replace with a design of three-lobe, offset bearing. The bearing [shown in Fig. 9(a)] has wide use for turbosets of the two bearings-per-rotor type. The important features of this bearing are feed scallops of 60° and a relief groove of depth $2.5c$ extending from scallop to scallop in the top half.

*See Acknowledgments.

The stability characteristic in Fig. 9(b) shows that a considerable improvement will result from replacement three-lobe bearings.

Pivoted Pad Bearings

Although this type of bearing has not been analyzed in this particular project, it is worthwhile to consider briefly the state of the art. Pivoted pad bearings are being increasingly used in European turbosets (22), (23) and in the USA. The design described in (22) is particularly interesting, and consists of three pads pivoted at approximately 20°, 160° and 260° from the vertical in the direction of rotation. The second pad of 110° extent is the largest and preload is supplied by spring loading of the top pad. It is claimed (page 335) that the dynamic behavior of the coupled rotors was "perfect."

A stability analysis of the simple type used in this work shows that pivoted-pad bearings with preload are always stable. However, there is some doubt as to their damping capacity. In the experimental investigations (2), (24), it is commented that, with flexible rotors, this class of bearing gave larger amplitudes at critical speeds than other types.

A contributing factor to low damping is shown in (23) to be thermal and elastic distortion of the pads. This is confirmed in (25) where the bearing coefficients of several complete assemblies were found experimentally. The

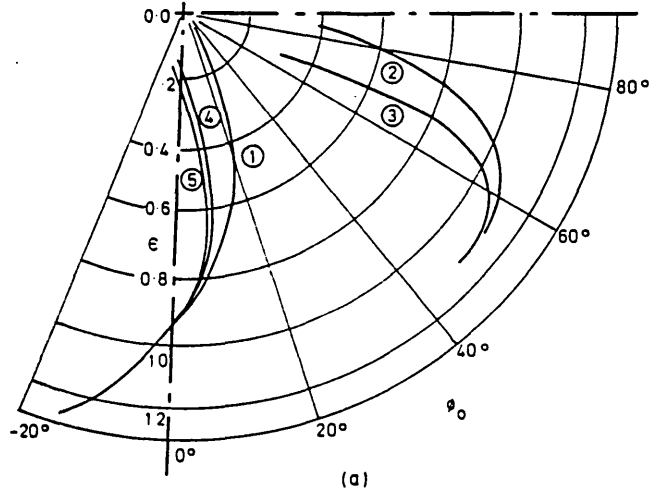
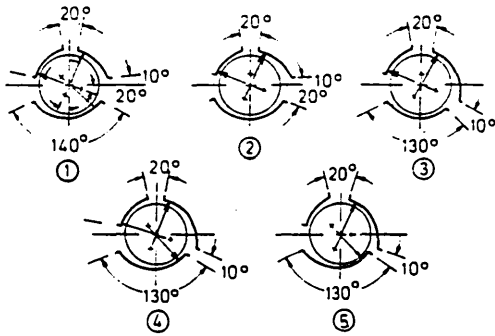


Fig. 8—The asymmetric three-lobe bearing with offset
(a) Locus paths due to static loading

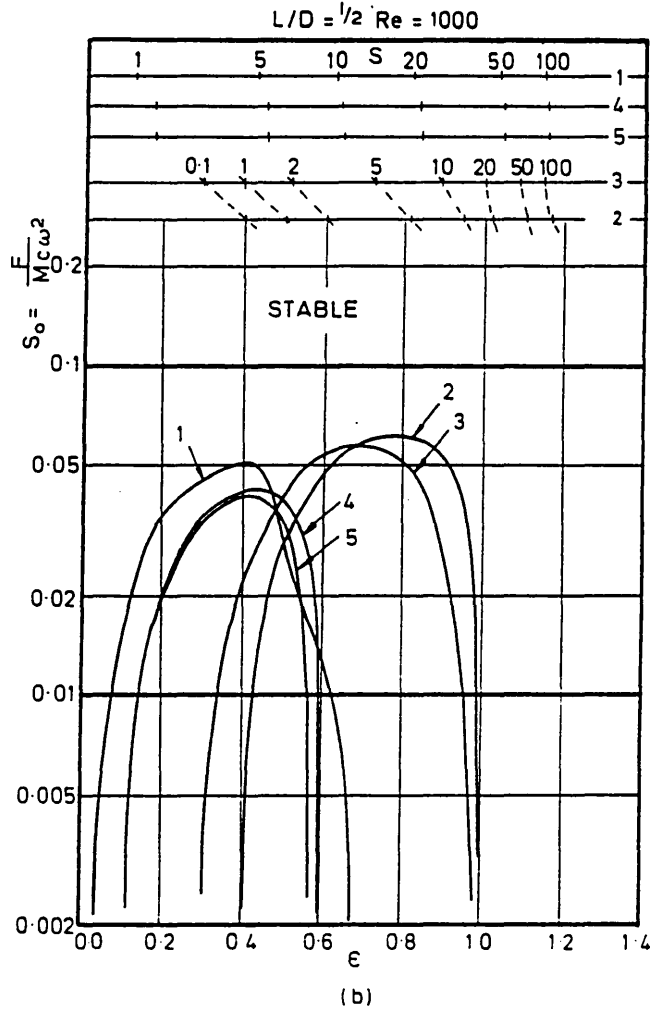


Fig. 8—The asymmetric three-lobe bearing with offset
(b) The effect of varying offset and groove size on stability

damping coefficients were found to be lower than the theoretical stiff pad values, particularly at high loads. Unpublished analysis work at the authors' college also confirms this trend.

A Comparison of Bearing Types

A review of Figs. 2 to 7 shows the preload and groove sizes are more important effects than the bore shape. In Fig. 10(a), the stability profiles are compared of all the bearing types considered in this work. Common values of $L/D = 1/2$, $\alpha = 60^\circ$ and $\delta = 0.6$ are used which represent usual design practice for bearings with two arcs. For three-lobe bearings, the same value of $\alpha = 60^\circ$ is inadmissible since this would give a bottom (load-carrying) arc of only 60° . A value of $\alpha = 20^\circ$ is used here for the symmetric type. Figure 10(a), therefore, gives a comparison of types for usual design practice. The reader can make an assessment for $\alpha = 20^\circ$ throughout for all the types considered by interpolation from Figs. 2, 3(b) and 5(b).

The various types of three-lobe bearing are clearly superior but this is partly due to small groove sizes considered. Figure 10(b) shows the Sommerfeld capacity of each type, and Fig. 11 presents the corresponding loci.

Response to Unbalance

Space limitations allow only a very brief review of this

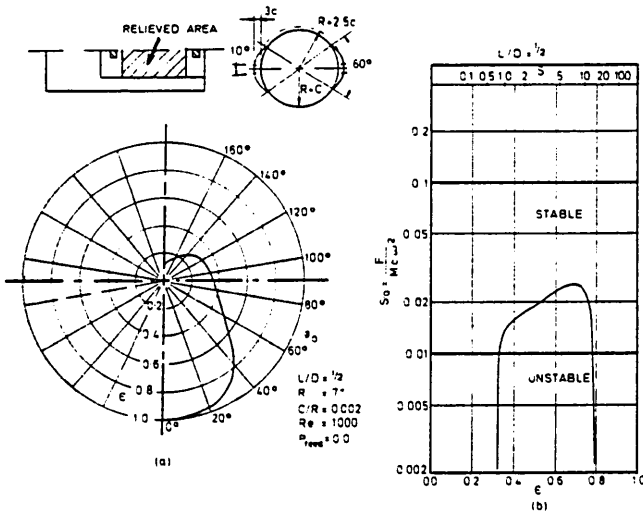


Fig. 9—The circular bearing with top half relief $L/D = 1/2$, $c/R = 0.002$, $Re = 1000$, zero feed pressure
(a) Locus path due to static loading
(b) Stability threshold

property, which is taken by some as being more important than stability. In practice, it is not possible to remove all forms of excitation, particularly those due to unbalance.

The simplified analysis in Appendix 2 derives the amplitude, X_n , normalized with respect to ϵ_n , the distance between the mass and geometric centers. With a stiff rotor, the amplitude of vibration increases as the stability threshold is approached. This is due to the reduction in system damping. Figure 12(a) shows the natural frequency of bearing vibration at the stability threshold. It should be noted that the frequency of the unstable motion is about 0.5ω only for the circular bearing.

Figure 12(b) shows the amplitude of vibration at a specific value of stability parameter, $S_0 = 0.3$, which is in the stable region for all types. The behavior of the lemon bore bearing is particularly interesting. Reference to the stability profile in Fig. 3(a) shows a peak (closest to the value $S_0 = 0.3$) is reached at $\epsilon \approx 0.3$. The response shows a marked increase at this point, and decreases as the stability threshold recedes from the value $S_0 = 0.3$. However, beyond $\epsilon \approx 0.8$, the amplitude increases rapidly. The response of a circular bearing is off scale.

Figure 12(b) illustrates a common fallacy that it is possible to stabilize a bearing by causing it to run at high eccentricity. Although all bearing types considered here show a "stable" area at high eccentricity, the damping is very low. This leads to high amplitudes of vibration which can be aperiodic (8).

CONCLUSIONS

1. The large feed grooves used in most turboset bearings exert a strong destabilizing effect. For purposes of stability, feed grooves should be as narrow as possible. Attempts at energy conservation by using severely "cutaway" bearings may have undesirable consequences for rotor behavior.
2. Increasing preload in all bore shape types exerts a strong, progressive stabilizing effect. However, when

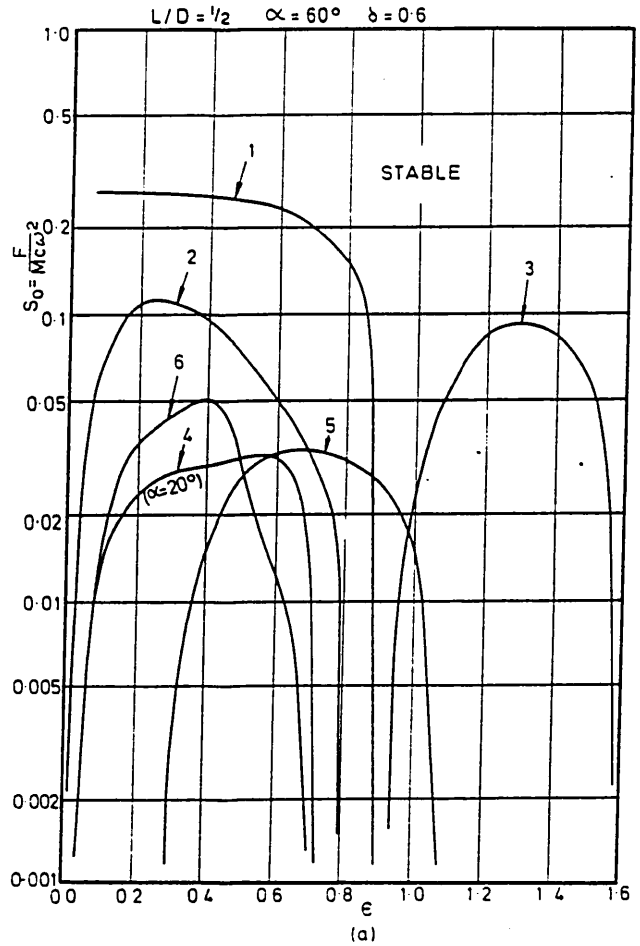


Fig. 10—A comparison of bearing types
(a) Stability threshold

viewing stability charts, it must be borne in mind that the reference clearance, c , must be increased approximately in proportion to preload.

3. The asymmetric three-lobe bearing with a large bottom arc is acceptable for practical purposes. The stability of this type is good but strongly dependent on preload.
4. Local variations of effective viscosity due to inertia or heating effects exert a mild destabilizing effect.
5. Groove size and preload exert a stronger influence on stability than bore shape. For typical fixed values of α , δ and L/D , the approximate order of increasing stability is: circular (least stable), lemon bore, offset halves, three-lobe.
6. Increasing L/D ratio exerts a destabilizing effect.
7. All bearing types are shown to be stable at high eccentricity ratio. However, vibration may be considerable due to low system damping.
8. The response to unbalance is a further important criterion for the assessment of a bearing design. The amplitude of vibration increases as the stability threshold is approached, but the rate of increase varies according to design.

ACKNOWLEDGMENTS

The authors wish to thank the following: C. E. G. B. West

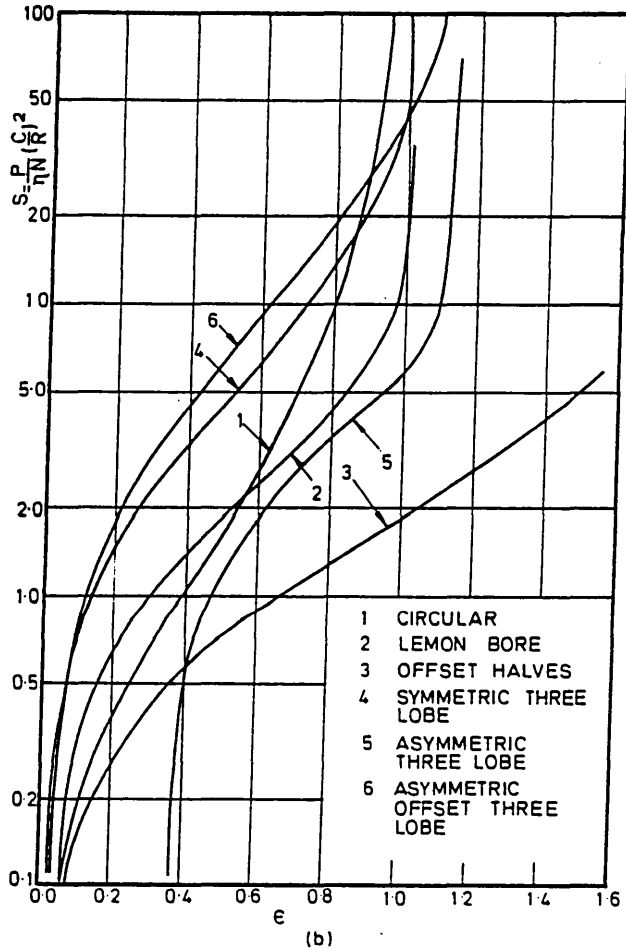


Fig. 10—A comparison of bearing types
(b) Sommerfeld capacity

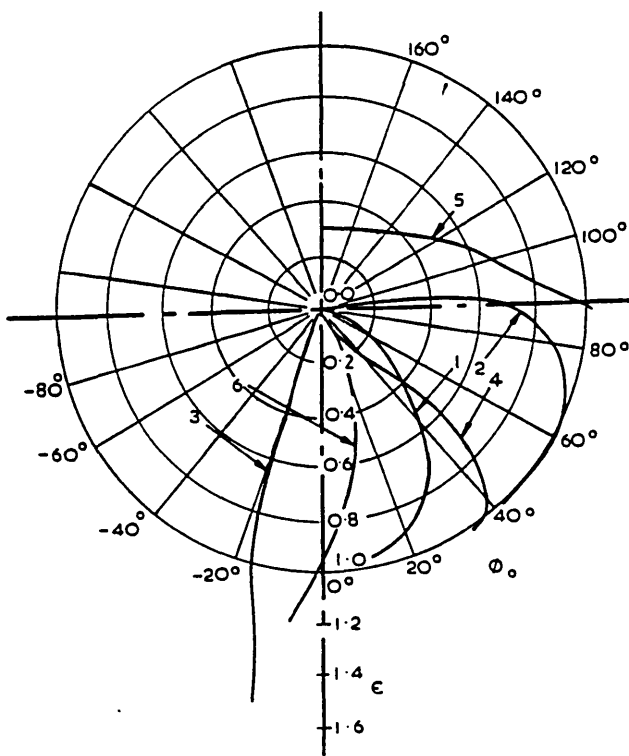


Fig. 11—A comparison of locus paths for different bearing types
 $L/D = 1/2$, $\delta = 0.6$, $\alpha = 60^\circ$ ($\alpha = 20^\circ$ for three lobe bearing)

Burton for commissioning this work; P. M. McGuire, of GEC Turbine Generators Limited, Rugby, for making available his suggestion of the asymmetric three-lobe bearing with offset of the arcs; the Science Research Council for support to M. Akkok under grant GR/A/1146.8.

REFERENCES

- (1) Lund, J. W., "Stability and Damped Critical Speeds of a Flexible Rotor in Fluid-Film Bearings," *ASME, J. Eng. Ind.*, p 509, May (1974).
- (2) Leader, M. E., Flack, R. D. and Allaire, P. E., "The Experimental Dynamic Response of a Single Mass Flexible Rotor with Three Different Journal Bearings," to be published *ASLE Trans.*
- (3) Wilcock, D. F., "Designing Turbulent Bearings for Reduced Power Loss," Second Leeds-Lyon Symp., Mech. Eng. Pubns., p 183, September 1975.
- (4) Black, H. F., Brown, R. D., France, D. and Jansen, D. N., "Theoretical and Experimental Investigations Relating to Centrifugal Pump Rotor Vibrations," *IME Conf. on Vibration in Rotating Machines*, p 198 (1972).
- (5) Lund, J. W. and Thomsen, K. K., "A Calculation Method and Data for the Dynamic Coefficients of Oil-Lubricated Journal Bearings," *Design Eng. Conf.*, May 1978.
- (6) Falkenhagen, G. L., Gunter, E. J. and Schuller, F. T., "Stability and Transient Motion of a Vertical Three Lobe Bearing System," *ASME, J. Eng. Ind.*, Paper 71-Vibr-76, 1976.
- (7) Akers, A., Michaelson, S. and Cameron, A., "Stability Contours for a Whirling Finite Journal Bearing," *ASME, J. Lubr. Tech.*, p 177, January (1971).
- (8) Holmes, A. G., Ettles, C. M. M. and Maves, I. W., "Aperiodic Behaviour of a Rigid Shaft in Short Journal Bearings," *Int. J. for Num. Methods in Eng.*, 12, p 695 (1978).
- (9) Ettles, C. M. M., Wells, D., Stokes, M. and Matthews, J. C., "An Investigation of Bearing Misalignment Problems in a 500 MW Turbo-Generator Set," *IME Proc.*, 188, Steam Plant Gp., p 403 (1974).
- (10) Holmes, A. G., Ettles, C. M. M. and Maves, I. W., "The Dynamics of Multi-Rotor Systems Supported on Oil Film Bearings," *ASME Paper No. 77-DET-29* (1977).
- (11) Lundholm, G., "The Circumferential Groove Journal Bearing Considering Cavitation and Dynamic Stability," *Acta Polytechnica Scandinavica*, ME42 UDC 621.822.57 (Box 3073, S-10242, Stockholm 5, Sweden) (1969).
- (12) Lundholm, G., "The Axial Groove Journal Bearing Considering Cavitation and Dynamic Stability," *Acta Polytechnica Scandinavica*, ME58 UDC 621.822.2 (1971).
- (13) Schuller, F. T., "Experiments on the Stability of Various Water-Lubricated Fixed Geometry Hydrodynamic Journal Bearings at Zero Load," *ASME, J. Lubr. Tech.*, p 434, October (1973).
- (14) Capone, E., "Oil Whirl in Journal Bearings Under No Load Conditions," *Wear*, 26, p 207 (1973).
- (15) Edwards, D. C., Khorzad, N. and Edwards, C. L., "Predicting Natural Frequencies of a Hydrodynamically Lubricated Journal Bearing With Constant Oil Supply Pressure," *ASME Paper No. 75-DET-72* (1973).
- (16) Akkok, M. and Ettles, C. M. M., "Load and Feed Pressure on Whirl in a Grooved Journal Bearing," *ASLE Paper No. 78-LC6B3* (1978).
- (17) Orcutt, F. K. and Arwas, E. B., "The Steady-State and Dynamic Characteristics of a Full Circular Bearing and a Partial Arc Bearing in the Laminar and Turbulent Flow Regimes," *ASME, J. Lubr. Tech.*, p 143, April (1967).
- (18) Morton, P. G., "Measurement of the Dynamic Characteristics of a Large Sleeve Bearing," *ASME, J. Lubr. Tech.*, p 143, January (1971).
- (19) Tondl, A., "Some Problems of Rotor Dynamics," Chapman and Hall, London, p 166, 1965.
- (20) Constantinescu, V. W., "The Pressure Equation for Turbulent Lubrication," *Conf. Lubr. and Wear, Proc. IME*, 182 (Part 3A), p 132 (1967-68).
- (21) Nikolajsen, J. L., "The Effect of Variable Viscosity on the Stability of Plain Journal Bearings and Floating Ring Journal Bearings," *ASME, J. Lubr. Tech.*, p 447, October (1973).
- (22) Varga, Z., "900 mm Pivoted-Pad Journal Bearing for Steam Turbines—Characteristics and Testing," *Brown Boveri Rev.*, 6, p 325 (1977).
- (23) Nilsson, L. R. K., "The Influence from Bearing Flexibility on the Dynamic Performance of Radial Oil Film Bearings," 5th Leeds-Lyon Symposium, MEP Limited, 1978.
- (24) Pollman, E. and Schwerdtfeger, H., "Characteristic Vibrations of Flexural Rotors in Journal Bearings," Paper C163/76, *IME Conf. on Vibrations in Rotating Machinery*, p 21 (1976).

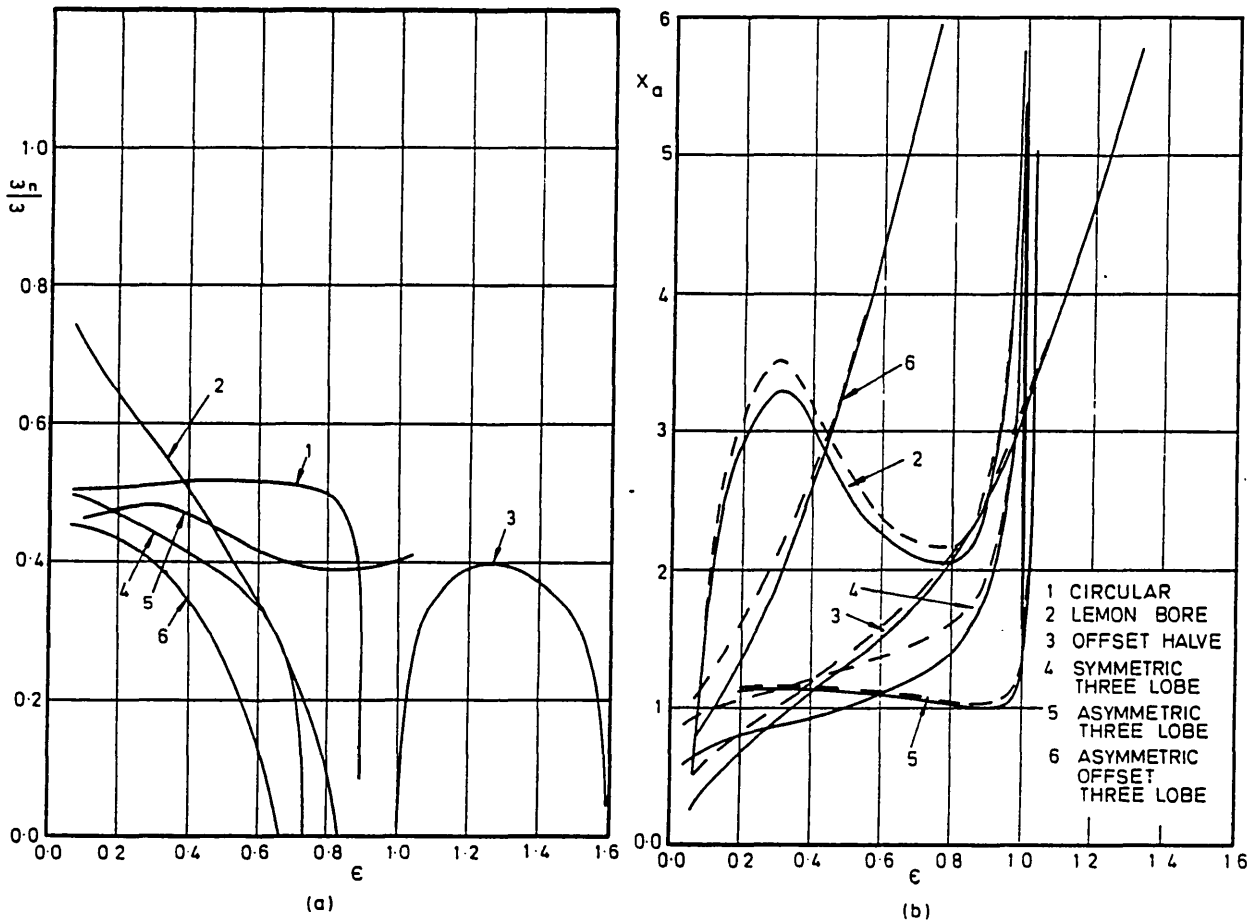


Fig. 12—A comparison of bearing types
 (a) Lowest natural frequency (as for Fig. 11)
 (b) Resonant amplitudes for $S_0 = 0.3$

(25) Malcher, L., "Die Federungs und Dämpfungseigenschaften von Gleitlagern für Turbomaschinen," Dipl. Ing. Thesis, Karlsruhe T. H., 1975.

APPENDIX 1

Stability Analysis

Considering a stiff symmetric rotor running in two identical journal bearings, the linearized equations of motion can be written:

$$M \ddot{x} + a_{xx} \dot{x} + a_{xy} \dot{y} + k_{xx} x + k_{xy} y = 0$$

$$M \ddot{y} + a_{yy} \dot{y} + a_{yx} \dot{x} + k_{yy} y + k_{yx} x = 0$$

where $2M$ is the mass of the rotor.

Introducing the following nondimensional variables:

$$X = x/c ; Y = y/c ; A = a c \omega / F$$

$$K = k c / F ; T = \omega t$$

The equations of motion become:

$$\ddot{X} / S_0 + A_{xx} \dot{X} + A_{xy} \dot{Y} + K_{xx} X + K_{xy} Y = 0$$

$$\ddot{Y} / S_0 + A_{yx} \dot{X} + A_{yy} \dot{Y} + K_{yx} X + K_{yy} Y = 0$$

Note that the stability parameter $S_0 = F/Mc\omega^2$ appears as a result of the nondimensionalization process.

Assuming a solution $X = C_1 e^{\lambda T}$, $Y = C_2 e^{\lambda T}$, and substituting this into the equations of motion, gives:

$$\begin{bmatrix} \lambda^2/S_0 + \lambda A_{xx} + K_{xx} & \lambda A_{xy} + K_{xy} \\ \lambda A_{yx} + K_{yx} & \lambda^2/S_0 + \lambda A_{yy} + K_{yy} \end{bmatrix} \begin{bmatrix} C_1 \\ C_2 \end{bmatrix} = 0$$

For a nontrivial solution, the determinant which is fourth order in λ must be zero. The roots of the equation usually occur in complex conjugate pairs:

$$\lambda_{1,2} = \gamma_1 \pm i \omega_{n1} ; \lambda_{3,4} = \gamma_2 \pm i \omega_{n2}$$

If both values of γ are negative, e.g. $\gamma_1 = -1/2$, $\gamma_2 = -3$, the system is stable. The value of interest is the largest value of γ (i.e. $\gamma_1 = -1/2$), since this represents the bearing damping. If disturbed slightly from the equilibrium position, the shaft vibrates with decaying amplitude at a combination of frequencies ω_{n1} and ω_{n2} .

The threshold value of S_0 where $\gamma_1 = 0$ can be found by trial and error or by applying the Routh criterion.

The bearing coefficients a_{xx} , k_{xx} , etc., were found from the linearization of the oil film forces about the equilibrium position, as described in (17). This can be expressed math-

ematically as a first order Taylor expansion. The Reynolds equation was solved by means of the finite difference method using the Reynolds boundary condition. The oil film forces were calculated from integration of the pressure distribution obtained for small displacements about the equilibrium position of the journal center and for small velocities of the journal center. The gradients of these forces with respect to the perturbations gave the bearing coefficients, the first index being the force direction and the second index the perturbation direction.

APPENDIX 2

Simplified Analysis for Response

The determinantal equation can be factorized as follows:

$$[\lambda - (\gamma_1 + i \omega_{n1})] [\lambda - (\gamma_1 - i \omega_{n1})] [\lambda - (\gamma_2 + i \omega_{n2})] [\lambda - (\gamma_2 - i \omega_{n2})] = 0$$

or:

$$[\lambda^2 - 2\gamma_1 \lambda + (\gamma_1^2 + \omega_{n1}^2)] [\lambda^2 - 2\gamma_2 \lambda + (\gamma_2^2 + \omega_{n2}^2)]$$

If $|\gamma_1| \ll |\gamma_2|$, which is usually the case, the fourth order equation can be reduced to second order:

$$\lambda^2 - 2\gamma_1 \lambda + (\gamma_1^2 + \omega_{n1}^2) = 0$$

which is the same as the characteristic equation of a single degree of freedom system with damping:

$$M \ddot{x} + c \dot{x} + kx = 0$$

If the mass of the rotor is distance e_u from the geometric center, the excitation is $M e_u \omega^2 \cos \omega t$.

After nondimensionalization, this leads to:

$$\ddot{X} + 2\mu (\omega_n/\omega) \dot{X} + (\omega_n/\omega)^2 X = \epsilon_u \cos T$$

where ω_n is the undamped natural frequency, and ω is the

frequency of excitation. The characteristic equation is:

$$\lambda^2 + 2\mu (\omega_n/\omega) \lambda + (\omega_n/\omega)^2 = 0$$

and the roots are:

$$\lambda_{1,2} = -\frac{\omega_n}{\omega} (-\mu \pm i \sqrt{1 - \mu^2}) = \gamma + i \beta$$

whence:

$$\gamma = -\mu \omega_n/\omega \quad (\text{growth or decay rate})$$

$$\beta = \frac{\omega_n}{\omega} \sqrt{1 - \mu^2}$$

$$\left(\frac{\omega_n}{\omega}\right)^2 = \gamma^2 + \beta^2$$

The response X_a (Fig. 12) is given by:

$$X_a = \frac{\epsilon_u (\omega/\omega_n)^2 \cos(T - \phi)}{[(2\mu \omega/\omega_n)^2 + (1 - (\omega/\omega_n)^2)^2]^{1/2}}$$

where $\tan \phi = (2\mu \omega/\omega_n)/(1 - (\omega/\omega_n)^2)$.

The value of ω/ω_n at which the maximum amplitude occurs is given by:

$$\left(\frac{\omega}{\omega_n}\right) = \frac{1}{\sqrt{1 - 2\mu^2}}$$

This is shown by dashed lines in Fig. 12(b). The effect of damping on the growth or decay of motion per revolution can be found as follows:

The envelope curve is:

$$\frac{R}{R_0} = e^{\gamma T}$$

so that the percentage growth per revolution is given by:

$$\frac{R - R_0}{R} = e^{\gamma} - 1$$

Errata: The numerical values on the vertical axis of Fig. 9 should be multiplied by ten. e.g.; 0.05 should become 0.5 etc.

an ASME
publication

\$3.00 PER COPY \$1.50 TO ASME MEMBERS

The Society shall not be responsible for statements or opinions advanced in papers or in discussion at meetings of the Society or at its Divisions or Sections, or printed in its publications. Discussion is printed only if the paper is published in an ASME journal or Proceedings. Released for general publication upon presentation. Full credit should be given to ASME, the Technical Division, and the author(s).

C. M. McC. Ettles
M. Akkoc
A. Cameron

Lubrication Laboratory,
Mechanical Engineering Department,
Imperial College,
London SW7 2BX,
Britain

Inverse Hydrodynamic Methods Applied to Mr. Beauchamp Tower's Experiments of 1885

The experiments of Mr. Beauchamp Tower and their subsequent interpretation by Professor Osborne Reynolds form the basis of all hydrodynamic lubrication theory. In the experiments described in his second report, Tower made nine pressure tapings in a 157 deg partial arc bearing. Reynolds assumed that the film shape corresponded to a circular bearing and analyzed the results on this assumption. Inverse hydrodynamic theory allows the calculation of the actual film shape from this measured pressure distribution. It is found that the film was a slightly convergent wedge which does not correspond to a fitted bearing as assumed by Tower and certainly not to the clearance bearing assumed by Reynolds.

Existing methods of inverse hydrodynamic analysis require the second differential of the pressure profile (or its equivalent in the two-dimensional case) to become zero at some point in the film. The film thickness can be found directly at this point and then elsewhere by the solution of a cubic equation. Two separate and more general methods are developed in this paper in which this requirement for the second differential is unnecessary.

Introduction

This paper describes a computer detective investigation. The Institution of Mechanical Engineers decided on February 20, 1879 to undertake three investigations, one on hardening steel, two on rivetted joints and three "should time and money be found to be sufficient, friction between solids at high velocities." The investigator they chose was Mr. Beauchamp Tower who during his research discovered hydrodynamic lubrication. To celebrate the centenary of this decision the Institution asked one of us to give the "Beauchamp Tower Centenary Lecture" [1].

Tower's results are contained in two reports, one of 1883 [2] and the other of 1885 [3]. The statement that there was a fluid film supporting the load is in the first report and nine pressure readings are in the second, which are shown in Fig. 1.

Reynolds in 1886 [4] derived the equations of hydrodynamic lubrication on which all subsequent theory is based. He used Tower's mid-plane pressure readings to confirm his theory and obtained a most impressive fit. To do this he assumed the bearing was a clearance bearing, though Tower several times comments how it "fitted the shaft beautifully," Reynolds assumed it ran at an eccentricity ratio of 0.5. Using the Laboratory's computer program the axial pressures were

calculated, which of course Reynolds could not do, and in no way did they fit a clearance bearing 4 in. diameter \times 6 in. long as used by Tower.

It occurred to the authors that the actual film shape in this bearing could be obtained by the application of inverse hydrodynamics using Tower's pressure readings. Unfortunately though Tower in his first report gave friction for a grooved bearing over a range of speeds and loads, there are not such data for the exact conditions used in the second paper. This means that the absolute values of viscosity, may be incorrect by 10-15 percent. While this is unfortunate from a historical view point it does not invalidate the technique which has several points of interest to the general public as Dr. Watson pointed out when writing his stories of Mr. Sherlock Holmes.

It is for this reason that this paper has been written and is submitted for publication.

The One-Dimensional Problem

A method of obtaining the film profile from a known pressure distribution is given in 1959 by Dowson and Higginson [5] for the one-dimensional case. An essential feature of the solution is that the second differential of the pressure d^2p/dx^2 passes through zero at some point in the domain. An initial inspection of the pressure distribution obtained by Tower indicated that the second differential was probably negative throughout, which required the development of an alternative and preferably more general solution.

For the one-dimensional case Reynolds equation can be written

Contributed by the Lubrication Division of THE AMERICAN SOCIETY OF MECHANICAL ENGINEERS for presentation at the ASME-ASLE Lubrication Conference, Dayton, Ohio, October 16-18, 1979. Manuscript received by the Lubrication Division July 10, 1979. Paper No. 79-Lub-25.

Copies will be available until July, 1980.

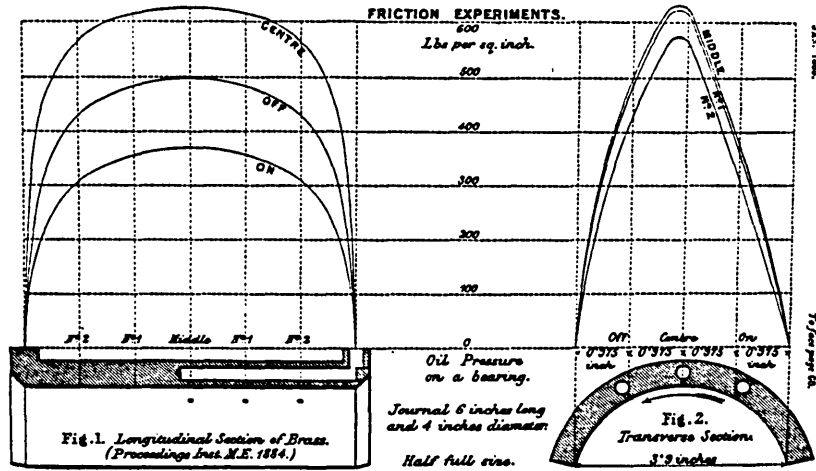


Fig. 1 Beauchamp Tower's axial and circumferential pressures

as

$$\frac{d}{dx} \left(\frac{h^3}{\eta} \cdot \frac{dp}{dx} \right) = 6U \frac{dh}{dx} \quad (1)$$

For the purposes of illustration the viscosity is assumed to be uniform. The following nondimensional substitutions are made;

$$\begin{aligned} x &= x^*B \\ h &= h^*h_i \\ p &= p^*6U\eta B/h_i^2 \end{aligned} \quad (2)$$

where h_i is the film thickness at the loading edge $x^* = 0$ and is unknown. Equation (1) becomes

$$\frac{d}{dx^*} \left(h^{*3} \frac{dp^*}{dx^*} \right) = \frac{dh^*}{dx^*} \quad (3)$$

The expansion of equation (3) allows the gradient dh^*/dx^* to be expressed as

$$\frac{dr^*}{dx^*} = \frac{h^{*3}(d^2p^*/dx^{*2})}{(1 - 3h^{*2}dp^*/dx^*)} \quad (4)$$

Equation (4) is in initial value or Runge-Kutta form, and allows the film profile to be "marched out" from $x^* = 0$ where $h^* = 1$. In actual fact equation (4) represents a special form of the Runge-Kutta formulation known as a shooting problem since the initial film thickness h_i is unknown. The solution proceeds as follows.

A low value of h_i is chosen corresponding to about 25 percent of the estimated value. The assignment of a value to h_i allows trial values of p^* and the differential terms to be evaluated throughout the film. Forwards or backwards differences must be used at the leading and trailing edges. The film profile is marched out through the domain, preferably using a corrector type formula. For example for the m th node.

$$h_m = h_{m-1} + \frac{1}{2} \cdot \Delta x (dh/dx_m + dh/dx_{m-1}) \quad (5)$$

A trial film shape has now been established. To verify that this is correct a finite difference solution for p^* is obtained for the trial shape. Let the pressure field found from the finite difference solution be P^* and the pressure field used for the solution of the film shape be p^* . The general magnitude of the pressures will be similar but the shape will be different. An estimate of the lack of fit can be obtained from the residual R

$$R = \sum_1^M |(1 - P^*/p^*)| \quad (6)$$

where M is the number of nodes. The initial film thickness h_i is varied until the residual is a minimum.

Fig. 2 shows the values of p^* , dp^*/dx^* and d^2p^*/dx^{*2} for a plane pad with convergence of 1.5:1. It should be noted that in this example the second differential is negative throughout. The dimensional pressure field to be used in the solution was obtained by choosing particular values of η , U and B , and an initial film thickness h_i of 1×10^{-3} in. The film shape produced by the Runge-Kutta method should therefore be a plane reducing from 1×10^{-3} in. at the inlet to two thirds of this value at the outlet. Fig. 3 shows for eleven nodes ($M = 11$) the film shapes obtained using successive values of h_i . The correct (plane) shape is shown as a dashed line. The behavior of the residual as h_i is varied is shown in Fig. 4 and reaches a sharp minimum at the known solution.

The pressure tapings made by Tower correspond to a mesh of five nodes in the circumferential (x) direction and four nodes in the axial (y) direction (i.e. $M = 5, N = 4$). The mesh in the x direction is non-uniform which was allowed for in the treatment of Tower's results. Since the mesh is extremely coarse a smoothing technique was used for all differential terms to give a more even distribution of values.

Nomenclature

A = shape constant for leading edge film; equation (17)
 B = length of pad in direction of motion
 c = radial clearance of journal bearing
 D = shaft diameter
 h = film thickness
 $H = h/\bar{h}$
 L = axial length of bearing
 m = node number in x direction
 M = total number of nodes in x or θ direction
 N = total number of nodes in axial (y) di-

rection
 p = pressure
 P = pressure found from finite difference solution
 R = residual; equation (6)
 U = sliding speed
 x = coordinate in direction of sliding (Fig. 8)
 y = coordinate in axial direction (Fig. 8)
 $\alpha = 4L^2/B^2$
 ϵ = eccentricity ratio of journal bearing
 η = viscosity

θ = coordinate in direction of sliding
 τ = shear stress
 ϕ = altitude angle of journal bearing

Superscripts

$*$ = nondimensional
 $-$ = where $\partial p/\partial x = 0$

Subscripts

a = value of x where $d^2p/dx^2 = 0$
 i = initial; value at $x = 0$
 o = at trailing edge

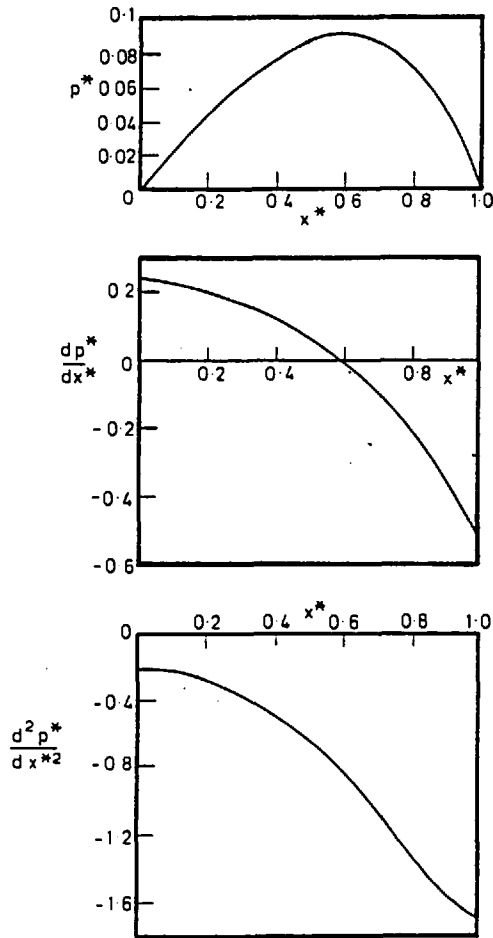


Fig. 2 Pressure profile and differential terms for an infinitely wide plane pad where $h_i/h_0 = 1.50$

For example at nodes two and node m

$$\left(\frac{dp}{dx}\right)_2 = \frac{2}{3} \left(\frac{dp}{dx}\right)_2 + \frac{1}{3} \left(\frac{dp}{dx}\right)_3$$

$$\left(\frac{dp}{dx}\right)_m = \frac{1}{4} \left(\frac{dp}{dx}\right)_{m-1} + \frac{1}{2} \left(\frac{dp}{dx}\right)_m + \frac{1}{4} \left(\frac{dp}{dx}\right)_{m+1}$$

Both the differential terms in each direction were smoothed in this way in the test cases and in Tower's results. In the majority of test cases the grid was uniform.

An examination of equation (4) shows that the method is likely to fail when the denominator term becomes zero, i.e. when

$$1 - 3h^2(dp^*/dx^*) = 0 \quad (7)$$

For the example in Figs. 2, 3, 4 this occurs at a value of h_i considerably greater than the solution value and is of no consequence. However this behavior cannot be guaranteed for all pressure profiles. Fig. 5 shows the pressure and differential terms for a plane one dimensional wedge of convergence 4:1. An important feature in this example is that the second differential passes through zero. Such a profile can be treated by the method of Dowson and Higginson [5] as follows.

Expanding equation (3) gives;

$$h^3 \frac{d^2p}{dx^2} + 3h^2 \frac{dh}{dx} \frac{dp}{dx} = \frac{dh}{dx} \quad (8)$$

The stars * have been omitted. At the point $x = a$ where the second differential is zero this reduces to;

$$\frac{dh}{dx} \left(1 - 3h^2 \frac{dp}{dx}\right)_a = 0 \quad (9)$$

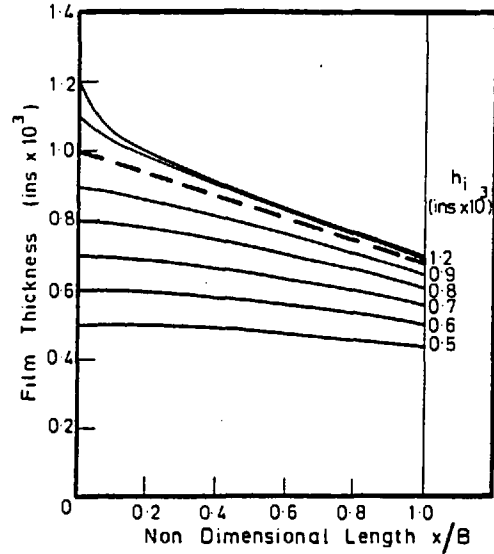


Fig. 3 Film shapes found for Fig. 2 by variation of h_i through the known value

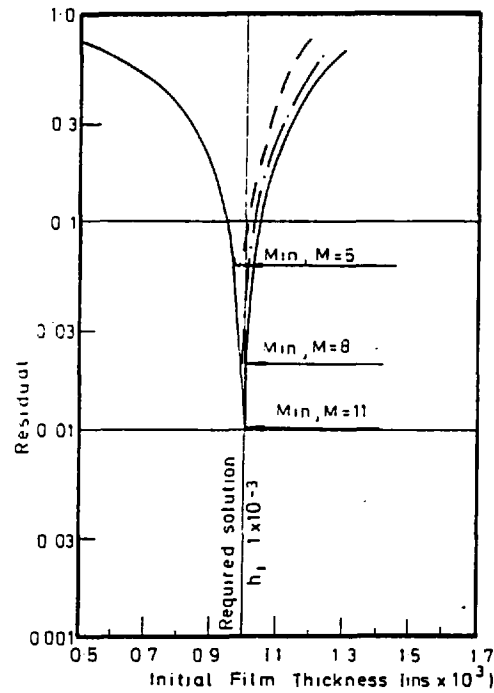


Fig. 4 Variation of residual for case in Fig. 2

This gives two solutions;

$$\left(\frac{dh}{dx}\right)_a = 0 \quad (10)$$

or

$$h_a = \sqrt{\frac{1}{3(dp/dx)_a}} \quad (11)$$

If (dh/dx) is known to be non zero at this point then the film thickness h_a can be found directly from (11) since the dimensional form of this equation is

$$h_a = \sqrt{\frac{2\eta U}{(dp/dx)_a}} \quad (12)$$

The substitution of (11) into the integrated form of (3) gives

$$\bar{h} = \frac{2}{3} h_a$$

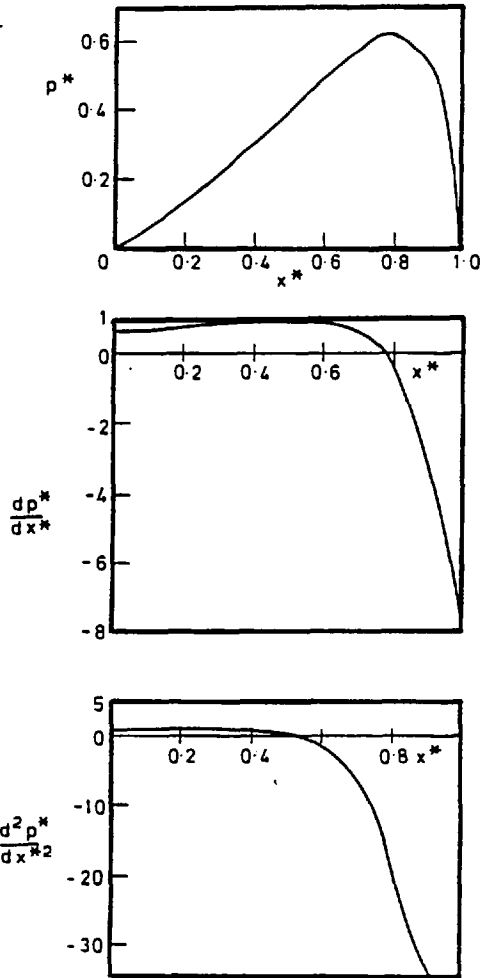


Fig. 5 Pressure profile and differential terms for an infinitely wide plane pad where $h_i/h_0 = 4.0$

The film thickness may now be determined at any point by rearranging equation (8) as

$$H^3 + \frac{H}{K} + \frac{1}{K} = 0 \quad (13)$$

where $H = h/\bar{h}$ and K in dimensional units is $K = \bar{h}^2(dp/dx)/6\eta U$.

The cubic equation can be solved at each node, giving two positive and one negative root or a positive and two complex roots. The behavior of the equation is discussed in detail by Ruskell [6]. In the case of two positive roots the "correct" value is usually obvious, and can be found by solving the equation at a node adjacent to $x = a$.

Equation (9) is also relevant to the Runge-Kutta method given in equation (4). In practice the failing case when $1 - 3h^2(dp/dx) = 0$ does not occur, since as this expression tends to zero the second differential also tends to zero. By L'Hopital's rule;

$$\left(\frac{dh}{dx}\right)_a = \lim_{h \rightarrow h_a} \frac{dh}{dx} = \sqrt{-\frac{1}{2} h_a^4 (d^3 p^*/dx^{*3})}$$

This is shown by Ruskell [6] and can be verified for any integrable function $h = f(x)$, e.g. $h = h_0 e^{\alpha x}$. In principle, therefore, there should be no difficulty in applying the Runge-Kutta method to a case such as Fig. 5 where the second differential does pass through zero, since a node at this point can be avoided by a suitable choice of mesh. However it was found that the corrector formula (5) failed to converge at the end of the first step in spite of heavy under relaxation, while any formula of the predictor type (forward integrators) produced unacceptable divergent oscillation. Similar problems can occur in nonlinear vibration analysis and must be treated using a "stiffly stable" method of which the backwards Euler formula is the sim-

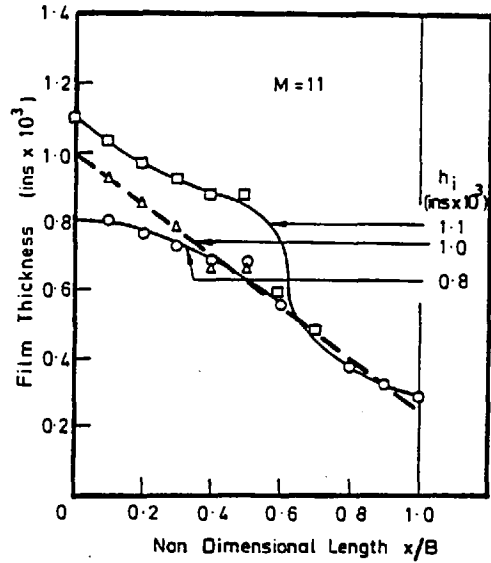


Fig. 6(a) Eleven nodes ($M = 11$)

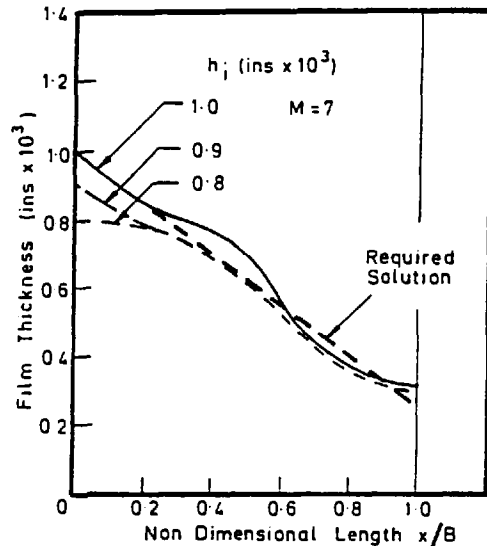


Fig. 6(b) Seven nodes ($M = 7$)

Fig. 6 Film shapes produced for Fig. 5 by variation of h_i through the known value

plest.

$$h_m = h_{m-1} + \Delta x \cdot (dh/dx)_m \quad (14)$$

This formula was applied to each step by varying h_m^* over the range 1.5 to 0 in steps of 0.001. Let h_{m1} be the trial value of h_m that is systematically varied and h_{m2} in the value of h_m obtained. A residual R is formed for each trial value as $R = |1 - (h_{m1}/h_{m2})|$ and stored in an array. When all trial values have been attempted the array is scanned for the minimum residual, giving the appropriate value of h_m . In general this method worked well although perhaps lacking in finesse. In some test cases where h_i was not the correct (known) value the residual curve formed a saddle at the correct value of h_m and reached a slightly lower minimum at some other value of h_m which apparently corresponded to the other real root of the cubic equation (13).

The film profiles for the plane pad with 4:1 convergence are shown in Figs. 6(a) and 6(b) for 11 and 7 nodes, respectively. The uneven shape in Fig. 6(a) occurs due to the very low local value of the second differential at $x^* = 0.5$ where a node occurs for $M = 11$. This value is avoided for $M = 7$ and a smoother curve results. The variation of re-

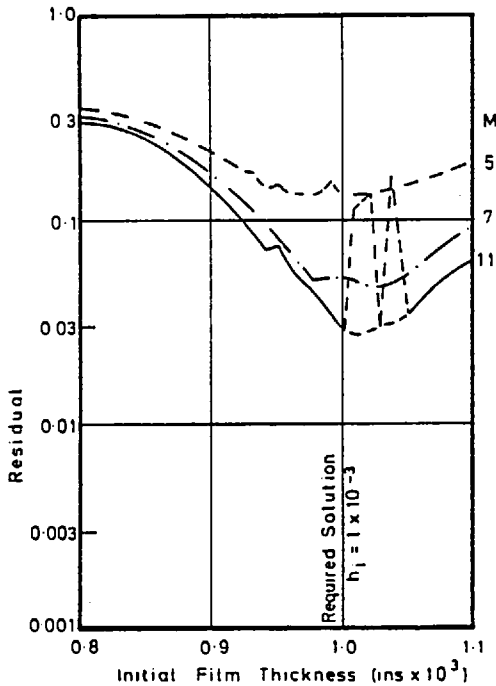


Fig. 7 Variation of residual for case in Fig. 5

residual with h_i is shown in Fig. 7. The discontinuities in the curves are due to the occasional selection of the wrong root, which apparently occurs due to truncation error.

Use of the Runge-Kutta Method in Two Dimensions

The nondimensional form of the Reynolds equation in two dimensions is;

$$\frac{\partial}{\partial x^*} \left(h^{*3} \frac{\partial p^*}{\partial x^*} \right) + \alpha \frac{\partial}{\partial y^*} \left(h^{*3} \frac{\partial p^*}{\partial y^*} \right) = \frac{\partial h^*}{\partial x^*} \quad (15)$$

Where the nondimensional forms given by equation (2) apply and in addition;

$$\alpha = 4B^2/L^2$$

$$y = y^*L/2$$

The equation can be set in Runge-Kutta form as;

$$\frac{\partial h}{\partial x} = \frac{h^3 \left(\frac{\partial^2 p}{\partial x^2} + \alpha \frac{\partial^2 p}{\partial y^2} \right) + 3ah^2 \frac{\partial h}{\partial y} \cdot \frac{\partial p}{\partial y}}{\left(1 - 3h^2 \frac{\partial p}{\partial x} \right)} \quad (16)$$

Since the cross gradient $(\partial h/\partial y)$ appears on the right-hand side, equation (16) must be applied recursively. Considering the mesh system shown in Fig. 8, the film thicknesses at any vertical line of nodes m can be found by initially assuming that $(\partial h/\partial y) = 0$. The set of film thicknesses so determined allows a new trial set of $(\partial h/\partial y)$ to be found and the cycle continues until convergence. The corrector

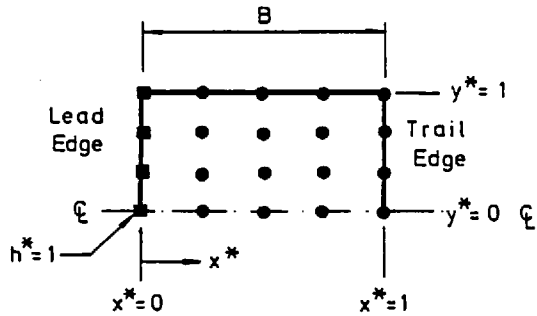


Fig. 8 Mesh system for two dimensional case

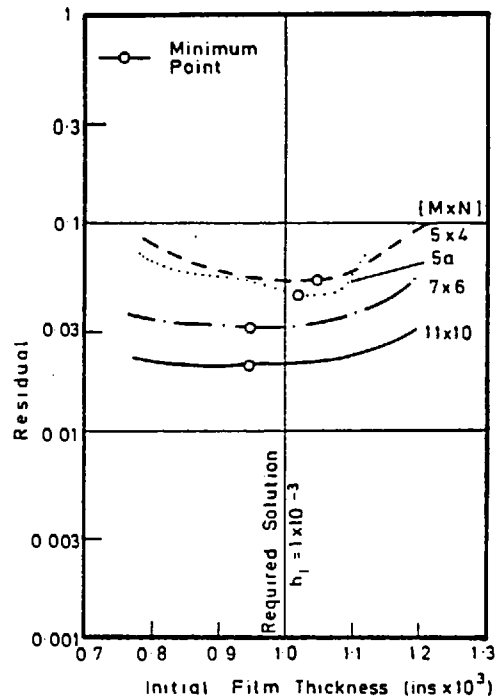


Fig. 9 Residual for a plane pad of $L/B = 1.114$ and convergence 2:1 as h_i is varied through the known value

formula (5) was used to advance from one line of nodes to the next so that an individual step involved two nested loops, for the cross gradients and for the closed integration of equation (16).

The pressure is nondimensionalized according to h_i , the film thickness on the center line at the leading edge where $h^* = 1$. It is essential to the method that the film thickness at other points on the leading edge are defined. In the analysis of Tower's results the leading film was defined as;

$$h_i = 1 + Ay^{*2} \quad (17)$$

Where A is unknown and is found by systematic variation to give the minimum residual. This is subsequently discussed. It should be

Table 1 Best film shape obtained for plane pad of $L/B = 1.114$ with 2:1 convergence. $M = 5$, $N = 4$. Distorted mesh according to tapping points used by Tower

	Outer Edge					
	1.040	.987	.815	.700	.619	
Leading Edge	1.040	.890	.761	.656	.564	Trailing Edge
	1.040	.846	.733	.640	.553	
Center line	1.040	.820	.721	.636	.550	Center line
Required Solution	1.000	.845	.750	.655	.500	

noted that equation (17) allows $(\partial h_i / \partial y)_{y=0} = 0$. In the analysis of Tower's data it was assumed that $(\partial h / \partial y) = 0$ at all nodes on the center line.

Fig. 9 shows the variation of residual with initial film thickness for various mesh sizes ($M \times N$), where N is the number of nodes in the axial direction. The test case considered is a plane pad of $L/B = 1.114$ (corresponding to Tower's dimensions) and a convergence of 2:1. In this case $A = 0$ in equation (17). In Fig. 9 the residual change with h_i is seen to be mild. The minimum points (according to the third significant figure of the residual) are marked in Fig. 9 as small circles. The case marked 5a is for a distorted mesh in the x direction corresponding to Tower's tapping points.

The "best" film shape for a 5×4 nonuniform mesh determined according to the minimum residual is given in Table 1. The required solution for the plane pad (where $\partial h / \partial y = 0$) is also shown. The film thickness along the outer edge is seen to be most in error. This is apparently due to truncation effects in the calculation of differential terms at the edge using offset differences. The agreement is considered acceptable considering the very coarse nonuniform mesh used.

The application of the Runge-Kutta method to Tower's results is given later and is compared to the results from a second method which will now be developed.

A Second Method Adapted From Morton [7]

The nondimensional form of Reynolds equation for a journal

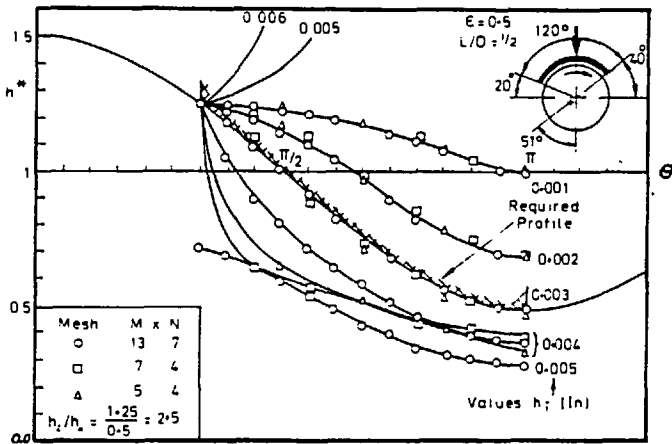


Fig. 10 Film shapes from the cubic equation method for a 120 deg partial arc bearing ($L/D = 1/2$, $\epsilon = 0.5$, $\partial h / \partial y = 0$) as h_i is varied through the known value

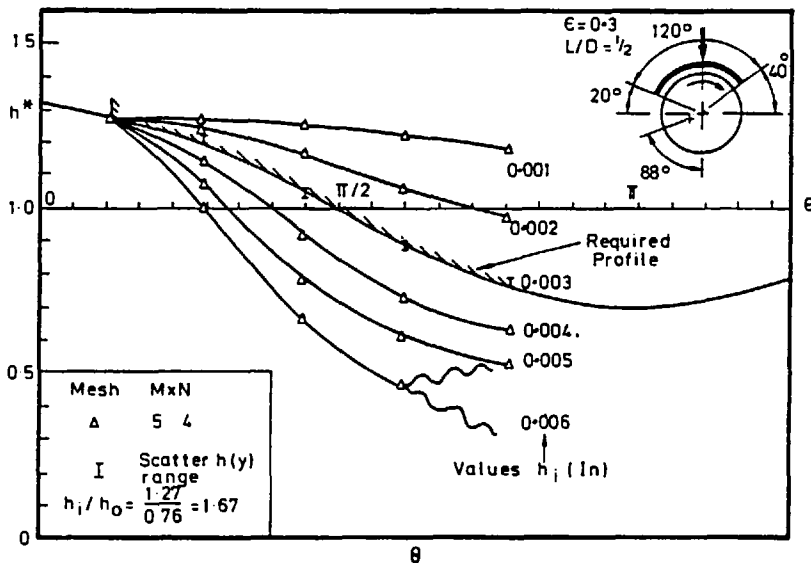


Fig. 11 Film shapes from the cubic equation method for 120 deg partial arc bearing where $h = f(\theta)$, $M = 5$, $N = 4$

bearing can be written;

$$\frac{\partial}{\partial \theta} \left(h^3 \frac{\partial p}{\partial \theta} \right) + \left(\frac{D}{L} \right)^2 \frac{\partial}{\partial y} \left(h^3 \frac{\partial p}{\partial y} \right) = \frac{\partial h}{\partial \theta} \quad (18)$$

In a short appendix in (7) Morton develops an inverse hydrodynamic method as follows. If $\partial h / \partial y = 0$ throughout and $\alpha = (D/L)^2$, equation (18) can be expanded as;

$$h^3 \left(\frac{\partial^2 p}{\partial \theta^2} + \alpha \frac{\partial^2 p}{\partial y^2} \right) + h^2 \cdot 2 \frac{dh}{d\theta} \frac{\partial p}{\partial \theta} - \frac{dh}{d\theta} = 0$$

For the point where

$$\frac{\partial^2 p}{\partial \theta^2} + \alpha \frac{\partial^2 p}{\partial y^2} = 0 \quad (19)$$

then $dh/d\theta = 0$
or

$$h_a = \sqrt{\frac{1}{3(\partial p / \partial \theta)_a}} \quad (20)$$

The dimensional form of (20) is similar to (12) so that provided (19) applies somewhere in the film, a dimensional value of film thickness can be determined at that point. Reynolds equation can then be set in cubic form similar to equation (13).

The restriction that (19) apply is actually unnecessary. If $h = f(\theta, y)$, Reynolds equation (18) can be integrated from zero to any θ as follows

$$\left(h^3 \frac{\partial p}{\partial \theta} \right)_\theta - \left(h^3 \frac{\partial p}{\partial \theta} \right)_0 + \alpha \int_0^\theta \frac{\partial}{\partial y} \left(h^3 \frac{\partial p}{\partial y} \right) = h - h_0 \quad (21)$$

with the boundary condition that $h(0, 0) = 1$ and $h(0, y)$ is defined. Equation (21) can be set in the form

$$h^3 \frac{\partial p}{\partial \theta} - h + G = 0 \quad (22)$$

where

$$G = h_0 - \left(h^3 \frac{\partial p}{\partial \theta} \right)_0 + \alpha \int_0^\theta \left(3h^2 \frac{\partial h}{\partial y} \frac{\partial p}{\partial y} + h^3 \frac{\partial^2 p}{\partial y^2} \right) d\theta$$

The calculation cycle proceeds as follows;

1. Assume a value of A in equation (17)
2. Assume a dimensioned value of h_i
3. Assume $h(0, y)$
4. Calculate G
5. Solve equation (22), obtaining $h(\theta, y)$
6. If $H(\theta, y) \neq h(\theta, y)$ return to 3

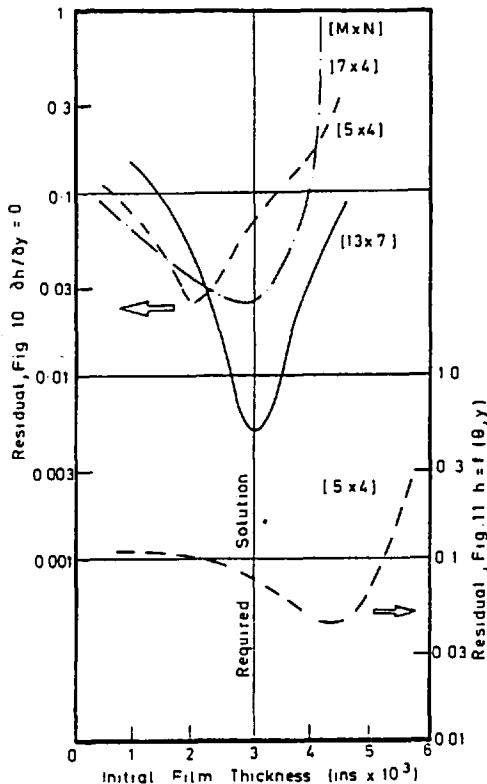


Fig. 12 Variation of residual for cases in Figs. 10, 11

7. Return to 2, varying h_i until a minimum residual compared to a finite difference solution is obtained.
8. Return to 1, varying A until the least residual is obtained.

Figs. 10 and 11 show the application of this method to two test cases of a partial arc bearing where $A = 0$. In both cases the required solution for h_i is 3×10^{-3} in. In Fig. 11 for 5×4 mesh, the scatter of results for h in the axial direction is seen to be small and a considerable improvement over the film shape shown in Table 1 for the Runge-Kutta method. The behavior of the residual for the two cases is shown in Fig. 12. The correct minimum position is obtained for a (13×7) or (7×4) mesh system but not for a (5×4) mesh which corresponds to Tower's case. This was subsequently improved by the use of smoothing of the pressure differential terms, as in the Runge-Kutta method.

The behavior of the residual for Tower's experimental results is shown in Fig. 13 for various values of A . It was found that $A = 0.1$ gave the least residual.

Determination of Mean Viscosity

The importance of viscosity in lubrication was not apparent until Reynolds' paper of 1886 and Tower in his second report gives no mention of the oil characteristics except to state that it was a "heavy mineral oil." A known value of viscosity is essential if absolute values of film shape are to be determined from inverse hydrodynamics. The absolute value of film shape is dependent on the ratio η/h_i^2 which is put equal to C_1 (say). All calculated film shapes were obtained assuming a viscosity of 5 poise.

Unfortunately Tower gives results for friction only at 20 rpm and not at 150 rpm, the speed he used when the pressure tappings were made. He states (second report) that "the pressure indicated by the pressure gauge at 20 revolutions per minute was the same as that at 150, thus showing that the brass was completely oil-borne at the lower speed as it had been at the higher."

Friction measurements were carried out at a range of loads, including 8008 lbs at which the pressure readings were taken. If both load and friction are known, as is the case for 20 rpm, then the viscosity can be found as follows.

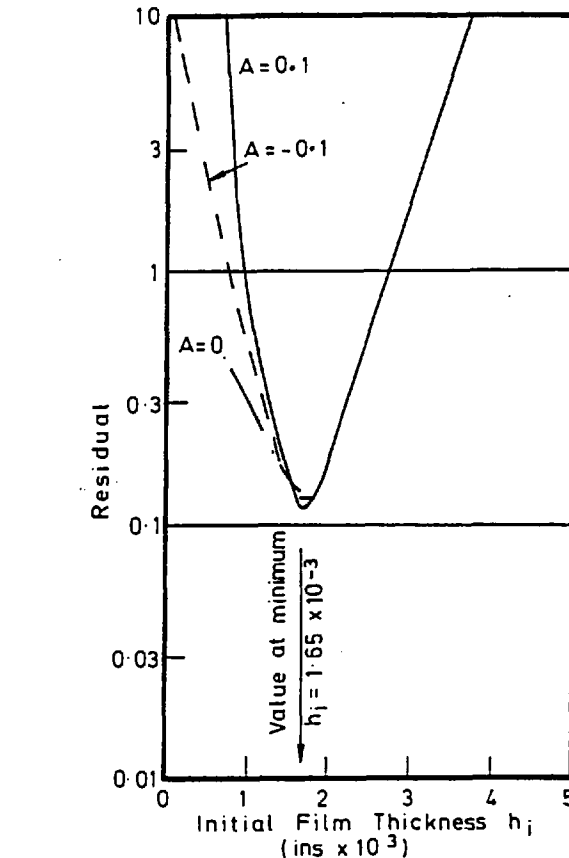


Fig. 13 Variation of residual for Tower's data using cubic equation method. "A" refers to film shape constant in equation (17)

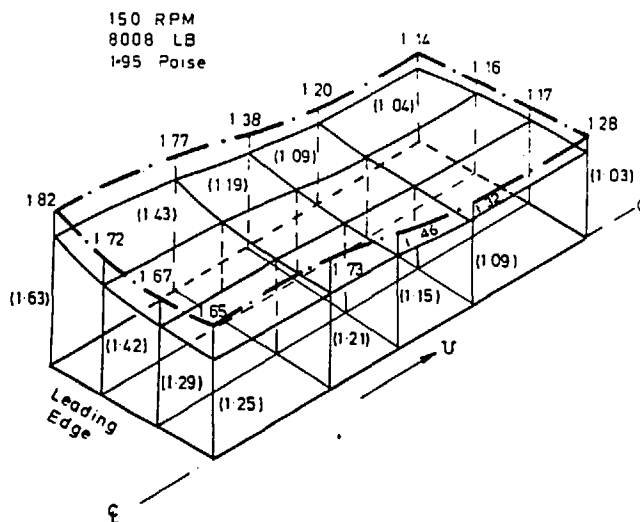


Fig. 14 Isometric view of film shape in Tower's bearing as found by the Runge-Kutta method (unbracketed values) and the cubic equation method (bracketed values). Units are in. $\times 10^{-3}$

The shear stress τ on the bearing is given by

$$\tau = \frac{\eta U}{h} + \frac{h}{2} \cdot \frac{\partial p}{\partial x}$$

and may be integrated to give the friction. The result for friction is dependent on the ratio $\eta/h_i = C_2$ (say). The numerical values for C_1 and C_2 were determined for 20 rpm on the somewhat shaky assumption that the pressure distribution was unchanged from 150 rpm. This allowed the calculation of viscosity and initial film thickness h_i as

$$\eta = 1.95 \text{ Poise}$$

$$h_i = 0.70 \times 10^{-3} \text{ Ins.}$$

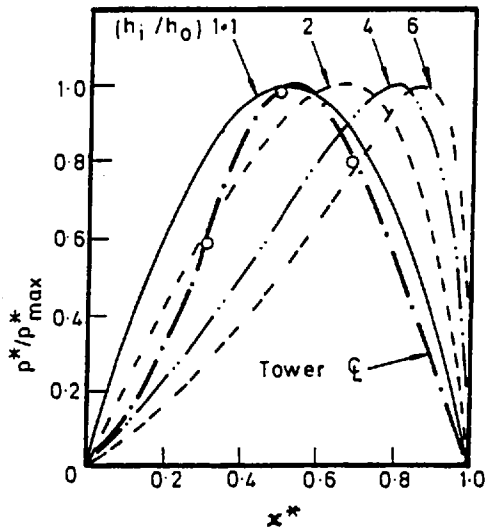


Fig. 15 A comparison of pressure profiles for a plane converging wedge with Tower's result on the bearing center line

Tower states that the oil bath was maintained at 90°F for all experiments and it is probably reasonable to assume that the same viscosity applies at 150 rpm. On this basis the value of h_i at 150 rpm was found to be 1.65×10^{-3} inches from the cubic equation method and 1.25×10^{-3} in. from the Runge-Kutta method.

Results for Tower's Bearing

The full film shape from both methods is shown in Fig. 14. The gap at the leading edge is found to be flared in both cases, and both methods produced a similar shape although with different absolute values. The average convergence in each case is small, being 1.35:1 for the Runge-Kutta and 1.44:1 for the cubic equation method. The low degree of convergence is to be expected from the general shape of Tower's pressure result. Fig. 15 shows the effect of convergence on film shape for a plane pad, and it is clear that the convergence in Tower's bearing is small.

Equation (16) for the two-dimensional Runge-Kutta method can be extended to include the effect of varying viscosity. Some trial runs were made in which the viscosity was assumed to decrease in the direction of motion by amounts varying between +40 and -10 percent. The minimum residual was in all cases higher than that with no viscosity change, and consequently the viscosity in the film was taken as uniform throughout.

The Use of Tower's Results by Reynolds

It was an obvious point of pride in both Tower's reports that the bearing was "beautifully fitted" to the shaft, implying that the radial clearance c was zero. The choice of a clearance must have been an enigma for Reynolds who also had to pick figures for viscosity and eccentricity ratio ϵ for his theory to apply. It appears that Reynolds chose a value of $\epsilon = 0.5$ on a fairly arbitrary basis and allowed c^2/η in the load number to be a disposable constant.

In Fig. 16 the authors rather ungraciously compare the result for $\epsilon = 0.5$ with the film shape found by the cubic equation method. An attitude angle $\phi = 45$ deg is assumed from established theory for a 157 deg arc with $\epsilon = 0.5$ and the curves have been made to coincide at the mid point of the bearing (i.e. on the load line). Fig. 16 shows that if Tower's bearing can be said to have a radial clearance then the value of c was 2.26×10^{-3} in which corresponds closely to modern practice.

Conclusions

Present methods in inverse hydrodynamics are based on the integration of Reynolds equation to form a cubic equation. If the second

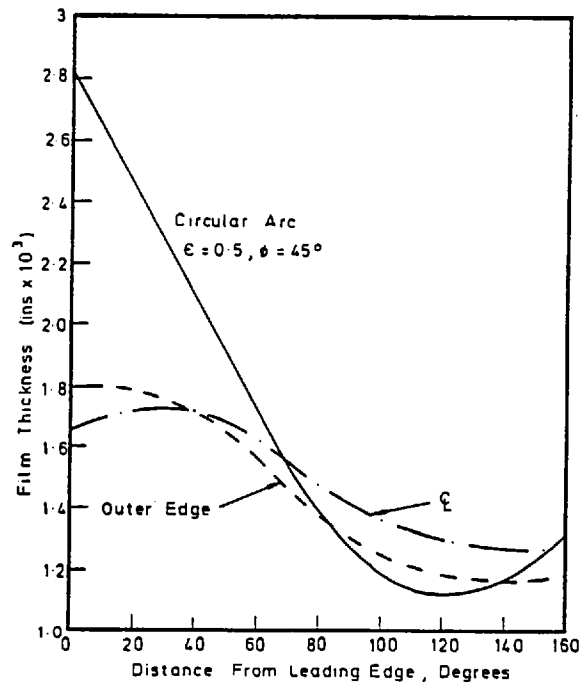


Fig. 16 The best fit for a circular bearing to the result from the cubic equation method

differential of the pressure profile (or its equivalent in the two-dimensional case) falls to zero at any point, the film thickness may be determined there directly, and elsewhere by the solution of the cubic. In this paper this method has been further developed so that the occurrence of a zero second differential is unnecessary. The calculation then becomes iterative, in which the appropriate value of dimensional film thickness h_i is varied to give the minimum residual between the pressure profile assumed and that obtained from a finite difference solution using the film shapes from successive trial values of h_i .

The inverse hydrodynamics problem can also be set up in Runge-Kutta form and film shape marched out from a trial value of h_i . Closure in the true value of initial film thickness is obtained as before by comparison with the finite difference solution. Both methods require the film profile at the leading edge to be defined, although this is not necessary if the method due to Morton can be applied.

Difficulties occur with the Runge-Kutta method where the second differential of pressure is positive. These can be overcome at the expense of accuracy by using a stiffly stable method of film thickness propagation such as the backwards Euler scheme.

In general the authors prefer the modified cubic equation method (as developed here) to the Runge-Kutta since

- (a) The method can be easily applied regardless of the second differential term, which (for the x direction) does not appear in the calculation;
- (b) The integration necessary is from the current node to the start of the film which imposes an increasing degree of smoothing as the calculation proceeds.

References

- 1 Cameron, A., "Beauchamp Tower Centenary Lecture," *Inst. Mech. Eng.*, London, 1979, Vol. 193, No. 25.
- 2 Tower, Beauchamp, First report, *Proc. Inst. Mech. Eng.*, 1883, Vol. 34, pp. 32-666.
- 3 Tower, Beauchamp, Second report, *Proc. Inst. Mech. Eng.*, 1885, Vol. 36, pp. 39-70.
- 4 Reynolds, O., *Phil. Trans. Roy. Soc.*, 1886, Vol. 177, pp. 157-234.
- 5 Dowson, D., and Higginson, G. R., *J.M.E.S.*, Vol. 1, 1959, pp. 6-15.
- 6 Ruskell, L. E. C., "Reynolds Equation and Elastohydrodynamic Lubrication in Metal Seals," *Proc. A. Soc. A*, Vol. 349, 1976, pp. 383-396.
- 7 Morton, P. G., "Measurement of the Dynamic Characteristics of a Large Sleeve Bearing," *ASME JOURNAL OF LUBRICATION TECHNOLOGY*, Jan. 1971, pp. 143-150.